Large-eddy simulation of purely buoyant diffusion flames

Li Ma

AIX-MARSEILLE UNIVERSITÉ

ECOLE DOCTORALE DES SCIENCES POUR L'INGÉNIEUR : MÉCANIQUE, PHYSIQUE, MICRO ET NANOÉLECTRONIQUE

UMR 7343 - Institut Universitaire des Systèmes Thermiques et Industriels

Thèse pour obtenir le grade universitaire de Docteur

Discipline: Sciences pour l'Ingénieur
Spécialité: Énergétique

Li MA

Large-eddy simulation of purely buoyant diffusion flames

Soutenue le 04 Novembre 2020

Arnaud TROUVÉ	University of Maryland	Rapporteur
Dany ESCUDIÉ	INSA de Lyon	Rapporteuse
Denis LEMONNIER	Université de Poitiers	Président du jury
Yi WANG	FM Global	Examinateur
Olivier VAUQUELIN	Aix-Marseille Université	Examinateur
Jean-Louis CONSALVI	Aix-Marseille Université	Directeur de thèse
Fatiha NMIRA	EDF R&D	Responsable industriel

Remerciement

Ces trois années de recherche est une très belle expérience au sein du département MFEE d'EDF R&D, en collaboration avec l'IUSTI d'Aix-Marseille Université. Le succès de cette thèse est le fruit des efforts grâce aux nombreuse personnes. Je tiens d'abord à remercier Isabelle Flour, Bruno Audebert et Christelle Raynaud pour leur accueil chaleureux dans le département. Je remercie également Olivier Pouliquen et Lounes Tadrist de m'avoir accueilli dans le laboratoire IUSTI.

Je remercie grandement mon encadrante industrielle, Fatiha Nmira, et le directeur de thèse, Jean-Louis Consalvi, qui m'a encadré tout au long de cette thèse. Grâce à leurs brillantes qualités scientifiques, professionnelles, aussi humaines, j'ai réussi à mener la thèse à son terme et développé beaucoup d'aptitudes pour la recherche et la carrière professionnelle.

J'adresse mes remerciements à Arnaud Trouvé, et à Dany Escudié, en acceptant d'être rapporteurs de cette thèse. En outre, je remercie vivement Denis Lemonnier, Yi Wang et Olivier Vauquelin d'avoir participé à la soutenance de cette thèse, malgré la circonstance sanitaire liée à la Covid-19.

J'exprime ma gratitude à Martin Ferrand, Erwan Le Coupanec et Yvan Fournier, pour leur conseils et aides très utiles à l'égard du développement et l'utilisation de *Code_Saturne* durant la thèse.

Merci aussi à Jean-Marc Hérard, il est intervenu plusieurs fois dans l'appui des travaux. J'ai beaucoup apprécié son expertise et ses propositions apportées.

Mes remerciements vont aussi aux collègues du groupe I8D pour leur chaleureux accueil et de bons moments d'échange entre nous. En particulier, merci à Hamza Boukili, il est très bienveillant et m'a beaucoup aidé. Les discussions et les pauses cafés ont formidablement enrichi la vie pendant ces trois années.

Je remercie les doctorants avec qui j'ai partagé le temps de recherche, Lucie Quibel, Vladimir Paul, Clément Colas, Riccardo Milani, Germain Davy et aussi Sarah Chatenet. Les moments avec eux resteront toujours dans ma mémoire.

En fin, je remercie ma mère, mon père, Yu Yang et tous mes amis. Leur soutien et encouragement me font passer cette page fabuleuse dans ma vie.

Résumé

Cette étude rapporte le développement d'un modèle numérique basé sur les simulations à grandes échelles en vue de simuler des panaches de feu bien-ventilés et sous-ventilés et entièrement contrôlés par les forces de flottabilité. Un nouvel algorithme de résolution pour les d'écoulements à densité variable à faible nombre de Mach, précis au second ordre en temps et espace, a été développé et vérifié afin de décrire avec précision les processus instationnaires forts liés à la nature purement contrôlée par les forces de flottabilité des écoulements. Des modèles de sous-maille à l'état de l'art pour la turbulence, la combustion et le rayonnement ont été développés, incluant les modèles non-adiabatiques SLF (steady laminar flamelet) et FPV (flamelet/progress variable). Le RCFSK a été considéré comme référence pour la modélisation des propriétés radiatives des gaz et la performance de modèles plus simples, tels que des versions non-grises et grises du modèle à somme pondérée des gaz gris, a été évaluée. Le modèle numérique a été intensivement validé en simulant plusieurs panaches de feu non-réactifs et réactifs. Le modèle s'est avéré capable de reproduire avec une grande fidélité les structures dynamiques et radiatives de ces panaches dans des configurations ventilées et sous-ventilées sans ajuster aucun des paramètres du modèle. En particulier, le modèle FPV permet de traiter des conditions d'oxydant dilué en oxygène proches de l'extinction. Plusieurs problèmes de modélisation spécifiques ont également été étudiés au cours de ce travail. L'importance de capturer directement les instabilités laminaires thermo-convectives, qui se forment périodiquement à la base des panaches de feux et croissent pour générer les larges tourbillons régissant le processus de mélange, a été démontrée. La formation et la croissance de ces instabilités sont significativement affectées par la géométrie du brûleur qui doit être scrupuleusement cohérente avec les expériences pour obtenir une description précise de la dynamique du panache de feu. Les versions grises des modèles à somme pondérée de gaz gris doivent être évitées tandis que les versions non-grises de ce modèle peuvent être une alternative raisonnable pour la simulation de feux de nappe sans suie. Finalement, les interactions rayonnement-turbulence de sous maille ont un effet non-négligeable sur la structure de flamme et les pertes radiatives et ce, même pour des feux de nappe à l'échelle du laboratoire.

Abstract

This study reports the development of a LES-based numerical model dedicated to the simulation of well-ventilated and under-ventilated purely buoyant fire plumes. A new second-order low-Mach number variable-density flow solver was developed and verified in order to describe accurately the strong unsteady processes related to the purely buoyant nature of the flow. State-of-the art subgrid-scale turbulence, combustion and radiation models were specifically developed, including the non-adiabatic SLF (steady laminar flamelet) and FPV (flamelet/ progress variable models). The RCFSK was considered as reference radiative property model whereas the performance of simpler models, including non-grey and grey versions of the weighted-sum-of-grey gases was assessed. The numerical model was exhaustively validated by simulating several well-documented non-reactive and reactive buoyant fire plumes. It was found capable to reproduce with high fidelity the dynamic and radiative structures of non-luminous fire plumes in both ventilated and under-ventilated configurations without adjusting any model parameters. In particular, the FPV allows addressing oxygen-diluted oxidizer conditions close to extinction. Several specific modelling issues were also investigated during the course of this work. The importance of resolving the laminar instabilities, which form periodically at the base of purely buoyant fire plumes and grow to generate energy containing structures that govern the mixing process, was demonstrated. The formation and growth of these instabilities are significantly affected by the burner geometry that has to be scrupulously consistent with the experiments to achieve an accurate description of the fire plume dynamics. The grey version of the weighted-sum-of-grey gases models have to be avoided whereas the non-grey versions can be a reasonable alternative for non-sooting pool fires. Finally, neglecting subgrid-scale turbulence-radiation interaction affects significantly the predictions of the fire plume structure and radiative heat flux even for lab-scale pool fires.

Contents

List of Figures

List of Tables

Abbrievation

CDS	Central difference scheme
CF	Continuous flame
CFL	Courant-Friedrichs-Lewy number
DEDM	Dynamic linear eddy diffusivity model
DGGM	Dynamic generalized gradient model
DLGGM	Dynamic full linear generalized gradient model
DOM	Discrete ordinates method
DSM	Dynamic Smagorinsky model
EDC	Eddy dissipation concept
EDM	Linear eddy diffusivity model
FDF	Filtered density function
FPV	Flamelet/Progress variable
FS	Full-spectrum
FSCK	Full-spectrum correlated-k-distribution model
FVM	Finite volume method
HRR	Heat release rate
IF	Intermittent flame
LES	Large-eddy simulation
MMS	Method of manufactured solution
PDF	probability density function
PIV	Particle image velocimetry
PLIF	Planar laser induced fluorescence
PRI	Plume resolution index
PSD	Power spectrum density
PSR	Perfectly stirred reactor
RANS	Reynolds averaged Navier-Stokes equations
RCFSK	Rank-correlated full-spectrum k-distribution model
RHT	Radiative heat transfer
RTE	Radiative transport equation
SGS	Subgrid-scale

SLF	Steady laminar flamelet
SLW	Spectral line based weighted-sum-of-grey gases
SM	Smagorinsky model
STE	Second-moment transport equation
TCI	Turbulence-chemistry interaction
TRI	Turbulence-radiation interaction
TVD	Total variation diminishing
VTE	Variance transport equation
WSGG	Weighted-sum-of-grey-gases
WSGG-G-CB	Cell based grey weighted-sum-of-grey-gases
WSGG-G-FB	Flame based grey weighted-sum-of-grey-gases
WSGG-NG	Non-grey weighted-sum-of-grey-gases

Nomenclature

$\bar{(\cdot)}$	Reynolds-filter operator
$\breve{(\cdot)}$	Test Favre-filter operator
$\hat{(\cdot)}$	Test Reynolds-filter operator
$\langle \cdot \rangle$	Average operator
$\tilde{(\cdot)}$	Favre-filter operator
a	Strain rate or stretching function for RCFSK or weight factor for WSGG
b	Plume radius
β	Beta distribution
c	Progress variable
c_{st}	Progress variable at stoichiometric mixture fraction
Cp_α	Heat capacity at constant pressure of species α
χ	Scalar dissipation rate of mixture fraction
χ_R	Radiant fraction
χ_{emi}	Ratio of total emission to HRR
χ_e	Scalar dissipation rate at extinction
$\chi_{R,S}$	Fractional radiative heat feedback towards the fuel surface
χ_{st}	Scalar dissipation rate at stoichimetric mixture fraction
C_I	Smagorinsky constant for subgrid-scale kinetic energy
C_s	Smagorinsky constant for subgrid-scale stress tensor

C_v	Smagorinsky constant for subgrid-scale scalar variance in algebraic equilibrium model
C_Z	Smagorinsky constant for subgrid-scale scalar flux
D	Kinematic molecular diffusivity
D^*	Plume characteristic length scale
D_t	Turbulent diffusivity
D_α	Kinematic molecular diffusivity of species α
D_{st}	Kinematic molecular diffusivity at stoichiometric mixture fraction
Da	Damköhler number
δ	Dirac distribution
δ_{ij}	Kronecker delta function
ΔT	Temperature rise above the ambient
Δt	Time step
Δ	Grid filter width
Δ_t	Test filter width
ε	Kinetic energy dissipation rate
η	Wave number
η_k	Kolmogorov lenght scale
Fr	Froude number
g	Gravitational acceleration
G_i	Local radiative intensity integrated over all directions
Γ	Gamma function
H	Heaviside function
h	Total enthalpy
h_{ad}	Total enthalpy under adiabatic condition
$h^0_{f,\alpha}$	Formation enthalpy at reference temperature of species α
I_i	Radiative intensity
$I_{b\eta}$	Spectral blackbody intensity
I_b	Blackbody intensity
I_{g0}	Radiative intensity at quadrature point
κ^{sgs}	Subgrid-scale kinetic energy
κ_η	Spectral absorption coefficient
κ_i	Non-grey absorption coefficient
Λ	Progress variable parameter
λ	Taylor length scale

l_d	Diffusive layer thickness
L_t	Integral length scale
M_α	Molecular weight of species α
$\mathbf{n}$	Outward normal vector to boundary faces
N_s	Species number
N_ϕ	Total number of azimuthal angles in the angular mesh
N_θ	Total number of polar angles in the angular mesh
N_g	Number of quadrature points for RCFSK or number of grey gases for non-grey WSGG
ν	Kinematic molecular viscosity
ν_t	Turbulent viscosity
ν_∞	Kinematic molecular viscosity at the ambient temperature
ω_c	Reaction rate of progress variable
ω_α	Reaction rate for species α
P	Probability density function
p	Hydrodynamic pressure
p_t	Thermodynamic pressure
ϕ^{fpv}	Any thermo-chemical variable computed by the flamelet/progress variable model
ϕ^{slf}	Any thermo-chemical variable computed by the steady laminar flamelet model
$\mathcal{P}$	Production of mixture fraction variance
$\dot{Q}$	Heat release rate
$\dot{Q}'''_{abs}$	Volumetric absorption
$\dot{Q}'''_{emi}$	Volumetric emission
$\dot{Q}_R$	Radiative source term
$\dot{Q}_\rho$	Mass equation source term in MMS
$\dot{Q}_{abs}$	Total absorption
$\dot{Q}_{emi}$	Total emission
$\dot{Q}_{R,S}$	Total radiative feedback towards the fuel surface
$\dot{Q}_{u_j}$	Momentum equation source term in MMS
$\dot{Q}_Y$	Any scalar equation source term in MMS
$\dot{q}''_R$	Radiative flux
$\dot{q}''_{R,S}$	Local feedback radiative flux towards the fuel surface
R	Universal gas constant
r^*	Normalised distance from the plume axis

Re	Reynolds number
Re_t	Turbulent Reynolds number
ρ	Mixture density
ρ_∞	Ambient density
S_{ij}	Strain rate tensor
Sc	Schmidt number
σ_T	Rms of temperature
σ_u	Rms of radial velocity
σ_w	Rms of axial velocity
T	Temperature
T_0	Reference temperature
T_p	Planck temperature
T_∞	Ambient temperature
T_b	Blackbody temperature
T_{st}	Temperature at the stoichiometric mixture fraction
τ	Subgrid turbulent time scale
$\tau_{u_i h}^{sgs}$	Subgrid-scale heat flux
$\tau_{u_i u_j}^{sgs}$	Subgrid-scale stress tensor
$\tau_{u_i Z}^{sgs}$	Subgrid-scale scalar flux
τ_Z	Subgrid mixing time scale of mixture fraction
Θ	Enthalpy defect parameter
$\boldsymbol{u}$	Velocity vector, $u_j = (u, v, w)$
u_0^{out}	Mean axial velocity on the plume centreline at outflow boundary face
u_c	Convective velocity at outflow boundary face
u_{inj}	Injection velocity at inlet boundary face
V_Z	Subgrid mixture fraction variance
x_α	Mole fraction of species α
x_i	Coordinate system (x, y, z)
X_R	Enthalpy defect
Y_α	Species mass fraction
Z	Mixture fraction
z^*	Normalised axial coordinate along the plume axis
$Z_{V,ReS}$	Resolved mixture fraction variance
$Z_{V,tot}$	Total mixture fraction variance

Chapter 1

Introduction

1.1 Context

Electricité de France (EDF), as an operator, is responsible for the safety of the nuclear power plants and defines, in agreement with the regulation, the means and the organisation implemented to ensure that its facilities do not present risks for the public and the environment.

Unwanted fires in nuclear plants is the most important risk for internal damage. Besides the safety of its staff and the operation of its facilities, EDF has an economical interest, related to the loss of material and immobilization, to reduce the fire risk by ensuring a high level of safety without using oversized fire-fighting means. The need for demonstration of the efficiency of fire safety with numerical models, thanks to the improvement of knowledge and computational resources, is increasing. Addressing these issues, with their complex economic and environmental implications, requires a better understanding of the fundamental physics of fire spreading and the development of reliable methods for modelling and analysing fire safety systems.

The modelling tools developed by EDF R&D have been used for several years to answer questions relative to fire safety. Today, the two-zone code MAGIC is used as reference. It is based on the assumption of a stratification of the hot gases above the fresh gases and can provide rapid answers due to its low computational cost. Although this approach is efficient, it is not able to capture all the processes of the fire phenomena. In addition, it becomes less relevant in absence of stratification.

The development of a large eddy simulation (LES) based CFD model of fire spread in nuclear plants is a natural way to circumvent these limitations. The present work is related to these developments. This model has to describe the fire dynamics and the related physics with fidelity. Before discussing the objectives of the present work, the next section will use the example of a pool fire to illustrate the main physical processes occurring during a fire and that has to be accurately modelled.

1.2 Physical processes governing a pool fire

Pool fires are natural canonical scenarios in fire safety science since they contain most of the coupled physical processes involved in fire problems, namely, buoyancy-controlled flows, buoyancy-induced turbulence, turbulent combustion, thermal radiation, soot generation, and burning rate. Figure 1.1 illus-

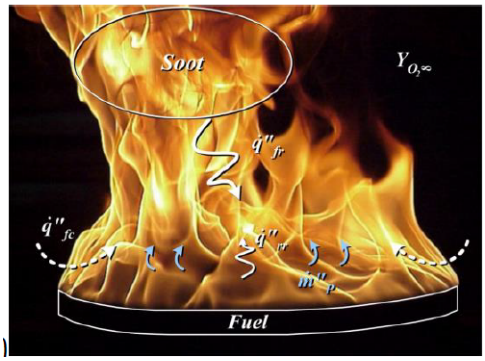

Figure 1.1: Flame structure of pool fire.

trates the main features which control the combustion of a pool fire. The condensed phase (liquid or solid) is transformed into gaseous fuels either by pyrolysis (thermal degradation of solids or heavy liquids) or by vaporization (for light liquids). The gasification processes occur due to the influence of the convective and radiative fluxes transferred from the flame to the condensed fuel surface and, the heat transfer mode controlling this process depends on the fire size: at small-scale the heat transfer is dominated by convection whereas for fires with diameter greater than about 0.2-0.3 m thermal radiation prevails (De Ris, 1979). This highlights the importance of radiation in real-sized fire problems. Gaseous combustion products (hydrocarbon fuels, CO_2, H_2O, CO) and soot are responsible of the radiative heat flux from the flame. Gaseous species emit radiation in some discrete bands, whereas the radiation from soot

is continuous, covering the entire thermal spectrum. The contribution of soot depends widely on the combustible.

The flame depicted in Fig. 1.1 is a diffusion flame characteristic of unwanted fires. The word diffusion means that fuel and oxidant are not initially premixed. The flow evolves within the buoyancy-driven regime with the fuel injection velocity being significantly lower than that induced by the gravitational acceleration, g. In fire problems the Froude number, $Fr = u_{inj}^2/gL$, is typically in the range $10^{-6} - 10^{-2}$ (Cox and Drysdale, 1995). In the previous expression, L is a characteristic length of the problem, the flame length or the diameter of the pan in the present example. The purely-buoyant nature of the flow leads to the formation and the growth of non-dissipative non-linear laminar instabilities near the edge of the pan that develops to become energy containing turbulent structures (Tieszen and Gritzo, 2008). These structures develop periodically to form energy containing large-scale toroidal vortices that govern the flow pattern, the air entrainment as well as the mixing and combustion processes. As discussed in Ref. (Tieszen et al., 2004; Tieszen and Gritzo, 2008), these instabilities are initially non-dissipative and the associated mixing cannot be captured by conventional subgrid-scale turbulence models that are dissipative in nature. The near field flow is thus rather complex. It exhibits a rapid transition from laminar to fully turbulent regime in the few first inlet diameters and a puffing motion characterized by a repetitive shedding of these coherent vortices (Cetegen and Ahmed, 1993).

Fires in nuclear plants are characterized by an additional difficulty related to the high level of enclosure, leading to conditions for combustion generally different from those encountered in well-ventilated fires. Air feeding the flame becomes rapidly vitiated, which leads to partial and/or total extinction and then to incomplete combustion. Gaseous combustibles, carbon monoxide, and soot escape then from the fire and are released into the surroundings. This can lead to extremely dangerous hazards, especially if the gaseous combustibles mix with air and encounter points with a sufficiently high temperature to ignite this mixture. Idealized experiments of under-ventilated fire plumes were performed at the University of Maryland (UMD) (White et al., 2015) by considering buoyant, turbulent line flames under oxidizer-dilution quenching conditions. This study highlighted the extinction mechanisms in oxygen diluted atmospheres, showing that flame extinction is preceded by a lift-off and occurs

for oxygen mole fractions of 0.151 for methane and 0.138 for propane. When an oxygen anchor is considered to suppress the lift-off, the flammable domain is extended to 0.130 for both fuels. Such extinction mechanism, characterized by the detachment of the base of the flame from the burner rim, its oscillation and eventually its extinction, as the oxygen is gradually diluted into a co-flowing oxidizer stream was also observed in laminar co-flow diffusion flames (Takahashi et al., 2007; Guo et al., 2010).

1.3 Objectives of the thesis

This thesis is a part of a research effort devoted to the development of a LES-based fire simulator including state-of-the-art submodels for the different physical processes involved in fire scenarios in nuclear plants. It focuses on gas phase processes with the main objective to develop a CFD model simulating with high fidelity non (or weakly) sooting well-ventilated and under-oxygenated fire plumes. The strategy adopted in these developments can be summarized as follows:

- As discussed previously, the near field of fire plumes is characterized by strongly unsteady processes related to the purely buoyant nature of the flow. The development and the implementation in *Code_Saturne*, the in-house code of EDF, of a new second-order Navier-Stokes solver for low-Mach variable-density flows will be then a natural prerequisite. Methods of manufactured solutions will be considered for the numerical verification step.

- The second step will focus on the implementation of variable-density subgrid-scale (SGS) stress tensor and scalar flux models. The dynamic Smagorinsky model for SGS stress tensor and advanced SGS scalar flux models, including the dynamic eddy diffusivity model, dynamic tensorial diffusivity models and gradient models. These models will be applied and assessed in LES of the 1 m helium plume investigated in Ref. (O'Hern et al., 2005).

- The third step will consider the SGS combustion and radiation models. This latter is important to account for SGS turbulence-radiation interaction (TRI). They will be based on non-adiabatic steady flamelet

approaches coupled to a presumed filtered density function (FDF) for turbulent flame thermochemical state tabulations. For well-ventilated fire plumes the non-adiabatic steady laminar flamelet (SLF) model will be considered whereas, for under-oxygenated fire plumes, a non-adiabatic flamelet/progress variable (FPV) methodology will be specifically developed. One of the main issues with the flamelet approaches is related to the modelling of the SGS scalar variance and filtered scalar dissipation. Models based on local equilibrium or non-equilibrium will be implemented and analysed in LES of the McCaffrey methane fire plume (McCaffrey, 1979) to select the most appropriate choice.

- Based on these conclusions, the capability of the model will be extensively assessed by simulating several medium-scale and large-scale fire plumes of the literature, including the 30 cm methanol pool fires investigated experimentally by Weckman and Strong (1996), the 50 cm ethanol pool fires investigated experimentally by Fischer et al. (1987), the 1 m methanol pool fire investigated experimentally by Sung et al. (2020), and the line fires investigated experimentally at UMD (White et al., 2015). Beyond the validation exercise, each experimental configuration will lead to the investigation of a given process. Burner boundary conditions, which were found to be of significant importance to capture the fire plume dynamics during the course of this work, will be investigated on the 30 cm methanol pool fire. The importance of SGS TRI will be discussed by considering the 50 cm ethanol pool fire. The UMD turbulent line fires, that consider methane as fuel burning either in air or nitrogen-diluted atmospheres up to flame extinction, will serve to evaluate the limitation of the SLF and the capability of the FPV to capture the weakening of the flame while reducing the oxygen concentration in the oxidizer stream and the subsequent flame extinction.

- Finally, several radiative property models, including the rank-correlated full-spectrum-k-distribution model (RCFSK) (Solovjov et al., 2018), and grey and non-grey versions of the weighted-sum-of-grey-gases (WSGG) (Modest, 2013), have been implemented. Their modelling capability will be investigated in the 1 m methanol pool fire. This fire plume will be also considered to investigate the effects of the angular discretization of the radiative transfer equation solver on radiative outputs.

1.4 Literature surveys

This section will discuss the current developments of LES-based fire simulator as well as the modelling of SGS combustion and radiation in the framework of fire modelling that are the core of this work.

1.4.1 Background

LES has become the standard for numerical modelling of turbulent fire over the last twenty years (Branley and Jones, 2001; Ma and Quintiere, 2003; Desjardin, 2005; Xi et al., 2005; Cheung and Yeoh, 2009; Wang et al., 2011; Chatterjee et al., 2015; Maragkos et al., 2017; Maragkos et al., 2019; Sikic et al., 2019; Maragkos and Merci, 2020). In LES, the governing equations are spatially filtered (Pope, 2000; Modest and Haworth, 2016); the large-scale dynamics (large turbulent eddies whose transient behaviour can be resolved numerically) are captured explicitly, while the effects of unresolved (subgrid) scales are modelled. LES is expected to be more accurate and general compared to Reynolds averaged Navier-Stokes (RANS) approaches, since at least some of the fluctuations (the largest, most energetic ones) are captured explicitly and only the (presumably) more universal small-scale dynamics require modelling. LES is also expected to capture phenomena that are difficult to accommodate in RANS, such as large-scale unsteadiness as observed in fire plumes (Wang et al., 2011).

The filtered Navier-Stokes equations contain the unclosed SGS tensor stress and scalar fluxes. In LES-based fire simulators, the standard Samgorinsky and linear eddy diffusivity (Pope, 2000) models are usually used to close these terms, although dynamic versions of these models (Moin et al., 1991b) were used to simulate fire plumes (Maragkos and Merci, 2020). Nevertheless, the linear eddy diffusivity model assumes a linear alignment with the large-scale scalar gradient which is inconsistent with the physics of turbulent convection and cannot correctly reflect the local geometric property of the SGS scalar flux vector at each time step (Peng and Davidson, 2002; Higgins et al., 2004; Wang et al., 2007b; Wang et al., 2007a). To correct this behaviour, other approaches were considered in the literature, such as those based on tensorial forms of the diffusivity for the SGS scalar flux modelling (Wang et al., 2008b) or those based on Taylor series expansion of the filtering operation (Fabre and Balarac,

2011).

In reacting radiating flows such as fires, the resulting set of filtered equations contains additional unclosed terms which are manifestations of turbulence-chemistry interactions (TCI) and turbulence-radiation interactions (TRI) (Poinsot and Veynante, 2005; Modest and Haworth, 2016). In particular, the LES of combustion processes introduces an important modelling issue since the combustion process occurs essentially at the smallest scales of the sub-filter level, and has to be modelled entirely (Pitsch, 2006). In addition, the importance of SGS TRI is not fully elucidated and has to be addressed (Liu et al., 2020a).

1.4.2 Combustion models and fire extinction

Current approaches

A significant part of the LES of fire scenarios reported to date used the eddy dissipation concept (EDC) proposed by Ertesvåg and Magnussen (2000), to model the turbulence-combustion interaction (Chatterjee et al., 2015; Maragkos et al., 2017; Maragkos et al., 2019; Sikic et al., 2019; Maragkos and Merci, 2020). In EDC, the reactions are assumed to occur only in the smallest eddies along the turbulence energy cascade, which are called fine structures. To account for detailed chemical kinetics, these fine structures are typically treated as a perfectly stirred reactors (PSRs) in which chemical reactions depend on the molecular mixing between the reactants. In fire research, the detailed kinetics is generally not retained and an infinitely fast chemistry single-step irreversible reaction is assumed. Due to non-linearity of the combustion process, the filtered reaction rate is modelled by introducing model constants. However, no universal values of these constants exist (Panjwani et al., 2010; Bösenhofer et al., 2018). Fire extinction models were also developed in the framework of EDC approach with simplified chemical kinetics. In the available fire extinction studies, critical flame temperature based models (Hu et al., 2007; Vaari et al., 2011; White et al., 2017) or Damköhler number based models (Narayanan et al., 2011; Lecoustre et al., 2011; Snegirev and Tsoy, 2015; Snegirev, 2015; Vilfayeau et al., 2015; Vilfayeau et al., 2016) are coupled with the EDC approach to perform LES of fire extinction and reignition problems. The critical flame temperature based model is simple and computationally less expensive, works well at low strain

rates but is not suitable to predict flame extinction at high strain rates, since chemical time scales are not considered. The Damköhler number based models accounts for chemical time scales and aerodynamic quenching effects.

On the other hand, only few LES of fire plumes have reported the use of mixture fraction based combustion models. Noticeable examples are the works of Desjardin (2005) and Cheung and Yeoh (2009) where a one-step reaction based SLF model was considered and that of Wang et al. (2011) who used Burke-Shumann state relationships. More recently, Le et al. (2019) and Xu et al. (2020) considered a steady and a non-steady flamelet model to simulate the UMD line fires (White et al., 2015). These studies considered a classical presumed FDF, parametrized by the filtered mixture fraction and SGS mixture fraction variance, to characterize the mixture fraction statistics at the subgrid scale.

Flamelet models

Flamelet models coupled to presumed FDF represent a relevant alternative to the EDC models usually used in fire simulations and their development will be an important part of this work.

In the flamelet modelling approaches, the turbulent reaction zone is represented by a collection of canonical laminar flames corresponding usually to 1D counter-flow diffusion flames (Peters, 1984). These simple 1D flames can be simulated with detailed chemical kinetics and molecular transport properties for a set of parameters that characterize the effects of the flow on the flamelet structure. Both steady and unsteady flamelet approaches were developed (Pitsch and Peters, 1998; Poinsot and Veynante, 2005), the steady approaches assuming that the flame structure immediately adjusts to local flow field conditions. Under this assumption, the SLF model provides state relationships for temperature, species mass fractions and, more generally all thermochemical variables as a function of two parameters: the mixture fraction and scalar dissipation rate (Peters, 1984; Poinsot and Veynante, 2005). This latter parameter measures the degree of departure from the equilibrium state and can be interpreted as the inverse of a characteristic diffusion time or as a diffusivity in the mixture fraction space (Poinsot and Veynante, 2005). The main limitation of the SLF model in view of under-ventilated fire applications is that, although it provides state relationship for the stable burning flamelet between equilibrium and ex-

tinction, it is not able to describe the extinction/re-ignition processes (Ihme et al., 2005; Ihme and Pitsch, 2008).

The flamelet progress variable (FPV) offers an attractive alternative to the SLF for modelling the fire extinction and reignition phenomena. As the SLF, the FPV is based on the steady assumption and is capable of incorporating detailed chemistry kinetics. The main differences is that a flamelet parameter based on a reactive scalar is used rather than the scalar dissipation rate in order to get access to both stable and unstable burning flamelets. This enables, in principle, prediction of extinction and reignition effects (Pierce and Moin, 2004; Ihme et al., 2005; Ihme and Pitsch, 2008; Shunn, 2009).

As discussed previously, radiative loss plays an important role in fire problems and its effects on the flamelet structure have to be taken into account. This is generally achieved by introducing an additional parameter characterizing the enthalpy loss. This leads to the non-adiabatic SLF or FPV models (Ihme and Pitsch, 2008; Carbonell et al., 2009).

In LES of non-premixed combustion, many important mixing and reaction processes occur at scales that are unresolved on the computational grid. As a consequence, the SGS fluctuations of the flamelet parameters and their statistical distribution need to be considered. In practice, once state relationships have been determined in terms of the reduced set of parameters, filtered thermochemical scalars are obtained using a statistical averaging based on presumed FDF to account for subgrid fluctuations of these parameters (Poinsot and Veynante, 2005; Echekki and Mastorakos, 2010).

In particular, SGS fluctuations of mixture fraction are characterized by subgrid mixture fraction variance and its dissipation rate. The subgrid variance quantifies the level of unmixedness at the subgrid scales and the filtered scalar dissipation rate describes the rate at which scalars relax towards a fully mixed state. The modelling of both quantities has received significant attention over the last years and several models using different assumptions can be found in the literature. Cook and Riley (1994) proposed a model based on the scale similarity assumption for the subgrid variance. Jiménez et al. (1997) showed that the model constant depends on the exponent of the scalar spectrum function in the large Reynolds number limit. Cook (1997) derived a method for calculating the coefficient and showed that it varies with the test filter scale and

the Reynolds number. Another approach to model the subgrid variance was developed by Pierce and Moin (1998) who assumes a local equilibrium between the production and dissipation of subgrid variance. The model coefficient is calculated by a dynamic procedure, thus eliminating the need to specify it *a priori*. The use of this equilibrium model leads to a simple model for the subgrid scalar dissipation rate. Balarac et al. (2008) modified the dynamic procedure of Pierce and Moin (1998) to include certain leading-order terms in the Taylor series expansion of the left hand side of the dynamic closure. Although being computationally efficient, it was reported that the dynamic local equilibrium-based models produce inaccurate estimation of scalar mixing and hence scalar dissipation rate (Kaul et al., 2009; Kaul and Raman, 2011; Knudsen et al., 2012; Kaul et al., 2013).

An alternative to equilibrium models is to consider a transport equation for the subgrid scalar variance. This approach, initiated by Jiménez et al. (2001), will be referred to as the VTE model hereafter. Kaul et al. (2009), Kaul and Raman (2011), and Kaul et al. (2013) proposed to solve the transport equation for the filtered second-moment of mixture fraction, referred to as the STE model hereafter, instead of directly solving the VTE. After the STE is solved, the subgrid mixture fraction variance is then computed by subtracting the square of filtered mixture fraction from the filtered second-moment of mixture fraction. The two models are identical at the level of their continuous equations, but give different results when discretized. Kaul et al. (2009) claimed that the calculation of production term of VTE introduces discrepancies due to the chain-rule of product operation at the discrete level, especially in high Reynolds number flows. The STE model does not consider this term and thus is not affected by this discrete chain-rule caused error. They also mentioned that another advantage of STE is to recover the maximum subgrid variance in the case where dissipation is negligible. Based on these reasons, they argued that the use of the STE model is more accurate than the VTE model. Kemenov et al. (2012) and Jain and Kim (2019) also addressed the differences between both models at the discrete level. Kemenov et al. (2012) performed a comparative grid refinement study for the two models on the Sandia Flame D. The VTE model was found to provide a better convergence behaviour with respect to grid refinement than the STE model. The discrepancy of the STE model was attributed to the conservation issue of the square of the filtered

mixture fraction at the discrete level, leading to the appearance of an extra source term, depending on grid spacing, in the subgrid scalar variance evolution for the STE model. The VTE model is inherently consistent and capable to enforce the conservation law for the square of filtered mixture fraction. Jain and Kim (2019) demonstrated in a planar jet flame study, that the VTE model predictions agree better with the direct numerical simulation (DNS) data, and the STE model may cause sharp oscillations of subgrid scalar variance.

Both two models require modelling for the scalar dissipation rate. Closure may be achieved through algebraic expressions using a turbulent time-scale (Jiménez et al., 2001; Knudsen et al., 2012). Alternatively, closure can also be performed by solving a transport equation for the filtered square gradient of mixture fraction (Knudsen et al., 2012).

Studies of these models for SGS scalar variance and dissipation rate were limited to momentum-driven turbulent jet flames and investigations of these models on purely buoyant fire plumes were not reported to date.

1.4.3 Radiation heat transfer

Experimental studies evidenced that radiation is the dominant mode of heat transfer to fuel surface for scales larger than about 0.2-0.3 m (De Ris, 1979). More quantitatively, Hamins et al. (1994) reported that radiation contributes to the total heat feedback for 55, 80, and 96% in the case of 0.3 m diameter methanol, heptane and toluene pool fires, respectively. This contribution generally increases with the fire size and the fuel sooting propensity (Ditch et al., 2013).

Consequently, the development of LES-based fire simulators over the last 20 years raised naturally the issue of the radiation modelling for fire applications (Xi et al., 2005; Wang et al., 2011; Chen et al., 2014b; Chen et al., 2014a; Chatterjee et al., 2015; Maragkos et al., 2017; Maragkos and Merci, 2017; Snegirev et al., 2018; Fraga et al., 2019; Maragkos et al., 2019; Sikic et al., 2019; Wu et al., 2020). At the same time, the radiative heat transfer community reported significant progresses in the modelling of radiation in turbulent flames (Modest and Haworth, 2016). This issue can be divided into three separate sub-problems, namely the RTE solver, the spectral dependence of radiating species, and TRI. Firstly, nowadays discrete ordinates methods (DOM) and

finite volume method (FVM) are widely used as radiative transfer equation (RTE) solver mainly due to their compatibility with the discretization of the fluid dynamics equations, ease to code, fairly good accuracy, and often acceptable computational efficiency (Coelho, 2014). Moreover, Monte Carlo techniques were also used in some recent simulations of flames (Wang et al., 2008a; Gupta et al., 2013; Rodrigues et al., 2019; Wu et al., 2020). Secondly, the absorption coefficient of the radiating combustion gases is strongly dependent on the wavenumber. The modelling of gas radiative properties has benefited from the development of accurate high-temperature high-resolution spectroscopic databases such as HITEMP 2010 (Rothman et al., 2010). Line-by-line (LBL) has then emerged as the reference for decoupled radiative heat transfer calculations and was combined to Monte Carlo techniques for coupled simulations (Wang et al., 2008a). However, LBL/Monte Carlo calculations are limited to academic configurations. Alternative global gas property models were developed based on the k-distribution concept, such as the full-spectrum correlated-k (FSCK) or the spectral line based weighted-sum-of-grey-gases (SLW). These models were found to provide a good compromise between accuracy and computational efficiency and to be adequate for engineering applications (Denison and Webb, 1993; Denison and Webb, 1995c; Denison and Webb, 1995a; Denison and Webb, 1995b; Modest and Zhang, 2002; Cai and Modest, 2014; Solovjov et al., 2017; Solovjov et al., 2018). Although having similar features with the WSGG model, these methods do not suffer from its limitation, namely its restriction to spatially constant absorption coefficients (Modest and Haworth, 2016). FSCK/SLW models can be also applied to mixtures of gases and non-grey soot (Modest and Riazzi, 2005). In addition, the development of look-up tables has significantly improved their computational efficiency (Pearson et al., 2014; Wang et al., 2016c; Wang et al., 2016a; Wang et al., 2016b; Wang et al., 2018; Wang et al., 2019). Finally, TRI results from the highly non-linear coupling between turbulent fluctuations in temperature, composition, and radiative intensity (Coelho, 2007). Accounting for TRI requires the modelling of two terms, namely absorption TRI and emission TRI. In LES, the contribution of turbulent fluctuations to TRI is decomposed into resolved-scale fluctuations and SGS fluctuations and only these latter require modelling. A consensus was reached that the SGS absorption TRI is negligible in both luminous and non-luminous flames (Gupta et al., 2013; Coelho, 2009; Consalvi et al., 2018). On the other hand, the importance of SGS emission TRI was found to depend on

the filter size (Coelho, 2009; Consalvi et al., 2018) and its modelling is strongly dependent on the turbulent combustion model. An appropriate way to model SGS emission TRI is to consider FDF approaches (Gupta et al., 2013; Miranda et al., 2019; Miranda et al., 2020).

One of the objectives of the fire simulators is to forecast the growth of fires at the scale of industrial fires. This introduces considerable challenges for the modelling of the physical processes involved and compromises between accuracy and computational resources have to be found. Consequently, less sophisticated radiation models were generally considered in most of the LES of fire plumes reported to date. These studies have mainly considered DOM and FVM as RTE solver (Xi et al., 2005; Wang et al., 2011; Chen et al., 2014b; Chen et al., 2014a; Chatterjee et al., 2015; Maragkos et al., 2017; Maragkos and Merci, 2017; Snegirev et al., 2018; Fraga et al., 2019; Maragkos et al., 2019; Sikic et al., 2019). Since the computational cost related to the solution of the RTE is relatively high, simplified radiative property models, assuming either an optically thin medium with the emission specified to reproduce the measured radiant fraction (Xi et al., 2005; Wang et al., 2011; Maragkos and Merci, 2017) or a grey medium (Chen et al., 2014b; Chen et al., 2014a; Chatterjee et al., 2015; Snegirev et al., 2018; Maragkos et al., 2019), were generally retained. Nevertheless, non-grey radiative property models, based on non-grey versions of the WSGG or box models (Fraga et al., 2019; Sikic et al., 2019), were also applied in LES of medium-scale methanol and ethanol pool fires. Sikic et al. (2019) assessed several radiative property models, including grey and non-grey implementations of the WSGG and the exponential wide band-based box model, to simulate 30 *cm* diameter methanol pool fires and recommended to use non-grey versions of the WSGG.

Concerning the modelling of SGS TRI, several works (Chatterjee et al., 2015; Snegirev et al., 2018; Sikic et al., 2019) have extended the moment-based closure, proposed by Snegirev (2004) for RANS, to model SGS emission TRI. This approach consists in approximating the filtered emission term by a Taylor series expansion and retaining only the lower-order moments. Nevertheless, moment-based methods introduce empirical adjustable coefficients that are generally tuned to match the experimental data (Chatterjee et al., 2015; Snegirev et al., 2018; Sikic et al., 2019). Wu et al. (2020) presented DNS of a 7.1 *cm* heptane pool fire using a very fine description of radiative heat transfer. In their work,

radiation was modelled using the LBL/Photon Monte Carlo proposed by Wang et al. (2008a), and the contributions of CO_2, H_2O, CO, CH_4, C_2H_4 and soot were taken into account.

1.5 Organisation of the manuscript

The present manuscript is organised as follow.

- Chapter 2 will be devoted to the description of the mathematical model. In particular, a special emphasis will be paid on the formulation of the SLF and the FPV models and on the description of the gas radiative property models used in the present study.
- Chapter 3 will present the LES filtering governing equations. The modelling procedures considered in the present study for the unclosed SGS stress and scalar flux will be described. The presumed FDF approach to close SGS combustion and TRI will be also discussed in details.
- Chapter 4 will describe in details the development and the verification of a new second-order Navier-Stokes solver for low-Mach variable-density flows.
- Chapter 5 will present LES of a non-reactive 1 m helium plume and predictions will be compared with measurements. The objective of this Chapter will be twofold: first to provide a further validation of the numerical algorithm developed in Chapter 4 and, second, to evaluate the capability of SGS stress tensor and scalar flux models to describe the buoyant mixing characteristic of fire plume. The main interest of considering a non-reactive helium plume for this latter task is that the mixing process is similar to that observed in fire plumes while avoiding difficulties related to the combustion and radiation processes.
- LES of well-documented well-ventilated medium-scale methane and methanol fire plume will be reported in Chapter 6. First, the McCaffrey methane fire plumes will be used to evaluate different strategies for the modelling of the SGS mixture fraction variance and the dissipation rate. The selected strategy will be further assessed by simulating the 30 cm methanol pool fire investigated experimentally by Weckman and

Strong (1996). This latter case will be also considered to investigate the effects of the burner boundary conditions on plume dynamics.

- Chapter 7 will focus on radiative heat transfer. The important of SGS TRI will be discussed by considering LES of well-ventilated synthetic ethanol pool fires of different diameters generated by scaling up the 50 cm pool fire investigated experimentally by Fischer et al. (1987). On the other hand, the gas radiative property models will be assessed from LES of the well-ventilated 1 m methanol pool fire investigated experimentally by Sung et al. (2020).
- Chapter 8 will investigate the modelling of under-ventilated fire plumes by considering the UMD line flames under oxidizer-dilution quenching conditions (White et al., 2015). This configuration will serve to assess the capability of the FPV model to describe the weakening of the flame and its subsequent extinction as the oxygen concentration in the oxidizer stream is progressively reduced.
- Finally, conclusions drawn from the present study are presented and perspectives for future works and developments will be outlined in Chapter 9.

1.6 Publications in the context of this thesis

- L. Ma, F. Nmira, J.L. Consalvi, Verification and Validation of a second-order variable-density scheme for fire safety applications, 11th Mediterranean Combustion Symposium, 16-20/06/2019, Spain.
- F. Nmira, L. Ma, J.L. Consalvi, Turbulence-radiation interaction in Large Eddy Simulation of non-luminous pool fires, Accepted for presentation at the 38th Symposium on Combustion, 2020.
- L. Ma, F. Nmira, J.L. Consalvi, Verification and validation of a variable–density solver for fire safety applications, Numerical Heat Transfer, Part B. Fundamentals, 76, 2019, pp. 107-129.
- F. Nmira, L. Ma, J.L. Consalvi, Turbulence-radiation interaction in Large Eddy Simulation of non-luminous pool fires, Proceedings of the Combustion Institute, 38, 2020.

- F. Nmira, L. Ma, J.L. Consalvi, Influence of gas radiative property models on Large Eddy Simulation of 1 m methanol pool fires, Combustion and Flame, 221, 2020, pp. 352-363.
- L. Ma, F. Nmira, J.L. Consalvi, Large eddy simulation of medium-scale methanol pool fires - effects of pool boundary conditions, Combustion and Flame, 222, 2020, pp. 336-354.
- L. Ma, F. Nmira, J.L. Consalvi, Exploring subgrid-scale variance models in LES of lab-scale methane fire plumes, Combustion Theory and Modelling, 2020, pp. 1-29.

Chapter 2

Mathematical formulation

2.1 Governing equations

The Navier-Stokes (NS) equations in low-Mach number formulation supplemented with transport equations for the species mass fractions, $(Y_\alpha)_{\alpha=1,N_s}$, total enthalpy, h, and the equation of state are expressed below. It can be assumed that the species diffusion and heat conduction follow the Fick and the Fourier laws, respectively.

Mass:

$$\frac{\partial \rho}{\partial t} + \frac{\partial \rho u_i}{\partial x_i} = 0 \tag{2.1}$$

Momentum:

$$\frac{\partial \rho u_j}{\partial t} + \frac{\partial \rho u_i u_j}{\partial x_i} = -\frac{\partial p}{\partial x_j} + \frac{\partial \tau_{ij}}{\partial x_i} + (\rho - \rho_\infty) g_j \tag{2.2}$$

Species:

$$\frac{\partial \rho Y_\alpha}{\partial t} + \frac{\partial \rho u_i Y_\alpha}{\partial x_i} = \frac{\partial}{\partial x_i}\left(\rho D_\alpha \frac{\partial Y_\alpha}{\partial x_i}\right) + \dot{\omega}_\alpha, \quad \alpha = 1, ..., N_s \tag{2.3}$$

Energy:

$$\frac{\partial \rho h}{\partial t} + \frac{\partial \rho u_i h}{\partial x_i} = -\frac{\partial q_i}{\partial x_i} - \nabla \cdot \dot{q}''_R \tag{2.4}$$

Equation of state:

$$p_t = \rho \sum_{\alpha=1}^{N_s} \frac{Y_\alpha}{M_\alpha} RT \tag{2.5}$$

where ρ is the local density and $u_i = (u, v, w)$ is the flow velocity, p, p_t are the hydrodynamic and thermodynamic pressure, respectively. $(\tau_{ij})_{i,j=1,3}$ is the viscous stress defined as:

$$\tau_{ij} = \mu \left(\frac{\partial u_i}{\partial x_j} + \frac{\partial u_j}{\partial x_i} \right) + \frac{2}{3} \delta_{ij} \mu \frac{\partial u_k}{\partial x_k} \tag{2.6}$$

with μ the dynamic viscosity.
$(D_\alpha)_{\alpha=1,N_s}$ are the species diffusion coefficients, N_s is the number of species and ω_α are the species reaction rates, which verify $\sum_{\alpha=1}^{N_s} \omega_\alpha = 0$.
h is the total enthalpy defined as:

$$h = \sum_{\alpha=1}^{N_s} Y_\alpha h_\alpha(T) = \sum_{\alpha=1}^{N_s} Y_\alpha \left(h_{f,\alpha}^0 + \int_{T_0}^{T} Cp_\alpha(T^{'}) \mathrm{d}T^{'} \right) \tag{2.7}$$

where $h_{f,\alpha}^0$ is the formation enthalpy at the reference temperature, T_∞, and Cp_α the heat capacity at constant pressure of species α, $(q_i)_{i=1,3}$ the heat flux modelled by the Fourier law:

$$q_i = -\lambda \frac{\partial T}{\partial x_i} \tag{2.8}$$

where λ is the heat conductivity, and $\nabla \cdot \dot{q}_R''$ is the radiative source term. T, R and M_α are the temperature, the universal gas constant and the molecular weight of the αth species, respectively.

Note that the system (2.1)-(2.5) can be transformed into a reduced dimension system in which scalar transport equations are solved for three quantities: the mixture fraction, Z, scalar dissipation, χ, or reaction progress variable, c, and total enthalpy h. All other thermochemical quantities are obtained from a property database as a function of these scalars.

2.2 Combustion modelling

The present study will consider flamelet approaches to model combustion of non-premixed flames. First, the mixture fraction is introduced. Second, the flamelet equations are described. Third, the SLF and FPV are presented. Finally, the incorporation of radiative loss into the flamelet models are discussed.

2.2.1 Mixture fraction

Non-premixed flames are a specific class of combustion problems where fuel and oxidizer are initially separated and have to mix prior to combustion (Poinsot and Veynante, 2005). A proper description of the mixing process is then a natural prerequisite to the modelling of these flames.

In general, the structure of non-premixed flames can be described by means of a conserved scalar. This variable is the mixture fraction, Z, (Peters, 1984), defined between 0 and 1. Z is a conserved scalar that accounts for the level of mixing between the oxidizer and the fuel and changes because of diffusion and convection, but not due to the chemical process. In the present study, following the formalism introduced by (Pitsch and Peters, 1998), the mixture fraction is defined from its transport equation:

$$\frac{\partial \rho Z}{\partial t} + \frac{\partial \rho u_i Z}{\partial x_i} = \frac{\partial}{\partial x_i}\left(\rho D \frac{\partial Z}{\partial x_i}\right) \tag{2.9}$$

where D is the diffusion coefficient for mixture fraction. Pitsch and Peters (1998) recommend to use the thermal diffusion for D.

2.2.2 Flamelet equations

A flame can be viewed as an ensemble of thin locally one-dimensional structures embedded within the flow field. Each element of the flame front can then be viewed as a small laminar flame also called flamelet (Peters, 1984; Poinsot and Veynante, 2005). Physically, the flame structure is considered locally one-dimensional and only depends on time and the coordinate normal to the flame front. A coordinate system attached to the surface of stoichiometric mixture fraction can be introduced and the flamelet equations can be derived (Peters, 1984). A transformation from the physical spatial-temporal space $(\boldsymbol{x}, t)$ to the mixture fraction-temporal space (Z, τ) can be applied to the governing equations of species and enthalpy. It is assumed that through the flame front, the combustion behaviour is one-dimensional. Terms corresponding to the gradients along the tangent directions to the flame front are neglected in comparison to those normal to the flame front. For simplicity, unity Lewis numbers are adopted in the following description, implying that all chemical species and enthalpy have the same diffusivity, D. A more general derivation including the

effect of non-unity Lewis numbers is given by Pitsch and Peters (1998). This coordinate transformation results in the flamelet equations:

$$\rho\frac{\partial Y_\alpha}{\partial \tau} = \frac{1}{2}\rho\chi\frac{\partial^2 Y_\alpha}{\partial Z^2} + \dot{\omega}_\alpha \tag{2.10}$$

$$\rho\frac{\partial h}{\partial \tau} = \frac{1}{2}\rho\chi\frac{\partial^2 h}{\partial Z^2} - \nabla\cdot\dot{q}''_R \tag{2.11}$$

χ, is the scalar dissipation rate and is defined as:

$$\chi = 2D\left(\frac{\partial Z}{\partial x_i}\frac{\partial Z}{\partial x_i}\right) \tag{2.12}$$

The scalar dissipation rate has the units of the inverse of a time and characterizes typical diffusion times in the flamelet (Poinsot and Veynante, 2005).

2.2.3 Steady laminar flamelet model

The SLF model views a turbulent diffusion flame as an ensemble of thin, steady laminar reaction zones embedded in a turbulent flow field. At sufficiently high Damköhler number or sufficiently high activation energy, the reaction zone is thinner than the surrounding turbulence eddies. In this regime, turbulent structures can deform and stretch the flame sheet, but are unable to penetrate the reaction zone and modify its structure. The combustion chemistry reaches a quasi-steady state and immediately adjusts to local flow-field conditions. Neglecting the temporal derivative in Eqs (2.10) and (2.11) leads to the SLF model:

$$-\frac{1}{2}\rho\chi\frac{d^2 Y_\alpha}{dZ^2} = \dot{\omega}_\alpha \tag{2.13}$$

$$-\frac{1}{2}\rho\chi\frac{d^2 h}{dZ^2} = -\nabla\cdot\dot{q}''_R \tag{2.14}$$

In order to solve this set of equations, a distribution of $\chi(Z)$ should be determined. The 1D flame structure is generally assumed to be represented by a counterflow diffusion flame. Peters (1984) obtained an analytic expression for $\chi(Z)$ based on the laminar counterflow configuration. Once this analytical expression of $\chi(Z)$ and an appropriate chemical mechanism are considered, Eqs. (2.13) and (2.14) can be solved as a function of a single parameter, χ_{st},

that represent the scalar dissipation rate at stoichiometric conditions. All thermochemical state variables, ϕ, consisting for instance of temperature, density, molecular viscosity and diffusivity, and species mass fractions can then be expressed in terms of Z and χ_{st} (Peters, 1984):

$$\phi = \phi^{slf}(Z, \chi_{st}) \tag{2.15}$$

It should be pointed out that, alternatively, these state relationships can be also obtained by solving all the transport equations (i.e. Eqs. (2.1)- (2.5) and (2.9)) in the physical space for a laminar counterflow configuration. The thermochemical variables are subsequently mapped into the mixture fraction space and the profile of scalar dissipation rate, $\chi(Z)$, is directly obtained from its definition (Eq. 2.12).

Numerical solutions of the SLF equations can be analysed by plotting the temperature at the stoichiometric mixture fraction, T_{st}, as a function of χ_{st}. This plot is referred to as the S-shaped curve in the literature and an illustration is provided in Fig. 2.1 for methane-air flame. The S-shaped curve can be divided into three general regions, describing different regimes of mixing and burning. χ_e represents the scalar dissipation rate at extinction. The upper branch, up to the quenching scalar dissipation rate χ_e, is denoted as the stable burning branch. The middle or unstable branch corresponds to transition or intermediate states between igniting and quenching flamelets. The bottom branch corresponds to the pure mixing line.
As discussed earlier, the SLF model parametrizes the flame state by the mixture fraction and χ_{st}. Since multiple solutions exist for certain values of χ_{st} (see Fig. 2.1), a unique parametrization of the flamelet solutions in terms of the scalar dissipation rate cannot represent the entire solution space. Typically, in applications of the SLF, only the stable burning branch of the S-shaped curve, that can be described uniquely by χ_{st}, is considered.

As discussed previously the SLF library can be established by solving the problem either in the mixture fraction-space or in the physical-space. In both cases, the strategy to establish the flamelet library is similar. Given a chemical mechanism, flamelet equations are solved by gradually increasing the strain rate from near equilibrium to conditions of local extinction. Solutions are parametrized by the mixture fraction and its dissipation rate at stoichiometric mixture frac-

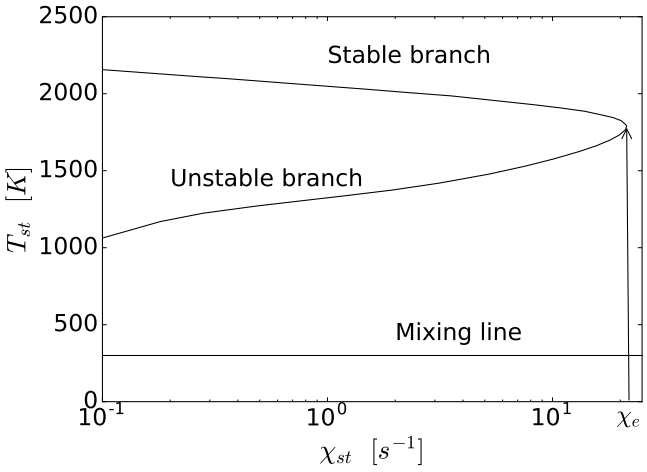

Figure 2.1: S-shaped curve: relationship between T_{st} and χ_{st}. Fuel: CH_4; Oxidizer: pure air.

tion. The thermochemical states of the flamelet are then represented by a two-dimensional manifold, $\phi = \phi^{slf}(Z, \chi_{st})$. By introducing a table inversion to eliminate χ_{st} in favour of χ, the thermochemical states are finally expressed as:

$$\phi = \phi^{slf}(Z, \chi) \tag{2.16}$$

Figure 2.2 illustrates the temperature profiles as a function of the mixture fraction for different values of χ_{st} in the case of a methane-air flame.

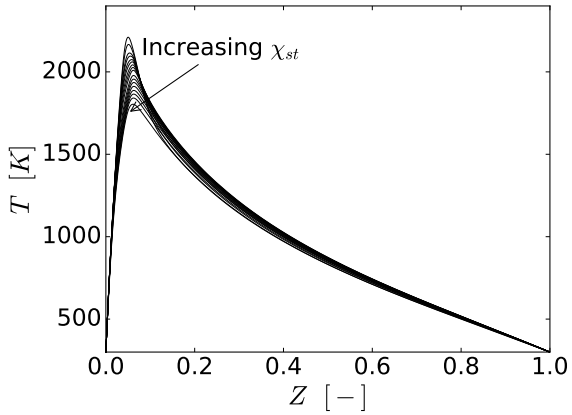

Figure 2.2: Temperature as a function of mixture fraction for different values of χ_{st}. Fuel: CH_4; Oxidizer: pure air.

2.2.4 Steady flamelet/progress variable model

The FPV approach has been developed to incorporate both stable and unstable states into the steady flamelet model (Pierce and Moin, 2004; Ihme et al., 2005; Ihme and Pitsch, 2008). In order to achieve this objective, a reaction progress variable, c, is used instead of the scalar dissipation rate. A reaction progress parameter, Λ, defined by evaluating c at stoichiometric conditions, $\Lambda = c_{st}$, is introduced to parametrize the chemistry tabulation. This definition ensures that the reaction progress parameter is independent of the mixture fraction (Ihme et al., 2005). Λ has to uniquely identify both stable and unstable branches in the library. Many definitions of the reaction progress variable are possible. It can be based either on the temperature or on linear combination of species mass fractions (Ihme et al., 2005; Ihme and Pitsch, 2008). In the present study, two definitions of progress variable, commonly used in the literature (Pierce and Moin, 2004; Shunn et al., 2012; Ihme et al., 2005; Ventosa, 2015), are considered:

$$\begin{aligned} c_1 &= Y_{CO_2} + Y_{H_2O} + Y_{CO} + Y_{H_2} \\ c_2 &= Y_{CO_2} + Y_{H_2O} \end{aligned} \tag{2.17}$$

The relationship between T_{st} and the progress parameters $c_{1,st}$ and $c_{2,st}$ is plotted in Fig. 2.3. This figure illustrates the bijective mapping of the entire S-shaped curve in the FPV approach.

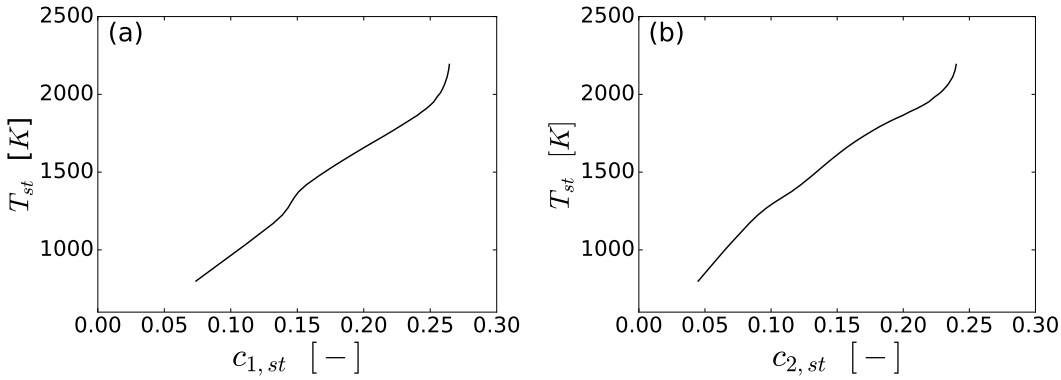

Figure 2.3: Profiles of temperature as a function of the reaction progress variable at stoichiometric conditions: (a) c_1 definition and (b) c_2 definition. Fuel: CH_4; Oxidizer: pure air.

After the flamelet equations are solved, state relationships can be then obtained

in terms of mixture fraction and Λ:

$$\phi = \phi^{fpv}(Z, \Lambda) \tag{2.18}$$

Nevertheless, the equation of conservation of Λ involves complicated model terms and is much more complex that of c (Ihme et al., 2005; Ihme and Pitsch, 2008). As a consequence, selecting c as a parameter is much more convenient for applications. In order to avoid this inconvenience, Ihme et al. (2005) propose a table inversion to eliminate Λ in favour of c, leading to tabulated flamelet solution for the thermochemical quantities of interest:

$$\phi = \phi^{fpv}(Z, c) \tag{2.19}$$

where c is readily obtained from its transport equation.

$$\frac{\partial \rho c}{\partial t} + \frac{\partial \rho u_i c}{\partial x_i} = \frac{\partial}{\partial x_i}\left(\rho D \frac{\partial c}{\partial x_i}\right) + \dot{\omega}_c \tag{2.20}$$

where $\dot{\omega}_c$ is the progress-variable reaction rate defined similarly to the progress-variable as a linear summation of species reaction rates.

The FPV tabulation provides a description of stable branch of the S-shaped curve that is identical to the SLF model, but also includes the unstable branch that characterizes intermediate or partially-burning states. As such, contrary to the SLF model, it is expected to capture local extinction and re-ignition processes (Ihme and Pitsch, 2008).

Figure 2.4 illustrates the temperature profiles as a function of the mixture fraction for the two branches. For the stable branch, the maximum temperature decreases when χ_{st} increases, while an opposite trend is observed for the unstable branch. Temperature profiles for the two branches meet at extinction. Figure 2.5 shows the evolution of c_1 and c_2 as a function of the mixture fraction for different flamelets covering both the stable and unstable branches in the case of CH_4-Air flame. It is interesting to investigate the profiles of c_1 and c_2 at small χ_{st} that characterizes usually combustion in fire scenarios. It can be observed that c_1 provides a better mapping in the stable branch than c_2 since some profiles of c_2 overlap in this region. In the opposite way, c_2 provides a better mapping in the unstable branch. These observations suggest that c_1 is expected to be a better choice if the combustion is dominated by the stable

branch whereas c_2 may become more attractive in cases where the unstable flamelet prevails.

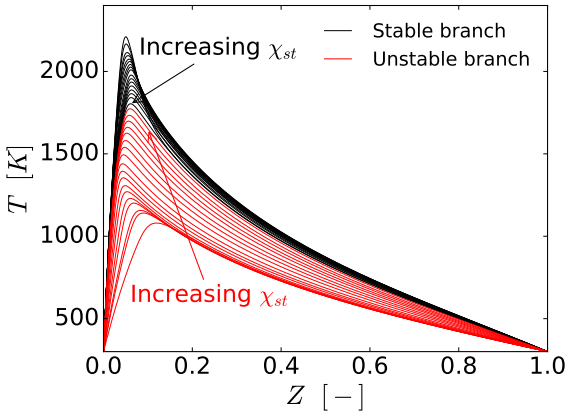

Figure 2.4: Profiles of Temperature as a function of mixture fraction in both stable and unstable branches with respect to χ_{st}. Fuel: CH_4; Oxidizer: pure air.

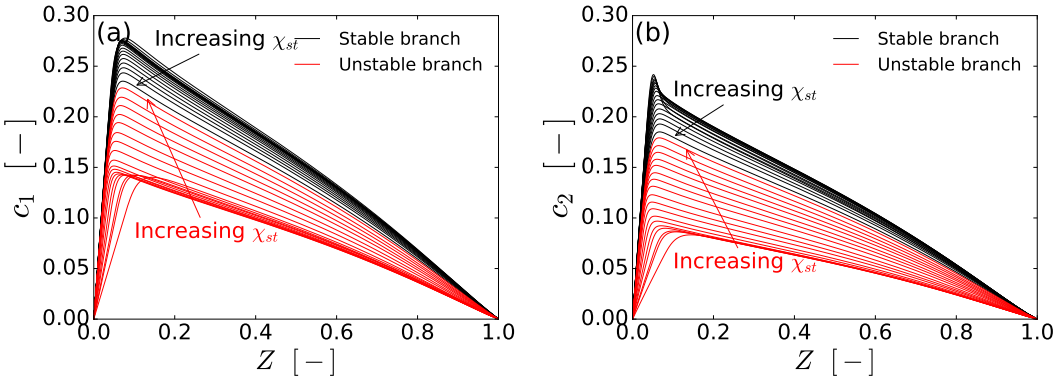

Figure 2.5: Profiles of reaction progress variable: (a) c_1 and (b) c_2 as a function of mixture fraction in both stable and unstable branches with respect to χ_{st}. Fuel: CH_4; Oxidizer: pure air.

2.2.5 Extended non-adiabatic flamelet model

Thermal radiation is an important phenomenon in reactive systems, especially for buoyant diffusion flames. Heat is released to the surroundings leading to additional interaction at the level of the flame structure. A model incorporating the effects of radiative loss on the flamelet is developed. The SLF or FPV models rely on the underlying assumption that the thermophysical state of

a particular flamelet relaxes to the steady-state solution on a sufficiently fast time-scale. However, radiative heat-loss processes evolve on time-scales that are slow compared to other processes in typical combustion applications (Ihme and Pitsch, 2008; Xu et al., 2020). Based on this observation, several extensions of the SLF have been proposed (Ihme and Pitsch, 2008; Carbonell et al., 2009) to incorporate the radiative loss. On the other hand, Xu et al. (2020) developed an unsteady flamelet model to couple combustion and radiation in a turbulent line fire. In the present study, the methodology described by Carbonell et al. (2009) was used to incorporate radiative loss in the flamelet library. The idea consists in generating flamelet profiles for each strain rate with different degrees of heat losses. A volumetric radiative heat sink term based on the optically-thin approximation was introduced in the flamelet energy equation (see Eq. 2.14) and was multiplied by a constant δ to allow variation in the degrees of radiative loss. For each strain rate, the flamelet temperature and species equations were solved for a set of prescribed δ factors ranging from 0 (adiabatic) to the maximum value which was adjusted to be near quenching conditions. For illustration, Fig. 2.6 presents temperature profiles with δ increasing from 0 to its maximum for a stable burning flamelet at a strain rate of $a = 8\ s^{-1}$. As δ increases, more enthalpy loses are introduced leading to a decrease in temperature. Figure 2.7 shows the same illustration in the case of the FPV. As expected, the same behaviour is observed as for the SLF model for the stable branch. An opposite trend is observed on the unstable branch with the temperature profile increasing with the degree of heat loss until it encounters the last non-adiabatic profile in the stable branch, which corresponds to the local quenching due to enthalpy loses (see Fig. 2.7).

Figure 2.8 shows the profiles of c_1 and c_2 as a function of the mixture fraction for different values of δ on both the stable and unstable branches. The strain rate was also $a = 8\ s^{-1}$. The progress variable c_1 follows the same trend as the temperature with δ increasing in both stable and unstable branches. On the opposite way, the behaviour of c_2 in the stable branch as δ increases is much intricate. This confirms that this latter definition of the progress variable may be not appropriate for stable burning flames.

As the total enthalpy is no longer conserved in a non-adiabatic flame, a new parameter characterizing the degree of heat loss has to be introduced to generate the look-up table. In the present study, the enthalpy defect, defined as

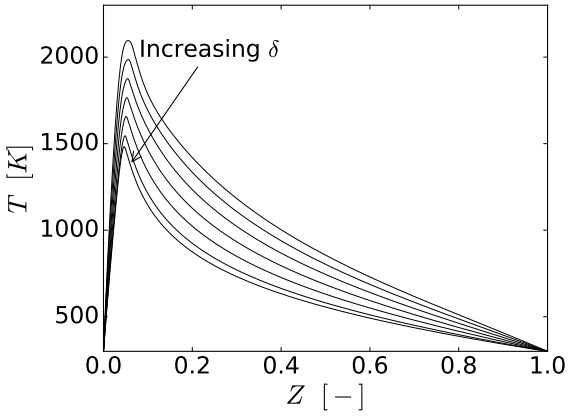

Figure 2.6: Temperature profiles as a function of mixture fraction with respect to δ for a stable burning flamelet at $a = 8\ s^{-1}$. Fuel: CH_4; Oxidizer: pure air.

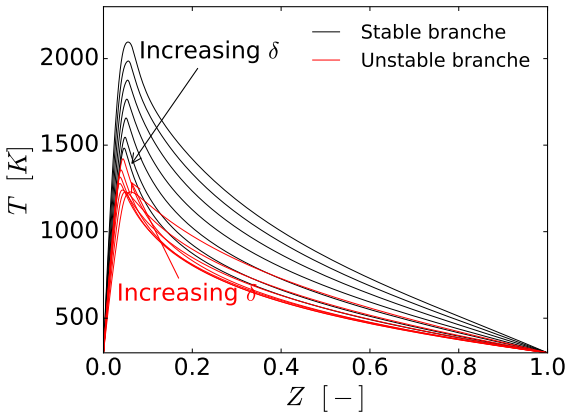

Figure 2.7: Temperature profiles as a function of mixture fraction in both stable and unstable branches with respect to δ for $a = 8\ s^{-1}$. Fuel: CH_4; Oxidizer: pure air.

the difference between the actual enthalpy and the adiabatic enthalpy of the same mixture, is considered:

$$X_R(Z) = h(Z) - h_{ad}(Z) \tag{2.21}$$

Similar to the progress variable parameter, an enthalpy defect parameter, independent of mixture fraction, is introduced.

$$\Theta = X_R | Z_{st} \tag{2.22}$$

As for the progress variable, a table inversion is then introduced to eliminate Θ in favour of X_R. As a consequence, the extended non-adiabatic flamelet states

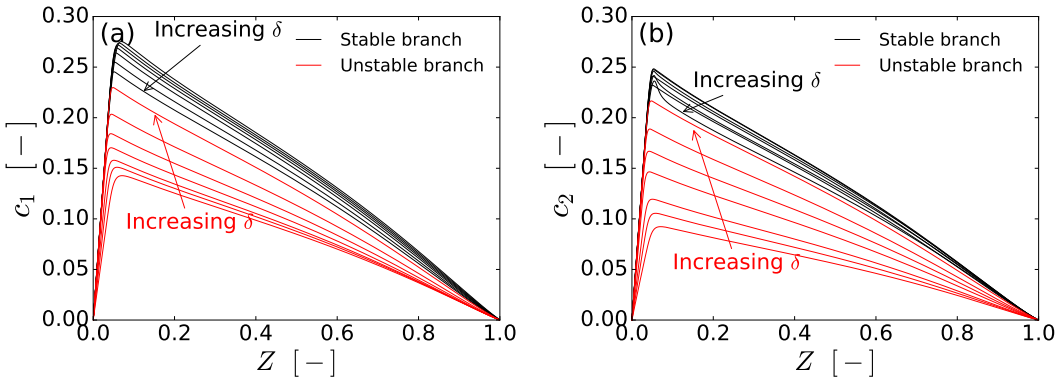

Figure 2.8: Profiles of reaction progress variable: (a) c_1 and (b) c_2 as a function of mixture fraction in both stable and unstable branches with respect to δ for $a = 8\ s^{-1}$. Fuel: CH_4; Oxidizer: pure air.

for SLF or FPV models are given by the following state relationships:

$$\begin{cases} \phi = \phi^{slf}(Z, \chi, X_R) & \text{for SLF} \\ \phi = \phi^{fpv}(Z, c, X_R) & \text{for FPV} \end{cases} \tag{2.23}$$

2.3 Radiation modelling

The present study focuses on non-sooting flames. As a consequence, water vapour and carbon dioxide are considered as the only radiating species since our simulations showed that the contribution of carbon monoxide is negligible. For all the gas radiative property models, the line parameters of CO_2 and H_2O are taken from HITEMP 2010 (Rothman et al., 2010).

Four radiative property models, namely the RCFSK, the non-grey WSGG, and two versions of the grey WSGG based on different evaluations of the mean path length are considered in the present work. The RTE can be written in a generic form as follows (Modest, 2013):

$$\frac{dI_i}{ds} + \kappa_i I_i = \kappa_i a_i I_b; \qquad i = 1, N_g \tag{2.24}$$

where I_i, κ_i, and I_b are the radiative intensity, non-grey absorption coefficient, and blackbody intensity, respectively. N_g and a_i are the number of quadrature points and the stretching function for the RCFSK or the number of grey gases and the weight factor for the non-grey WSGG, respectively. For the grey

models, only one RTE ($N_g = 1$) has to be solved and the weight factor is set equal to 1.

2.3.1 RCFSK model

The RCFSK model belongs to the family of the global k-distribution-based gas radiation models as the SLW or the classical FSCK. The RCFSK preserves the total emission and does not require any specification of a reference state (Solovjov et al., 2018). In configurations relevant for combustion applications, the RCFSK was found to provide an overall very good agreement with reference LBL or narrow band calculations in both emission and absorption dominated problems (Solovjov et al., 2018; Liu et al., 2020b; Consalvi et al., 2019). Consequently, it will be used as reference in the present study. Full-spectrum (FS) cumulative k-g distribution function is defined as (Modest and Haworth, 2016; Modest and Zhang, 2002):

$$g(k,\phi,T_p) = \frac{\int_0^\infty H[k-\kappa_\eta(\phi)] I_{b\eta}(T_p) d\eta}{I_b(T_p)} \tag{2.25}$$

where $\phi = \{x_{CO_2}, x_{H_2O}, T\}$ is an array of thermodynamic variables affecting the spectral absorption coefficient, κ_η, at the wavenumber η. H is the Heaviside function, k a given value of the absorption coefficient, and $I_{b\eta}(T_p)$ the spectral blackbody intensity at the Planck temperature T_p. In the present study, mixed FS k-g distributions (for mixtures of H_2O and CO_2) are constructed from HITEMP 2010 (Rothman et al., 2010) by using the procedure proposed by Modest and Riazzi (2005), and a 10-point Gauss-Legendre quadrature scheme ($N_g = 10$) is used (see Eq. (2.24)). For each quadrature point, g_i, the RCFSK scheme determines the absorption coefficient, κ_i, and the stretching function, $a_i(T)$, by solving (Solovjov et al., 2018):

$$g(\kappa_i,\phi,T_p) = g_i \tag{2.26}$$

$$a_i(T) = \frac{g[\kappa_i,\phi,T] - g[\kappa_{i-1},\phi,T]}{\Delta g}; \qquad \Delta g = g_i - g_{i-1} \tag{2.27}$$

The divergence of the radiative flux is then computed from the following equation:

$$\nabla \cdot \dot{q}_R'' = \underbrace{\sum_{i=1}^{N_g} 4\pi\kappa_i a_i I_b \Delta g}_{\dot{Q}'''_{emi}} - \underbrace{\sum_{i=1}^{N_g} \kappa_i G_i \Delta g}_{\dot{Q}'''_{abs}} \tag{2.28}$$

where $G_i = \int_{4\pi} I_i d\Omega$ with Ω being the solid angle. As expected, predictions were found insensitive to the choice of T_p. In the present simulations, T_p was set equal to 1500 K.

2.3.2 WSGG model

The WSGG assumes that the total emissivity, ϵ, can be computed as follows (Modest and Haworth, 2016):

$$\epsilon = \sum_{i=1}^{N_g} a_i(T)[1 - exp(-\kappa_i L)] \tag{2.29}$$

with

$$\kappa_i = (x_{CO_2} + x_{H_2O})p_0\kappa_{p,i} \quad and \quad a_i = \sum_{k=0}^{K} b_{i,k}T^k \tag{2.30}$$

L is the mean path length. In the present study, $p_0 = 1$ atm, $N_g = 4$ and $K = 4$. The constant WSGG parameters, $\kappa_{p,i}$ and $b_{i,k}$, derived in Ref. (Coelho and França, 2018) for $x_{H_2O}/x_{CO_2} = 2$, are used. These parameters were optimized to fit total emissivities determined from HITEMP 2010 (Rothman et al., 2010) for a set of specified temperatures and optical path-lengths.

The non-grey WSGG solves 4 RTEs ($N_g = 4$). For each RTE, κ_i and a_i are computed from Eq. (2.30). This approach will be referred to as WSGG-NG, hereafter. The divergence of the radiative flux is then determined as:

$$\nabla \cdot \dot{q}_R'' = \underbrace{\sum_{i=1}^{N_g} 4\pi\kappa_i a_i I_b}_{\dot{Q}'''_{emi}} - \underbrace{\sum_{i=1}^{N_g} \kappa_i G_i}_{\dot{Q}'''_{abs}}; \quad with \quad G_i = \int_{4\pi} I_i d\Omega \tag{2.31}$$

The grey WSGG consists in determining a grey absorption coefficient, κ, from the WSGG emissivity (Eq. 2.29):

$$\kappa = -\frac{ln(1-\epsilon)}{L} \tag{2.32}$$

There is no theoretical procedure to determine L in Eqs. (2.29) and (2.32). Two approaches were considered in the literature. The first approach consists in using a cell-based mean path length whereas the second assumes a domain or flame-based mean path length. The two options are considered in the present study. The cell-based approach is referred to as WSGG-G-CB hereafter and, following the recommendation of Refs. (Fraga et al., 2019; McGrattan et al.,

2014), L is determined as five times the characteristic local grid size. On the other hand, the flame-based determination of L is arbitrary since it depends on the way to define the flame. In the present study, $L = 4V/A$, where V and A are the flame volume and surface, respectively. The flame shape is assumed to be a cone with a circular base of diameter equal to the pool diameter and a height defined by the iso-contour 600 K. This value was selected since it is expected to characterize the intermittent flame tip (McCaffrey, 1979). Varying this temperature between 500 and 700 K was found to effect the radiant fraction by less than 1.5%. This approach will be referred to as WSGG-G-FB, hereafter.

Chapter 3

Large-eddy simulation

LES is based on a separation of scales. This separation is commonly introduced by a filtering operation which decomposes the velocity and scalar fields into a resolved (filtered) part and an unresolved (subgrid-scale) part. In addition, for variable density flow, the resolved quantities are density-weighted (Favre filtered) as defined by $\bar{\rho}\tilde{\phi} = \overline{\rho\phi}$. The Favre-filtered Navier-Stokes equations in low Mach number formulation supplemented with transport equations for the filtered enthalpy, $\tilde{h}$ and mixture fraction, $\tilde{Z}$, are:

$$\frac{\partial \bar{\rho}}{\partial t} + \frac{\partial \bar{\rho}\tilde{u}_i}{\partial x_i} = 0 \tag{3.1}$$

$$\frac{\partial \bar{\rho}\tilde{u}_j}{\partial t} + \frac{\partial \bar{\rho}\tilde{u}_i\tilde{u}_j}{\partial x_i} = -\frac{\partial \bar{p}}{\partial x_j} + \frac{\partial}{\partial x_i}\left(2\tilde{\mu}\tilde{S}_{ij}\right) + \frac{\partial \tau^{sgs}_{u_i u_j}}{\partial x_i} + (\bar{\rho} - \rho_0)g_i \tag{3.2}$$

$$\frac{\partial \bar{\rho}\tilde{h}}{\partial t} + \frac{\partial \bar{\rho}\tilde{u}_i\tilde{h}}{\partial x_i} = \frac{\partial}{\partial x_i}\left(\bar{\rho}\tilde{D}\frac{\partial \tilde{h}}{\partial x_i}\right) + \frac{\partial \tau^{sgs}_{u_i h}}{\partial x_i} - \bar{\dot{Q}}_R \tag{3.3}$$

$$\frac{\partial \bar{\rho}\tilde{Z}}{\partial t} + \frac{\partial \bar{\rho}\tilde{u}_i\tilde{Z}}{\partial x_i} = \frac{\partial}{\partial x_i}\left(\bar{\rho}\tilde{D}\frac{\partial \tilde{Z}}{\partial x_i}\right) + \frac{\partial \tau^{sgs}_{u_i Z}}{\partial x_i} \tag{3.4}$$

Note that Z can be represent the mixture fraction or passive scalar. The filtering process removes instantaneous small-scale fluctuations, but these subfilter quantities still exert a statistical effect on the resolved scales via subgrid-scale terms namely subgrid-scale stress, $\tau^{sgs}_{u_i u_j}$, and subgrid-scale scalar fluxes, $\tau^{sgs}_{u_i h}$ and $\tau^{sgs}_{u_i Z}$, which require modelling.

3.1 Subgrid stress tensor

The SGS momentum stress is modelled by extending the dynamic Smagorinsky model (DSM) of *Code_Saturne* (Archambeau et al., 2004; *Code_Saturne* n.d.) to density-weighted test filtering as described by Moin et al. (1991a), Desjardin et al. (2004), and Pierce and Moin (2004). The subgrid term appearing in Eq. (3.2) can be expressed as:

$$\tau^{sgs}_{u_iu_j} = -\bar{\rho}(\widetilde{u_iu_j} - \tilde{u}_i\tilde{u}_j) \approx 2C_s\bar{\rho}\Delta^2|\tilde{S}|\tilde{S}_{ij} \tag{3.5}$$

$$\mu_t = 2C_s\bar{\rho}\Delta^2|\tilde{S}| \tag{3.6}$$

where $|\tilde{S}| = \sqrt{2\tilde{S}_{ij}\tilde{S}_{ij}}$ is the norm of the resolved strain rate tensor and μ_t is the subgrid-scale viscosity. The coefficient C_s is dynamically adjusted to the local structure of the flow. The dynamic procedure consists in using a test filter with width $\Delta_t = 2\Delta$. The test-filtered stress is defined by analogy to the SGS stress, $\tau^{sgs}_{u_iu_j}$:

$$T_{u_iu_j} = -\left(\widehat{\bar{\rho}\widetilde{u_iu_j}} - \hat{\bar{\rho}}\breve{\tilde{u}}_i\breve{\tilde{u}}_j\right) \approx 2C_s\hat{\bar{\rho}}\Delta_t^2|\breve{\tilde{S}}|\breve{\tilde{S}}_{ij} \tag{3.7}$$

where $\widehat{(\cdot)}$ represents the filtering test operation and $\breve{\tilde{\phi}} = \frac{\widehat{\bar{\rho}\tilde{\phi}}}{\hat{\bar{\rho}}}$ denotes a density-weighted test filtered quantity. Using Germano's identity, the Leonard stress, $L_{u_iu_j}$, that represents the resolved SGS correlations at the test filter level can be expressed as:

$$L_{u_iu_j} = T_{u_iu_j} - \hat{\tau}^{sgs}_{u_iu_j} = -(\widehat{\bar{\rho}\tilde{u}_i\tilde{u}_j} - \hat{\bar{\rho}}\breve{\tilde{u}}_i\breve{\tilde{u}}_j) \tag{3.8}$$

Combining Eqs. (3.5), (3.7) and (3.8) yields:

$$C_sM_{u_iu_j} = L_{u_iu_j} \tag{3.9}$$

where $M_{u_iu_j}$ represents the difference between the SGS model expressed in terms of test filtered quantities and the SGS model test filtered:

$$M_{u_iu_j} = 2\hat{\bar{\rho}}\Delta_t^2|\breve{\tilde{S}}|\breve{\tilde{S}}_{ij} - 2\bar{\rho}\widehat{\Delta^2|\tilde{S}|}\tilde{S}_{ij} \tag{3.10}$$

The least-squares approach (Lilly, 1992) is applied to Eq. (3.9) to calculate the constant C_s:

$$C_s = \frac{< L_{u_iu_j}M_{u_iu_j} >}{< M_{u_iu_j}M_{u_iu_j} >} \tag{3.11}$$

where $< \cdot >$ denotes a local spatial averaging operation. In addition to local smoothing, entropy limit condition ($\mu + \mu_t \geq 0$) are enforced to limit the amount of backscatter in the simulations.

3.2 Subgrid scalar flux

In this section, closures for the subgrid-scale scalar flux terms are introduced by modelling the subgrid-scale diffusivity, D_t. Depending on the subgrid scalar flux model, D_t can be either scalar or tensor, thus will be expressed specifically according to each model. Furthermore, the subgrid-scale diffusivity is only computed through one scalar field, and then applied to all other scalars fields. The Dynamic linear eddy diffusivity model (DEDM) model will be first presented, followed by two models based on tensorial forms of the diffusivity for the SGS scalar flux, namely the dynamic generalized gradient model (DGGM) and dynamic full linear generalized gradient model (DLGGM) (Wang et al., 2008b). In addition, two mixed models, adding a gradient model (based on Taylor expansion of the filtering operation) to either the DEDM or the DGGM, will be introduced.

3.2.1 Dynamic linear eddy diffusivity model

The DEDM proposed by Moin et al. (1991a) expresses the SGS scalar flux, $\tau_{u_iZ}^{sgs}$, appearing in Eq. (3.4) as:

$$\tau_{u_iZ}^{sgs} = -\bar{\rho}(\widetilde{u_i Z} - \tilde{u}_i\tilde{Z}) \approx \bar{\rho}D_E\frac{\partial\tilde{Z}}{\partial x_i} \tag{3.12}$$

$$\bar{\rho}D_E = C_I\bar{\rho}\Delta^2|\tilde{S}| \tag{3.13}$$

The same dynamic procedure, as described above, gives:

$$C_I = \frac{< L_{u_iZ}M_{u_iZ} >}{< M_{u_iZ}M_{u_iZ} >} \tag{3.14}$$

with

$$L_{u_iZ} = -(\widehat{\bar{\rho}\tilde{u}_i\tilde{Z}} - \breve{\hat{\bar{\rho}}}\breve{\tilde{u}}_i\breve{\tilde{Z}}) \tag{3.15}$$

$$M_{u_iZ} = \hat{\bar{\rho}}\Delta_t^2|\breve{\tilde{S}}|\frac{\partial\breve{\tilde{Z}}}{\partial x_i} - \widehat{\bar{\rho}\Delta^2|\tilde{S}|\frac{\partial\tilde{Z}}{\partial x_i}} \tag{3.16}$$

3.2.2 Dynamic generalized gradient diffusion model

This model is inspired from the generalized gradient diffusion hypothesis (GGDH) proposed by Daly and Harlow (1970) in the RANS approach. In

the LES context, Wang and co-workers (Wang et al., 2008b) expressed the SGS scalar flux as follows:

$$\tau_{u_iZ}^{sgs} \approx \bar{\rho} D_{ik,G} \frac{\partial \tilde{Z}}{\partial x_k} \tag{3.17}$$

$$\bar{\rho} D_{ik,G} = C_{II} \mathscr{T} \tau_{u_i u_k}^{sgs} \tag{3.18}$$

where $D_{ik,G}$ is the tensor diffusivity which is a homogeneous linear tensor function of $\tau_{u_i u_k}^{sgs}$. $\mathscr{T}$ is a characteristic subgrid time scale, which can be evaluated by $1/|\tilde{S}|$. The coefficient C_{II} is calculated dynamically from:

$$C_{II} = \frac{< L_{u_iZ} G_{u_iZ} >}{< G_{u_iZ} G_{u_iZ} >} \tag{3.19}$$

with

$$G_{u_iZ} = \frac{T_{u_i u_k}}{|\breve{\tilde{S}}|} \frac{\partial \breve{\tilde{Z}}}{\partial x_k} - \widehat{\frac{\tau_{u_i u_k}^{sgs}}{|\tilde{S}|} \frac{\partial \tilde{Z}}{\partial x_k}} \tag{3.20}$$

L_{u_iY}, $T_{u_i u_k}$, and $\tau_{u_i u_k}^{sgs}$ are calculated by Eqs. (3.15), (3.7), and (3.5), respectively.

3.2.3 Dynamic full linear generalized gradient diffusion model

The tensor diffusivity, $D_{ik,E}$, for the DEDM is a function of S_{ij} of the zeroth order while the tensor diffusivity, $D_{ik,G}$, for the DGGM is a function of $\tau_{u_i u_k}^{sgs}$ of the first order. According to the theory of the polynomial functions, a DLGGM can be constructed by both zeroth and first parts of $\tau_{u_i u_k}^{sgs}$. Therefore, the DLGGM can be regarded as a combining form of the DEDM and DGGM, expressed as (Wang et al., 2008b):

$$\tau_{u_iZ}^{sgs} \approx \bar{\rho} D_{ik,L} \frac{\partial \tilde{Z}}{\partial x_k} \tag{3.21}$$

$$\bar{\rho} D_{ik,L} = C_{III} \mathscr{T} |\tau^{sgs}| \delta_{ik} + C_{II} \mathscr{T} \tau_{u_i u_k}^{sgs} \tag{3.22}$$

where $|\tau^{sgs}| = \sqrt{2 \tau_{u_i u_j}^{sgs} \tau_{u_i u_j}^{sgs}}$.

By using the least squares method, the computation of the two model constants, C_{III} and C_{II}, can be recast to solving a local linear system as (Wang et al., 2008b):

$$\begin{bmatrix} < P_{u_iZ}P_{u_iZ} > & < P_{u_iZ}G_{u_iZ} > \\ < G_{u_iZ}P_{u_iZ} > & < G_{u_iZ}G_{u_iZ} > \end{bmatrix} \cdot \begin{bmatrix} C_{III} \\ C_{II} \end{bmatrix} = \begin{bmatrix} < L_{u_iZ}P_{u_iZ} > \\ < L_{u_iZ}G_{u_iZ} > \end{bmatrix} \tag{3.23}$$

with

$$P_{u_iZ} = \frac{|T|}{|\breve{\tilde{S}}|}\frac{\partial \breve{\tilde{Z}}}{\partial x_i} - \frac{\widehat{|\tau^{sgs}|}}{|\tilde{S}|}\frac{\partial \tilde{Z}}{\partial x_i} \tag{3.24}$$

where $|T| = \sqrt{2T_{u_iu_k}T_{u_iu_k}}$. L_{u_iY}, $T_{u_iu_k}$, $\tau^{sgs}_{u_iu_k}$, and G_{u_iY} are calculated by Eqs. (3.15), (3.7), (3.5), and (3.20), respectively.

3.2.4 Dynamic Clark model

The gradient model is a classical structural-based model coming from the Taylor series expansion of the filtering operation (Bedford and Yeo, 1993):

$$\tau^{sgs}_{u_iZ} = -\bar{\rho}\frac{\Delta_k^2}{12}\frac{\partial \tilde{u}_i}{\partial x_k}\frac{\partial \tilde{Z}}{\partial x_k} + \mathcal{O}(\Delta^4) \tag{3.25}$$

where Δ_k is the filter width in the direction k. This model is known to have high correlation level with the SGS unknown term, but is numerically unstable due to an incorrect prediction of the dissipation and the amount of kinetic energy backscatter (Vreman et al., 1994; Lu and Porté-Agel, 2013). As a consequence, the Clark model consists in combining a gradient model with an eddy diffusivity model to provide a relative accurate representation of the SGS term (gradient model) and the appropriate level of dissipation (eddy diffusivity model) (Vreman et al., 1997). The Eq. (3.25) becomes (Fabre and Balarac, 2011):

$$\tau^{sgs}_{u_iZ} = -\bar{\rho}\frac{\Delta_k^2}{12}\frac{\partial \tilde{u}_i}{\partial x_k}\frac{\partial \tilde{Z}}{\partial x_k} + \bar{\rho}D_{ik}\frac{\partial \tilde{Z}}{\partial x_k} \tag{3.26}$$

In the present study, DEDM and DGGM are considered to model the tensor diffusivity, D_{ik}, leading to the M1 and M2, respectively. Recently, Fabre and Balarac (2011) proposed a new dynamic procedure based on a Taylor series expansion of L_{u_iZ} to determine the model constants:

$$C = \frac{< (L_{u_iZ} - H_{u_iZ})N_{u_iZ} >}{< N_{u_iZ}N_{u_iZ} >} \tag{3.27}$$

L_{u_iZ} is the Leonard term, Eq. (3.8) , N_{u_iZ} and H_{u_iZ} are written as

$$N_{u_iZ} = \begin{cases} \hat{\bar{\rho}}\Delta_t^2|\breve{\tilde{S}}|\frac{\partial\breve{\tilde{Z}}}{\partial x_i} & \text{for M1} \\ \frac{T_{u_iu_k}}{|\breve{\tilde{S}}|}\frac{\partial\breve{\tilde{Z}}}{\partial x_k} & \text{for M2} \end{cases} \tag{3.28}$$

$$H_{u_iZ} = -\hat{\bar{\rho}}\frac{\Delta_{t,k}^2}{12}\frac{\partial\breve{\tilde{u}}_i}{\partial x_k}\frac{\partial\breve{\tilde{Z}}}{\partial x_k} \quad \text{for both models} \tag{3.29}$$

3.3 Subgrid chemistry closure

In LES of non-premixed combustion, many important mixing and reaction processes occur at scales that are unresolved on the computational grid. Combustion-related variables such as the mixture fraction fluctuating quantities and their statistical distribution need to be considered. Subgrid fluctuations of the combustion variables can have an important impact on the filtered properties due to the sensitivity and non-linearity of combustion processes. To account for subgrid fluctuations in the combustion variables, filtered combustion variables are obtained by integrating the state equation over the joint FDF of either (Z, χ and X_R) for the SLF model or (Z, c and X_R) for the FPV model.

In the case of SLF, the filtered combustion variables are given by:

$$\tilde{\phi} = \int \phi^{slf}(Z,\chi,X_R)\tilde{P}(Z,\chi,X_R)dZd\chi dX_R \tag{3.30}$$

Z,χ and X_R are assumed to be statistically independent and the marginal FDFs are modelled by a beta distribution for Z and delta distributions for χ and X_R:

$$\tilde{P}(Z,\chi,X_R) = \beta(Z;\tilde{Z},V_Z)\delta(\chi-\tilde{\chi})\delta(X_R-\tilde{X}_R) \tag{3.31}$$

The beta distribution is given by:

$$\beta(Z;\tilde{Z},V_Z) = Z^{a-1}(1-Z)^{b-1}\frac{\Gamma(a+b)}{\Gamma(a)+\Gamma(b)} \tag{3.32}$$

with

$$a = \frac{\tilde{Z}(\tilde{Z}-\tilde{Z}^2-V_Z)}{V_Z} \quad b = \frac{(1-\tilde{Z})(\tilde{Z}-\tilde{Z}^2-V_Z)}{V_Z} \tag{3.33}$$

where V_Z is the subgrid mixture fraction variance.

In the case of FPV approach, the filtered combustion variables are given:

$$\tilde{\phi} = \int \phi^{fpv}(Z,c,X_R)\tilde{P}(Z,c,X_R)dZdcdX_R \tag{3.34}$$

By assuming the statistically independent Z, c, and X_R, the joint FDF is expressed as:

$$\tilde{P}(Z, c, X_R) = \beta(Z; \tilde{Z}, V_Z)\delta(c - \tilde{c})\delta(X_R - \tilde{X}_R) \tag{3.35}$$

Once the flamelet library is computed and assumed FDF integrals are evaluated, a look-up table can be generated to provide the filtered thermo-chemical variables as functions of the quantities readily available from LES (Pierce and Moin, 2004).

$$\begin{cases} \tilde{\phi} = \tilde{\phi}^{slf}(\tilde{Z}, V_Z, \tilde{\chi}, \tilde{X}_R) & \text{for SLF} \\ \tilde{\phi} = \tilde{\phi}^{fpv}(\tilde{Z}, V_Z, \tilde{c}, \tilde{X}_R) & \text{for FPV} \end{cases} \tag{3.36}$$

The filtered reaction progress variable, $\tilde{c}$, will be obtained by solving the following transport equation:

$$\frac{\partial \bar{\rho}\tilde{c}}{\partial t} + \frac{\partial \bar{\rho}\tilde{u}_i\tilde{c}}{\partial x_i} = \frac{\partial}{\partial x_i}\left(\bar{\rho}D\frac{\partial \tilde{c}}{\partial x_i}\right) + \frac{\partial \tau^{sgs}_{u_i c}}{\partial x_i} + \overline{\dot{\omega}_c} \tag{3.37}$$

and,

$$\overline{\dot{\omega}_c} = \bar{\rho}\int \frac{\dot{\omega}_c^{fpv}(Z, \tilde{c}, \tilde{\chi}_R)}{\rho^{fpv}(Z, \tilde{c}, \tilde{\chi}_R)}\beta(Z; \tilde{Z}, V_Z)dZ \tag{3.38}$$

Sperious heat release

In variable density low-Mach Navier-Stokes solver, inconsistencies between changes in density from the pre-tabulated non-linear equation of state and changes in density from the continuity equations can induce spurious density fluctuations, which may result in large spurious fluctuations of velocity and pressure that destabilize the simulation (Shunn, 2009). The same procedure to control spurious density fluctuations as proposed by Vreman et al. (2008) is adopted in the present study. It consists in removing the smallest resolved scale by explicit filter operations with a filter width equal to 2Δ. The density is filtered by the explicit filter after the retrievals from the flamelet look-up table, such that each $\bar{\rho}$ appearing in the left-hand side of Eqs. (3.1) to (3.4) is replaced by the filtered density computed as:

$$\begin{cases} \hat{\bar{\rho}} = \bar{\rho}^{slf}(\widehat{\tilde{Z}, V_Z, \tilde{\chi}}, \tilde{X}_R), & \text{for SLF} \\ \hat{\bar{\rho}} = \bar{\rho}^{fpv}(\widehat{\tilde{Z}, V_Z}, \tilde{c}, \tilde{X}_R), & \text{for FPV} \end{cases} \tag{3.39}$$

3.4 Subgrid scalar variance and dissipation

3.4.1 Non-equilibrium models

The subgrid scalar variance V_Z, required to retrieve solutions from the filtered flamelet look-up table, is defined in terms of a FDF as (Jiménez et al., 2001) :

$$V_Z(\mathbf{x},t) = \widetilde{Z^2}(\mathbf{x},t) - \tilde{Z}^2(\mathbf{x},t) \tag{3.40}$$

The appearance of the second moment $\widetilde{Z^2}$ makes the variance unclosed. The subgrid scalar variance can be computed by using its transport equation (VTE) (Jiménez et al., 2001):

$$\frac{\partial \bar{\rho} V_Z}{\partial t} + \frac{\partial \bar{\rho}\tilde{u}_i V_Z}{\partial x_i} = \frac{\partial}{\partial x_i}\left(\bar{\rho}\left(\tilde{D}+D_t\right)\frac{\partial V_Z}{\partial x_i}\right) + \mathcal{P} - \bar{\rho}\tilde{\chi} \tag{3.41}$$

where the production term is defined as:

$$\mathcal{P} = 2\bar{\rho}\left(\tilde{D}+D_t\right)\frac{\partial \tilde{Z}}{\partial x_i}\frac{\partial \tilde{Z}}{\partial x_i} \tag{3.42}$$

Another way to compute the subgrid-scale variance consists in solving the transport equation for the second moment of the mixture fraction $\widetilde{Z^2}$, (STE) (Kaul et al., 2009; Kaul and Raman, 2011). Once the second moment $\widetilde{Z^2}$ and $\tilde{Z}$ are resolved, the subgrid scalar variance V_Z thus can be computed from its definition, Eq. (3.40).

$$\frac{\partial \bar{\rho}\widetilde{Z^2}}{\partial t} + \frac{\partial \bar{\rho}\tilde{u}_i\widetilde{Z^2}}{\partial x_i} = \frac{\partial}{\partial x_i}\left(\bar{\rho}(\tilde{D}+D_t)\frac{\partial \widetilde{Z^2}}{\partial x_i}\right) - \bar{\rho}\tilde{\chi} \tag{3.43}$$

In both VTE and STE models, the filtered scalar dissipation rate term, $\tilde{\chi}$, is unclosed and requires modelling. Jiménez et al. (2001) proposed to model the filtered scalar dissipation rate by relating the subgrid-scale scalar mixing time scale to the subgrid-scale turbulent time scale. The characteristic mixing time is assumed proportional to the turbulent characteristic time. In LES, the subgrid-scale scalar mixing time can be defined as:

$$\frac{1}{\tilde{\tau}_Z} = \frac{\tilde{\chi}}{V_Z} \tag{3.44}$$

An equivalent subgrid-scale turbulent characteristic time $\bar{\tau}$ is introduced as the ratio between subgrid-scale kinetic energy, $\kappa^{sgs} = 1/2(\widetilde{u_i u_i} - \tilde{u}_i\tilde{u}_i)$, and the

filtered kinetic energy dissipation rate, $\tilde{\varepsilon} = \tilde{\nu}\widetilde{\frac{\partial u_i}{\partial x_j}\frac{\partial u_i}{\partial x_j}}$. Given a proportionality between both time scales, the model for, $\tilde{\chi}$, is derived as:

$$\frac{\tilde{\chi}}{V_Z} = \frac{1}{\tilde{\tau}_Z} \approx \frac{C}{\tilde{\tau}} = C\frac{\tilde{\varepsilon}}{\kappa^{sgs}} \tag{3.45}$$

The filtered kinetic energy dissipation rate and the subgrid-scale kinetic energy are modelled as:

$$\tilde{\varepsilon} = 2\left(\tilde{\nu} + \nu_T\right)\tilde{S}_{ij}\tilde{S}_{ij} \tag{3.46}$$

$$\kappa^{sgs} = 2C_I\Delta^2\tilde{S}_{ij}\tilde{S}_{ij} \tag{3.47}$$

As proposed by Jiménez et al. (2001), $C = 1/Sc$, and C_I can be computed by dynamic approach. Therefore, the filtered scalar dissipation rate $\tilde{\chi}$ can be written as:

$$\tilde{\chi} = \frac{\tilde{D} + D_t}{C_I\Delta^2}V_Z \tag{3.48}$$

3.4.2 Algebraic equilibrium model

If production and destruction of the SGS mixture fraction variance is assumed to be in equilibrium (Pierce and Moin, 1998), the scalar dissipation rate can be computed as:

$$\tilde{\chi} = 2\left(\tilde{D} + D_t\right)\frac{\partial\tilde{Z}}{\partial x_i}\frac{\partial\tilde{Z}}{\partial x_i} \tag{3.49}$$

With the local equilibrium assumption (LEA), the SGS mixture fraction variance is computed through a scale similarity model (Pierce and Moin, 1998), denoted hereafter as the algebraic model:

$$V_Z = C_v\Delta^2\frac{\partial\tilde{Z}}{\partial x_i}\frac{\partial\tilde{Z}}{\partial x_i} \tag{3.50}$$

where C_v is calculated dynamically.

3.5 Subgrid-scale TRI

The filtered RTE can be written in a generic form as follows (Modest and Haworth, 2016):

$$\frac{d\overline{I_i}}{ds} + \overline{\kappa_i I_i} = \overline{\kappa_i a_i I_b}; \qquad i = 1, N_g \tag{3.51}$$

The filtered absorption term, $\overline{\kappa_i I_i}$, is closed by neglecting the SGS absorption TRI, leading to $\overline{\kappa_i I_i} \approx \overline{\kappa_i}\overline{I_i}$. This approximation was found to be valid in LES of non-luminous and luminous lab- and large-scale diffusion flames in which about 80% of the turbulent fluctuations are resolved (Gupta et al., 2013; Coelho, 2009; Consalvi et al., 2018). The absorption coefficient and the emission term depend only on temperature and mole fractions of CO_2 and H_2O. Therefore, the filtering operation for these terms can be performed accurately by using the FDF approach (Modest and Haworth, 2016):

$$\overline{\kappa_i} = \bar{\rho} \int \frac{(\kappa_i)^{slf}(Z, \tilde{\chi}, \tilde{\chi}_R)}{\rho^{slf}(Z, \tilde{\chi}, \tilde{\chi}_R)} \beta(Z; \tilde{Z}, V_Z) dZ \tag{3.52}$$

$$\overline{\kappa_i a_i I_b} = \bar{\rho} \int \frac{(\kappa_i a_i I_b)^{slf}(Z, \tilde{\chi}, \tilde{\chi}_R)}{\rho^{slf}(Z, \tilde{\chi}, \tilde{\chi}_R)} \beta(Z; \tilde{Z}, V_Z) dZ \tag{3.53}$$

Eqs. (3.52) and (3.53) are expressed in the case of the SLF model. Similar equations can be obtained for the FPV model.

Chapter 4

Numerical algorithm and verification

CFD codes devoted to the simulations of turbulent buoyant fire plumes and, more generally, flows encountered in fire safety applications are based on low Mach number variable-density Navier-Stokes solvers (*FireFoam* n.d.; McGrattan et al., 2014). These mathematical approaches represent the basis of the CFD code and physical sub-models for turbulence, combustion and radiation are then implemented to achieve numerical simulations of practical problems (Yuen et al., 2015; Yuen et al., 2016). An important step in the development of a CFD code is the verification and validation processes which establish the degree of confidence in a computational model for specific applications (Oberkampf and Trucano, 2002; Shunn et al., 2012; Mullyadzhanov et al., 2016). The verification step checks that the numerical models are well implemented and satisfy the desired accuracy through analytical solutions or method of manufactured solutions (MMS). In this chapter, a new low-Mach variable-density Navier-Stokes equations solver is developed. Its verification through method of manufactured solutions is realised in order to prove the second-order accuracy in both time and space. Then this solver is used to simulate the Rayleigh-Taylor instability case and results are compared with those reported in the literature (Desjardins et al., 2008; Mullyadzhanov et al., 2016).

4.1 Numerical algorithm

The governing equations in the low Mach number form for mass, momentum, and scalar, as well as the equation of state are expressed in a compact form:

$$\frac{\partial \rho}{\partial t} + div(\rho \boldsymbol{u}) = \dot{Q}_{\rho} \tag{4.1}$$

$$\frac{\partial \rho \boldsymbol{u}}{\partial t} + div(\rho \boldsymbol{u} \otimes \boldsymbol{u}) = -\nabla p + div\left(2\mu \boldsymbol{S}\right) + \dot{Q}_{\boldsymbol{u}} \tag{4.2}$$

$$\frac{\partial \rho Y}{\partial t} + div(\rho \boldsymbol{u} Y) = div(\rho D \nabla Y) + \dot{Q}_{Y} \tag{4.3}$$

$$\rho = f(Y) \tag{4.4}$$

where $\boldsymbol{S}$ is the strain rate tensor given by:

$$\boldsymbol{S} = \frac{1}{2}(\nabla \boldsymbol{u} + \nabla^{T} \boldsymbol{u}) - \frac{1}{3} div(\boldsymbol{u}) \boldsymbol{I} \tag{4.5}$$

The variables ρ, $\boldsymbol{u}$, p, and Y denote the density, velocity vector, $\boldsymbol{u} = (u, v, w)$, pressure, and additional scalar field, respectively. μ and D are the dynamic viscosity and kinematic diffusivity, respectively. The source terms $\dot{Q}_{\rho}$, $\dot{Q}_{\boldsymbol{u}}$, and $\dot{Q}_{Y}$ are used to construct the manufactured solutions.

The following iterative procedure is implemented into *Code_Saturne*, a finite-volume code developed at EDF, employing cell-centred collocated grids (Archambeau et al., 2004; *Code_Saturne* n.d.). In the following, the superscripts n and $n+1$ denote the known value at $n\Delta t$ and the value to be computed at $(n+1)\Delta t$, respectively. The superscript k refers to the solution at each sub-iteration within one time step. At each time step, the scalar equation is first resolved to get the new scalar and density fields. Then a pressure-velocity step is performed by resolving the momentum and Poisson equations with the computed density. At each time step, sub-iterations were performed to achieve second-order accuracy and numerical stability. The second-order Crank-Nicolson scheme is employed for time advancement. For the scalar, a second-order Superbee-TVD scheme (Versteeg and Malalasekera, 2007) is used for the convective term whereas a second-order central difference scheme is used for diffusion. For the momentum equation both convective and diffusive terms are discretized by using a second-order central difference scheme. The sub-iteration procedure is described below:

1. Initialization of mass flux, pressure, source terms, and density:

$$(\rho \boldsymbol{u})^{n+\frac{1}{2},0} = 2(\rho \boldsymbol{u})^{n+\frac{1}{2}-1} - (\rho \boldsymbol{u})^{n+\frac{1}{2}-2} \tag{4.6}$$

$$p^{n+\frac{1}{2},0} = p^{n+\frac{1}{2}-1} \tag{4.7}$$

$$(\dot{Q}_{\boldsymbol{u}})^{n+\frac{1}{2}} = \frac{3}{2}\dot{Q}_{\boldsymbol{u}}^{n} - \frac{1}{2}\dot{Q}_{\boldsymbol{u}}^{n-1} \tag{4.8}$$

$$(\dot{Q}_{Y})^{n+\frac{1}{2}} = \frac{3}{2}\dot{Q}_{Y}^{n} - \frac{1}{2}\dot{Q}_{Y}^{n-1} \tag{4.9}$$

   The source terms $\dot{Q}_{\boldsymbol{u}}$ and $\dot{Q}_{Y}$ are extrapolated by the Adams-Bashforth method which provides a second-order estimation. The density is initialized as $\rho^{n+1,0} = 3\rho^{n} - 3\rho^{n-1} + \rho^{n-2}$ to be compatible with $(\rho \boldsymbol{u})^{n+\frac{1}{2},0}$ and ensure the conservation.

2. Solve the scalar transport equation to get the provisional scalar value, $\hat{Y}^{n+1,k+1}$.

3. Get $\rho^{n+1,k+1}$ from Eq. (4.4) with $\hat{Y}^{n+1,k+1}$.

4. Update the scalar field to ensure the conservativity:

$$Y^{n+1,k+1} = \frac{\rho^{n+1,k}\hat{Y}^{n+1,k+1}}{\rho^{n+1,k+1}} \tag{4.10}$$

5. Solve the momentum equation to get the predicted velocity, $\hat{\boldsymbol{u}}^{n+1,k+1}$.

6. A constant coefficient Poisson equation for pressure is obtained by introducing the continuity equation into the momentum equation and solved to ensure mass conservation. This equation is written as:

$$div(\rho^{n+1,k}\boldsymbol{u}^{n+1,k+1}) - div(\rho^{n+1,k}\hat{\boldsymbol{u}}^{n+1,k+1}) = -div(\Delta t \boldsymbol{\nabla} \delta p^{n+1,k+1}) \tag{4.11}$$

   The first term of Eq. (4.11) can be extrapolated by the Adams-Bashforth scheme:

$$div(\rho^{n+1,k}\boldsymbol{u}^{n+1,k+1}) = \frac{3}{2}div(\rho \boldsymbol{u})^{n+\frac{1}{2},k+1} - \frac{1}{2}div(\rho \boldsymbol{u})^{n-\frac{1}{2}} \tag{4.12}$$

   In addition, mass conservation implies:

$$\frac{\rho^{n+1,k+1} - \rho^{n}}{\Delta t} + div(\rho \boldsymbol{u})^{n+\frac{1}{2},k+1} = 0 \tag{4.13}$$

   Combining Eqs. (4.11), (4.12) and (4.13) yields the Poisson equation for the pressure increment:

$$div(\Delta t \boldsymbol{\nabla} \delta p^{n+1,k+1}) = div(\rho^{n+1,k}\hat{\boldsymbol{u}}^{n+1,k+1}) + \frac{3}{2}\frac{\rho^{n+1,k+1} - \rho^{n}}{\Delta t} + \frac{1}{2}div(\rho \boldsymbol{u})^{n-\frac{1}{2}} \tag{4.14}$$

Once the pressure increment is obtained, the variables are updated as:

$$p^{n+\frac{1}{2},k+1} = p^{n+\frac{1}{2},k} + \delta p^{n+1,k+1} \tag{4.15}$$

$$(\rho^{n+1,k}\boldsymbol{u}^{n+1,k+1}) = -\Delta t \boldsymbol{\nabla} \delta p^{n+1,k+1} + (\rho^{n+1,k}\hat{\boldsymbol{u}}^{n+1,k+1}) \tag{4.16}$$

$$\boldsymbol{u}^{n+1,k+1} = \frac{(\rho^{n+1,k}\boldsymbol{u}^{n+1,k+1})}{\rho^{n+1,k}} \tag{4.17}$$

7. Reconstruct the mass flux:

$$(\rho \boldsymbol{u})^{n+\frac{1}{2},k+1} = \frac{2}{3}(\rho^{n+1,k}\boldsymbol{u}^{n+1,k+1}) + \frac{1}{3}(\rho \boldsymbol{u})^{n+\frac{1}{2}-1} \tag{4.18}$$

8. The process is repeated from step 2 until convergence is achieved. The sub-iteration process is assumed to be converged when $\varepsilon_{iter} < 10^{-8}$ with ε_{iter} defined as:

$$\varepsilon_{iter} = \frac{||X^{n+1,k+1} - X^{n+1,k}||_{L_2}}{||X^n||_{L_2}} \tag{4.19}$$

where X represents the numerical solution for both the scalar and velocity components and $||\cdot||_{L_2}$ is the L_2-norm.

4.2 Algorithm verification by MMS

This section presents the verification tests for the numerical algorithm proposed above. Three manufactured solutions proposed by Shunn et al. (2012) are considered. In these three cases, the L_2-error for the variable X is defined as:

$$E_{L_2}(X) \equiv \frac{||X_e - X||_{L_2}}{||X_e||_{L_2}} \tag{4.20}$$

where X and X_e are the numerical and exact solutions, respectively.

1D-D	value	2D-AD	value	2D-ODF	value
(ρ_0,ρ_1)	(20,1)	$(\rho_0,\ \rho_1)$	(20,1)	(ρ_0,ρ_1)	(5,1)
w_0	50	(u_f,v_f)	(1,0.5)	$u_f = v_f$	0.5
$\rho D = \mu$	0.03	$\rho D = \mu$	0.001	$\rho D = \mu$	0.001
(k_1, k_2)	(4,2)	(k,ω)	(4π,1.5)	$k = \omega$	2
		(a,b)	(0.2,20)		

Table 4.1: Calculation parameters for the MMS (Shunn et al., 2012).

4.2.1 *One-dimensional Diffusion*

We consider firstly a one-dimensional diffusion manufactured solution (1D-D):

$$\begin{aligned} Y(x,t) &= \frac{exp(-k_1 t) - cosh(w_0 x exp(-k_2 t))}{exp(-k_1 t)(1-\rho_0/\rho_1) - cosh(w_0 x exp(-k_2 t))} \\ \rho(x,t) &= \left(\frac{Y(x,t)}{\rho_1} + \frac{1-Y(x,t)}{\rho_0} \right)^{-1} \\ u(x,t) &= 2k_2 exp(-k_1 t) \frac{\rho_0 - \rho_1}{\rho(x,t)} \left(\frac{\hat{u}}{\hat{u}^2+1} + \frac{(k_1/k_2 - 1)(arctan\hat{u} - \pi/4)}{w_0 exp(-k_2 t)} \right) \end{aligned} \tag{4.21}$$

where $\hat{u} = exp(w_0 x exp(-k_2 t))$, and k_1, k_2, and w_0 are constant parameters given in Table 4.1. This manufactured solution satisfies the continuity and momentum equations with $\dot{Q}_\rho = 0$, $\dot{Q}_u = 0$. On the other hand, a non-zero source term, $\dot{Q}_Y$, appears in the scalar transport equation. This pseudo-diffusion problem is actually controlled by the relative values of the parameters k_1 and k_2, and is independent of the physical scalar diffusivity, ρD. The diffusivity still appears in the MMS problem, but only affects the shape and magnitude of the source term, $\dot{Q}_Y$. The computational domain for this problem is $x \in [0, 2]$ and $t \in [0, 1]$. The inlet boundary conditions are Dirichlet condition with a prescribed value of 0 for the velocity and Neumman condition for pressure and scalar. At the domain exit, an outflow boundary condition is used.

Figures 4.1(a) and (b) investigate the spatial and temporal convergences, respectively. Grid resolutions consisting of n_x= 100, 200, 400, 800, 1600, 3200, and 6400 uniform control volumes and time steps ranging from 0.04 (number of time steps $n_t = 25$) to 0.00125 ($n_t = 800$) are considered. In Fig. 4.1(a), the time step is fixed at 0.00125 ($n_t = 800$). At such a time step the error with respect to the spatial resolution exhibits a second-order convergence up to n_x = 3200 where the temporal error starts to contaminate the solution. Similarly, for the highest grid resolution ($n_x = 6400$) a second-order convergence is observed in Fig. 4.1(b) up to $n_t = 400$ ($\Delta t = 0.0025$). For larger n_t, the spatial error dominates and the temporal convergence starts to stall. Figures 4.1(c) and (d) show the time evolution of the L_2-error for the scalar and velocity fields for different spatial resolutions and a time-step of 0.00125 ($n_t = 800$). These figures confirm the convergence of the algorithm. Figure 1e depicts the L_2-error as a function of n_x for a constant Fourier number, $Fo = D\Delta t/\Delta x^2$

of 6. This figure confirms the second-order accuracy of the scheme for this problem.

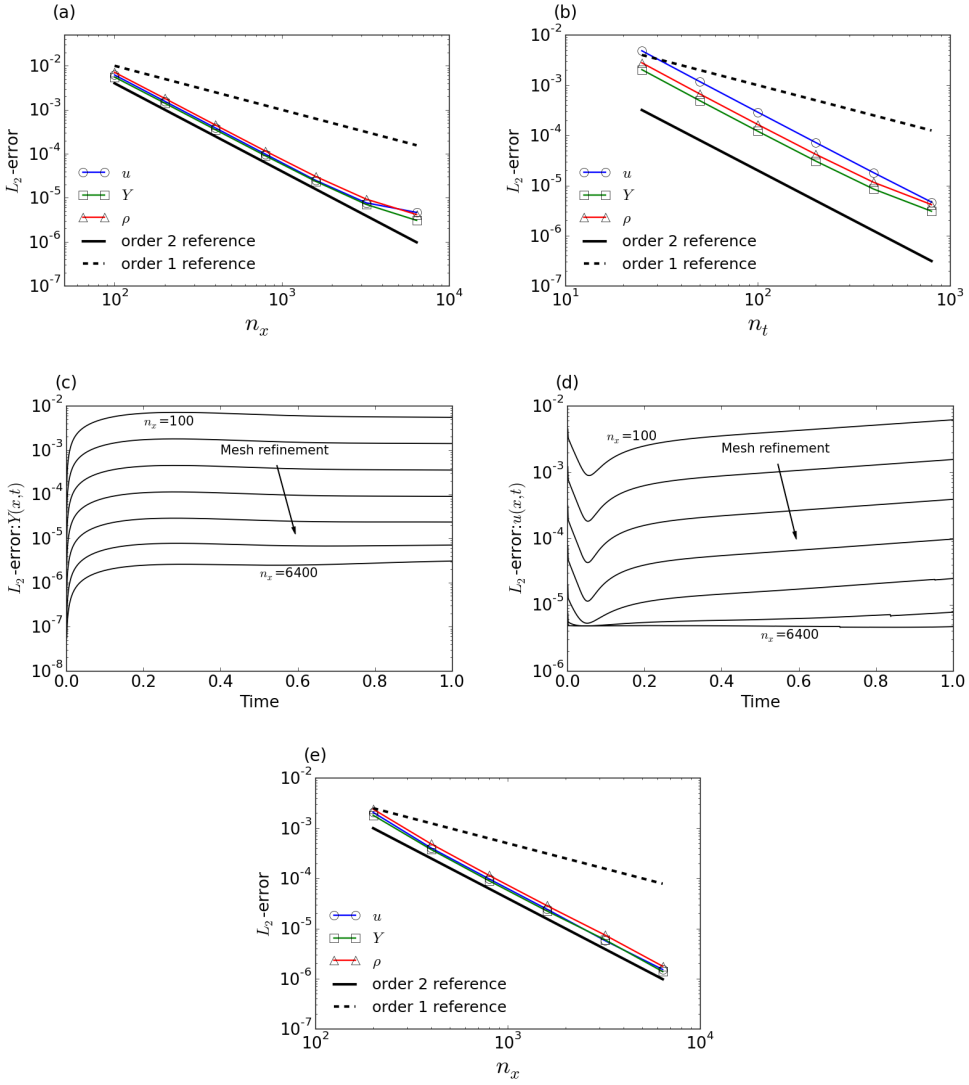

Figure 4.1: 1D-D MMS. (a) L_2-error as a function of the spatial resolution for $\Delta t = 0.00125$. (b) L_2-error as a function of the temporal resolution for $n_x = 6400$, (c) Time evolution of the L_2-error for density, (d) Time evolution of the L_2-error for velocity, (e) L_2-error as a function of the spatial resolution for a constant $Fo = 6$.

4.2.2 *Two-dimensional advection and diffusion*

The second MMS problem involves a two-dimensional corrugated front with advection and diffusion (2D-AD):

$$\begin{aligned}
Y(x,y,t) &= \frac{1+tanh(b\hat{x}exp(-\omega t))}{(1+\rho_0/\rho_1)-(1-\rho_0/\rho_1)tanh(b\hat{x}exp(-\omega t))} \\
\rho(x,y,t) &= \left(\frac{Y(x,t)}{\rho_1}+\frac{1-Y(x,t)}{\rho_0}\right)^{-1} \\
u(x,y,t) &= \frac{\rho_1-\rho_0}{\rho(x,t)}\left(-\omega\hat{x}+\frac{\omega\hat{x}-u_f}{exp(2b\hat{x}exp(-\omega t))+1}\right. \\
&\qquad \left. +\frac{\omega log(exp(2b\hat{x}exp(-\omega t))+1)}{2bexp(-\omega t)}\right) \\
v(x,y,t) &= v_f \\
p(x,y,t) &= 0
\end{aligned} \tag{4.22}$$

where $\hat{x}(x,y,t) = u_f t - x + acos(k(v_f t - y))$. a, b, k, ω, u_f, and v_f are constant parameters (see Table 4.1). The computational domain for this problem is $-1 \leq x \leq 3$, $-1/2 \leq y \leq 1/2$, and $0 \leq t \leq 1$. This set of equations satisfies the continuity equation with $\dot{Q}_\rho = 0$. Non-zero source terms appear in the x-, y-momentum, and scalar transport equations. The density front advects diagonally across the domain according to the relative values of u_f and v_f. The steepness of the initial density profile in the x-direction is governed by the value of b, while a and k dictate the x-amplitude and wavenumber of the sinusoidal perturbation, respectively. The rate at which the front broadens with time is determined by the inverse time scale, ω. Dirichlet boundary conduction is used at $x = -1$, an outflow boundary condition is applied at $x = 3$, and periodic boundary conditions are imposed at $y = \pm\frac{1}{2}$. The calculations are conducted with seven meshes ($n_x \times n_y$) of $200 \times 50, 400 \times 100, 800 \times 200, 1600 \times 400, 3200 \times 800$, 6400×1600, and 12800×3200 cells. For each mesh, the time step is selected to keep the convective CFL based on u_f constant and equal to 0.5. Figure 4.2(a) shows the L_2-error convergence, indicating the second-order accuracy of the proposed scheme. This conclusion is confirmed in Table 4.2 which reports the error data for the scalar, velocity components, and pressure. Figures 4.2(b), (c), (d) show that the L_2-error remains on the whole smooth over the simulation. In addition, these figures confirm that the second-order accuracy of the algorithm is maintained over the entire simulation.

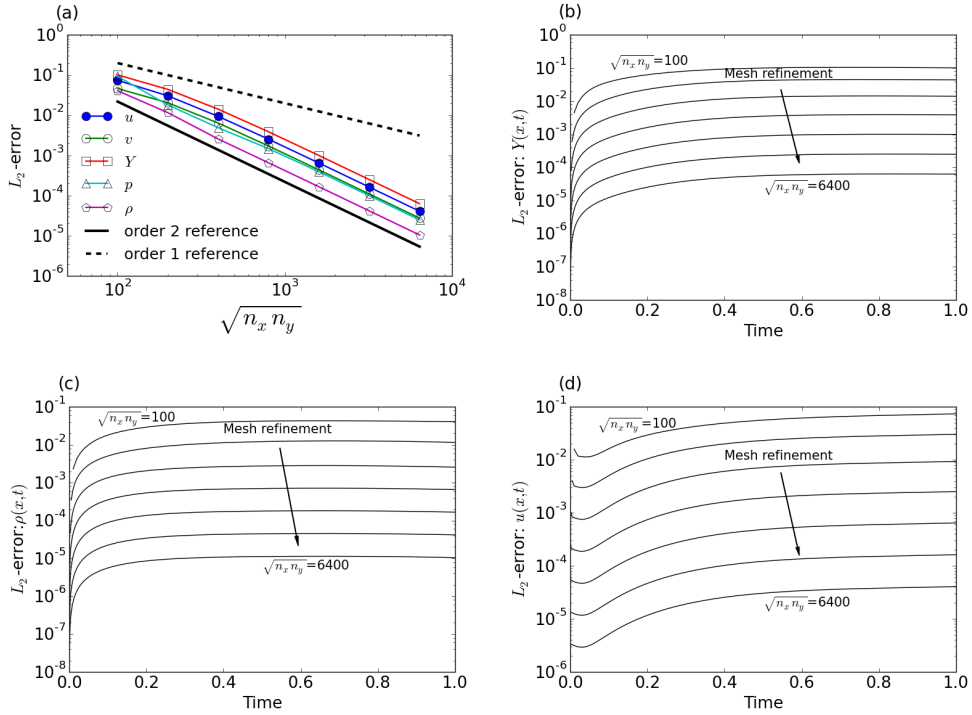

Figure 4.2: 2D-AD MMS. (a) L_2-error as a function of the spatial resolution for a constant CFL of 0.5. (b),(c) and (d) Time evolution of the L_2-error for scalar, density and velocity, respectively.

$\sqrt{n_x n_y}$	Y	u	v	p
100				
200	1.198	1.282	1.178	2.371
400	1.640	1.701	1.677	1.883
800	1.867	1.888	1.900	1.728
1600	1.963	1.967	1.973	1.915
3200	1.991	1.992	1.994	1.980
6400	1.998	1.998	1.998	2.004

Table 4.2: Observed order for the 2D-AD MMS for CFL = 0.5.

4.2.3 *Two-dimensional oscillating density field*

The final MMS problem describes an oscillating density field convecting with a constant velocity through the domain (2D-ODF):

$$\begin{aligned} Y(x,y,t) &= \frac{1+sin(k\pi\hat{x})sin(k\pi\hat{y})cos(\omega\pi t)}{1+\frac{\rho_0}{\rho_1}+\left(1-\frac{\rho_0}{\rho_1}\right)sin(k\pi\hat{x})sin(k\pi\hat{y})cos(\omega\pi t)} \\ \rho(x,y,t) &= \left(\frac{Y(x,y,t)}{\rho_1}+\frac{1-Y(x,y,t)}{\rho_0}\right)^{-1} \\ u(x,y,t) &= -\frac{(\rho_1-\rho_0)\omega}{\rho(x,y,t)4k}cos(k\pi\hat{x})sin(k\pi\hat{y})sin(\omega\pi t) \\ v(x,y,t) &= -\frac{(\rho_1-\rho_0)\omega}{\rho(x,y,t)4k}sin(k\pi\hat{x})cos(k\pi\hat{y})sin(\omega\pi t) \\ p(x,y,t) &= \frac{1}{2}\rho(x,y,t)u(x,y,t)v(x,y,t) \end{aligned} \tag{4.23}$$

where $\hat{x}=x-u_f t$ and $\hat{y}=y-v_f t$. k and ω are constant parameters given in Table 4.1. The computational domain for this problem is $0 \leq x \leq 2$, $0 \leq y \leq 2$ and $0 \leq t \leq 1$. This manufactured solution satisfies the continuity equation with $\dot{Q}_\rho = 0$. Non-zero source terms appear in the x-, y-momentum, and scalar transport equations. Similar to the problem 2D-AD, the scalar field convects through the domain with horizontal and vertical velocities u_f and v_f, respectively. The spatial and temporal periods of the variable-density structures are controlled by the wavenumber, k, and the frequency, ω, respectively. All of the boundary conditions are periodic.

The spatio-temporal convergence of the algorithm is evaluated by using meshes $(n_x \times n_y)$ of $32\times32, 64\times64, 128\times128, 256\times256, 512\times512, 1024\times1024$, and 2048×2048 cells. For each mesh, the time step is selected to keep the convective CFL based on u_f constant and equal to 0.2. Results in Fig. 4.3(a) show the second-order accuracy. The corresponding observed order are reported in Table 4.3. Figures 4.3(b), (c), and (d) show that the L_2-error remains on the whole smooth over the simulation. In addition, these figures confirm that the second-order accuracy of the algorithm is maintained over the entire simulation.

4.2.4 Rayleigh-Taylor Instability

The two-dimensional Rayleigh-Taylor instability problem is considered to check the ability of the solver to simulate variable density flows accurately. The configuration consists of two miscible fluids separated by a horizontal perturbed

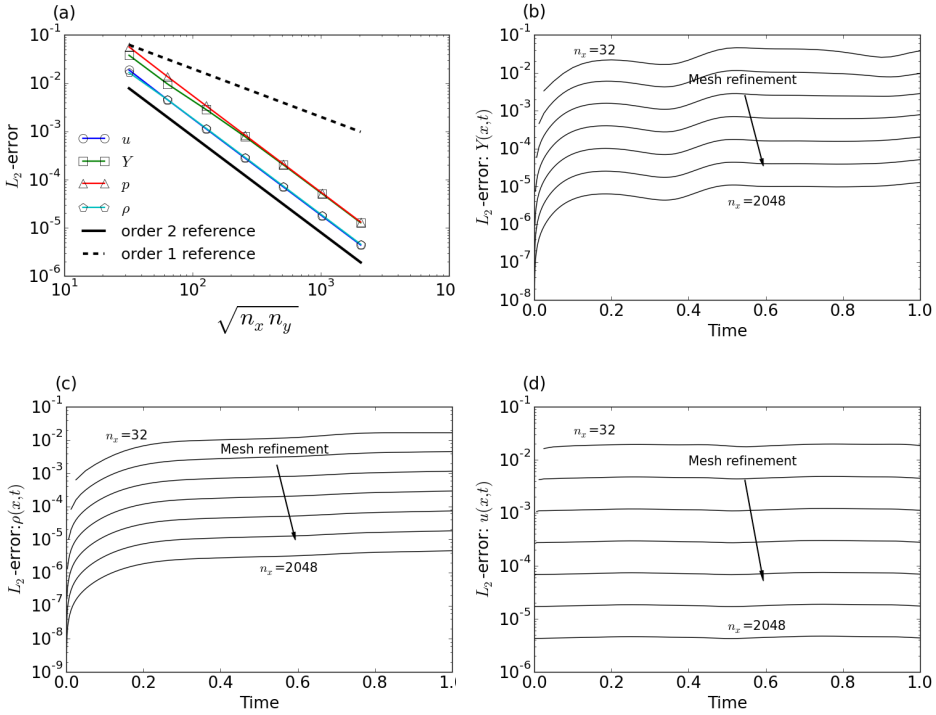

Figure 4.3: 2D-ODF MMS. (a) L_2-error as a function of the spatial resolution for a constant CFL of 0.2. (b), (c) and (d) Time evolution of the L_2-error for scalar, density and velocity, respectively.

$\sqrt{n_x n_y}$	Y	u	p
32			
64	1.986	2.058	2.054
128	1.762	2.008	2.012
256	1.854	2.002	2.002
512	1.956	2.001	2.002
1024	1.989	2.000	2.001
2048	1.998	2.000	2.001

Table 4.3: Observed order for the 2D-ODF MMS for CFL = 0.2.

interface. The heavy fluid ($\rho_0 = 1\ kg \cdot m^{-3}$) is above the light fluid ($\rho_1 = 0.1\ kg \cdot m^{-3}$). The mean interface is located at $y = 0$ in a domain size of $x \times y = [-0.5, 0.5] \times [-0.5, 0.5]\ m^2$. The exact location of the interface is given by

$$y_{\text{int}}(x) = -\alpha \sum_{k=1}^{7} \cos(\omega_k \pi x) \tag{4.24}$$

where the amplitude of the sinusoidal waves is $\alpha = 0.001$ and the wave numbers are $\omega_k = 4$, 14, 23, 28, 33, 42, 51, 59, respectively, following the test case of Desjardins et al. (2008), A mixture fraction scalar field is introduced as

$$Y(x,y) = \frac{1}{2}\left(1 + \tanh\left(\frac{y_{\text{int}}(x) - y}{2\delta}\right)\right) \tag{4.25}$$

where the interface thickness is $\delta = 0.0002$. Finally, the density is computed from the mixture fraction using the same equation of state as previously used in the MMS verification step. The two fluids have identical kinematic viscosity $\nu = 0.001\ m^2 \cdot s^{-1}$ and kinematic diffusivity $D = 5 \times 10^{-4}\ m^2 \cdot s^{-1}$. The value for the gravity acceleration is $g = 9\ m \cdot s^{-2}$ so that the Reynolds number is $Re = \sqrt{gL_y}L_x/\nu = 3000$. In this case, a Superbee TVD convection scheme (Versteeg and Malalasekera, 2007) is used for the scalar transport equation in order to ensure the positivity and to prevent undershoot and overshoot of the density. Simulations have been performed on four different meshes composed of $N_x \times N_y = 128 \times 128$, 256×256, 512×512 and 1024×1024 cells, respectively. The corresponding time steps are $\Delta t = 1 \times 10^{-3}$, 5×10^{-4}, 2.5×10^{-4} and $1.25 \times 10^{-4}\ s$, respectively. A no-slip boundary condition is applied at the top while a wall condition is considered at the bottom. Periodic conditions are imposed at the left and right sides.

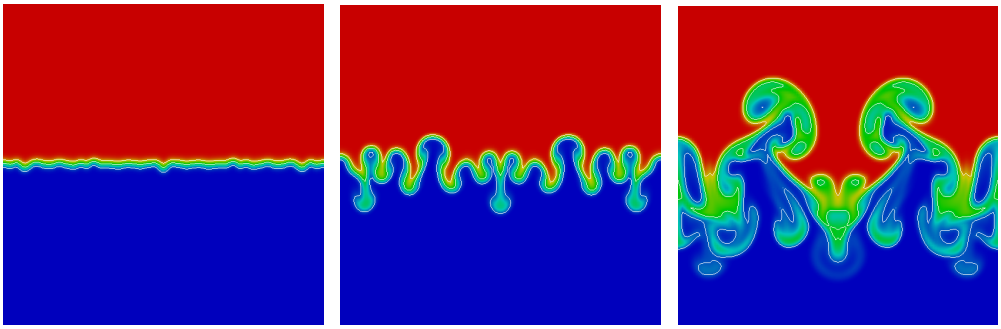

Figure 4.4: Contour plot of ρ at $t = 0.1\ s$ (left), $t = 0.4\ s$ (middle) and $t = 0.75\ s$ (right) computed on mesh 128×128. The lines correspond to $\rho = 0.2$, 0.5 and 0.8 levels. Red colour corresponds to the heavy fluid ($\rho = 1\ kg \cdot m^{-3}$) and blue colour to the light one ($\rho = 0.1\ kg \cdot m^{-3}$).

Figure 4.4 shows the density fields at $t = 0.1\ s$, $t = 0.4\ s$, and $t = 0.75\ s$, simulated on the mesh 128×128. They compare well with the density fields in Fig. 4.5 reported by Mullyadzhanov et al. (2016). In addition, density fields at $t = 0.75\ s$ for the three finer meshes are also displayed in Fig. 4.6. The density

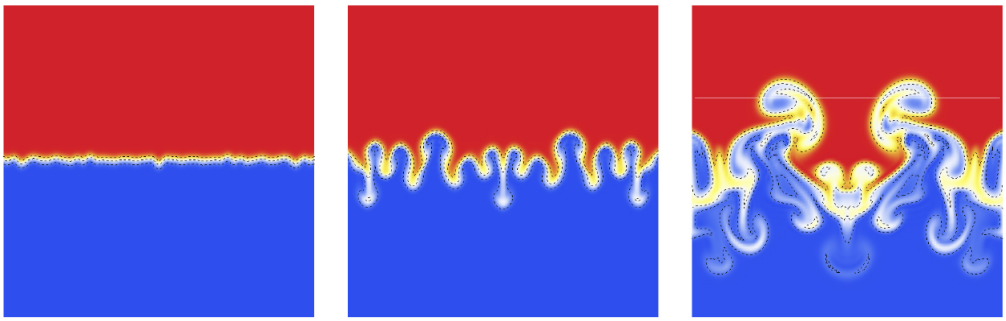

Figure 4.5: Contour plot of ρ at $t = 0.1\ s$ (left), $t = 0.4\ s$ (middle) and $t = 0.75\ s$ (right) computed on a 128×128 mesh in Mullyadzhanov et al. (2016). The lines correspond to $\rho = 0.2$, 0.5 and 0.8 levels. Red colour corresponds to the heavy fluid ($\rho = 1\ kg \cdot m^{-3}$) and blue colour to the light one ($\rho = 0.1\ kg \cdot m^{-3}$). These plots are taken from (Mullyadzhanov et al., 2016).

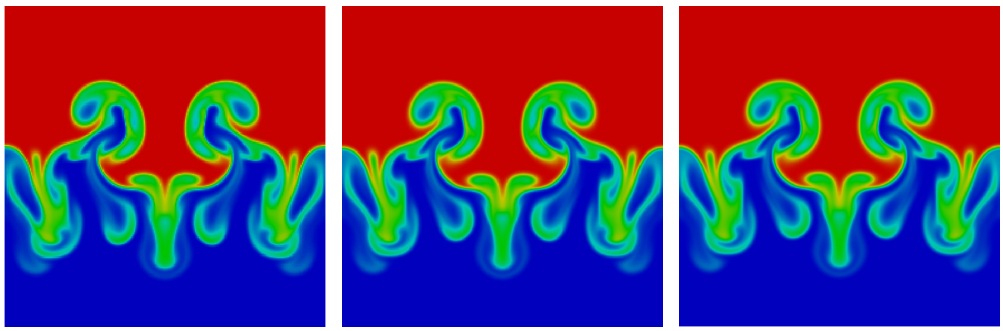

Figure 4.6: Density fields at $t = 0.75\ s$ computed on mesh 256×256 (left), 512×512 (middle), 1024×1024 (right).

profiles at $y = 0.2\ m$ and $t = 0.75\ s$ computed on four meshes are presented in Fig. 4.7. It is observed that the density solution is converged for meshes finer than 256×256. To further investigate the results, Fig. 4.8 compares the density profiles on meshs 128×128 and 512×512 with Desjardins et al. (2008) and Mullyadzhanov et al. (2016). A good agreement is observed between the current simulation and those of Mullyadzhanov et al. (2016) whereas noticeable differences are seen with those of Desjardins et al. (2008). These differences may be due to an inconsistency in the boundary conditions as discussed in Mullyadzhanov et al. (2016). The current work uses the same boundary conditions as Mullyadzhanov et al. (2016) whereas the boundary conditions used by Desjardins et al. (2008) were not reported. Another possible reason is that the Superbee TVD convection scheme is applied to scalar transport equation, while neither of the two authors adopt it in their tests.

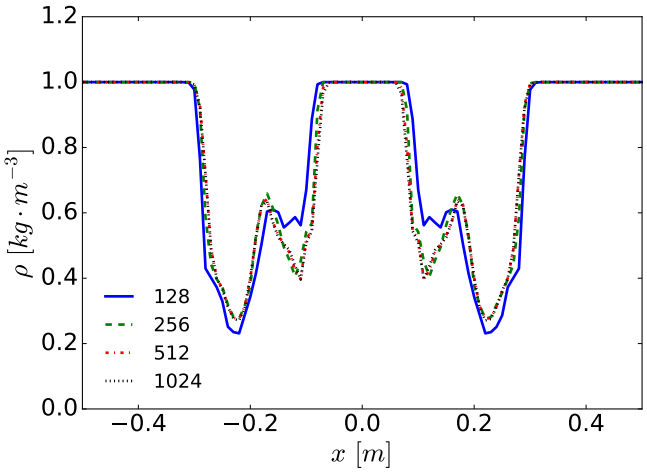

Figure 4.7: Density profiles at $y = 0.2\ m$ and $t = 0.75\ s$ computed on four meshes.

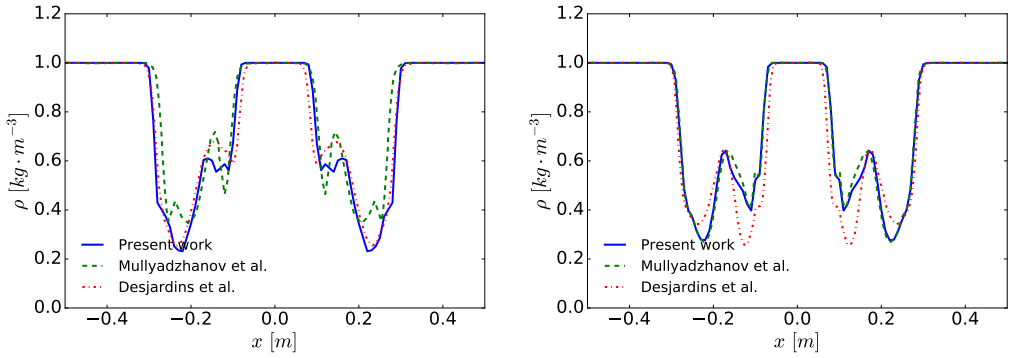

Figure 4.8: Comparison with results in literatures for mesh 128×128 (left), and for mesh 512×512 (right).

4.3 Conclusions

The proposed numerical solver for low-Mach variable-density NS equations is verified by three MMS cases and numerical results confirmed the second-order spatio-temporal accuracy. Through the Rayleigh-Taylor instability case, the solver is capable of accurately capturing the complex variable-density instability features and yield results in good agreement with those of the literature. In the next chapter, this solver will be validated by simulating a 1 m diameter turbulent helium plume with LES.

Chapter 5

Helium plume

Turbulent buoyant fire plumes are a canonical configuration in fire safety science. The far-field region of these flows is rather-well understood and self-similarity correlations were reported for temperature and velocity profiles (see for example Ref. (Shabbir and George, 1994)). The near field flow is more complex, exhibiting a rapid transition from laminar to fully turbulent regime in the few first inlet diameters and a puffing motion characterized by a repetitive shedding of coherent vortices (Cetegan and Ahmed, 1993). Rayleigh-Taylor (RT) and Kelvin-Helmotz (KH) instabilities have been proposed to explain the nature of puffing. Some authors suggested that the KH instability is the dominant mechanism (Ghoniem et al., 1993) whereas other works (Cetegen and Kasper, 1996; Desjardin et al., 2004; Tieszen et al., 2004) suggested that the RT instability prevails. These vortical structures control the air entrainment and the resulting turbulent mixing and combustion processes which in turn affect the density and scalar fields.

Before applying the low-Mach variable density NS equations solver to turbulent buoyant fire plumes studies, this chapter presents a LES of turbulent helium plumes for the purposes of validating the numerical solver. Similarly to density ratio between hot gases and cold air in fire plumes, the density ratio of helium and air is a factor of seven. Medium- to large-scale helium plumes ($0.1\ m < d < 1\ m$) are also characterized by a rapid transition from a laminar to a turbulent flow and puffing motions. The principal difference arises from the fact that heat is released locally from the combustion process in fire plumes whereas, in helium plumes, the buoyancy is produced only near the source

where large density gradients are present. Large helium plumes are thus good candidate to mimic buoyant fire plumes while avoiding the complexities related to combustion and heat transfer processes (O'Hern et al., 2005). O'Hern et al. (2005) made significant experimental efforts to provide comprehensive turbulent velocity and helium concentration statistics in the 1 m diameter helium plume. These data were intensively used as a validation step for LES-based CFD models (Desjardin et al., 2004; Blanquart and Pitsch, 2008; Brown et al., 2018; Chung and Devaud, 2008; Maragkos et al., 2013).

5.1 Experimental setup

O'Hern et al. (2005) investigated experimentally the characteristics of near field turbulent buoyant helium plumes. The main objectives of these experiments were to provide data to validate CFD models suitable for fire modelling. The dimensions of the main chamber are $6.1 \times 6.1 \times 7.3\ m^3$. The chamber converges to a square chimney outlet at the top with dimensions of 2.4 m on each side. The plume source, with a diameter of 1 m, is located in the centre of the chamber 2.45 m above the floor. A gas mixture is composed of 96.4% helium, 1.7% acetone, and 1.9% oxygen by volume, with a molecular weight of 5.45 $g \cdot mol^{-1}$. This mixture is released into ambient air at a Reynolds-averaged velocity of 0.325 $m \cdot s^{-1}$ corresponding to a Favre-averaged velocity of 0.339 $m \cdot s^{-1}$, approximately. Measurements were obtained using particle image velocimetry (PIV) for velocity field measurements and planar laser induced fluorescence (PLIF) for helium mass fraction. The experimental data include the puffing frequency, radial profiles of mean and rms of axial and radial velocities and mean and rms of helium mass fraction. The experimental uncertainty on the measured velocities, concentrations, turbulent statistics and concentration fluctuations is estimated to be around $\pm$20, $\pm$18, $\pm$30 and $\pm$21%, respectively.

5.2 Literature survey

The experiments of O'Hern et al. (2005) were used to validate LES and RANS models. Table 5.1 summarizes the grids, the SGS stress models, and the SGS scalar sub-models considered in these studies. This literature survey is limited

Ref.	Domain	Grid resolution	SGS Stress	SGS SF	Code
Desjardin et al. (2004)	Cubic: $4 \times 4 \times 4\ m^3$	2 non-uniform meshes: $\Delta = 2.8, 1.6\ cm$	DSM	DEDM	In-house Code
Tieszen et al. (2004)	-	3 non-uniform meshes: $(n_r, n_\theta, n_z) =$ $54 \times 64 \times 80$ $104 \times 64 \times 160$ $208 \times 64 \times 320$	DSM	DEDM	NGA
Chung and Devaud (2008)	Cubic: $4 \times 4 \times 4\ m^3$	4 non-uniform meshes: $\Delta = 10, 5, 2.5, 1.25\ cm$	SM Adjusted C_s	EDM	FDS
Blanquart and Pitsch (2008)	Cylindrical: (r, z)=$6m \times 7m$	$(n_r, n_\theta, n_z) =$ $187 \times 64 \times 192$	DSM	DEDM	NGA
Maragkos et al. (2013)	Cylindrical: (r, z)=$4m \times 4m$	2 non-uniform meshes: $\Delta = 2.54, 1.23\ cm$	SM Adjusted C_s	EDM	FireFoam
NIST (Brown et al., 2018)	$3 \times 3 \times 3\ m^3$	$\Delta = 1.5\ cm$	Deardorff	EDM	FDS
IRSN (Brown et al., 2018)	-	$\Delta = 2.5\ cm$	SM Adjusted C_s	EDM	ISIS

Table 5.1: Computation details for the previous LES of the O'Hern helium plume O'Hern et al. (2005).

to modelling approaches based on a LES description of turbulence.

These modelling studies used either standard or dynamic Samgorinsky (SM or DSM) and standard or dynamic linear eddy diffusivity (EDM or DEDM) models to close the SGS stress tensor and scalar flux, respectively. Desjardin et al. (2004) elucidated the mechanisms responsible for puffing. They showed that vortices are generated at the base of the plume near the outer edge where vorticity generation from buoyancy is the greatest. These vortices are then quickly destabilized leading to the formation of "finger-like" instabilities that contribute to the breakdown of the large-scale vortices and enhance the local mixing. More generally, all the reported LES were found to be able to capture the large-scale dynamics. However, the mixing rate was systematically under-estimated, leading to overpredictions of mean and fluctuation of the helium concentration near the plume centreline. These discrepancies were attributed to a lack of resolution of the buoyancy-induced turbulence mixing.

The present simulations considered the DSM as SGS stress model. The EDM model assumes a linear alignment with the large-scale scalar gradient which is inconsistent with the physics of turbulent convection and cannot correctly reflect the local geometric property of the SGS scalar flux vector at each time step (Peng and Davidson, 2002; Higgins et al., 2004; Wang et al., 2007b; Wang

et al., 2007a). To correct this behaviour, two other approaches are also considered in the present work. The first is based on tensorial forms of the diffusivity for the SGS scalar flux modelling (Wang et al., 2008b), leading to the dynamic generalized gradient model (DGGM) and the dynamic full linear generalized gradient model (DLGGM). The second consists in adding a gradient model (based on Taylor expansion of the filtering operation) to either the DEDM or the DGGM. These two models will be denoted as M1 and M2, hereafter. All these SGS models are described in details in the Chapter 3.

5.3 Computational details

The Favre-filtered governing Eqs. (3.1) to (3.4) are solved by the proposed solver described in the Chapter 4. The second-order Crank-Nicolson scheme is used for time advancement. The Total Variation Diminuishing (TVD) scheme, Superbee (Versteeg and Malalasekera, 2007), is applied for convection in the mixture fraction transport to limit numerical oscillation whereas a second-order central difference scheme (CDS) is used for diffusion. For the momentum equation both convective and diffusive terms are discretized by using a second-order CDS.

Simulations were performed on a simplified cubic domain with dimensions (x, y, z) of $4 \times 4 \times 4\ m^3$. Helium was released through a $1\ m$ diameter orifice with an inlet Favre-averaged velocity fixed at $0.339\ m \cdot s^{-1}$. The molecular weight of helium was set to $5.45\ g \cdot mol^{-1}$ to be consistent with the experiments. A low coflow was injected with a velocity of $0.01\ m \cdot s^{-1}$. These conditions for the helium and coflow velocities correspond to the test 4 in Ref. (O'Hern et al., 2005) that was dedicated to get the Favre-averaged statistics. In order to examine the effect of the grid resolution on the LES results, two grid systems with $135 \times 135 \times 114$ and $192 \times 192 \times 132$ control volumes were used. A uniform grid refinement was used in the region where turbulent mixing is expected resulting in grid-spacing of 1.6 cm and 1 cm, respectively. For convenience we will subsequently refer to them as coarse and fine grid, respectively. A constant time step of $5 \times 10^{-4}\ s$ was considered to provide an averaged CFL equal to 0.5. Simulations were run for 30 s and the density-weighted time-averaged mean and rms values were collected from 15 to 30 s. The first 15 s of simulation were used to establish a statistically stationary flow.

5.4 Results and discussions

5.4.1 Puffing frequencies

Figure 5.1 compares the experimental centreline axial velocity at $z/d = 0.5$, where d is the source diameter, with that computed with the DGGM on the finer grid. Model predictions in terms of amplitude are in satisfactory agreement with the experimental data. In addition, a clear puffing frequency is evidenced for both the model and experiments. The model predicts a total of 8 cycles over the 6 s sequence whereas only 7 cycles are observed experimentally. A Fast Fourier Transform of the numerical signal confirms that the model overestimates the puffing frequency, predicting 1.50 Hz as compared to 1.37 ± 0.1 Hz for the experiments. However, a better agreement is obtained with the frequency of 1.45 Hz measured in test 4 (see Ref. (O'Hern et al., 2005)). The predicted value of 1.5 Hz was found to be insensitive to both SGS

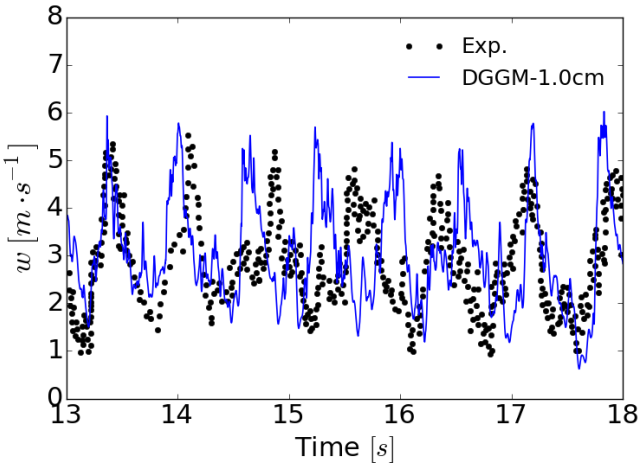

Figure 5.1: Time series of the centreline axial velocity at $z/d = 0.5$.

scalar flux model and grid resolution. This is consistent with the behaviour reported by Desjardin et al. (2004) and Maragkos et al. (2013) who showed that, for mesh refinement comparable to that considered in this study, the puffing frequency is not affected by the SGS model.

5.4.2 Mean and rms velocities

Model predictions for radial profiles of axial and radial mean velocities and rms values of radial velocities at different heights are displayed in Figs. 5.2 to 5.4,

respectively. For these quantities, only the simulations with the DEDM model and the coarse grid (1.6 cm) are shown since their predictions were found to be insensitive to the different SGS scalar flux closures and grid refinements. Tieszen et al. (2004) reported the same observation for the mean radial velocity. Figures 5.2 to 5.4 show that model predictions are in good agreement with the experimental data, being on the whole within the experimental uncertainty. The largest discrepancies are observed for the mean radial at $x = -0.2\ m$ (Fig. 5.3). Nevertheless, it should be pointed out that the experimental profiles are not perfectly symmetric and a much better agreement is observed at $x = 0.2$ m. Radial velocity controls air entrainment in pool fires and the resulting combustion process and, as such, should be accurately predicted.

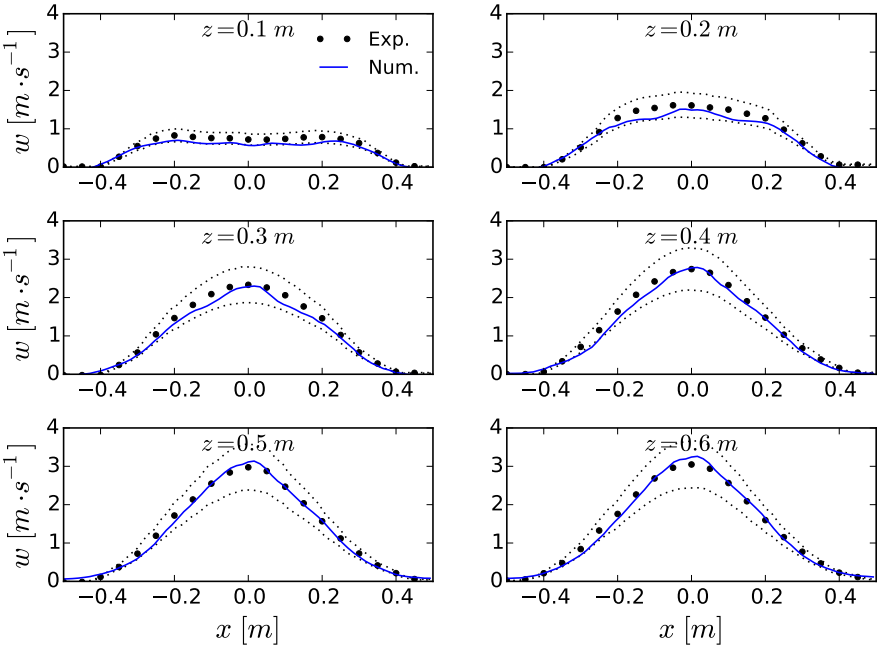

Figure 5.2: Radial profile of density-weighted time-averaged axial velocity at different heights. The numerical simulation were performed with the DEDM on the coarser grid. The experimental data (O'Hern et al., 2005) are represented by the largest black circles with the experimental uncertainties delimited by the dotted lines.

Figure 5.5 shows the radial profiles of rms values of axial velocity at different heights. The predictions reported in this figure were obtained using the coarser mesh (grid spacing of 1.6 cm). Simulations obtained with the DEDM are in good agreement with the experiments from the edges of the plume to $x = \pm 0.1$

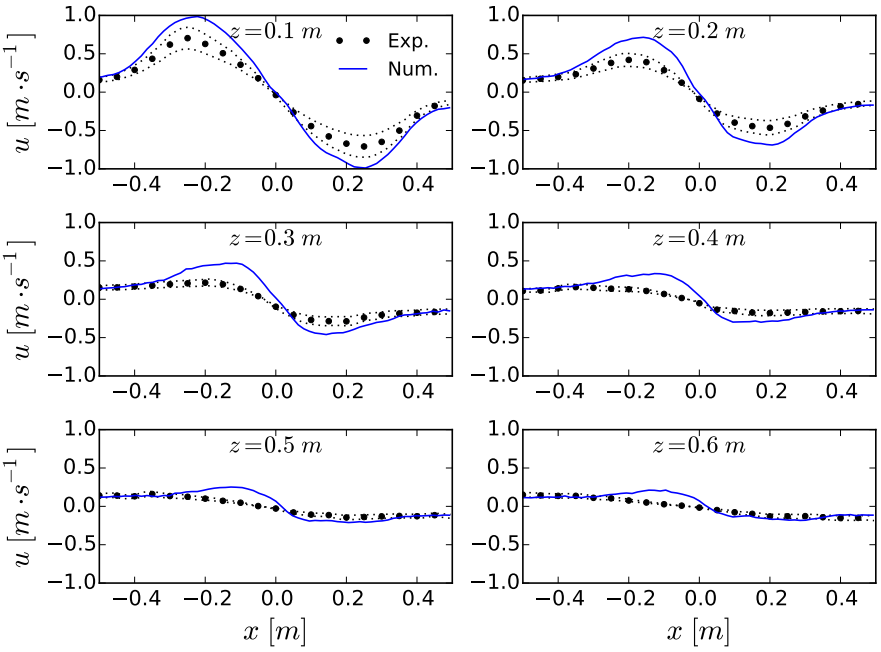

Figure 5.3: Radial profile of density-weighted time-averaged radial velocity at different heights. Num. and Exp. are the same as Figure 5.2.

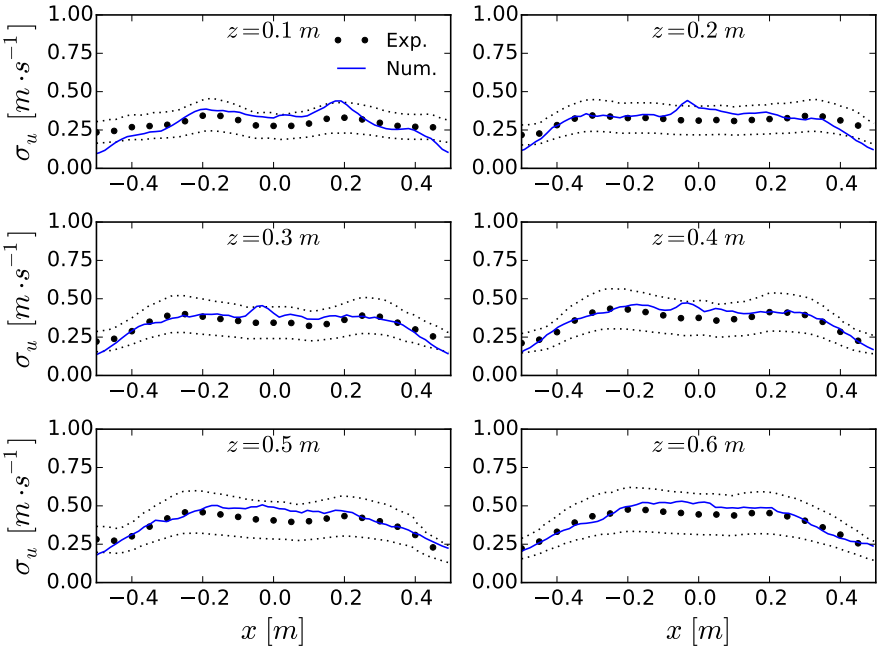

Figure 5.4: Radial profile of density-weighted time-averaged rms values of radial velocity at different heights. Num. and Exp. are the same as Figure 5.2.

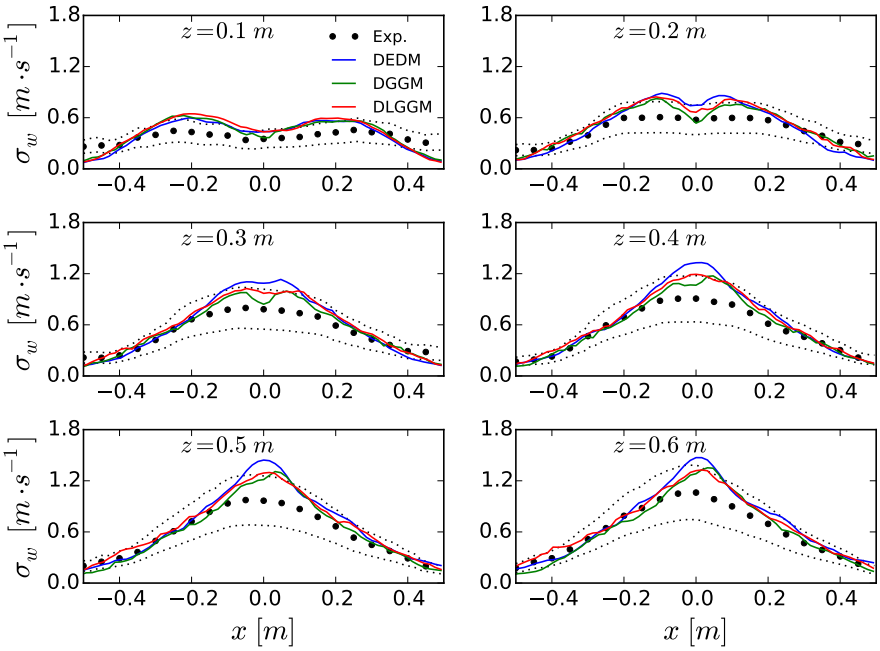

Figure 5.5: Radial profile of density-weighted time-averaged rms values of axial velocity at different heights on the coarser grid.

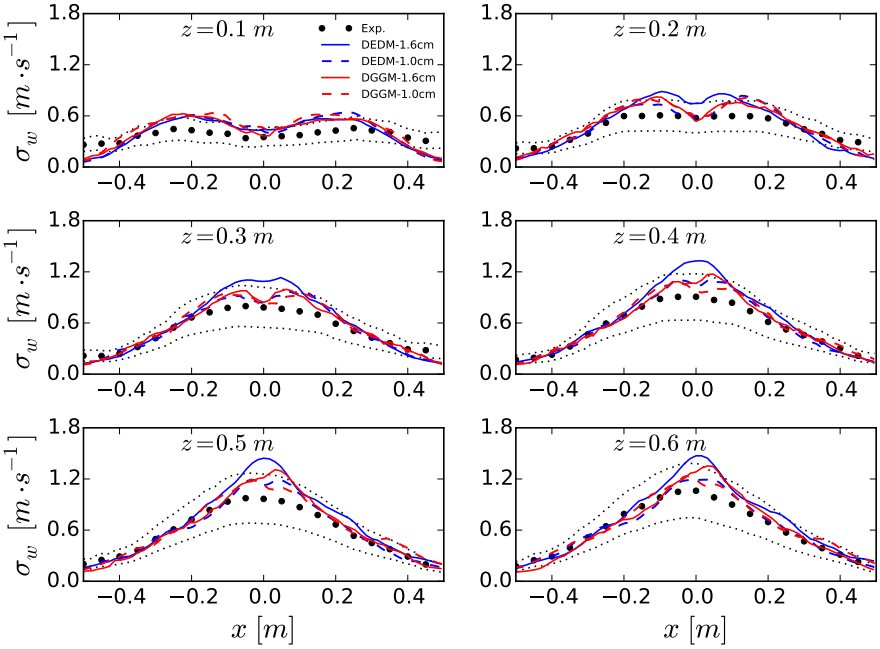

Figure 5.6: Radial profile of density-weighted time-averaged rms values of the axial velocity at different heights.

m. However, this model overestimates the experiments near the centre of the plume. Similar discrepancies were reported by Desjardin et al. (2004) with similar SGS scalar flux model and grid resolution. These authors attributed these discrepancies to a lack of resolution of the buoyancy-induced turbulence from the small-scale of motion. Figure 5.5 shows also that the performance of the DGGM and DLGGM is similar, leading to a better agreement with the experimental data than the DEDM. Both the DGGM and DLGGM reduce by 12% approximately the computed peaks at $z = 0.4\ m$ and $z = 0.6\ m$ as compared to the DEDM. We compare in Fig. 5.6 the predictions of axial velocity fluctuations based on two different grid resolutions for the DEDM and DGGM. Refining the mesh improves clearly the DEDM predictions in the region between $x = -0.1\ m$ and $0.1\ m$ for $z \geq 0.2\ m$. Interestingly, the DEDM predictions obtained with the finer mesh become comparable to the DGGM solutions on the coarser grid. Figure 5.6 shows also that the axial velocity fluctuations computed with the DGGM are relatively insensitive to mesh refinement.

5.4.3 Mean and rms helium mass fraction

Figure 5.7 shows the radial profiles of mean and rms values of helium mass fraction predicted by the DEDM, DGGM, and DLGGM models on the coarser grid, respectively. Mean helium mass fraction near the base of the plume ($z \leq 0.2\ m$), where the flow transits from a laminar to a turbulent state, is well predicted by the DEDM (see Fig. 5.7). For $z > 0.2\ m$, as observed for the axial velocity fluctuations, the DEDM reproduces well the experimental mean helium mass fraction from the edge of the plume to about $x = \pm 0.1$ m whereas it under-predicts the mixing rate close to the centreline (see Fig. 5.7). These discrepancies increase with the height (see Fig. 5.7). Figure 5.8 shows that the DEDM over-predicts significantly the helium mass fraction fluctuations whatever the height. The discrepancies reported in Figs. 5.7 and 5.8 for the DEDM simulations were also observed in previous studies (Desjardin et al., 2004; Maragkos et al., 2013; Chung and Devaud, 2008). As discussed previously, these discrepancies were attributed to deficiencies in the modelling of unresolved mixing due to buoyancy. Figures 5.7 and 5.8 show that the DGGM and DLGGM models provide similar solutions, with the DLGGM being slightly more accurate. Up to $z = 0.4\ m$, helium mass fractions computed

with these models are on the whole within the experimental uncertainty and represent better the experimental data than the DEDM (see Fig. 5.7).

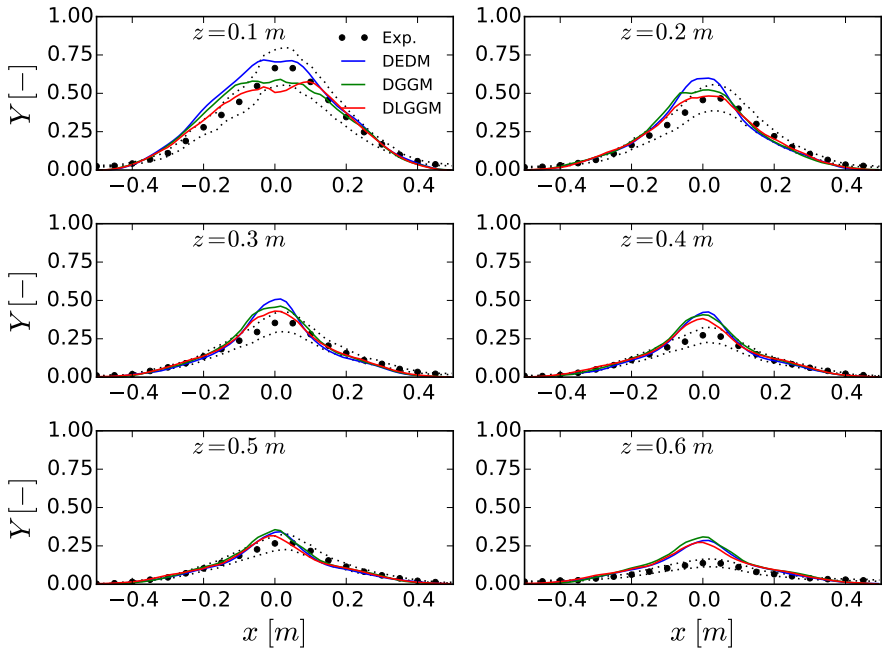

Figure 5.7: Radial profile of density-weighted time-averaged helium mass fraction at different heights on the coarser grid.

However, this improvement weakens as the height increases to become imperceptible for $z = 0.5\ m$ and $z = 0.6\ m$ (see Fig. 5.7). The DGGM and DLGGM improve also the predictions of helium mass fraction fluctuations at the vicinity of the centreline. As for the mean helium mass fraction, the improvement is reduced as the height decreases.

The effect of combining the DEDM and DGGM with the gradient model is illustrated in Figs. 5.9 and 5.10. M1 improves the DEDM and is comparable to the DGGM. On the other hand, M2 has no noticeable effects as compared to the DGGM. It should be pointed out that the same trends were observed for the axial velocity fluctuations (not shown).

As discussed above, the DGGM and DLGGM give similar results. As a consequence, Figs. 5.11 and 5.12 illustrate the effects of mesh refinement on the predictions of mean and rms helium mass fraction only for the DEDM and DGGM. It appears clearly that grid refinement improves significantly both the DEDM and DGGM predictions at each height. As for the axial velocity fluctu-

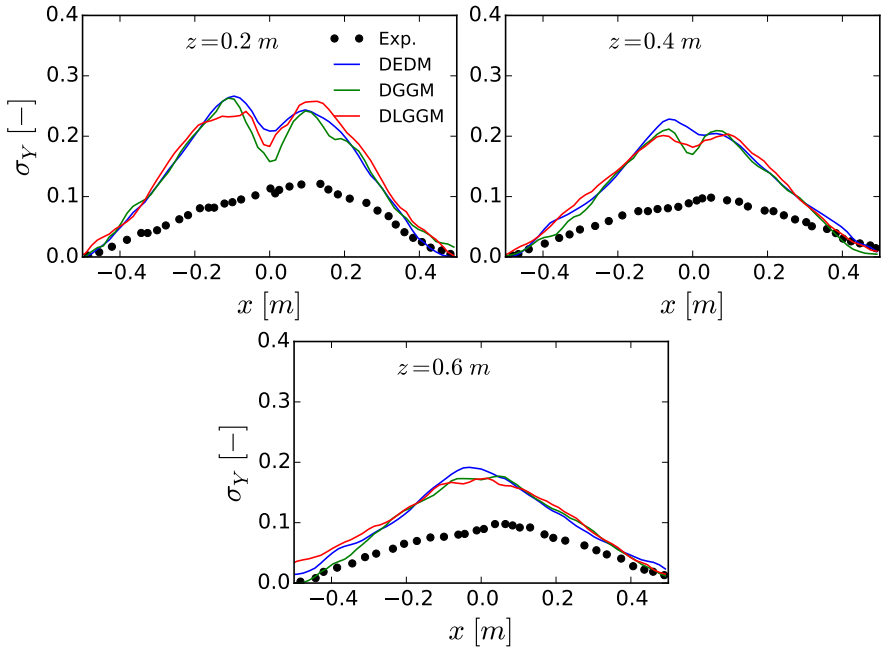

Figure 5.8: Radial profile of mass-weighted time-averaged rms values of helium mass fraction at different heights.

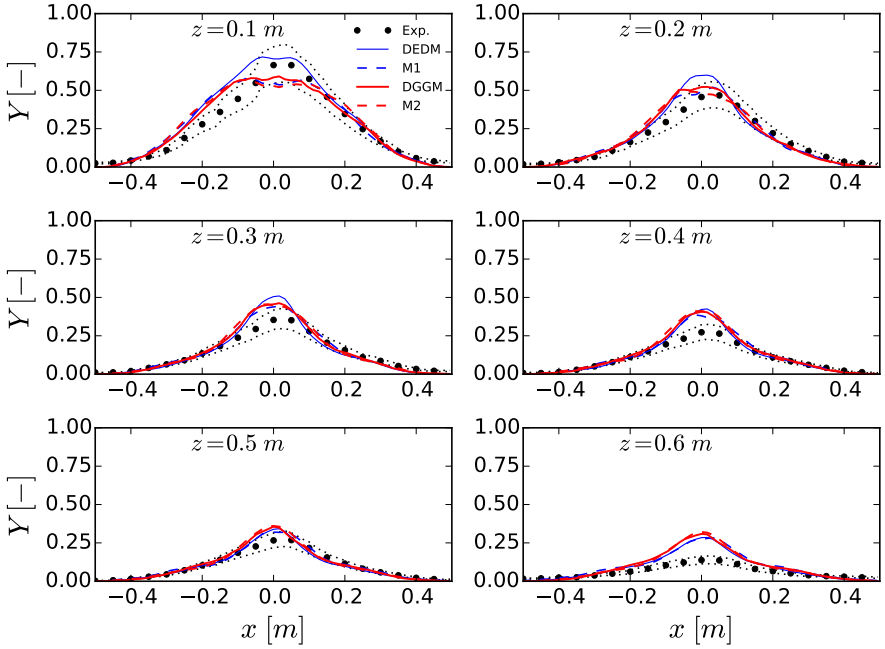

Figure 5.9: Radial profile of density-weighted time-averaged helium mass fraction at different heights on the coarser grid.

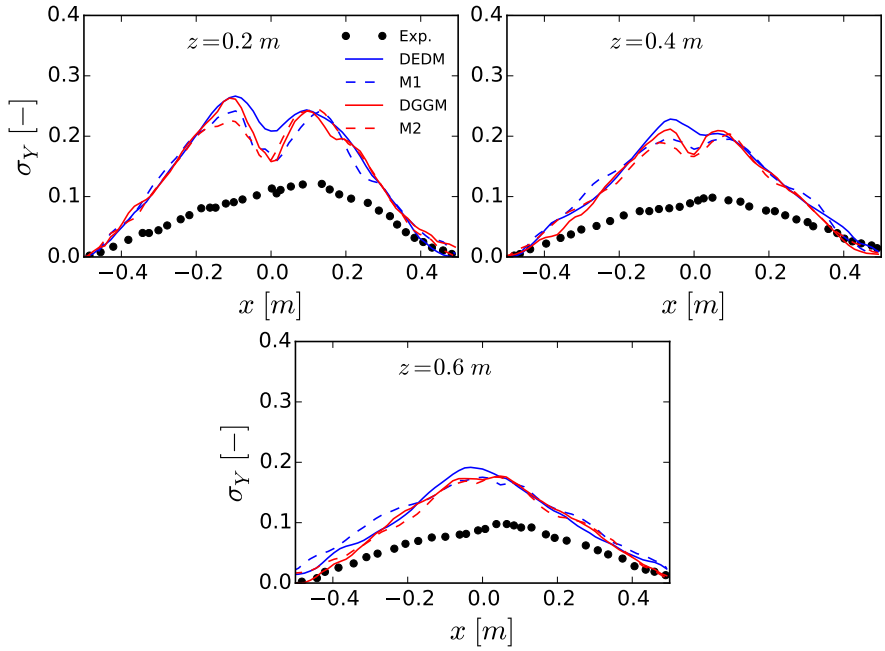

Figure 5.10: Radial profile of density-weighted time-averaged rms values of helium mass fraction at different heights.

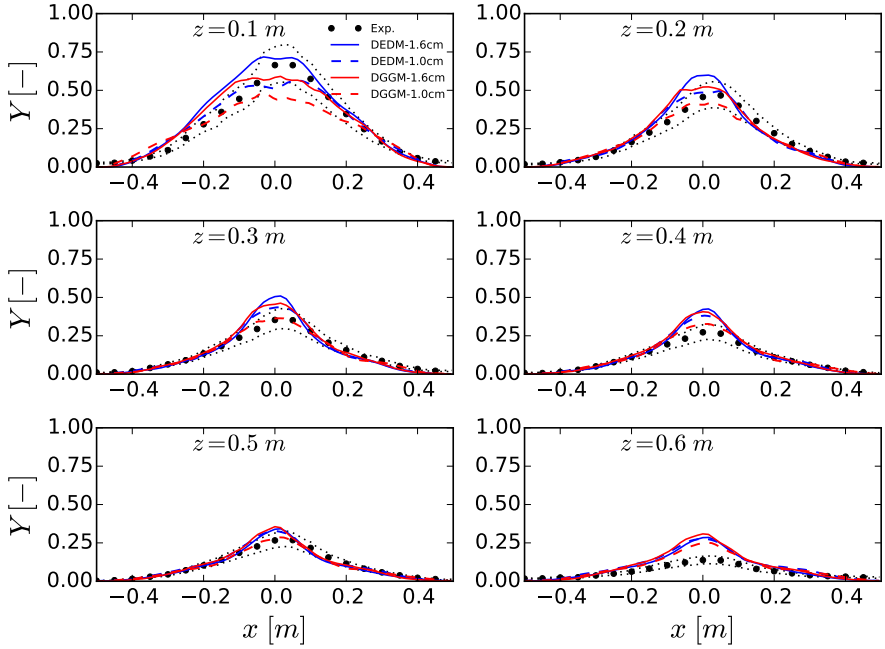

Figure 5.11: Radial profile of density-weighted time-averaged helium mass fraction at different heights on the coarser grid.

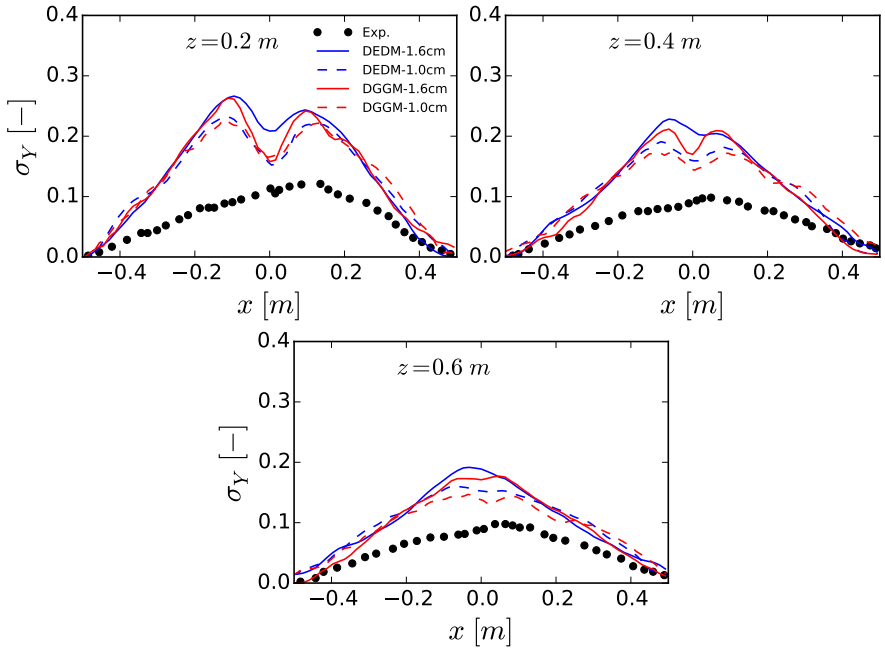

Figure 5.12: Radial profile of time-averaged rms values of helium mass fraction at different heights.

ations, DEDM predictions of the mean helium mass fraction obtained with the finer grid become comparable to the DGGM solution on the coarser grid (see Fig. 5.11). These results show that grid refinement effects are more pronounced than SGS scalar flux closures. This suggests that small-scale buoyancy effects are not fully resolved by the present LES.

5.5 Comparison with solutions of other fire simulators

Figure 5.13 illustrates the comparison of the present LES obtained with the DGGM on the finer grid and other LES reported at the IAFSS Working Group on Measurement and Computation of Fire Phenomena workshop (Brown et al., 2018) and obtained with widely-used CFD models devoted to fire simulations. This comparison is made at $z = 0.4\ m$. Table 5.1 provides the computational details for these simulations. NIST used an official version of FDS (version 6.5.3) (Brown et al., 2018) with a grid resolution of 1.5 cm. The Deardoff SGS model was considered with the constant set to the literature value of 0.1 and a turbulent Schmidt number equal to 0.5. Brown et al. (2018) used the

CFD package FireFOAM version 6 with a grid-resolution of 1.23 cm and the standard Smagorinsky SGS model. The model constant is adjusted to 0.1 and the turbulent Schmidt number is set equal to 0.5.

The objective of Fig. 5.13 is not to make a direct comparison since different physical sub-models are considered but to demonstrate that the *Code_Saturne* provides state-of-the-art predictions for this problem.

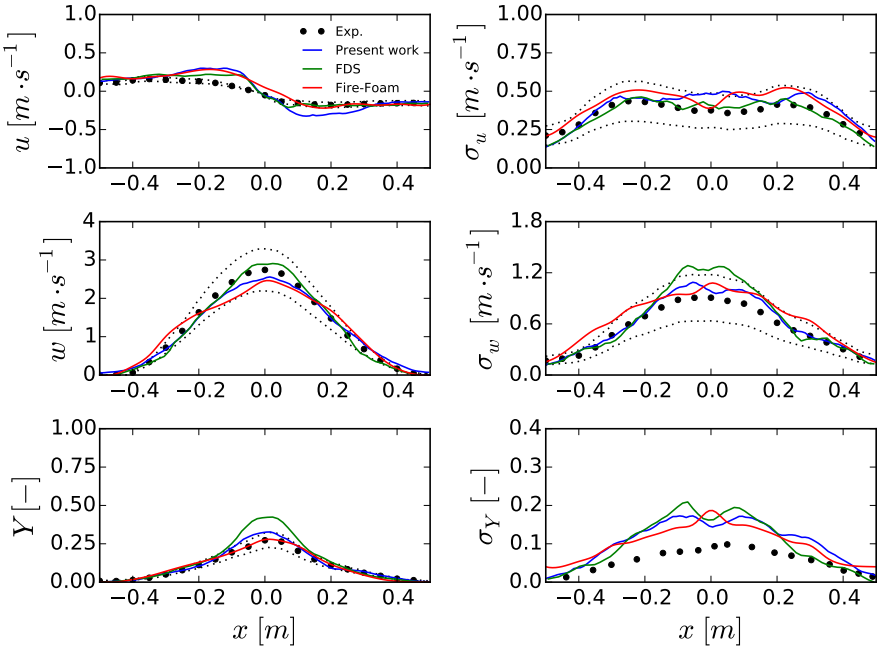

Figure 5.13: Radial profile at $z = 0.4\ m$: (a) radial velocity, (b) rms values of radial velocity, (c) axial velocity, (d) rms values of axial velocity, (e) helium mass fraction and (f) rms values of helium mass fraction. FDS and Fire-Foam results are taken from (Brown et al., 2018).

5.6 Conclusions

From these simulations the following conclusions can be drawn:

1. Predictions with DSM and DEDM capture the plume dynamics but underestimate the mixing rate at vicinity of the plume centreline.

2. Puffing frequency, mean axial velocity and mean and fluctuations of radial velocity are insensitive to grid refinements and SGS scalar flux models. This result is of significant importance for fire modelling since radial ve-

locity controls the air entrainment. In opposite way, fluctuations of axial velocity and mean and fluctuations of helium concentration are affected by both mesh refinement and SGS scalar flux models.

3. The DGGM and DLGGM provide similar results and improve mixing rate predictions as compared to the DEDM, especially for $z \leq 0.4\ m$. Adding gradient model with the DEDM improves the DEDM whereas combining it to the DGGM has no noticeable effects on the predictions of the DGGM.

4. Grid refinement improves more significantly helium mass fraction and its fluctuation than SGS scalar closures. Based on this observations, the DEDM model will be used in all the simulations reported hereafter.

Chapter 6

Fire plume dynamics

The first part of this chapter will be dedicated to the combustion model and, more particularly, to the modelling of subgrid mixture fraction variance and filtered scalar dissipation rate closures. This study will be made by considering the McCaffrey fire plumes (McCaffrey, 1979). The second part will be devoted to the modelling of the well-documented methanol pool fire investigated experimentally by Weckman and Strong (1996) for an exhaustive validation of the LES-based model. In addition, the effects of burner boundary conditions on the flame structure will be investigated.

These two purely buoyant diffusion flames belong to the list of target flames identified by the workshop MacFP (Brown et al., 2018; *The 1st Measurement and Computation of Fire Phenomena (MaCFP) Workshop* 2017) recently initiated by members of the fire community. The goals of this workshop are to develop and validate predictive models of fire plume, to identify well-defined target flames that are suitable for modelling, and to archive detailed data sets for these target flames.

6.1 Subgrid variance modelling

As discussed in the introduction, estimation of subgrid quantities is a crucial procedure for LES. Among other subgrid quantities, the subgrid variance of the mixture fraction is particularly important for LES of non-premixed combustion because of the role it plays in the prediction of mixing at the molecular level. This section focuses on investigating existing SGS mixing models for mix-

ture fraction variance prediction in the framework of the SLF/presumed FDF model. Three different models are studied: the first is based on the equilibrium between the production and dissipation of the variance at these subgrid scales with a dynamic estimation of the model constant whereas the two others are non-equilibrium models, namely the variance transport equation (VTE) and the second moment transport equation (STE). Both non-equilibrium models incorporate the same model for the scalar dissipation rate. The reader can refer to the section 3.3 for a detailed description.

Following Kemenov et al. (2012) the comparison of LES solutions will be based on the convergence properties of their statistics with respect to the filter size, Δ. As discussed by Pope and co-workers (Pope, 2000; Kemenov et al., 2012), characterizing the dependence of predicted statistics on Δ must be part of the overall LES methodology and gains importance in combustion problems since the rate-controlling processes such as reactant mixing and chemical reactions are modelled at the subgrid-scale level. Such convergence studies are rare in the LES modelling of fire plumes and were limited to mean temperature and/or axial velocity (Sikic et al., 2019; Koo et al., 2017). The present study reports a more exhaustive convergence study on grids of different resolution involving mean and rms of mixture fraction, temperature and velocity.

6.1.1 Numerical resolution

Throughout this chapter, the Favre-filtered governing Eqs. 3.1 to 3.4 are solved by the proposed solver described in the Chapter 4. The second-order Crank-Nicolson scheme is used for time advancement. The Superbee-TVD scheme (Versteeg and Malalasekera, 2007) is applied for convection in the mixture fraction transport to limit numerical oscillation whereas a second-order CDS is used for diffusion. For the momentum equation both convective and diffusive terms are discretized by using a second-order CDS. The subgrid contribution to the momentum stress and scalar flux is computed using DSM and DEDM model, respectively. The non-adiabatic SLF model is used to obtain the local thermochemical state relationship, ϕ^{slf}, as a function of the mixture fraction, Z, the scalar dissipation rate, χ, and the enthalpy defect, $X_R = h - h_{ad}$. The flamelet library was generated by solving the governing equations of counter-flow diffusion flames in the physical space at a series of specified strain rates using the CHEMKIN code (Lutz et al., 1996). Starting with a low strain rate,

flamelet was calculated by gradually increasing the strain rate until the local quenching occurs. Radiative loss was incorporated in the flamelet library by using the methodology described in the Chapter 2. The Favre-filtered thermochemical quantities are then obtained from the state relationships by convolution with the presumed FDF. The RCFSK model is retained for radiative property modelling, its detailed description is found in the Chapter 2.

6.1.2 Computational domain and boundary conditions

Five methane fire plumes in open conditions, investigated experimentally by McCaffrey (1979), were simulated. These flames were generated from a burner of 0.3 m in diameter with heat release rates (HRR, $\dot{Q}$) of 14.4, 21.7, 33, 45 and 57.5 kW, respectively. Simulations were performed in the rectangular domain of $3 \times 3 \times 3$ m^3 in a Cartesian coordinate. Consistently with the experiments, the burner is lifted by 0.3 m above the floor to prevent the influence of the ground. The flamelet library was generated using the full chemical kinetic scheme developed by Qin et al. (2000). The filtered RTE is solved by using the DOM with a S8 quadrature scheme (Modest, 2013). This angular resolution was selected based on Jensen et al. (2007), which demonstrated that a S4 quadrature is sufficient within the flame, where radiation is isotropic, whereas a finer quadrature is required to predict accurately flux outside the fire.

In order to examine the effect of the grid resolution on the LES results, five grids G1, G2, G3, G4 and G5 have been used with progressively increasing the resolution in the three directions from 0.909 to 6.32 million cells. These grids are uniform in the region $0.3 \times 0.3 \times 1.0$ m^3 which results in a minimal grid spacing equal to 1.5, 1.25, 1.0, 0.75 and 0.5 cm, respectively (see Table 6.1). Outside this region, all grids are progressively stretched in all the directions. Throughout all simulations, time step is set to 5×10^{-4} s which corresponds to an averaged maximum CFL of 0.6. Simulations were run for 25 s and the time-averaged mean and root mean square values were collected over the last 19 s. The first 6 s of simulation were used to establish a statistically stationary flow. The convergence of statistics will be investigated for the 57.5 kW fire plume at heights above the burner of 0.1, 0.2, 0.4 and 0.6 m, respectively. The corresponding normalized heights are $z^* = z/\dot{Q}^{2/5} = 0.019$, 0.039, 0.079, and 0.119 $m \cdot kW^{-2/5}$, showing that they are located close to the burner, in the continuous flame region (CF, $z^* \leq 0.08$ $m \cdot kW^{-2/5}$), at the transition

Grids	G1	G2	G3	G4	G5
Number of cells in $0.3 \times 0.3 \times 1.0\ m^3$	$20 \times 20 \times 66$	$24 \times 24 \times 80$	$30 \times 30 \times 100$	$40 \times 40 \times 133$	$60 \times 60 \times 200$
$\Delta\ (cm)$	1.5	1.25	1.00	0.75	0.50
λ/Δ	1.04	1.25	1.56	2.08	3.12
l_d/Δ	0.95	1.14	1.42	1.90	2.85
Δ/η_k	17.8	14.8	11.9	8.9	5.9

Table 6.1: Resolution parameters for the LES calculations.

between the CF and the intermittent flame regions (IF) and in the IF region ($0.08 < z^* \leq 0.2\ m \cdot kW^{-2/5}$), respectively (McCaffrey, 1979). These locations cover all the reactive parts of the fire plume where SGS mixing and resulting combustion processes are expected to be the most important. In addition, it should be pointed out that the positions $z = 0.1$ and $0.2\ m$ are located in the CF where the mixing is controlled by the formation and growth of laminar instabilities (Tieszen and Gritzo, 2008).

The Kolmogorov length scale, η_k, the Taylor length scale, λ, and the diffusive layer thickness, l_d, at the CF tip can be estimated from the data of McCaffrey (1979) and Cox and Chitty (1982) following the analysis proposed in Refs. (Williamson et al., 2007; Wu et al., 2020).The integral length scale, L_t, is assumed to be one-half of the equivalent burner diameter (Williamson et al., 2007; Wu et al., 2020), i.e. $L_t = 0.17\ m$. Based on the turbulent intensity reported by Cox and Chitty (1982), the fluctuating velocity, w', is assumed to be 30 % of the mean axial velocity at the CF tip, w_{CF}. This latter is estimated from the correlation of McCaffrey (1979), leading to $w_{CF} = 1.93\dot{Q}^{1/5} = 4.33\ m \cdot s^{-1}$ and $w' = 1.3\ m \cdot s^{-1}$, respectively. The kinematic viscosity is computed from $\nu = \nu_\infty(1 + \Delta T_{CF}/T_\infty)^{1.7} = 187 \times 10^{-6}\ m^2 \cdot s^{-1}$ (Williamson et al., 2007) where $\nu_\infty = 15 \times 10^{-6}\ m^2 \cdot s^{-1}$ is the kinematic viscosity at the ambient temperature, $T_\infty = 293\ K$, and $\Delta T_{CF} = 1000\ K$ is the temperature rise at the continuous flame tip (Cox and Chitty, 1982). The turbulent Reynolds number is then computed as $Re_t = w' L_t/\nu = 1175$, leading to a Kolmogorov length scale, $\eta_k = L_t {Re_t}^{-3/4}$, of about $0.82\ mm$. The Taylor length scale can then be deduced from $\lambda = \sqrt{10} L_t {Re_t}^{-1/2} \approx 15\ mm$ (Pope, 2000). In addition, the diffusive layer thickness is estimated as $l_d = \sqrt{D_{st}/\chi_{st}} \approx 14\ mm$, where D_{st} and χ_{st} are the molecular diffusivity and the scalar dissipation rate at stoichiometry, respectively. The scalar

dissipation rate is determined from $\chi_{st} = a_t \varphi exp[-2(erfc^{-1}(2Z_{st}))^2]$ with $\varphi = 3[(T_{st}/T_\infty)^{1/2}+1]^2/(4[2(T_{st}/T_\infty)^{1/2}+1]^2)$. $T_{st} = 2000\ K$ and $Z_{st} = 0.055$ are the temperature and the mixture fraction at the stoichiometry, respectively. The strain rate is calculated from $a_t = 0.28\tau_k$ (Williamson et al., 2007) where $\tau_k = \eta_k/w_k$ and $w_k = w' Re_t^{-1/4}$ are the Kolmogorov time scale and velocity scales, respectively. Table 6.1 shows that the present LES are resolved beyond the Taylor microscale and the diffusive layer thickness for all the grids. In addition, the finest filter size, G5, is about 6 times the Kolmogorov length scale.

Concerning the boundary conditions, an inlet velocity was imposed at the burner to ensure the specified HRR for each methane flame. Fixed values of fuel mass flow rate and enthalpy flow rate are maintained according to the specified HRR. Both convective and diffusive mass and enthalpy fluxes are accounted for at the inlet. Typical entrainment boundary conditions are used for lateral sides. At the domain exit, a convective condition was used:

$$\frac{\partial \tilde{\phi}}{\partial t} + u_c \frac{\partial \tilde{\phi}}{\partial \mathbf{n}} = 0 \tag{6.1}$$

where $\phi = \{u_j, Z, Z^2, V_Z, h\}$. Following Craske and Reeuwijk (2013), the convective velocity u_c is given by a Gaussian profile, $u_c = u_0^{out} exp(-r^2/b^2)$. The mean axial velocity on the plume centreline, u_0^{out}, and the plume radius, b, at the exit height were obtained from the Heskestad correlations (Heskestad, 1984). Homogeneous Neumann condition is used for the pressure. In the rest domain, the classical wall boundary condition is imposed.

6.1.3 Impact of grid spacing

The performance of algebraic equilibrium, VTE and STE models are examined based on the convergence of the LES statistics with respect to the filter width, Δ, in the 57.5 kW fire plume. For a consistent LES, time-averaged values must converge, root-mean-square (rms) resolved values must increase and the SGS variance diminishes when Δ decreases (Boudier et al., 2008). These three models differ by the calculation of the SGS mixture fraction variance. Consequently, the convergence properties of mean mixture fraction and mixture fraction variance are first analysed (Kemenov et al., 2012):

$$\langle Z \rangle = \langle \tilde{Z} \rangle + \langle Z'' \rangle = \langle \tilde{Z} \rangle \tag{6.2}$$

$$\langle Z'^2 \rangle = \langle Z^2 \rangle - \langle Z \rangle^2 = \underbrace{(\langle \tilde{Z}^2 \rangle - \langle Z \rangle^2)}_{\langle Z_{V,ReS} \rangle} + \underbrace{(\langle \widetilde{Z^2} - \tilde{Z}^2 \rangle)}_{V_Z} \tag{6.3}$$

For sufficiently fine LES, it is reasonable to expect that the residual mixture fraction, $\langle Z'' \rangle$, is equal to 0 (Kemenov et al., 2012). Note that this assumption has been used to express Eq. (6.3).

Impact of grid spacing on VTE and STE

Let us start by investigating the effects of the turbulent resolution scale Δ on VTE and STE. Radial profiles of time-averaged mixture fraction, $\langle Z \rangle$, SGS variance, $\langle V_Z \rangle$, resolved-scale variance, $\langle Z_{V,ReS} \rangle$, and total variance, $Z_{V,tot}$, at different heights of 0.1, 0.2, 0.4 and 0.6 m, computed with the VTE and STE models on the different grids, are presented in Figs. 6.1 to 6.4, respectively. The SGS variance reaches on the whole maximum values along the plume axis at all the heights (see Fig. 6.2). As a consequence, the dependence of mean mixture fraction, SGS mixture fraction variance and total mixture fraction variance on Δ along the plume centreline is further investigated in Figs. 6.15 in order to provide more quantitative information. Figure 6.1(g) and (h) and the diagram (b_1) in Fig. 6.15 show clearly that the STE model exhibits convincing convergence for mean mixture fraction on the different grids at $z = 0.4$ m and 0.6 m. In the CF region ($z = 0.1$ m and 0.2 m), the STE solutions are more grid-dependent, especially along the plume wings (see Fig. 6.1(e) and (f)). Nevertheless, a reasonable convergence state is reached along the plume axis for these heights on the grids G3-G5 (see Fig. 6.15(b_1)). On the other hand, the convergence of VTE is more complicated whatever the height at the vicinity of the fire plume axis (see Fig. 6.1 (a)-(d) and 6.15(a_1)). In addition, similar grid effects as for STE are observed along the plume wings in the CF region (see Figs. 6.1(a) and (b)). Figure 6.1 shows also that the VTE model predicts higher mixture fraction close to the fire plume axis (see also Fig. 6.15) whereas the STE model predicts slightly wider radial distributions. The radial profiles of SGS mixture fraction variance are plotted in Fig. 6.2 for all the grids. In accordance with the criterion of consistent LES, $\langle V_Z \rangle$ decreases continuously as Δ is reduced for STE. This behaviour is further highlighted in the diagram (b_2) of Fig. 6.15. The rate of decrease for VTE is in overall slower than that of STE up to G4 and accelerates between G4 and G5 as illustrated in the diagram (a_2) of Fig. 6.15. Figure 6.2 shows also that, for a given grid up to G4, the VTE model predicts lower $\langle V_Z \rangle$ than the STE model close to the centreline at

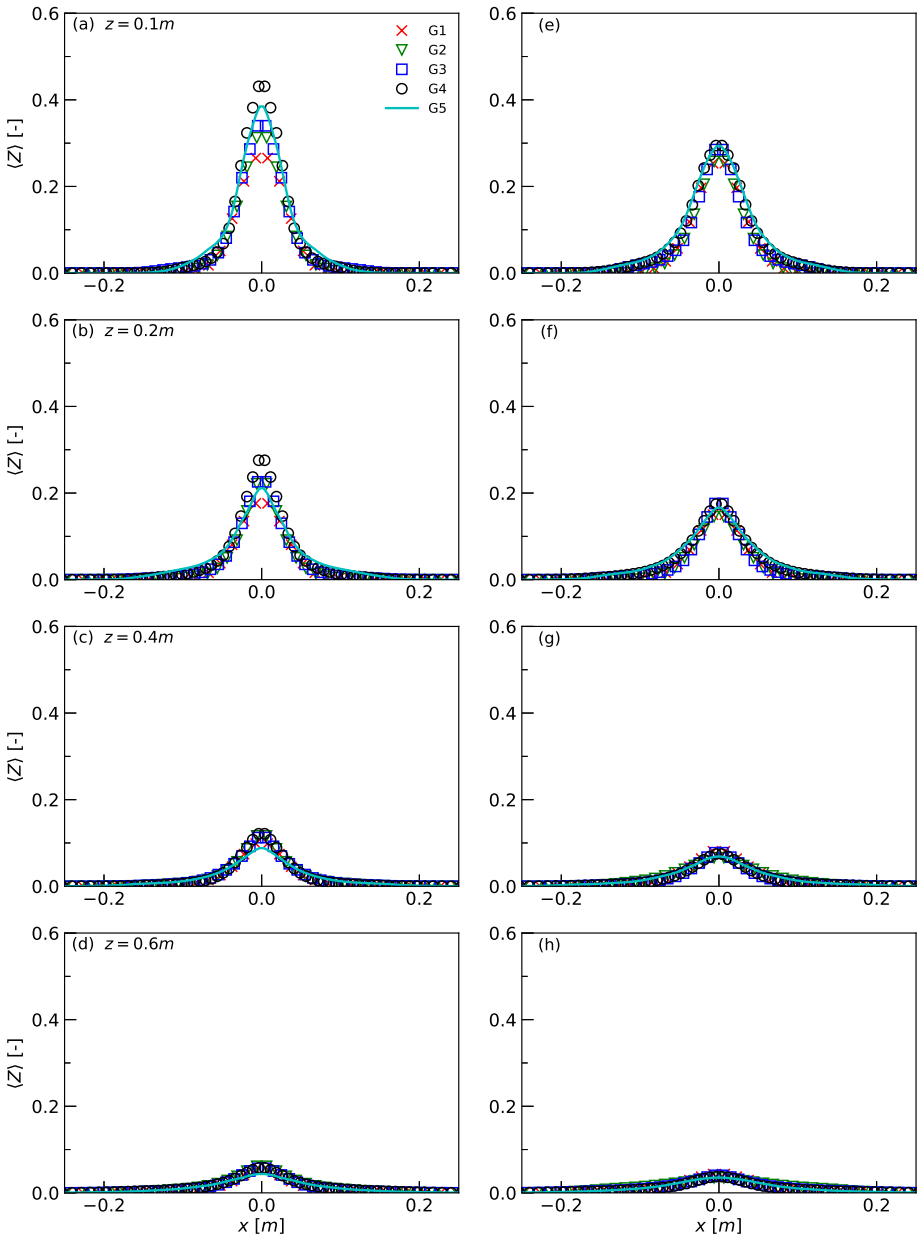

Figure 6.1: Radial distribution of time-averaged mixture fraction with VTE model (a)-(d) and STE model (e)-(h) at different heights for the 57.5 kW fire plume.

$z = 0.1\ m$ and $z = 0.2\ m$ (see also the diagrams (a_2) and (b_2) of Fig. 6.15) and in the profile wings at all heights. This behaviour is consistent with the observations made in other flame configurations (Kaul et al., 2009; Kaul and Raman, 2011; Kemenov et al., 2012; Jain and Kim, 2019) and is attributed to numerical errors stemming from an underresolved discrete representation of the squared-gradient term in the production rate of the SGS mixture fraction

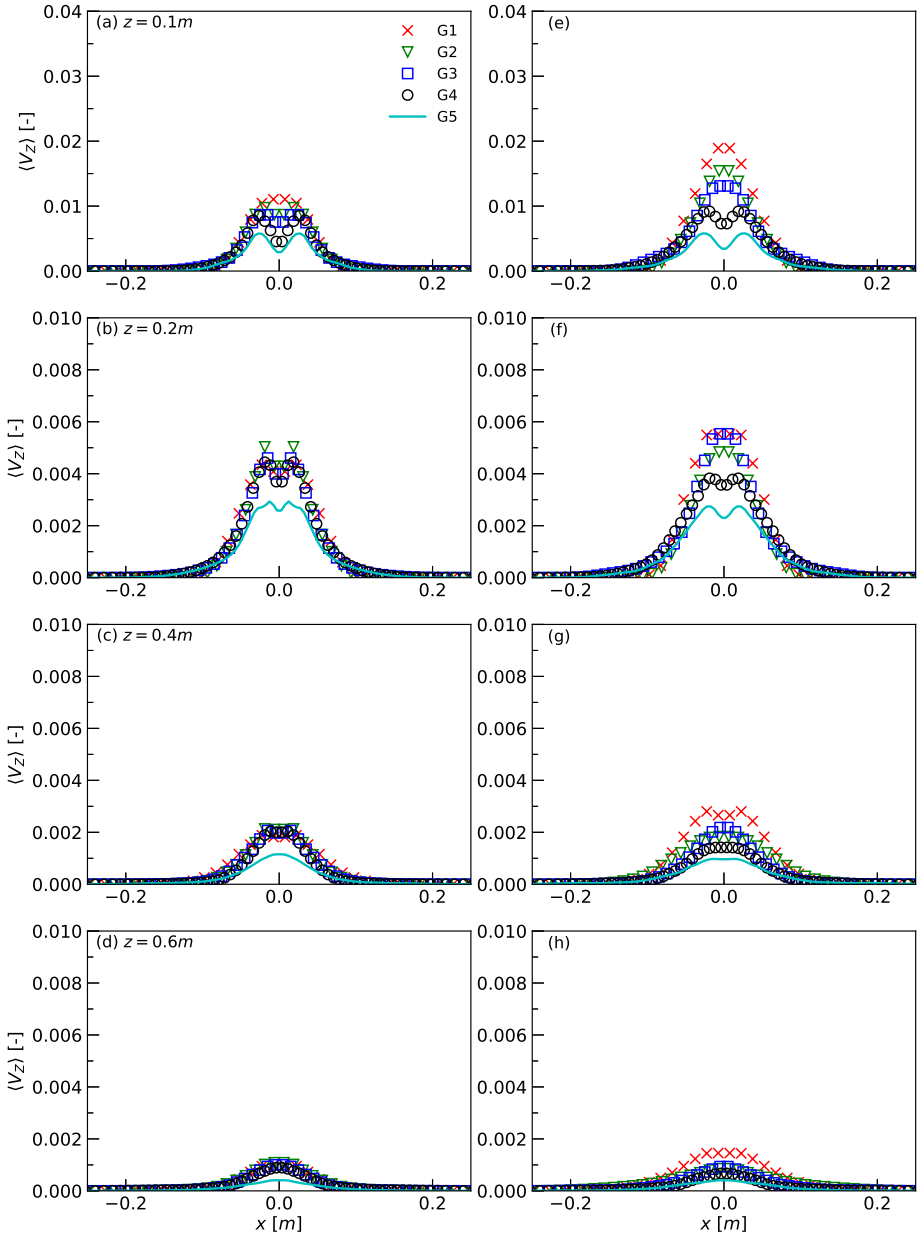

Figure 6.2: Radial distribution of subgrid mixture fraction variance with VTE model (a)-(d) and STE model (e)-(f) at different heights for the 57.5 kW fire plume.

variance (see Eq. 3.42). This production term is explicitly involved in the VTE model (see Eq. 3.41) but not in the STE model that does not suffer from these approximations. For the finest grid G5, a detailed examination of the results shows that both models predict the similar radial profiles of $\langle V_Z \rangle$ at all the heights. This latter result suggests that the aforementioned numerical errors affecting the VTE model are reduced when the grid is sufficiently fine and

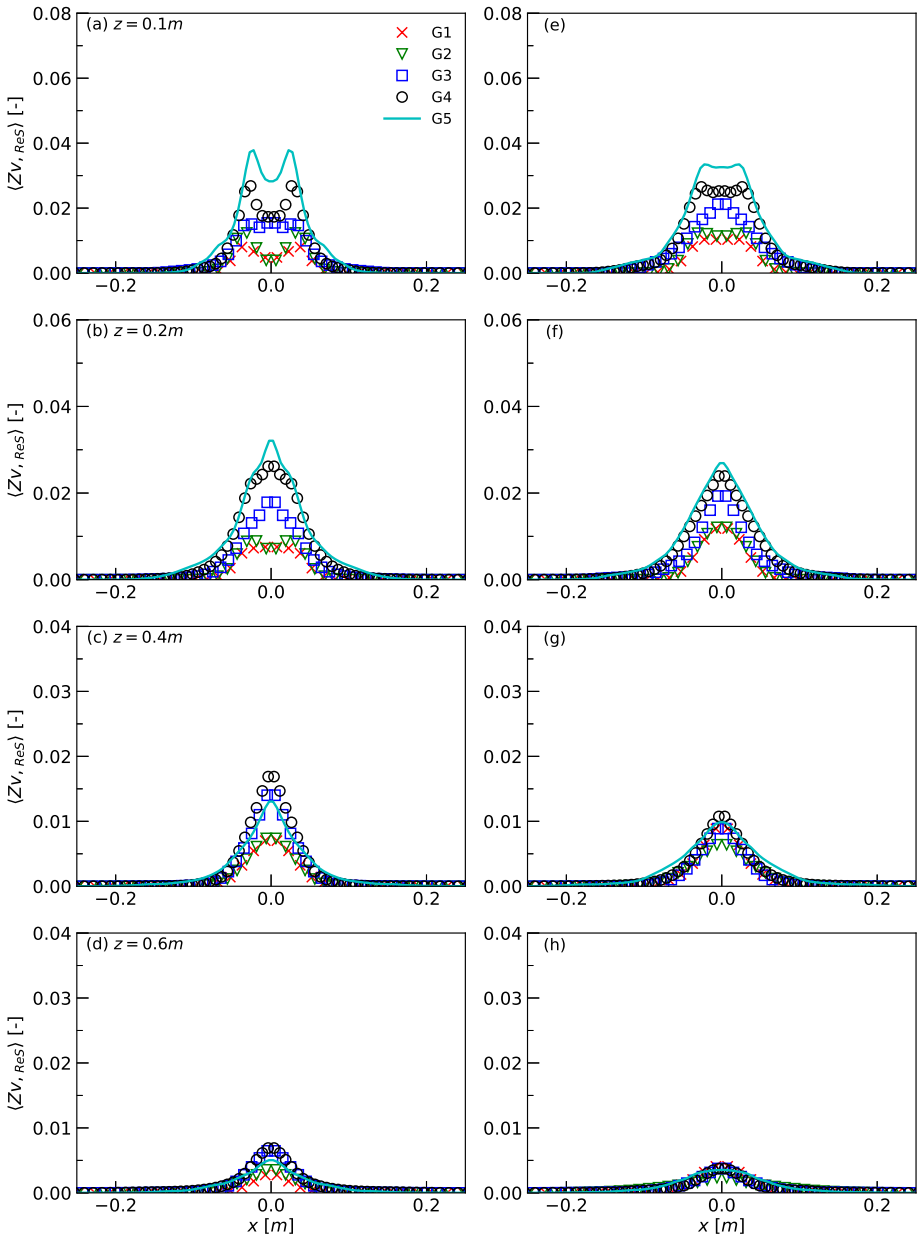

Figure 6.3: Radial distribution of resolved mixture fraction variance with VTE model (a)-(d) and STE model (e)-(h) at different heights for the 57.5 kW fire plume.

that both models tend towards similar solutions. As expected, Fig. 6.3 shows that $\langle Z_{V,ReS} \rangle$ increases as the grid becomes finer and finer up to G4 for both models. In addition, it can be observed that the corresponding rate of increase is higher close to the source ($z = 0.1\ m$ and $0.2\ m$). For G5, $\langle Z_{V,ReS} \rangle$ keeps on increasing for both models at $z = 0.1\ m$ and $0.2\ m$ whereas the shape of the radial profiles changes at $z = 0.4\ m$ and $0.6\ m$, resulting in lower values close

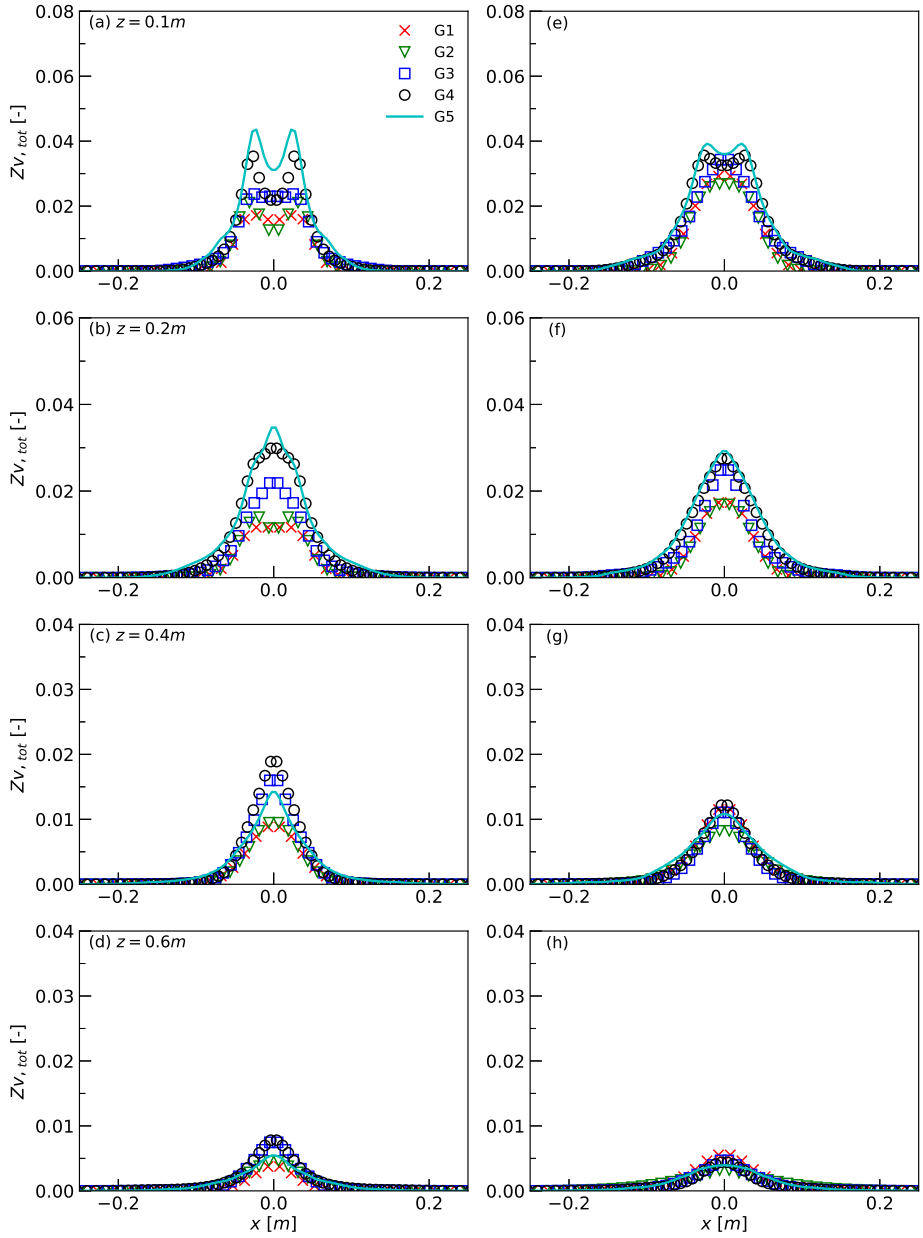

Figure 6.4: Radial distribution of total mixture fraction variance with VTE model (a)-(d) and STE model (e)-(h) at different heights for the 57.5 kW fire plume.

to the centreline and wider radial extensions. STE reaches an approximate convergent state on G3–G5 grids for $Z_{V,tot}$ as shown in Fig. 6.4(e)-(h). This is confirmed by the diagram (b_3) of Fig. 6.15. On the other hand, Fig. 6.4(a)-(d) and the diagram (a_3) of Fig. 6.15 show that the convergence is less convincing for VTE whatever the height, especially close to the fire plume axis. A careful examination of the results shows that the differences between VTE and STE

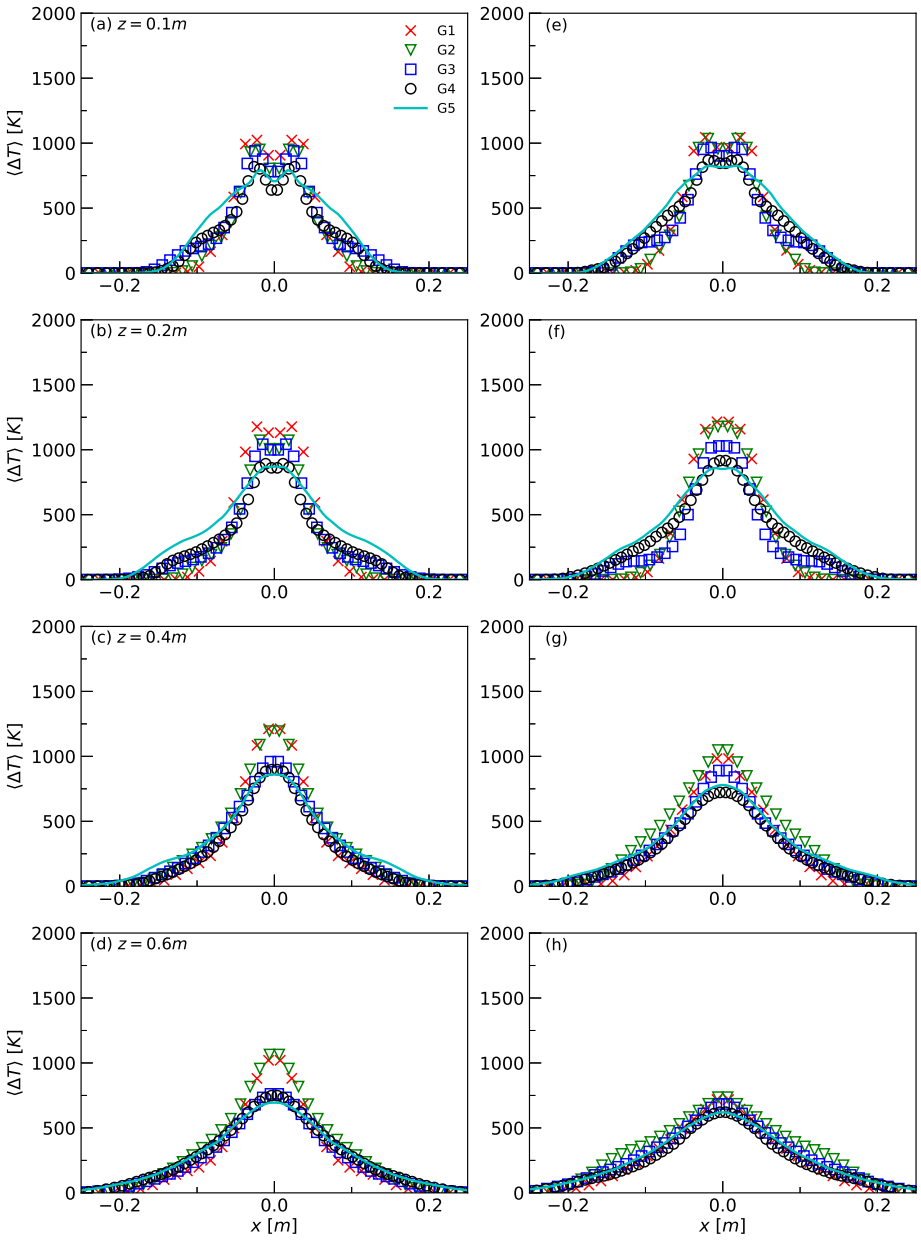

Figure 6.5: Radial distribution of time-averaged temperature with VTE model (a)-(d) and STE model (e)-(h) at different heights for the 57.5 kW fire plume.

are substantially less important on G5 than on G4 and G3, which reinforces the feeling that both models converge towards the same solution when the grid becomes sufficiently fine. These differences between VTE and STE are the following. First at $z = 0.1\ m$, the VTE model exhibits a more pronounced double-peak radial profile than the STE model. This behaviour is also observed for $\langle V_Z \rangle$ and $\langle Z_{V,ReS} \rangle$ (see Figs. 6.2 and 6.3). Second, close to the plume axis, the VTE model predicts slightly higher $Z_{V,tot}$ than the STE model (see the

diagrams (a_3) and (b_3) of Fig. 6.15). Third, it appears also that the STE model predicts a slightly higher lateral spreading. In order to complete the

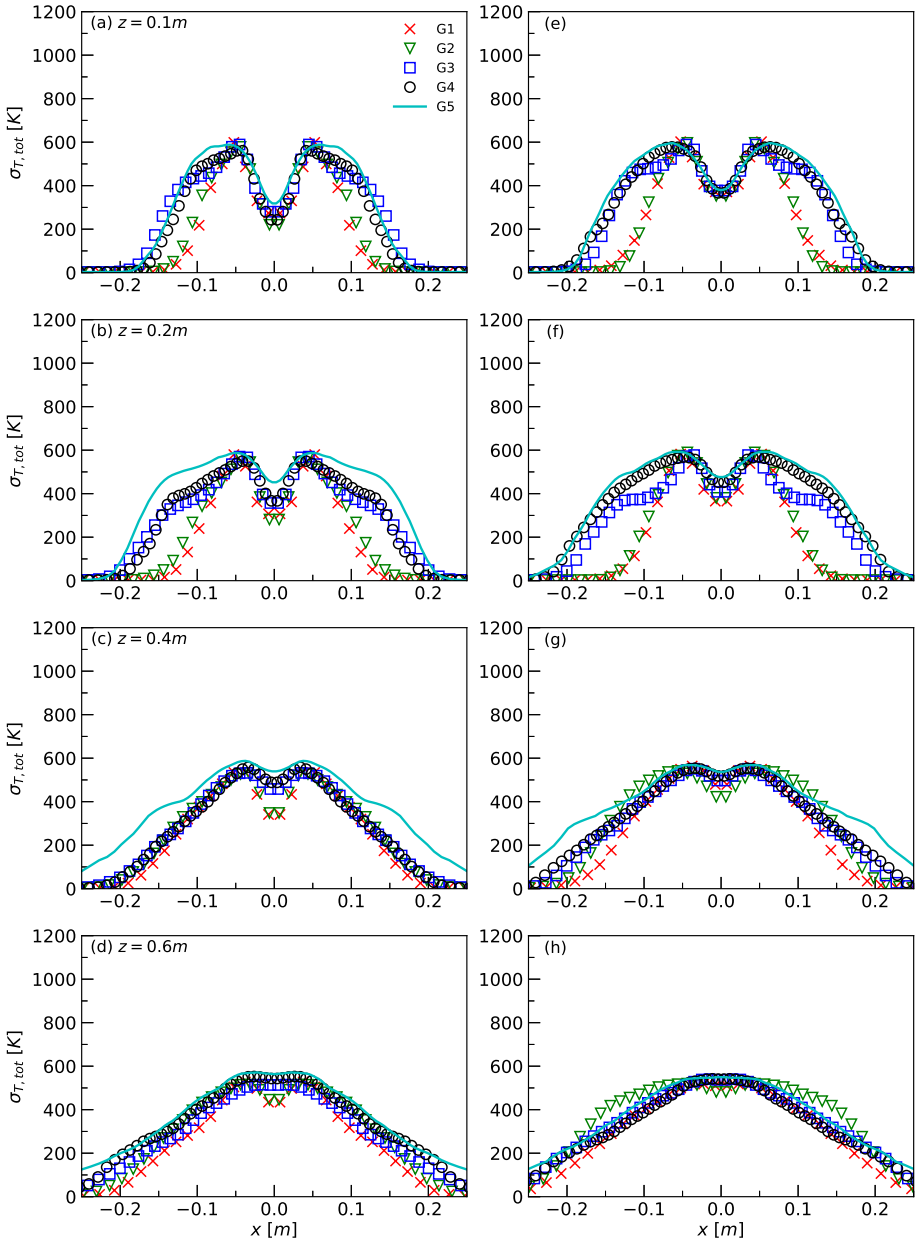

Figure 6.6: Radial distribution of total rms temperature with VTE model (a)-(d) and STE model (e)-(h) at different heights for the 57.5 kW fire plume.

previous discussion, time-averaged temperature rise above the ambient, $\langle \Delta T \rangle$, rms of total temperature fluctuations, $\sigma_{T,tot}$, defined in accordance with Eq. 6.3, time-averaged axial velocity, $\langle w \rangle$, and rms of axial velocity fluctuations, σ_w, are plotted for the two models on the different grids in Figs. 6.5 to 6.8, respectively. These figures indicate that the grids G1 and G2, that have a

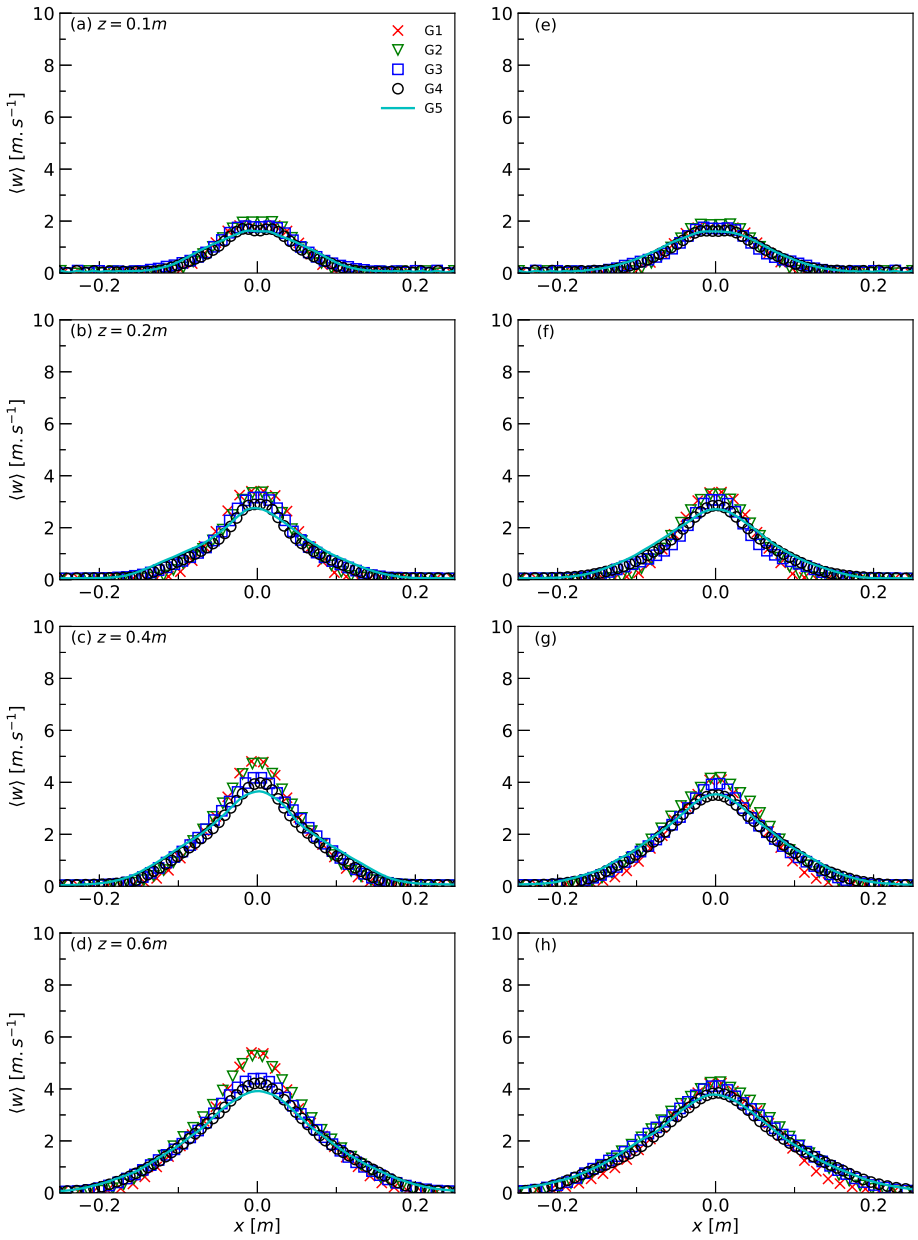

Figure 6.7: Radial distribution of time-averaged axial velocity with VTE model (a)-(d) and STE model (e)-(h) at different heights for the 57.5 kW fire plume.

resolution larger than 1 cm, predict a significantly narrower radial spreading of the fire plume than the grids G3-G5, especially in the CF region ($z = 0.1\ m$ and $0.2\ m$). These mesh effects are particularly remarkable for $\langle \Delta T \rangle$, $\sigma_{T,tot}$ and σ_w whereas they are less pronounced for $\langle w \rangle$. In addition, the radial extensions of $\langle w \rangle$ and σ_w are insensitive to further grid refinement from G3 to G5 whereas those of $\langle \Delta T \rangle$ and $\sigma_{T,tot}$ keep on being enhanced in the CF region. This latter behaviour is less pronounced for STE than for VTE. The mixing in the lower

part of the CF region is driven by the formation and growth of initially laminar non-dissipative instabilities in the near source region of the flow (Tieszen and Gritzo, 2008). These instabilities grow through the vortex dynamic and become nonlinear and energy bearing. This process is illustrated in Fig. 6.9 that shows

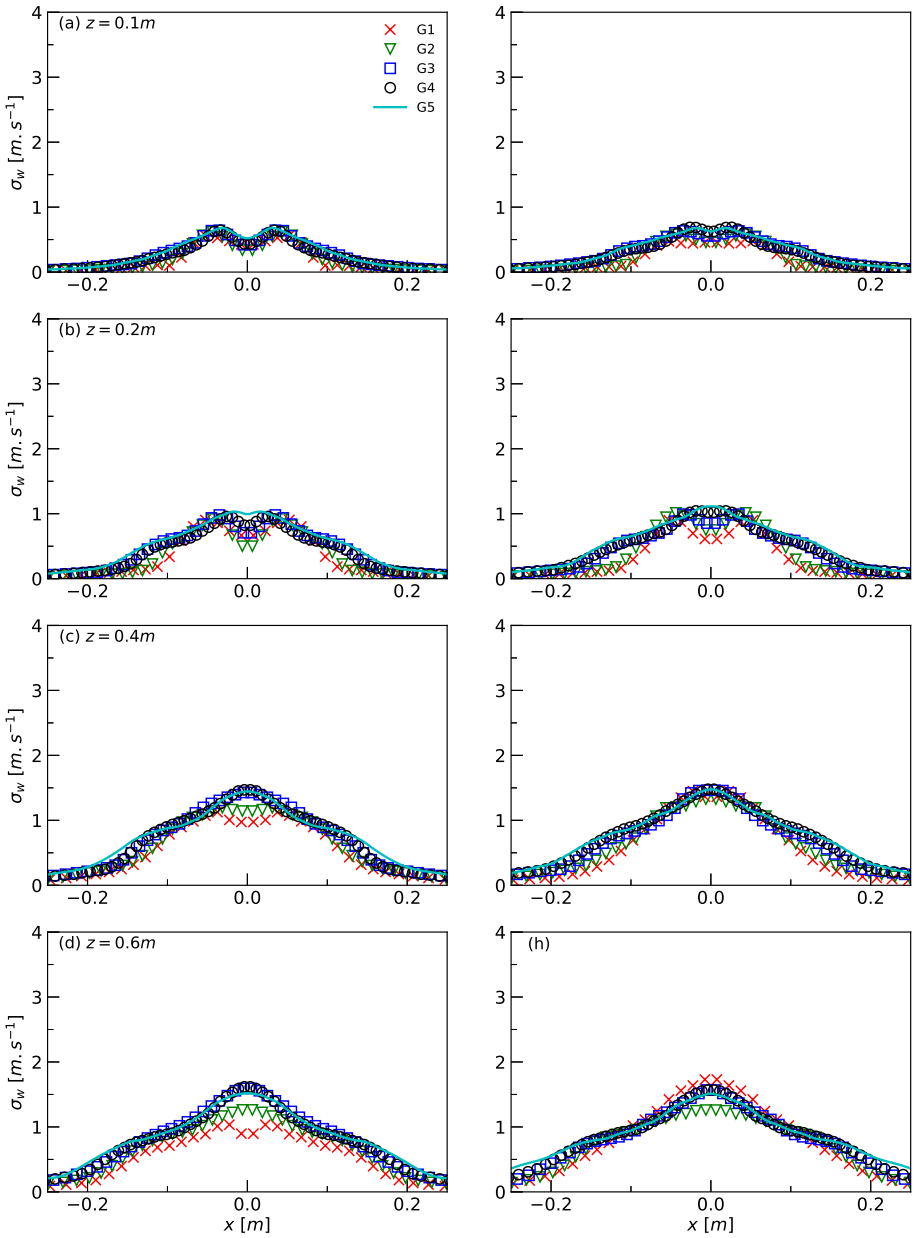

Figure 6.8: Radial distribution of rms resolved axial velocity with VTE model (a)-(d) and STE model (e)-(h) at different heights for the 57.5 kW fire plume.

instantaneous snapshots of the density field in the centreline $x - z$ plane over a sequence of 0.4 s. The formation and the growth of initially laminar bubble structures is clearly observed for the grids G3 to G5 whereas G1 and G2 are

not sufficiently fine to capture these details. In addition, this figure shows that these instabilities become better resolved as the grid is refined from G3 to G5. As discussed in Ref. (Tieszen et al., 2004), the dynamic SGS turbulence model considered in the present study is dissipative in nature and is not capturing the mixing resulting from these structures. As a consequence, the present results evidence that grid resolution has a profound impact on the dynamic of the flow in the CF region and suggest that grid resolutions coarser than 1 cm are not able to describe adequately the formation of the initial base instability near the edge of the fire plume. These observations are in accordance with those of Tieszen et al. (2004) for 1 m diameter helium plume, who also showed that too coarse grids cannot capture the formation of the instabilities and their subsequent growth. In addition, Figs. 6.5 to 6.8 emphasize the main observations made previously. i) STE exhibits a better convergence behaviour than VTE on G3 to G5 for the temperature statistics (see Figs. 6.5 and 6.6). On the other hand, both models exhibits a reasonable convergence on G3-G5 for the axial velocity statistics (see Figs. 6.7 and 6.8). ii) A careful examination of Figs. 6.5 to 6.8 shows that the differences between VTE and STE are significantly more pronounced on G3 and G4 than on G5 where both STE and VTE predictions tend to become similar. This behaviour is further highlighted in Figs. 6.10 to 6.13 that compare VTE and STE solutions on G4 and G5. The observed differences are consistent with those described for mean mixture fraction and mixture fraction variances and are evidenced by the comparison of VTE and STE solutions on G4 reported in the Figs. 6.10 to 6.13. STE exhibits in overall a wider fire plume spreading at all heights. In addition, as for mixture fraction variances, the double peak radial profiles, observed for $\langle \Delta T \rangle$, $\sigma_{T,tot}$ and σ_w at $z = 0.1\ m$ and resulting from the fact that close to the burner the high-temperature combusting sheets occur predominately close to the plume edge, are more pronounced for VTE than for STE. Finally, it can be also observed that $\sigma_{T,tot}$ is higher for STE than for VTE (see Fig. 6.11). The differences between STE and VTE originate from different formulations at the discrete level of the transport equation of the SGS mixture fraction variance. Numerical errors stemming from finite differences lead to an underestimation of the SGS variance production term, which appears explicitly in the VTE formulation as discussed in Kaul et al. (2009) and Kaul and Raman (2011). For the present fire plume, as discussed previously, this results in SGS variance lower for VTE than for STE in the CF region ($z = 0.1\ m$ and $z = 0.2\ m$), which, in turn,

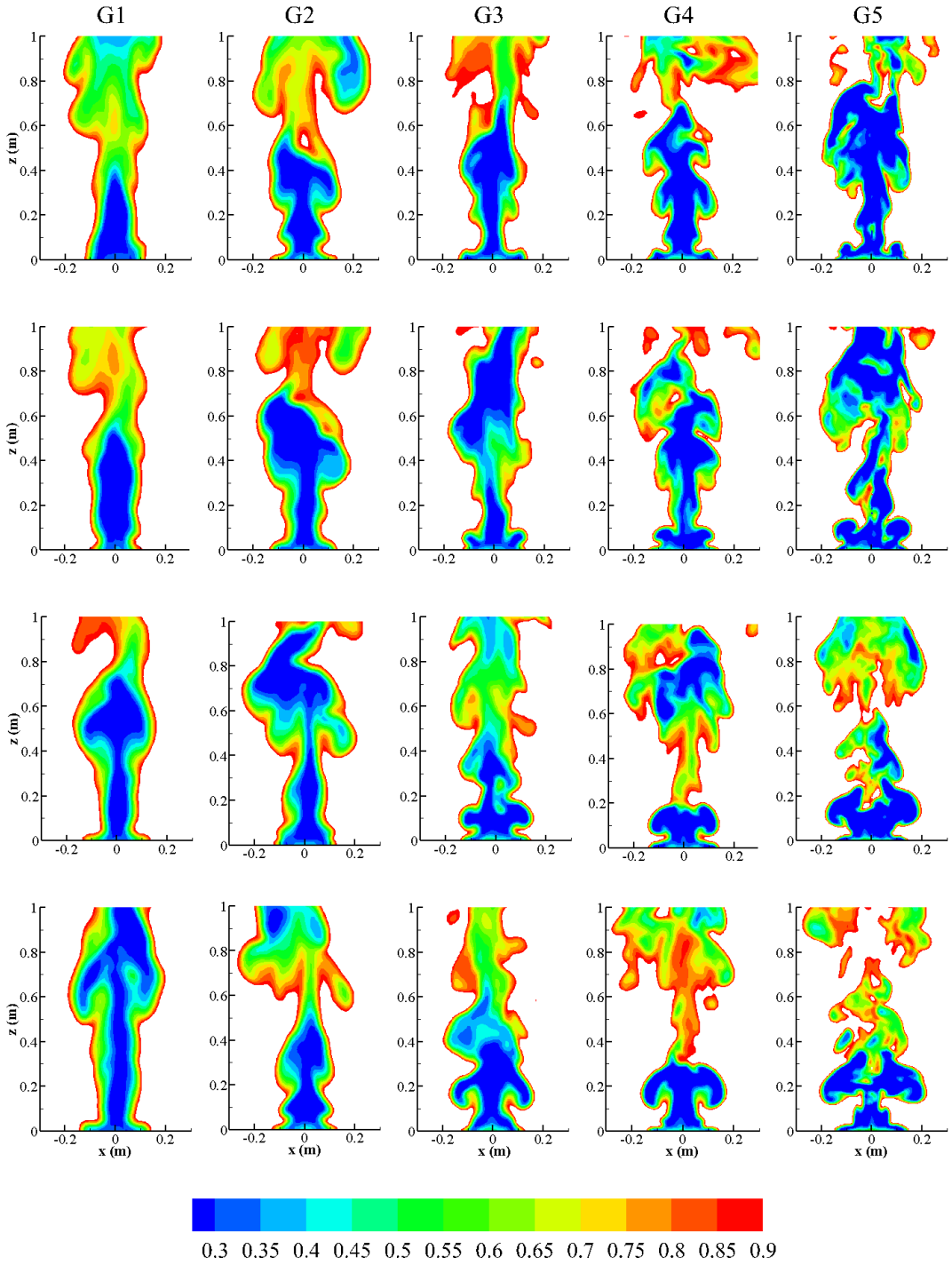

Figure 6.9: Instantaneous snapshots of the density field, computed with the STE model on the different grids, in the centreline (x-z) plane over a sequence of 0.4 s for the 57.5 kW fire plume.

affects the combustion process that occurs at the SGS level. In particular, in the CF region ($z = 0.1\ m$ and $z = 0.2\ m$), the temperature and, as a result, the

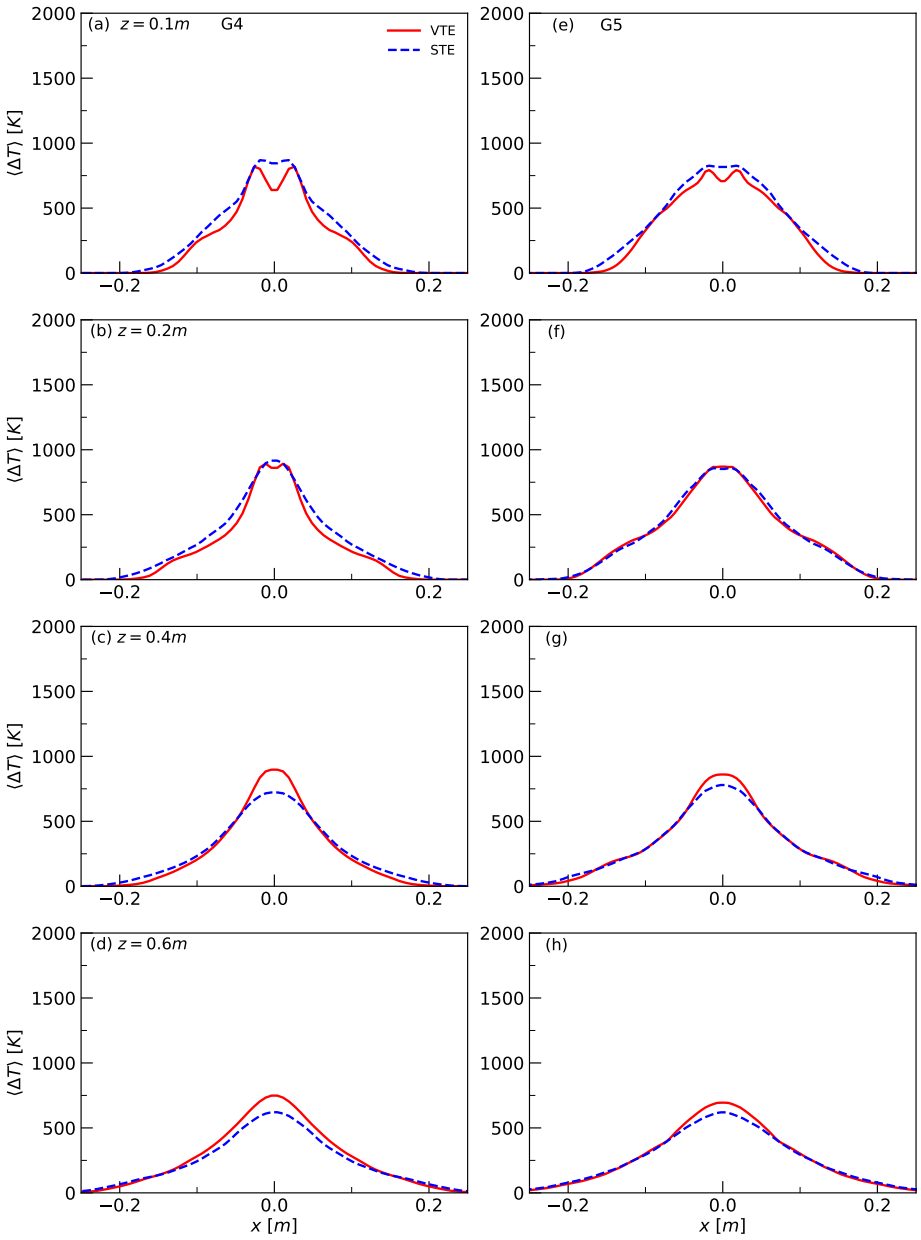

Figure 6.10: Radial distribution of temperature with VTE and STE models on G4 ((a)-(d)) and G5 ((e)-(h)) at different heights for the 57.5 kW fire plume.

temperature gradient that drives the formation and the growth of the laminar instabilities in the near source region of the flow, are higher for STE than for VTE.

This is evidenced in Fig. 6.10 that compares the temperature rise above the ambient for STE and VTE on G4. Therefore, the resolved-scale mixing is stronger for STE than for VTE. This is illustrated in the Fig. 6.14 that com-

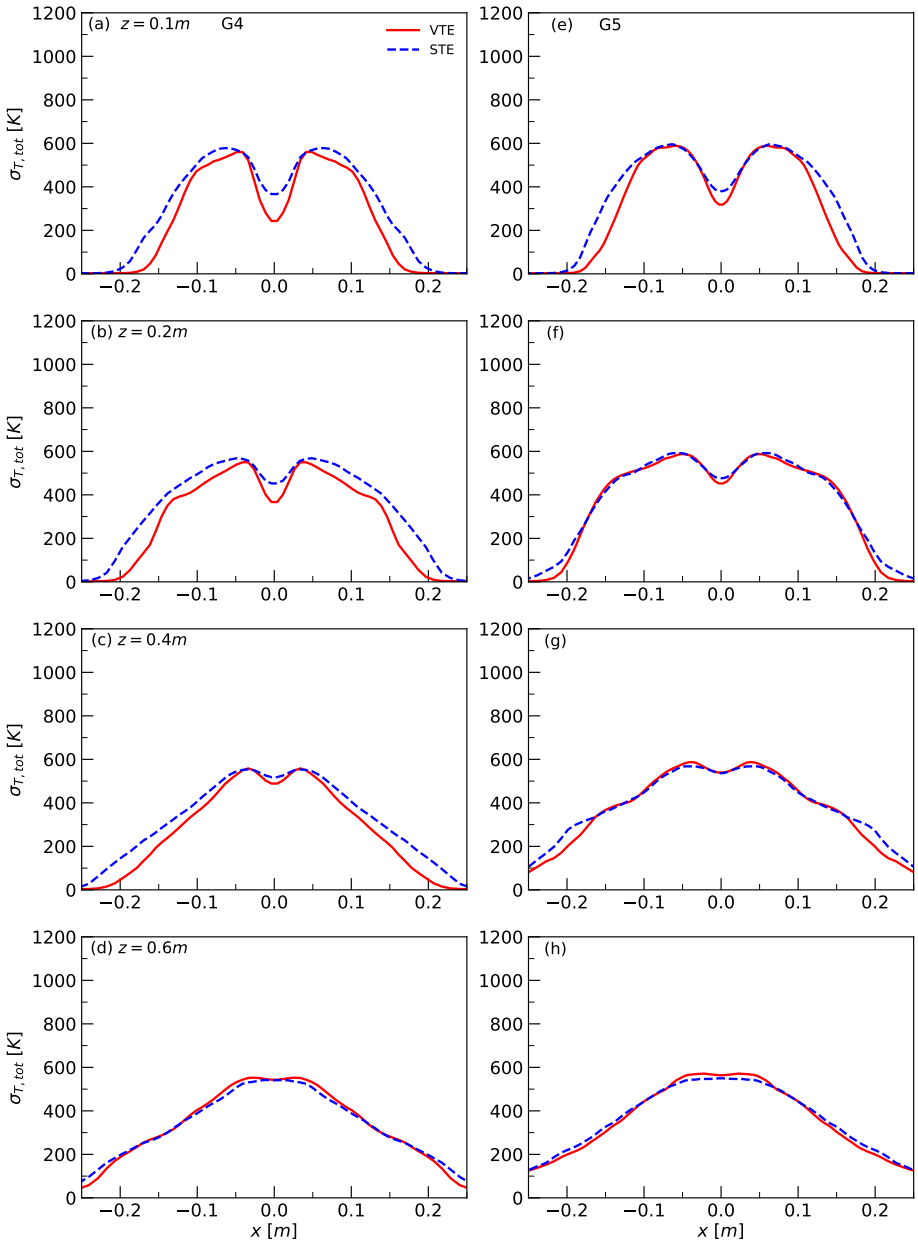

Figure 6.11: Radial distribution of total rms temperature with VTE and STE models on G4 ((a)-(d)) and G5 ((e)-(h)) at different heights for the 57.5 kW fire plume.

pares the resolved temperature fluctuation predicted by STE and VTE on G4. This explains that STE predicts in overall wider radial profiles and lower centreline mixture fraction. This explains also why the double peak radial profiles observed for $\langle V_Z \rangle$, $\langle Z_{V,ReS} \rangle$, $Z_{V,tot}$, $\langle \Delta T \rangle$, $\sigma_{T,tot}$ and σ_w at $z = 0.1\ m$ are less pronounced for STE than for VTE.

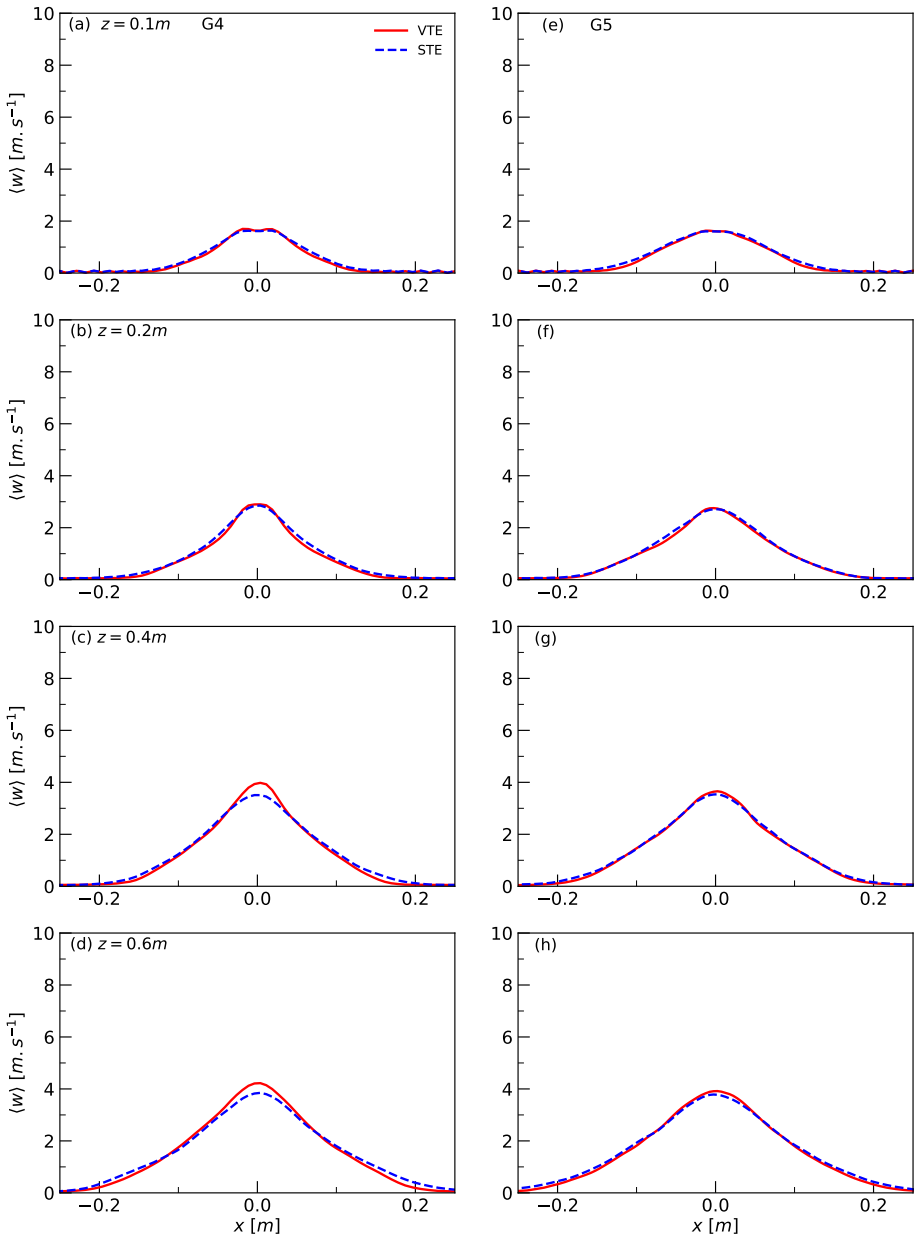

Figure 6.12: Radial distribution of mean axial velocity with VTE and STE models on G4 ((a)-(d)) and G5 ((e)-(h)) at different heights for the 57.5 kW fire plume.

In addition, these interactions between SGS mixing and resolved-scale mixing in the CF region through the combustion process may explain that the differences between VTE and STE are higher in the present configuration than for the SANDIA flame D where, as stated by Kemenov et al. (2012), the flow is relatively insensitive to the incurred errors on the SGS variance. Table 6.2 shows the puffing frequency, f, predicted by both VTE and STE for the differ-

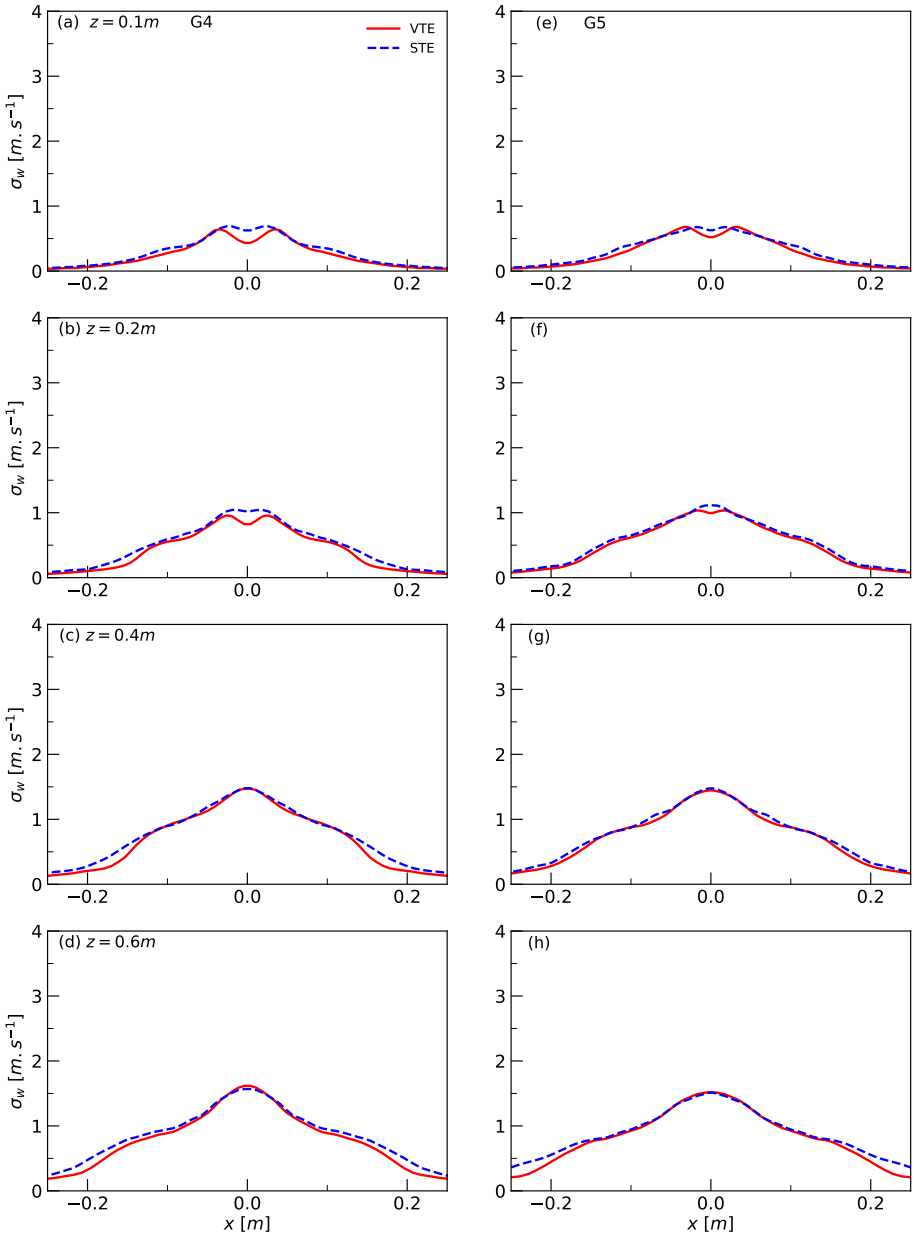

Figure 6.13: Radial distribution of rms resolved axial velocity with VTE and STE models on G4 ((a)-(d)) and G5 ((e)-(h)) at different heights for the 57.5 kW fire plume.

ent grids. These predictions can be compared with the correlation of Cetegen and Ahmed (1993), i.e. $f = 1.5\sqrt{1/D_{eq}} = 2.58\ Hz$ where $D_{eq} = 0.34\ m$ is the equivalent burner diameter. It can be observed that the puffing frequencies computed with STE and VTE converge towards 2.5 Hz on G3-G5. The dependence of the radiant fraction and the optical thickness, defined as the part of the radiative emission reabsorbed within the flame (Nmira et al., 2020a),

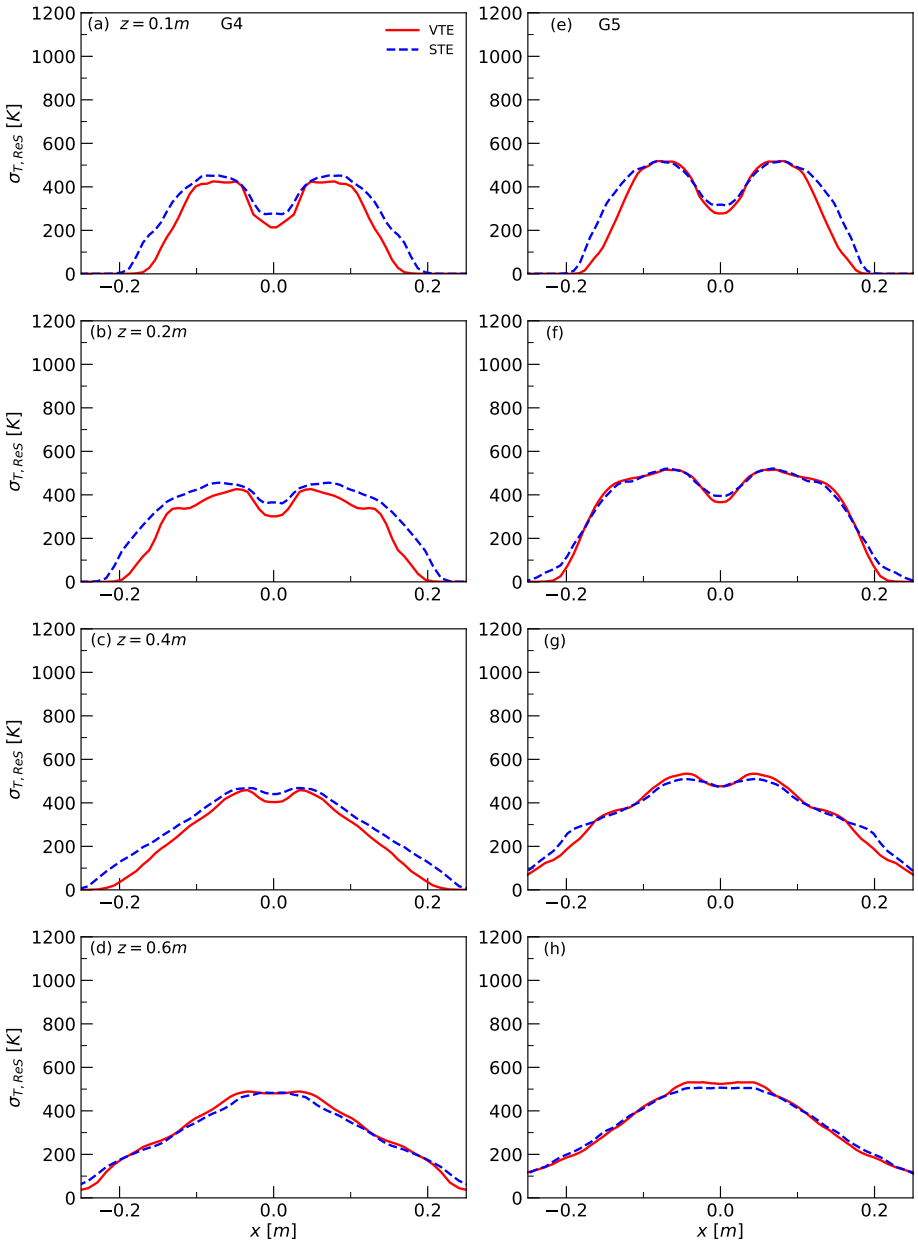

Figure 6.14: Radial distribution of rms resolved temperature with VTE and STE models on G4 ((a)-(d)) and G5 ((e)-(h)) at different heights for the 57.5 kW fire plume.

$\dot{Q}_{abs}/\dot{Q}_{emi}$, on Δ are reported in Table 6.3. The radiant fraction computed with STE is nearly constant on G3-G5 with a value around 0.27 whereas that computed with VTE is more sensitive to the grid. It can be also observed that the differences between the two models are reduced as the grid is refined from G3. The flame optical thickness is less sensitive to the grid resolution than the radiant fraction and is around 0.47-0.48 on G3-G5 for the two models. These

Grids	G1	G2	G3	G4	G5
VTE	3.3	3.5	2.3	2.5	2.5
STE	2.5	3.0	2.5	2.5	2.5
algebraic model	3.4	3.3	3.0	1.7	2.4

Table 6.2: Puffing frequency computed by VTE, STE and algebraic closure models for the 57.5 kW fire plume on the different grids.

Grids	Model	G1	G2	G3	G4	G5
Radiant fraction	VTE	0.288	0.293	0.272	0.269	0.271
	STE	0.276	0.261	0.255	0.261	0.269
Optical thickness	VTE	0.470	0.473	0.477	0.477	0.482
	STE	0.470	0.468	0.474	0.473	0.480

Table 6.3: Radiant fraction and optical thickness computed by VTE and STE for the 57.5 kW fire plume on the different grids.

results show clearly that this fire plume cannot be assumed as optically-thin.

Impact of grid spacing on the algebraic model

The convergence behaviour of the algebraic model is investigated in Fig. 6.15(c). Figure 6.15c_1 shows that mean mixture fraction exhibits a good convergence for all the grids at $z = 0.4\ m$ and $z = 0.6\ m$. On the other hand, the convergence is not established in the CF region ($z = 0.1\ m$ and $z = 0.2\ m$) where the mean mixture fraction increases continuously as the turbulence resolution scale is reduced (see Fig. 6.15(c_1)). The SGS mixture fraction variance does not behave as expected for consistent LES along the plume axis at $z = 0.1\ m$, $z = 0.2\ m$ and $z = 0.6\ m$ where it increases as the grid is refined up to G3 before reaching a nearly constant value as Δ is further reduced (see Fig. 6.15(c_2)). The mean total variance increases continuously as the grid size is refined and, therefore, does not convergence whatever the grid resolution more particularly in the CF region (see Fig. 6.15(c_3)). In addition, Table 6.2 shows that the convergence is not established for the puffing frequency whatever the grid. It can be also observed by comparing the diagram (c_2) and the diagrams (a_2) and (b_2) of Fig. 6.15 that, whatever the grid, the algebraic model predicts substantially lower centreline SGS scalar variance at $z = 0.1\ m$ and

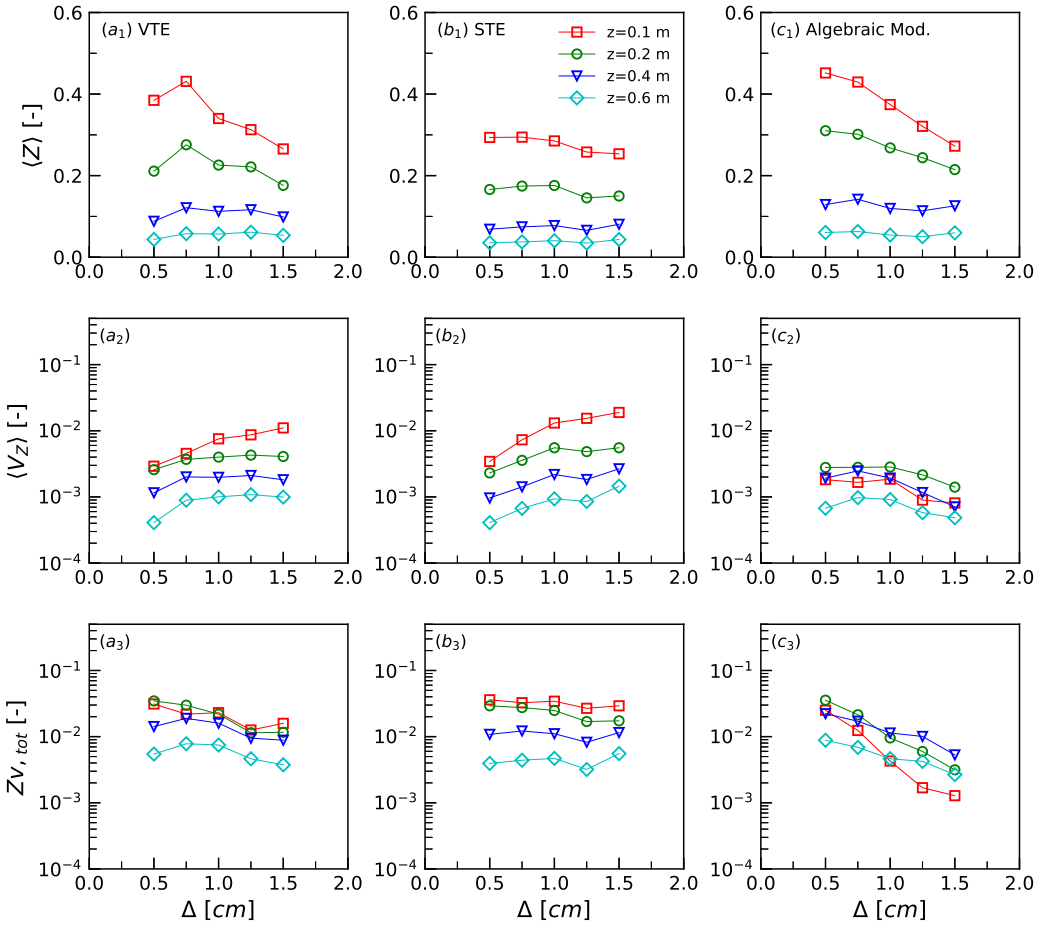

Figure 6.15: Convergence of mean mixture fraction (index 1), subgrid mixture fraction variance (index 2) and total mixture fraction variance (index 3) with grid spacing along the plume axis for: (a) VTE, (b) STE and (c) the algebraic model.

$z = 0.2\ m$ than both STE and VTE models. This underprediction is in line with observations made in other simpler flames (Jiménez et al., 2001; Kaul et al., 2009; Knudsen et al., 2012; Jain and Kim, 2019) and, for the present fire plume configuration, can be related to the highly non-equilibrium nature of buoyancy-driven flows as described by Bakosi and Ristorcelli (2010). Figure 6.16 compares the time-averaged production and dissipation rates of the SGS variance. It indicates clearly that the local equilibrium assumption is not satisfied in the CF region although it seems to become more valid as the height increases in the IF region and in the plume. These results evidence the limitation of algebraic equilibrium based models for the simulation of fire related flows.

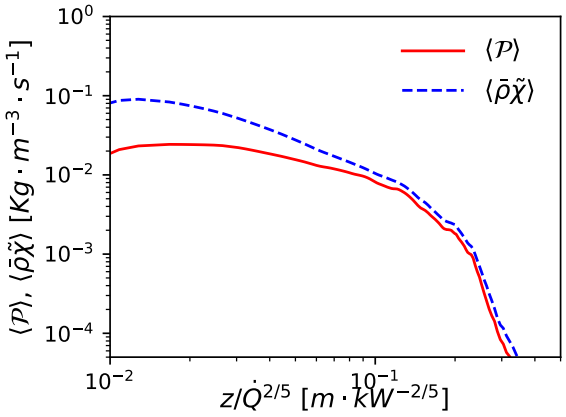

Figure 6.16: Axial evolution of the time-averaged production and dissipation rates of the subgrid mixture fraction variance computed by VTE on the grid G5 for the 57.5 kW fire plume.

6.1.4 Comparisons with experimental data

Figures 6.17 shows the axial profiles of mean axial velocity (first line, index 1), mean temperature rise (second line, index 2), resolved temperature fluctuation (third line, index 3) and total temperature fluctuation (fourth line, index 4) as a function of the normalized height for the five plumes investigated experimentally by McCaffrey (1979). Model predictions obtained on G3 with VTE (first column, diagrams a), STE (second column, diagrams b) and the algebraic model (third column, diagrams c) are compared with experimental data.

McCaffrey (1979) found that scaling the height and axial velocity by $\dot{Q}^{2/5}$ and $\dot{Q}^{1/5}$, respectively, allows collapsing the experimental data for mean temperature rise above the ambient and mean axial velocity on a single curve independent of the HRR. Let us start to discuss the solutions obtained with VTE and STE (Figs. 6.17(a_1), (a_2), (b_1) and (b_2)). Both predictions are similar and follow the same scaling as the experiments. For velocity, the deviation of these models from the correlation near the burner surface shows a similar trend and magnitude as the deviation of the measurement points to the correlation. The temperatures reported by McCaffrey were not corrected for thermocouple radiation which explains the over-prediction by both VTE and STE models, especially in the CF and IF regions. A much better agreement is observed with the correlation of Cox and Chitty, obtained also from 30 cm diameter methane fire plumes of different HRR (Cox and Chitty, 1980) and corrected

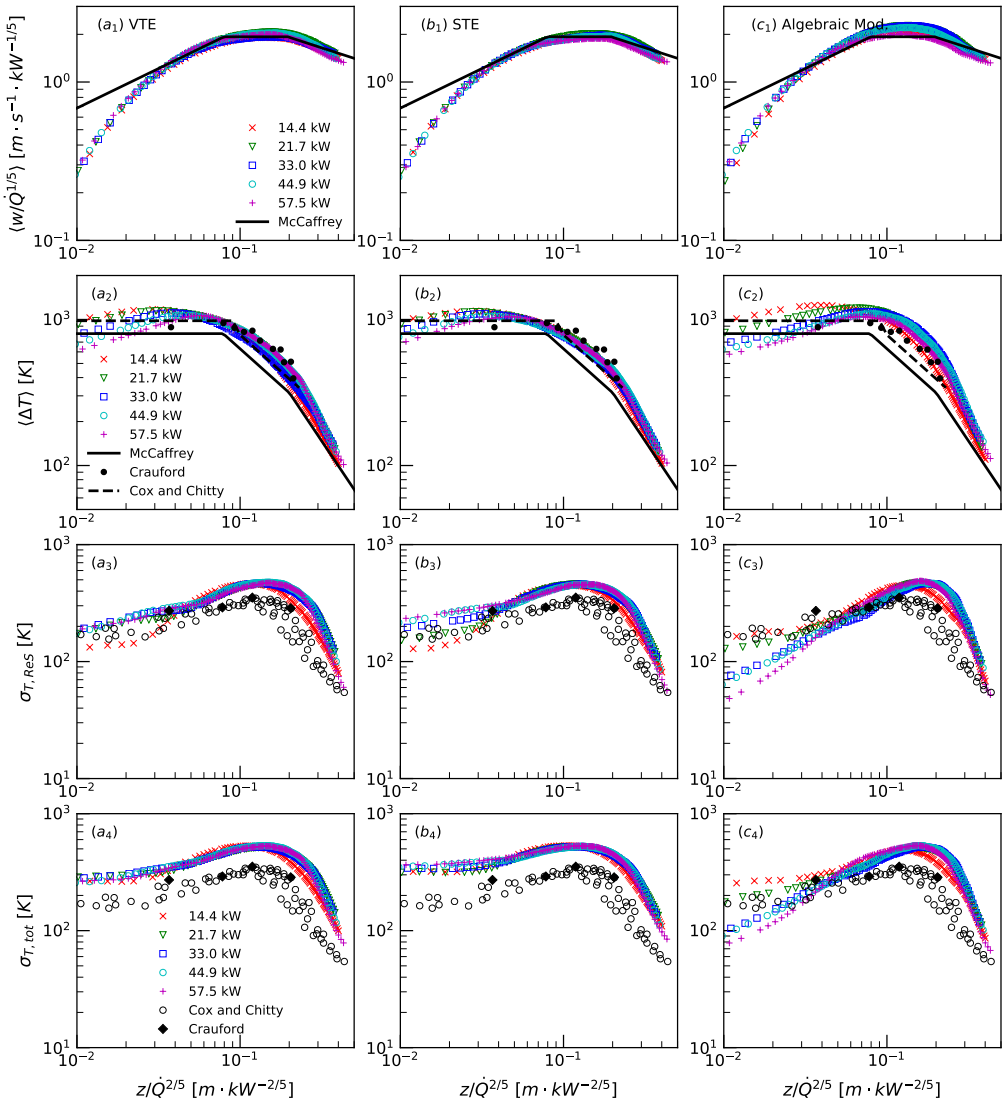

Figure 6.17: Axial distribution of axial velocity (index 1), mean temperature (index 2), resolved temperature fluctuation (index 3) and total temperature fluctuation (index 4) for the five fire plumes as a function of the normalized height with: (a) VTE, (b) STE and (c) the algebraic model.

for thermocouple radiation (Cox and Chitty, 1984), and the data reported by Crauford et al. (1985) for a 28 kW methane fire plume generated by circular burner with a diameter of 25 cm. The algebraic model, meanwhile, provides a less satisfactory agreement with the experimental correlations and data than the STE and VTE models. First, it introduces more scatter for the data corresponding to the different HRR than observed experimentally and predicted by both VTE and STE. Second, it overestimates the temperature and the axial

velocity in IF region.

The axial resolved and total temperature fluctuations are compared with the data of Cox and Chitty (1982) and Crauford et al. (1985) (see the last two lines of Fig. 6.17). Cox and Chitty (1982) measured temperature fluctuations by using uncompensated 13 μm thermocouples. An analysis performed by these authors showed that these probes can adequately follow signals with frequency up to 10 Hz. Crauford et al. (1985) also measured temperature fluctuations by using 50 μm thermocouple with a compensation technique based on a thermocouple time constant of 30 ms thorough the flame zone. They suggested that their data may significantly underestimate the temperature fluctuations. The data of Crauford et al. (1985) follow quantitatively the same trends as those of Cox and Chitty (1982). Both VTE and STE predictions reproduce correctly similar scaling and trends as the experiments (see Figs. 6.17(a_3), (b_3), (a_4) and (b_4)). The total rms of temperature fluctuation overestimate the experimental data which can be attributed, as discussed above, to the measurement techniques (see Fig. 6.17(a_4) and (b_4)). Nevertheless, it is interesting to note that the resolved temperature fluctuations predicted by both VTE and STE models are in better agreement with the experimental data (see Fig. 6.17(a_3) and (b_3)). As for mean temperature and axial velocity, the algebraic model introduces more scatter for the different HRR than observed experimentally and predicted by both VTE and STE, especially in the CF region (see Figs. 6.17(c_3) and (c_4)). In addition, as expected from the discussion in section 6.1.3, the resolved and total fluctuating temperatures are significantly underestimated in the CF region, especially for HRRs higher than 33 kW (see Figs. 6.17(c_3) and (c_4)). Figure 6.18 compares VTE and STE radial profiles of mean temperature on G3 and G4 with data extracted from the experimental results of McCaffrey for the 45 kW fire plume at different heights. The correlations of Cox and Chitty (1980) for a 47 kW fire plume are also reported. The two sets of experimental data are in good accordance at heights of 0.1, 0.5 and 0.6 m but present large discrepancies for heights of 0.2 to 0.4 m. On G3, the largest discrepancies between the model and the experimental data are observed at 0.2 and 0.3 m that correspond to regions where the intermittency is the largest. At these heights, the model underestimates significantly the measurements for $r > 0.05$ m and the maximum deviations between the calculations and the data of McCaffrey are of about 200 K at $z = 0.2$ m and $r \approx 0.05$ m. As the

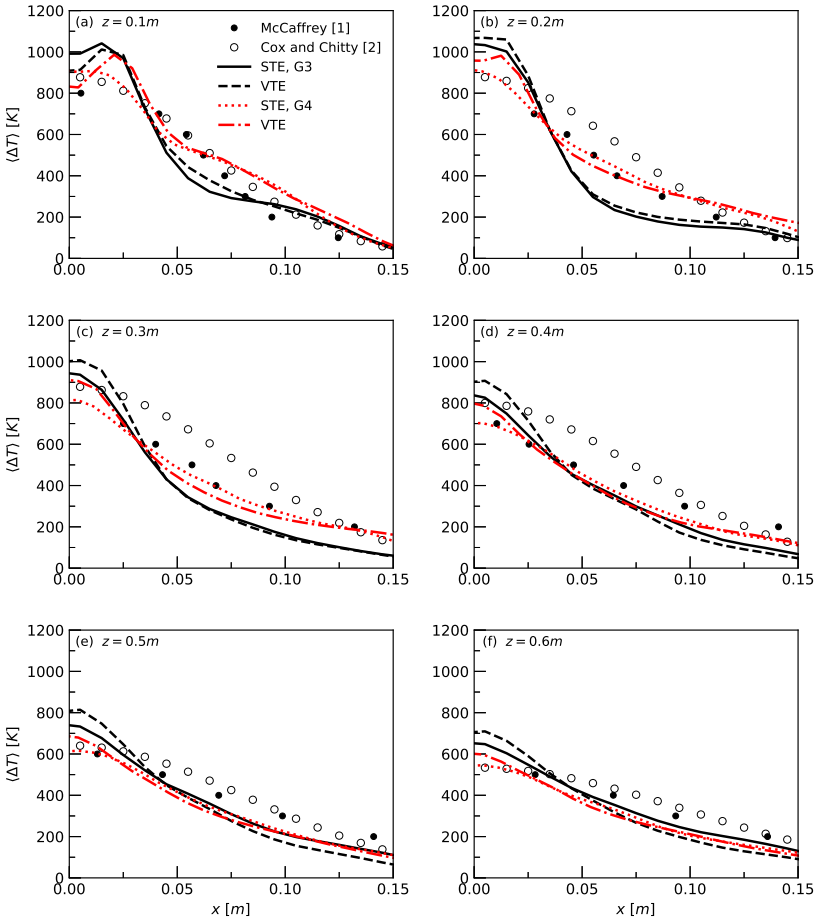

Figure 6.18: Radial distribution of mean temperature at different heights for the 45 kW fire plume.

grid is refined to G4, a much better agreement is observed at these heights. As expected the STE predicts on the whole slightly wider radial profiles than the VTE.

6.1.5 Conclusions

The following conclusions can be drawn:

1. The simulations confirm the limitations of equilibrium algebraic model for purely buoyant flows.

2. The simulations with non-equilibrium transport models show that computational grids with resolutions coarser than about 1 cm cannot adequately resolve the initial base instability near the edge of the fire plume that plays an important role to describe accurately the mixing process,

especially in the continuous flame.

3. For resolutions finer than about 1 cm, the STE model is less sensitive to grid refinement than the VTE formulation and predicts a higher mixing that results in a slightly larger lateral expansion of the fire plume. The differences between the two models tend to be reduced with the turbulent resolution scale and comparable predictions are obtained on the finest grid.

4. For grids finer than 1 cm, both VTE and STE are in quantitative agreement with available experimental data in terms of axial velocity, temperature and rms of temperature fluctuations.

5. Following these conclusions, we adopt the STE model in the remaining of the simulations reported in this work.

6.2 Effects of burner's geometry

Experimental studies revealed the importance of burner boundary conditions on the fire plume dynamics. Orloff (1981) and Orloff and De Ris (1982) observed that the fuel lip height, defined as the fuel level below the burner rim, has significant effects on the fire plume structure. A non-zero lip height was found to result in thicker and shorter fires (Orloff, 1981), which was attributed to effects on the transition to turbulence (Orloff and De Ris, 1982; Ditch et al., 2013). Weckman and Sobiesiak (1988) considered different burner arrangements in medium-scale acetone pool fires in order to modify the air entrainment at the pool basis. They found that the puffing frequency as well as the behaviour of large-scale structures are extremely dependent on the burner boundary conditions and recommended to specify them in future experimental works. In most of the experimental studies of pool fires and fire plumes published to date, a great attention was generally paid to the design of the burner boundary conditions and a detailed description was provided. From the early works of McCaffrey (1979), Cox and Chitty (1980), Cox and Chitty (1982), and Cox and Chitty (1984) and Crauford et al. (1985), the burner is generally set at least one-pool diameter above the floor to minimize the effects of surrounding surfaces on the fire behaviour. In the case of pool fires, the descriptions of the experimental set-up report also the fuel lip height. Nev-

ertheless, burner boundary conditions in most of the modelling studies of fire plumes are either not consistent with the experiments considered for comparison (Fraga et al., 2019; Wu et al., 2020) or not specified. Exceptions are the works of Chatterjee et al. (2015) and Maragkos et al. (2019). Chatterjee et al. (2015) simulated the 30 cm heptane pool fire investigated experimentally by Klassen and Gore (1992). The burner was 15 cm above the floor in line with the experimental setup but the authors did not mention if the experimental fuel lip height of 5 mm was reproduced. Maragkos et al. (2019) simulated the 30 cm methanol pool fire investigated experimentally by Weckman and Strong (1996). They reported that it was important to reproduce the experimental fuel lip height in order to capture the pool dynamics. However, they did not specify if they considered a burner located one-pool diameter above the floor as in the experiments.

As a consequence, the objective of this section is, on the one hand, to further assess the capability of the present LES-based numerical model to reproduce the dynamics of medium-scale methanol pool fires investigated experimentally by Weckman and Strong (1996) and, on the other to, investigate the effects of burner boundary conditions on the predictions. A special attention will be paid to the influence of the fuel lip height and on floor effects.

6.2.1 Experimental and computational details

The baseline configuration is the 30.5 cm diameter methanol pool fire investigated experimentally by Weckman and Strong (1996). In these experiments, the methanol feed rate was maintained at 1.35 $cm^3 \cdot s^{-1}$. The corresponding heat release rate (HRR, $\dot{Q}$) is 22.45 kW. Weckman and Strong reported measurements of mean and rms velocity and temperature. Velocities were measured by using a two-component laser Doppler anemometer with uncertainties of $\pm$ 5% on mean values and $\pm$ 15% on rms values. In addition, power spectral density (PSD) computed from time series of radial and axial velocities revealed a puffing frequency of 2.8 Hz. Temperatures were measured with 50 μm diameter bare-wire Pt-Pt/10% Rh thermocouples with bead diameters in the range of 75-100 μm. Temperature measurements were corrected to account for the thermal inertia of the thermocouple bead. The compensation technique was based on an instantaneous time constant computed from the thermocouple geometry and an estimation of the flow conditions for the convective heat

transfer. The uncertainties on mean temperature were estimated to be $\pm$ 5% whereas those on the rms values were found to be difficult to estimate mainly due to the uncertainty on the compensation method. However, uncertainties as high as 25-30% were reported using thermocouples to obtain measurements of fluctuating temperature (Crauford et al., 1985; Weckman and Strong, 1996; Weckman and Sobiesiak, 1987). This set of experimental data is completed by those obtained by Hamins et al. (1994), Hamins and Lock (2016) and Kim et al. (2019) who also considered 30 cm diameter methanol pool fires. Hamins et al. (1994) measured the radiative feedback towards the fuel surface. Hamins and Lock (2016) reported axial and radial distributions of mean temperature that were in good accordance with the measurements of Weckman and Strong (1996). They also reported axial distribution of species volume fractions. Kim et al. (2019) measured radial (at the level of the burner rim) and axial (at a distance of 60 cm from the pool axis) distributions of radiative flux. In addition, they measured the local total heat flux in the downward direction at 13 mm above the fuel surface.

In the baseline case, consistently with the experimental configurations reported in Refs. (Weckman and Strong, 1996; Hamins and Lock, 2016; Kim et al., 2019), the burner stands at one-pool diameter above the floor and fuel lip height is set equal to 1 cm (see Fig. 6.19(a)). Two other configurations are considered by modifying the burner boundary conditions while keeping the pool diameter and HRR unchanged. In order to investigate the effects of the fuel lip height on the pool fire dynamics, the first configuration, referred to as NoLip hereafter, considers the same configuration as the baseline case, except that the fuel level coincides now with the pan rim (see Fig. 6.19(b)). The second configuration, referred to as NoLipNoEnt hereafter, modifies the NoLip configuration by considering that the burner rim is now floor flush, altering thus the air entrainment at the pool basis (see Fig. 6.19(c)). Simulations were performed in a computational domain (x, y, z) of $3 \times 3 \times 3$ m^3. The mesh is uniformly refined in the region of $0.4 \times 0.4 \times 0.1$ m^3 centred around the burner, with a minimal grid spacing equal to 2.5 mm. Outside this region, Δx and Δy are stretched progressively towards the sides of the computational domain. In the vertical direction, Δz is stretched from $z = 0.1$ m to $z = 0.2$ m to reach 5 mm. An uniform $\Delta z = 5$ mm is then applied up to $z = 0.6$ m. Above $z = 0.6$ m, Δz is stretched progressively. The flamelet library was generated using the

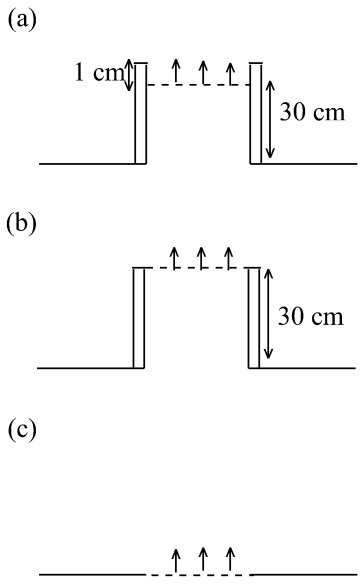

Figure 6.19: A schematic diagram of the three burner boundary conditions for the: (a) baseline case, (b) NoLip case, and (c) NoLipNoEnt case.

full chemical kinetic scheme developed by Li et al. (2007). The Filtered RTE is solved by using FVM with an angular mesh of $N_\theta \times N_\phi = 16 \times 24$ control angles (Modest, 2013). N_θ and N_ϕ represent the polar and azimuthal angles, respectively.

The mean flame height was measured as 0.51 m (Hamins et al., 1994). As discussed above, the grid resolution is lower than 5 mm in the flaming region and can be compared to estimations of the Kolmogorov length scale, η_k, and the Taylor length scale, λ. Applying the same analysis as used in the previous section, the Kolmogorov length scale and the Taylor length scale are found to be about 0.9 mm and 15.5 mm, respectively. This analysis shows that the present LES are resolved well beyond the Taylor scale and that the filter size is about 6 times the Kolmogorov length scale.

Concerning the boundary conditions, typical outflow/inflow boundary conditions are used for open boundaries at the sides. At the inlet, a spatially uniform and steady inlet velocity is imposed to provide the specified HRR and both convective and diffusive mass and energy fluxes are accounted for. The inlet temperature is set to the boiling point of methanol, i.e. 338 K. At the domain exit, a convective condition is used. In the rest of the domain, the classical wall boundary condition is imposed.

Throughout all simulations, the time step is set to 5×10^{-4} s which corresponds to an averaged maximum CFL of 0.6. Simulations were run for 25 s and the time-averaged mean and rms values were collected over the last 19 s. The first 6 s of simulation were used to establish a statistically stationary flow.

6.2.2 Quality of LES

The ratio of resolved temperature variance, $\langle \widetilde{T'^2}_{ReS} \rangle = \langle \tilde{T}^2 \rangle - \langle \tilde{T} \rangle^2$, to the total temperature variance, $\langle \widetilde{T'^2} \rangle = \langle \widetilde{T^2} \rangle - \langle \tilde{T} \rangle^2$, is considered to assess the quality of the present LES, where the term $\widetilde{T^2}$ is computed by integrating T^2 with FDF, then compiled into the look-up library. Figure 6.20 shows radial profiles of this ratio at different heights above the burner covering the flaming region. It can be observed that more than 80% of temperature variance is on the whole resolved by the present LES.

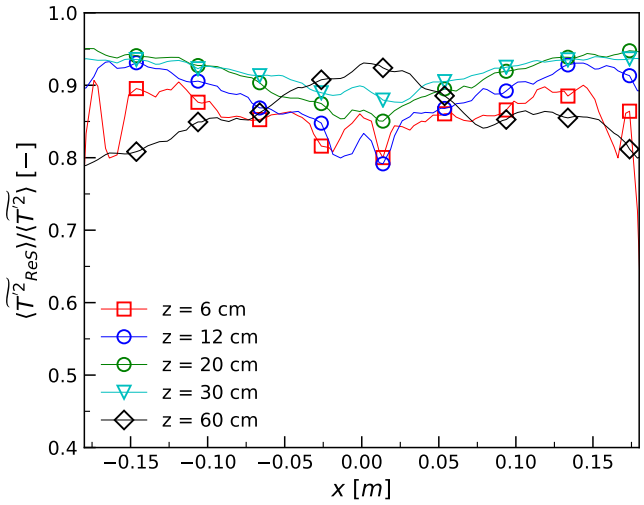

Figure 6.20: Radial evolution of resolved part of temperature variance at different heights.

6.2.3 Comparison with available experimental data

Model predictions for the baseline case are compared to the available experimental data.

The predicted puffing frequency of 2.37 Hz was estimated from a Fast Fourier Transform of the time series of the axial velocity along the axis at $z = 0.2$

m. This location was selected because the corresponding experimental PSD was found to exhibit a distinct puffing frequency (Weckman and Strong, 1996). This computed puffing frequency underestimates the experimental one of 2.80 Hz by about 18%.

Figure 6.21 shows the mean temperature as a function of the normalized height, ($z^* = z/\dot{Q}^{2/5}$), defined by McCaffrey (1979). Experimental data shows that the axial temperature increases with z^* up to $z^* \approx 0.02\ m \cdot kW^{-2/5}$, reaches a plateau of about 1300 K between $z^* \approx 0.02\ m \cdot kW^{-2/5}$ and $z^* \approx 0.04\ m \cdot kW^{-2/5}$, and decreases as z^* is further increased. The model reproduces well the temperature peak as well as the experimental profile for $z^* \geq 0.03\ m \cdot kW^{-2/5}$. For lower z^*, the axial temperature is underpredicted although it is in overall within the measurement uncertainty of Hamins and Lock (2016).

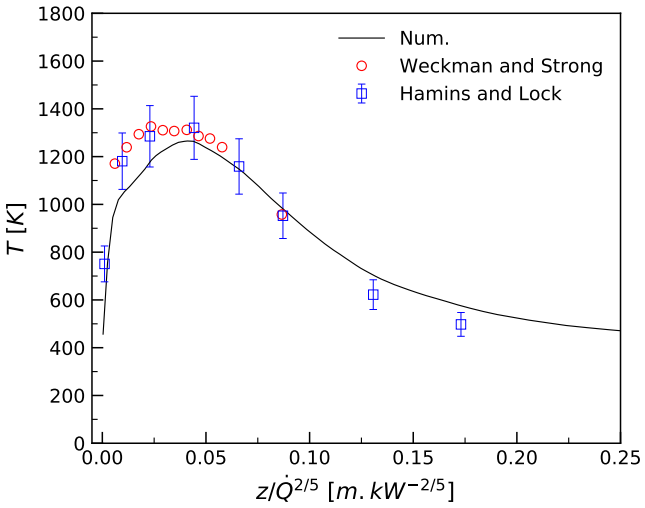

Figure 6.21: Axial profile of mean temperature. The experimental data are taken from Refs. (Weckman and Strong, 1996; Hamins and Lock, 2016).

Figures 6.22 to 6.27 display the radial profiles of mean and rms temperature, axial velocity and radial velocity at different heights. Model predictions present an overall good agreement with the experimental data. In particular, the simulations capture well the radial spreading of the fire plume. The profiles of mean temperature are on the whole well reproduced by the model at all the heights (see Fig. 6.22). However, in the lower part of the fire plume ($z \leq 10\ cm$), the predicted mean temperature exhibits M-shaped profiles that are not observed experimentally (see Fig. 6.22). This results in an underestimation of the

centreline temperature in this region as discussed previously. Measurements of temperature by 50 μm thermocouples may lead to a significant underestimation of temperature fluctuations despite the use of compensation technique (Crauford et al., 1985; Weckman and Strong, 1996; Weckman and Sobiesiak, 1987). Consequently, the overprediction of the temperature fluctuations by the model observed in Fig. 6.23 is not surprising. However, Fig. 6.23 shows that the predicted temperature fluctuations follow the same trends as the experiments.

Figures 6.24 and 6.25 show that the radial profiles of mean axial velocity and rms values of axial velocity fluctuations exhibit an overall good agreement with the experimental data. However, close to the pool surface ($z = 2$ and $z = 4$ cm), the predicted axial velocity exhibits a M-shaped profile that is not observed experimentally and overestimates the measurements along the flame wings (see Fig. 6.24). On the other hand, axial velocity fluctuations are slightly overpredicted for $z > 14$ cm (see Fig. 6.25).

Figures 6.26 and 6.27 show that the comparison is less satisfactory for radial velocity statistics than for axial velocity statistics. A careful examination of Fig. 6.26 shows that the experimental profiles of mean radial velocity are not symmetric with respect to the fire plume axis and that the values at the centreline are not equal to zero. This asymmetry, although less pronounced, is also observed for the radial velocity fluctuation at some heights (see Fig. 6.27) and reflects the difficulty to make accurate measurements of radial velocity, especially at vicinity to the flame axis. Figure 6.26 shows a reasonable agreement with measurements in the wings of the profiles for $z > 8$ cm despite an overall 10% underprediction. For $z \leq 8$ cm, larger discrepancies are observed. At these heights, the experimental maximum value (in absolute), observed at about $x = 10$ cm, is significantly underestimated and its predicted location is shifted away from the plume axis as compared to the measurements. Concerning the radial profiles of rms radial velocity, a good accordance between simulations and measurements is observed at the tails of the profiles (see Fig. 6.27). Nevertheless, the computed fluctuations exhibit well pronounced M-shaped profiles whereas the measured ones are flatter, which results in an underestimation of the fluctuations of radial velocity close to the centreline.

Figure 6.28 shows the axial profiles of the molar fractions of CH_3OH, O_2, CO_2, H_2O, CO and H_2. The model reproduces quantitatively the experimental data

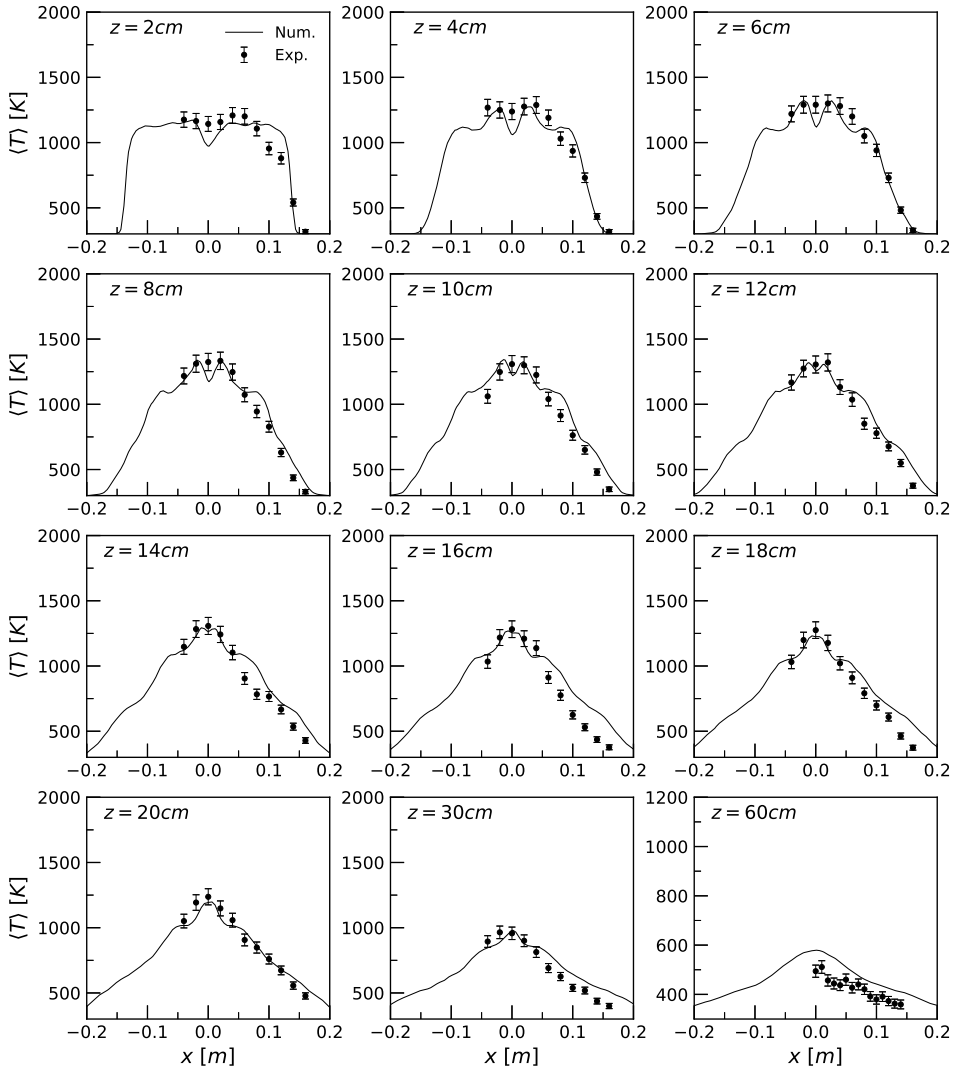

Figure 6.22: Radial profiles of mean temperature at different heights. The experimental data are taken from Ref. (Weckman and Strong, 1996), except the radial profile at $z = 0.6\ m$ that is taken from Ref. (Hamins and Lock, 2016).

for CH_3OH, O_2, CO_2, CO and H_2. The rapid decrease in the mole fraction of CH_3OH as well as the depletion of O_2 in the flaming zone are well predicted. The profiles of mole fractions of CO, CO_2, and H_2 are also in good agreement with the experiments although the peak of CO mole fraction is overestimated. Finally, the model underestimates significantly the H_2O molar fraction over the entire fire plume axis. Surprisingly, such large discrepancies are only observed for H_2O whereas, as discussed previously, a rather good agreement is observed for the other species. An examination of the error bars reported by Hamins

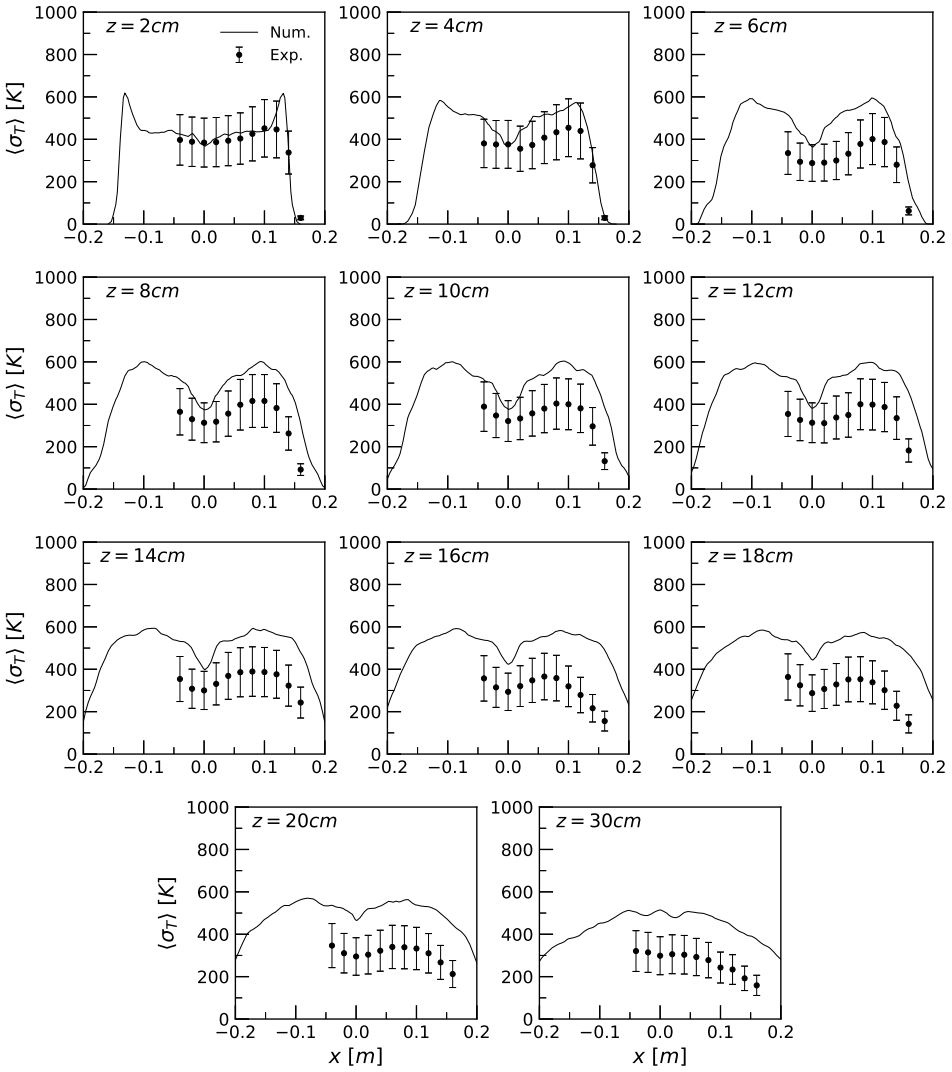

Figure 6.23: Radial profiles of rms value of temperature at different heights. The experimental data are taken from Ref. (Weckman and Strong, 1996).

and Lock (2016) (see Fig. 6.28) shows that the experimental uncertainties associated to the measurements of H_2O are significantly higher than for the other species. This can explain, at least partially, these large discrepancies.

The radiant fraction is computed by integrating the time-averaged divergence of the radiative flux over the computational domain, $\chi_R = \int \nabla \cdot \dot{q}''_R dV/\dot{Q}$. The predicted radiant fraction is 0.261 and overestimates the measured one of 0.24 $\pm$ 25% by about 8.75%. Figure 6.29a shows the vertical distribution of radiative flux at a distance of 0.6 m from the fire plume axis. The distribution exhibits ray effects when computed with the 16 $\times$ 24 angular mesh. A frozen field radiative calculation was performed with a finer angular mesh with 48

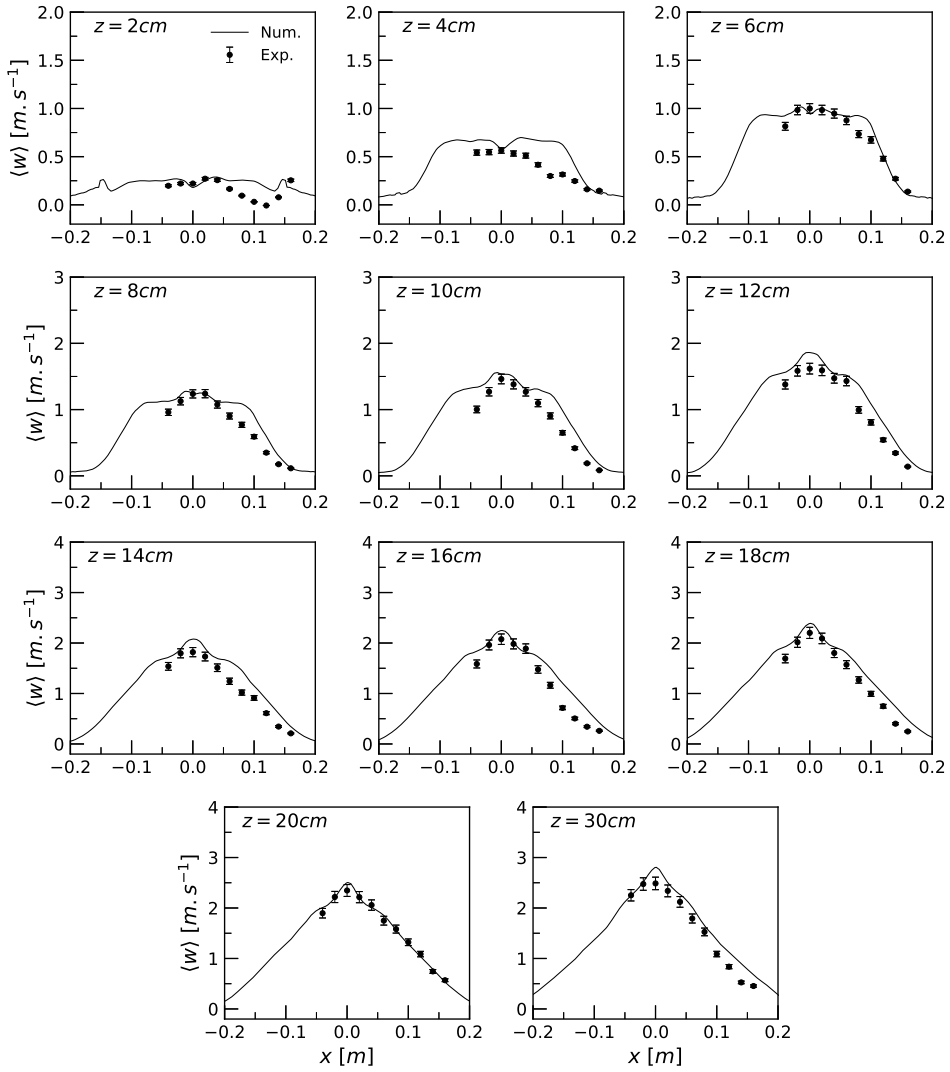

Figure 6.24: Radial profiles of mean axial velocity at different heights. The experimental data are taken from Ref. (Weckman and Strong, 1996).

$\times$ 96 control angles in order to improve this behaviour and the corresponding prediction is plotted in Fig. 6.29a.

In this calculation, instantaneous fields of absorption coefficient and emission term, computed with the 16 $\times$ 24 angular mesh, are saved during the statistically stationary state. These fields are used to solve the instantaneous RTE with the finer angular mesh and, subsequently compute the time-averaged radiative outputs. This approach is justified by the fact that the finer mesh was found to have no influence on the prediction of the radiative heat transfer inside the flame and to change only the radiative flux outside the flame. These observations are in line with those reported by Jensen et al. (2007) who

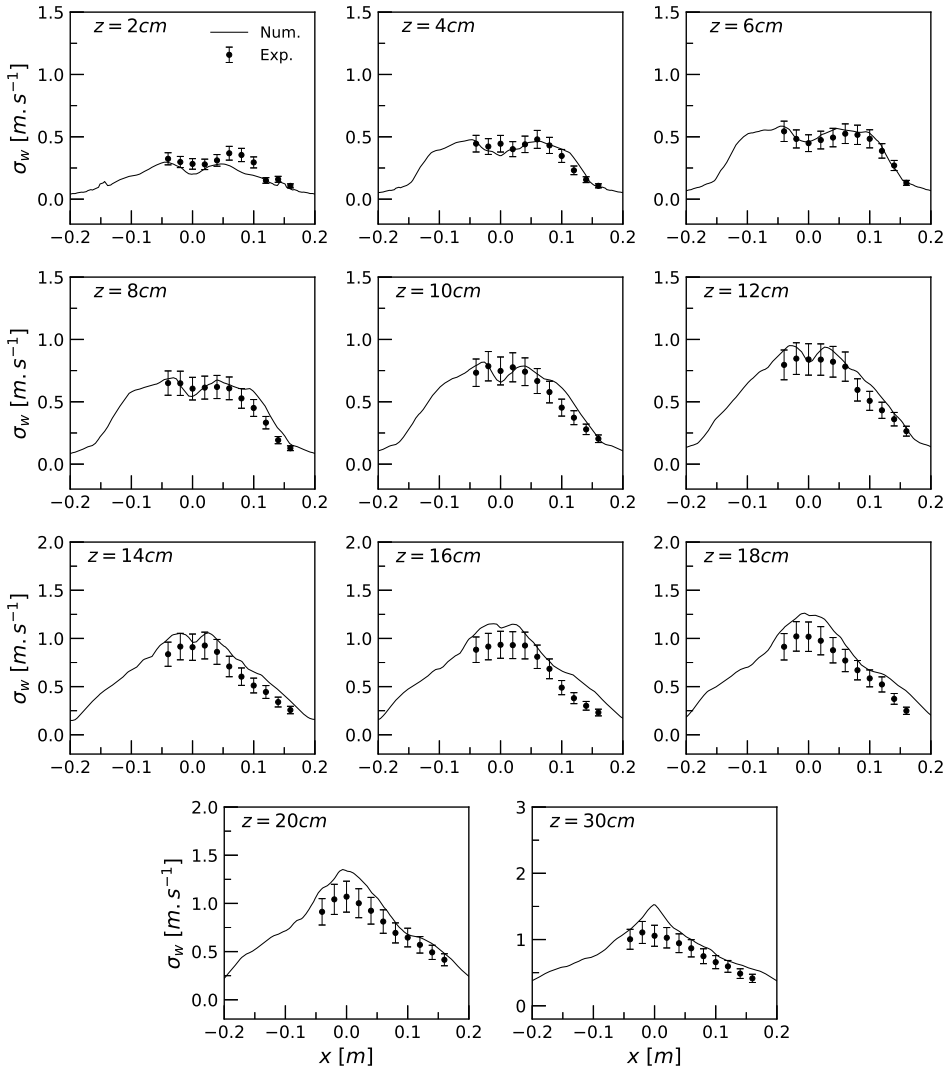

Figure 6.25: Radial profiles of rms value of axial velocity at different heights. The experimental data are taken from Ref. (Weckman and Strong, 1996).

showed that radiative outputs within the flame, where radiation is isotropic, can be accurately computed with a coarse angular discretization whereas a finer one is required to avoid ray effects on radiative flux outside the flame. Figure 6.29a shows that the model overestimates the radiative flux, especially for $0 \leq z \leq 0.5\ m$. A better agreement is observed downstream.

Figure 6.29(b) shows the radial distribution outside the burner along the plane of the burner rim. Predictions, obtained with the 16×24 angular mesh, are in overall good agreement with the experimental data. Nevertheless, the model overpredicts the radiative flux at vicinity of the burner. Figure 6.29(c) shows both radiative and total heat feedback towards the fuel surface. The reported

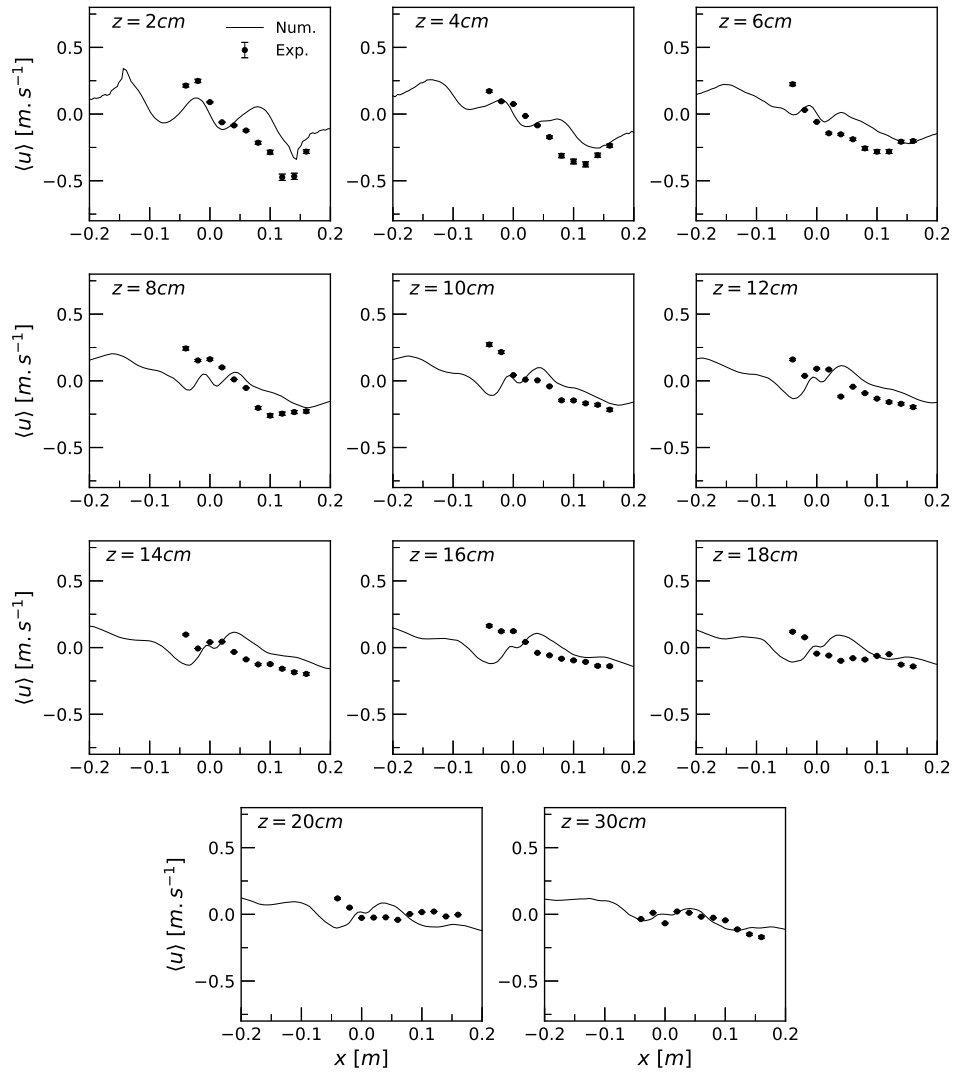

Figure 6.26: Radial profiles of mean radial velocity at different heights. The experimental data are taken from Ref. (Weckman and Strong, 1996).

fluxes were also computed with the 16×24 angular mesh. As discussed by Hamins et al. (1994), the experimental radiative feedback decreases continuously from the centre towards the edge. This continuous decrease is also observed for the simulations although it is less pronounced. In addition, the model overestimates the experimental data. The model ignores the radiative contribution of the methanol whose the importance for estimating the radiative feedback is recognized (Wakatsuki et al., 2007). This can explain at least partially the discrepancies between the model and the experiments. Another source of discrepancies may be attributed to the difference in fuel lip heights between the simulations and the experiments. The simulations considered a

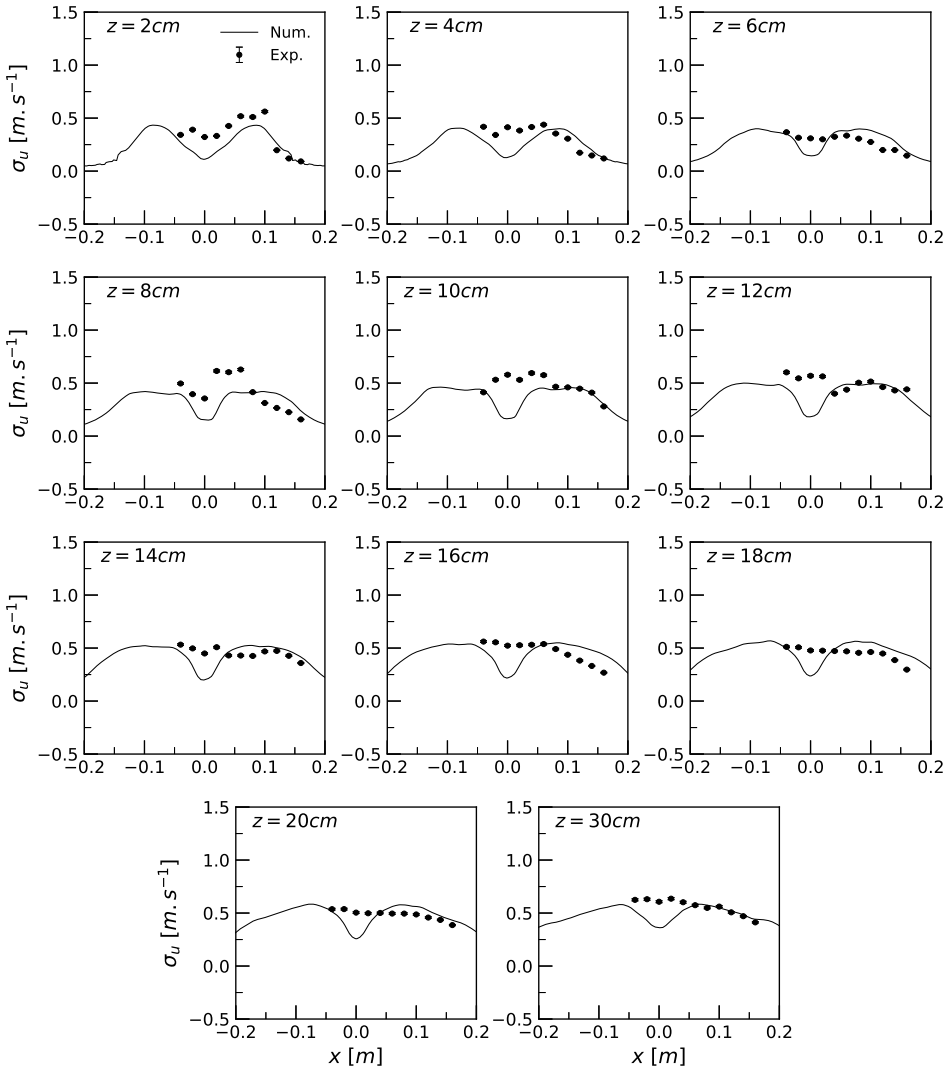

Figure 6.27: Radial profiles of rms value of radial velocity at different heights. The experimental data are taken from Ref. (Weckman and Strong, 1996).

fuel lip height of 1 cm whereas that reported by Hamins et al. (1994) was 0.5 cm. Figure 6.29(c) compares the predicted total heat feedback at the fuel surface with that measured by Kim et al. (2019). The experimental heat flux is approximately constant for $x < 6$ cm with a value around 26 $kW \cdot m^{-2}$ and, then, decreases with distance towards the pool edge to reach 16 $kW \cdot m^{-2}$ at $x = 13$ cm. As the distance towards the pool edge is further increased, a very sharp decrease of the total heat flux is observed to reach 3.7 $kW \cdot m^{-2}$ at $x = 14.5$ cm. The model reproduces correctly this behaviour. Nevertheless, the computed total heat flux underestimates in overall the measurements with a maximum deviation of about 20% at $x = 10$ cm.

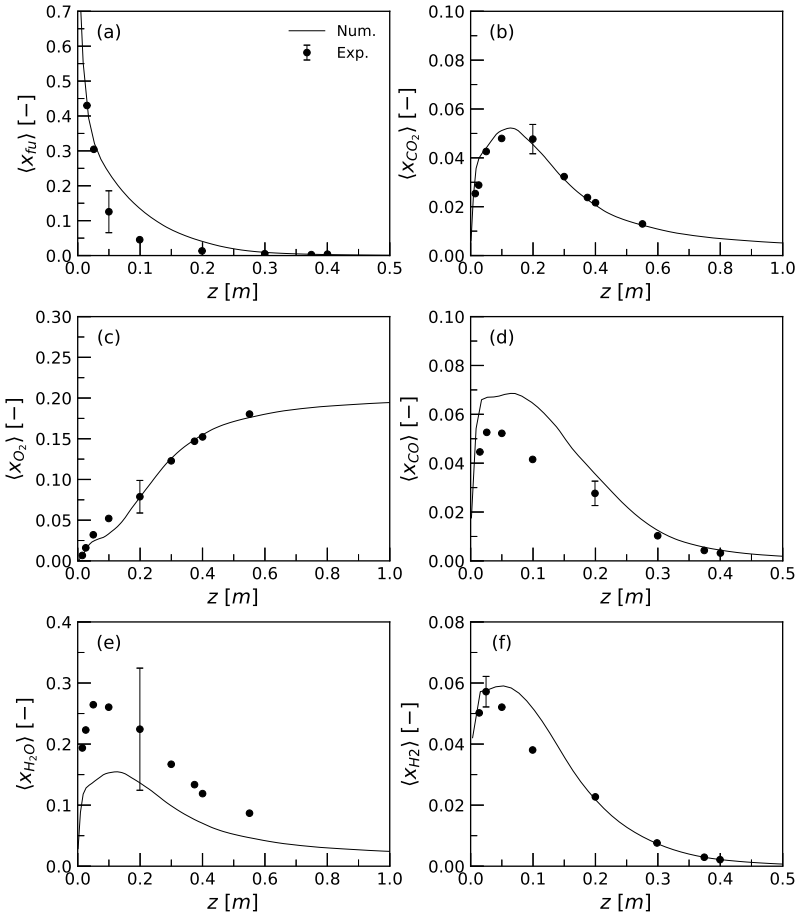

Figure 6.28: Axial profiles of mean molar fractions for: (a) methanol, (b) carbon dioxide, (c) oxygen, (d) carbon monoxide, (e) water vapor and (f) hydrogen. The experimental data are taken from Ref. (Hamins and Lock, 2016).

6.2.4 Pool boundary condition effects

This section analyses the differences induced by the different burner boundary conditions on the fire plume structure. These differences can be attributed to effects on the formation and growth of the flame base non-dissipative laminar instability near the edge of the pool that develops periodically to form energy containing large-scale toroidal vortices (Tieszen and Gritzo, 2008). These vortices govern the flow pattern, the air entrainment as well as the mixing and combustion processes (Cetegen and Ahmed, 1993; Cetegen, 1998; Hu et al., 2015). Once generated near the edge of the source due to baroclinic and gravitational torques, these vortices convect upward and act like a pump, inducing the necking-in behaviour at the base of the flame beneath them where air is

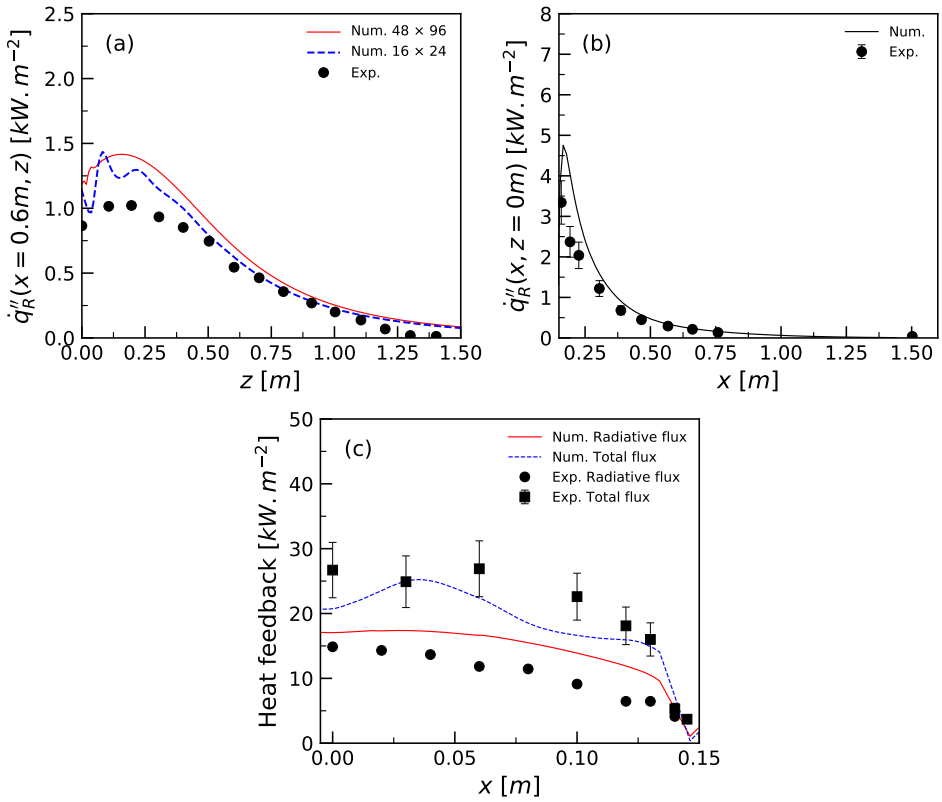

Figure 6.29: Heat fluxes: (a) Vertical distribution of radiative flux at a distance $x = 0.6\ m$ from the pool axis, (b) radial distribution of the radiative heat flux in the downward direction outside the burner, and (c) radiative heat feedback towards the fuel surface and total heat feedback measured at 13 mm elevation above the fuel surface. The experimental data are taken from Ref. (Kim et al., 2019), except those for the radiative feedback that are taken from Ref. (Hamins et al., 1994).

engulfed. Figures 6.30, 6.31, and 6.32 show sequences of snapshots of temperature in the centreline (x-z) plane for the baseline case, the NoLip case and the NoLipNoEnt case, respectively. On each figure, the time step between two snapshots is 0.06 s. In these figures, the arrows indicate the directions of the density gradients, $\nabla\rho$, the pressure gradient, ∇p, and the gravity, $\boldsymbol{g}$. These snapshots are supplemented by, on the one hand, time-averaged axial and radial profiles at different heights of mean temperature and axial velocity (see Fig. 6.33) and, on the other hand, radial distributions of rms values of temperature and axial velocity (see Fig. 6.34).

Let us start to describe the sequence for the baseline case (see Fig. 6.30).

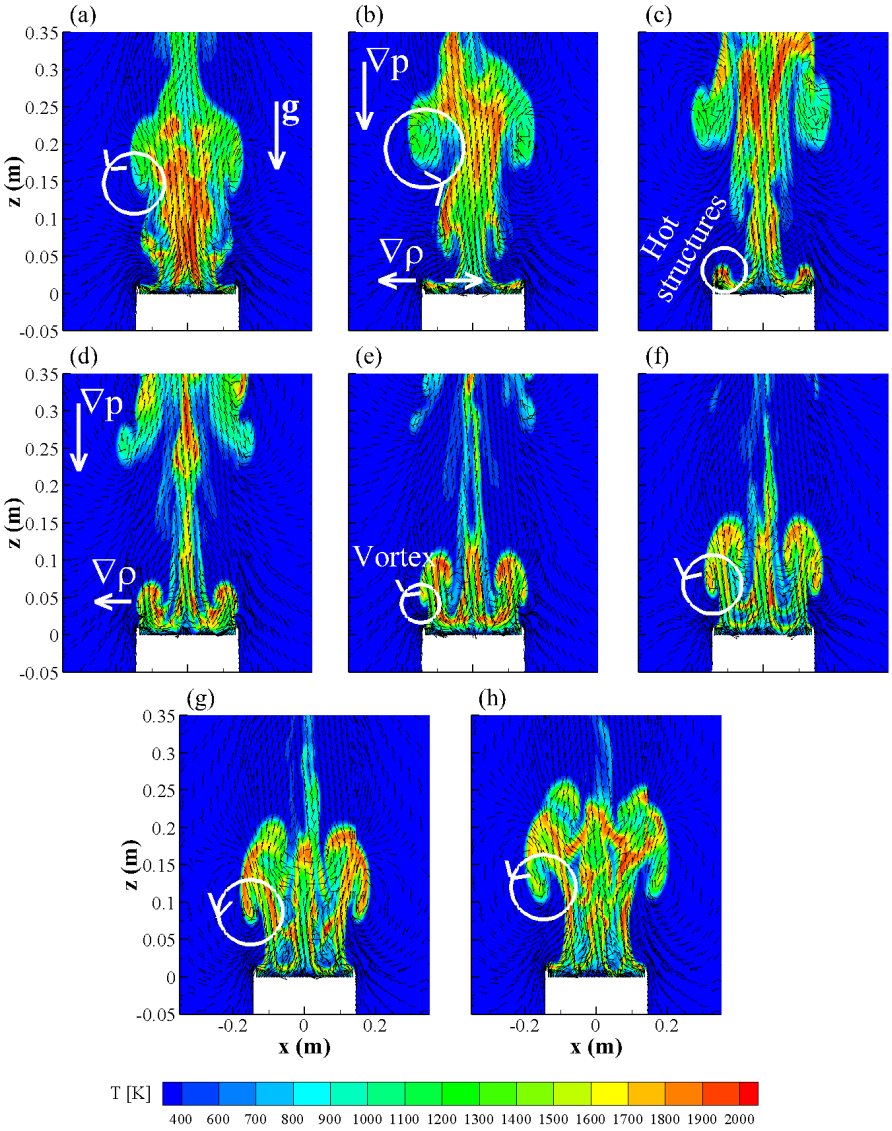

Figure 6.30: Snapshots of temperature at different times for the baseline case. The time between two snapshots is 0.06 s. Uniform velocity vectors are plotted to illustrate the flow pattern.

Figure 6.30(a) shows a coherent structure in the middle of the image. On the other hand, the flame is anchored on the top of the burner rim in accordance with the experimental observations made by Weckman and Sobiesiak (1988). The air entrained at the pool basis bypasses the rim and leads to a wrinkling of the flame sheet. This wrinkled flame sheet is subjected to a Rayleigh-Taylor instability as illustrated in Fig. 6.30(b). This results in the formation of a raising hot "bubble" structure whereas the air flows towards the fuel surface as evidenced in Fig. 6.30(c). The growth of the hot structure results in an-

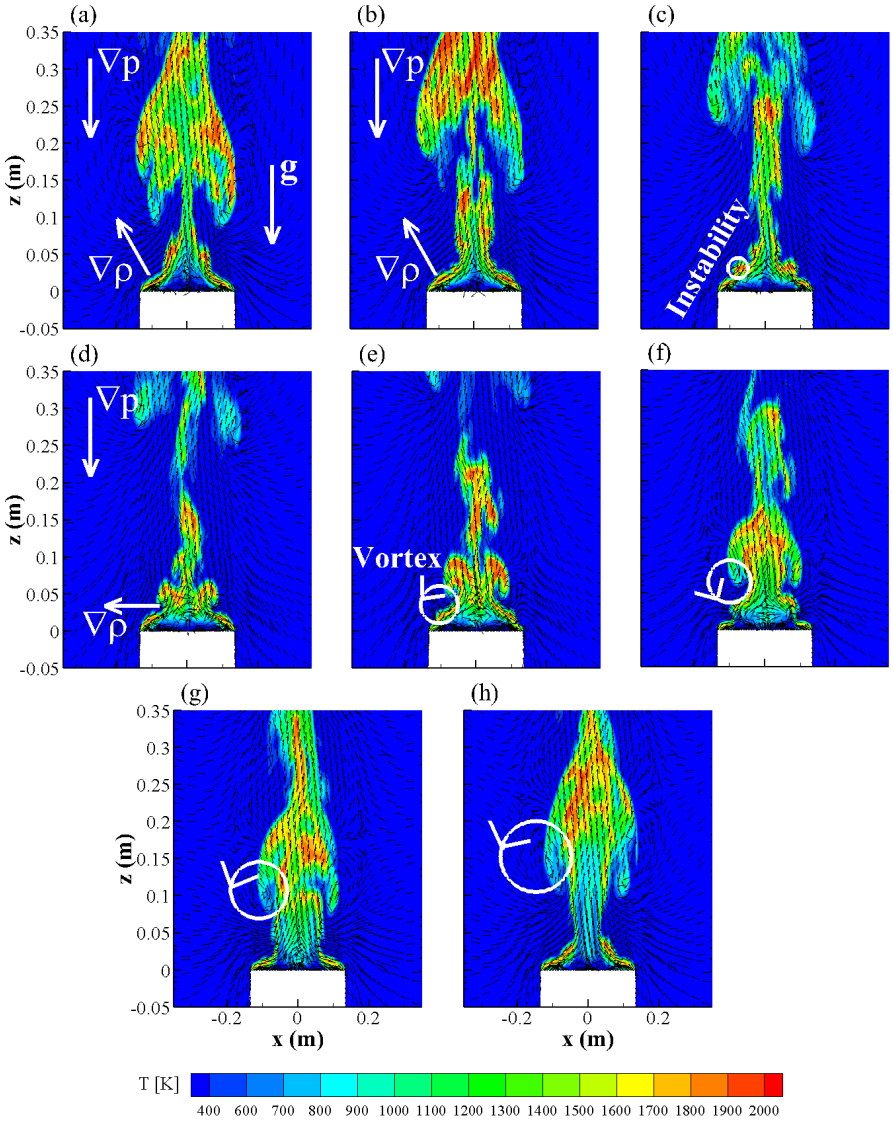

Figure 6.31: Snapshots of temperature at different times for the NoLip case. The time between two snapshots is 0.06 s. Uniform velocity vectors are plotted to illustrate the flow pattern.

other unstable configuration (see Fig. 6.30(d)), which produces buoyant and baroclinic vorticity generation. In Fig. 6.30(e), the resulting vortex sheet begins to roll up into what will become the next coherent turbulent structure. The growth of this coherent structure and the characteristic necking behaviour beneath it are illustrated in Fig. 6.30(f) to (h). Figure 6.31 shows a similar sequence for the NoLip configuration. The flame is anchored to the burner edge (see Fig. 6.31(a)). Contrary to the baseline configuration, no wrinkling of the flame sheet is observed near the edge of the pan and the misalignment between,

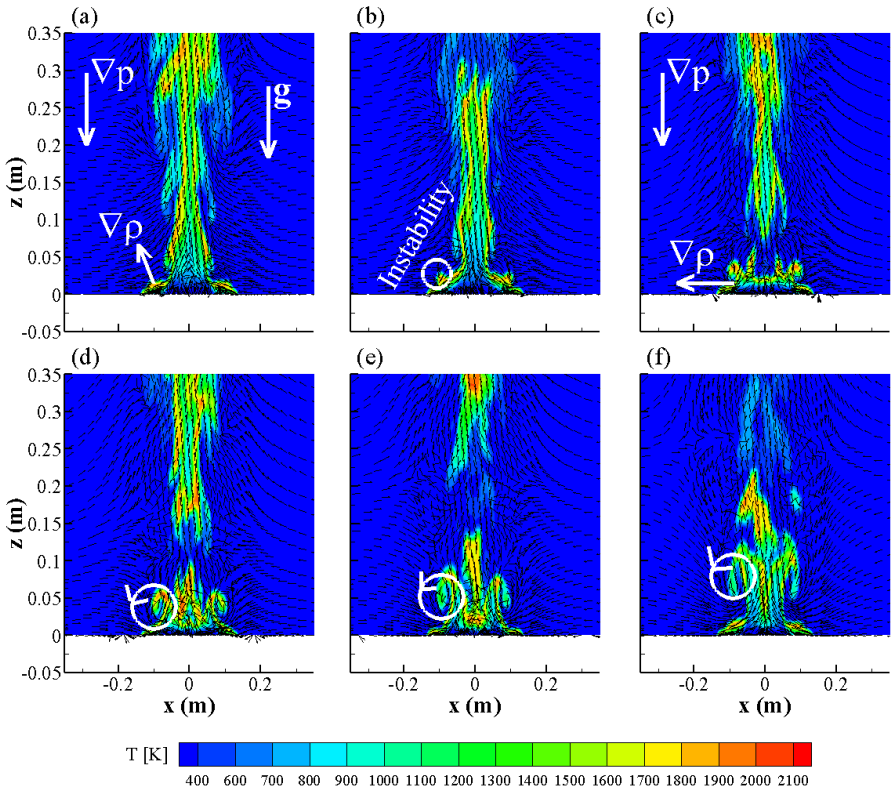

Figure 6.32: Snapshots of temperature at different times for the NoLipNoEnt case. The time between two snapshots is 0.06 *s*. Uniform velocity vectors are plotted to illustrate the flow pattern.

on the one-hand, the density gradient and, on the other hand, gravity and pressure gradient, although still presents, is lower than for the baseline case (see Figs. 6.31(a) and (b)). As a result, the formation of the hot "bubble" structure as described for the baseline case is not observed although Fig. 6.31(c) shows the appearance of smaller instabilities. As for the baseline case, the growth of this instability results in an unstable configuration (see Fig. 6.31(d)) and in the generation of a vortex that develops as it convects upward (see Figs. 6.31(e) to (h)).

This comparison illustrates the significant effects of the fuel lip height on the formation of instabilities. The inclusion of the fuel lip height modifies considerably the flow pattern due to the formation of hot "bubble" structures stemming from the interactions between the air entrainment at the pool basis, the burner rim and the flame sheet. These hot structures contribute to enhance significantly the mixing at vicinity of the burner as illustrated by the much wider

fire plume (see Figs. 6.33 and 6.34) and the higher temperature and velocity fluctuations (see Figs. 6.34) observed when the fuel lip height is considered. In addition, Figs. 6.33b-d and f-h show that the fire plume close to the burner is hotter and rises at a higher velocity in presence of the fuel lip height. As described by Orloff (1981) and Orloff and De Ris (1982) from their experiments, this enhanced mixing results in a shorter flame, as illustrated in Fig. 6.33(a) and (e) by the lower temperature and axial velocity observed along the axis in the intermittent flame region and in the inert plume ($z^* > 0.05\ m \cdot kW^{-2/5}$). On the other hand, considering or not the fuel lip height has weak effect on the puffing frequency that is 2.27 Hz for the NoLip case instead of 2.37 Hz for the baseline case.

Comparing Figs. 6.31 and 6.32 shows that modifying the air entrainment at the base of the pool changes the flow pattern. In the case where the pool is located one-pool diameter above the floor (NoLip), the air entrained at the edge of the pan comes from both the sides and the bottom (see Fig. 6.31(a)) whereas, in the NoLipNoEnt case, the floor prevents the part coming from the bottom and air entrainment comes only from the sides (see Fig. 6.32(a)). This stronger lateral air entrainment in the NoLipNoEnt case has two effects. First, it pushes the flame sheet anchored to the pan edge towards the liquid surface and, as a result, reduces the misalignment between density gradient and both gravity and pressure gradient as compared to the NoLip case (see Figs. 6.31(a) and 6.32(a)). This reduces both gravitational and baroclinic torques and, in turn, the strength of the first instability. This is illustrated by comparing Figs. 6.31(c) and 6.32(b). Second, the coherent vortices, generated from the second instability, are significantly smaller than in the NoLip case as observed by comparing Fig. 6.31(e) to (h) with Figs. 6.32(e) and (f). As a consequence, the pumping capacity is lower in the NoLipNoEnt case which accelerates the formation of a new vortex (Hu et al., 2015), leading to a flame puffing frequency of 2.97 Hz higher than that of 2.27 Hz observed for the NoLip case. Such increase in the puffing frequency as the air entrainment at the flame base is altered can be also observed in the PSD reported by Weckman and Sobiesiak (1987) from their experiments in 30 cm acetone pool fires. The fact that air is entrained preferentially from the sides explains also why the fire plume is narrower in the NoLipNoEnt case (see Figs. 6.33 and 6.34). On the other hand, the axial profiles of temperature and velocity are not notably

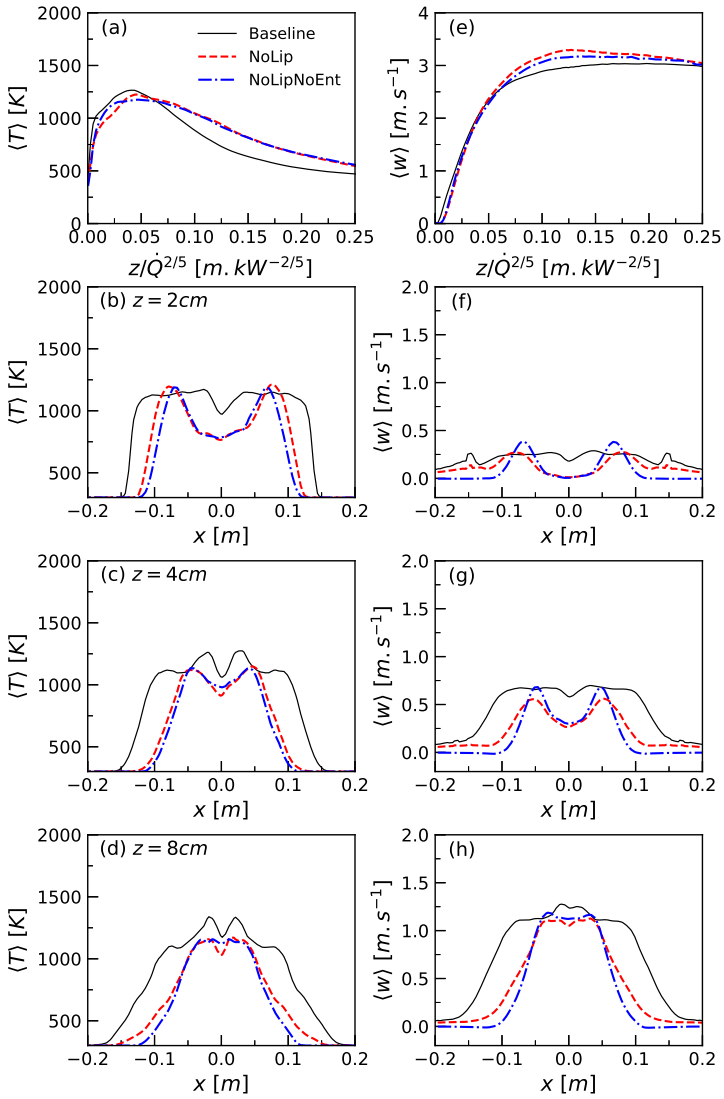

Figure 6.33: Effects of pool boundary conditions on axial and radial profiles at different heights: (a)-(d) rms of temperature and (e)-(h) axial velocity.

affected, despite that the axial temperature profile is steeper in the continuous flame region for the NoLip case (see Figs. 6.33).

Figure 6.35 shows the influence of the fuel boundary conditions on both radiative and total heat feedback towards the fuel surface. Before started the discussion, it should be reminded that these predictions have been obtained by considering the fuel burning per unit area unchanged for the different boundary conditions. This figure shows that the heat feedback for the NoLip and the NoLipNoEnt cases are very similar. This is not surprising since these two boundary conditions lead to similar thermal and flow fields (see Figs. 6.33 and

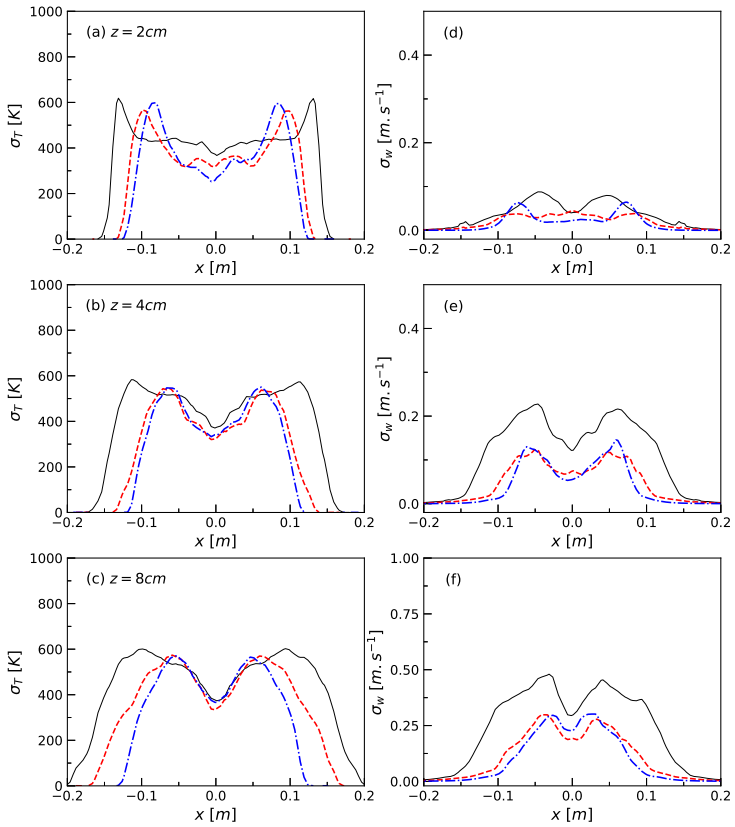

Figure 6.34: Effects of pool boundary conditions on radial profiles at different heights: (a)-(d) rms of temperature and (e)-(h) axial velocity.

6.34). On an opposite way, the inclusion of the fuel Lip height in the simulations (baseline case) induces significant modifications in both radiative and total fluxes. As discussed by Babrauskas (1983), the presence of the fuel lip height produces a more emissive flame volume, resulting in a higher radiative flux (see Fig. 6.35(a)). This increase in flame emissivity can be explained by the enhanced mixing process produced by the fuel lip height that leads, as discussed previously, to a wider, hotter, and more turbulent fire at vicinity of the fuel surface (see Figs. 6.33 and 6.34). Figure 6.35(b) shows that, for the same reasons, the total heat flux for $z < 10\ cm$ is higher for the baseline case. Close to the burner rim, the total heat fluxes predicted for the NoLip and NoLipNoEnt cases increases sharply owing to an increase in the convective flux. This increase in convection results from the higher proximity between the flame sheet and the fuel surface at the edge of the burner in these configurations. This is not observed for the baseline case where the flame sheet is anchored at the top of the burner rim, leading to lower temperature at vicinity

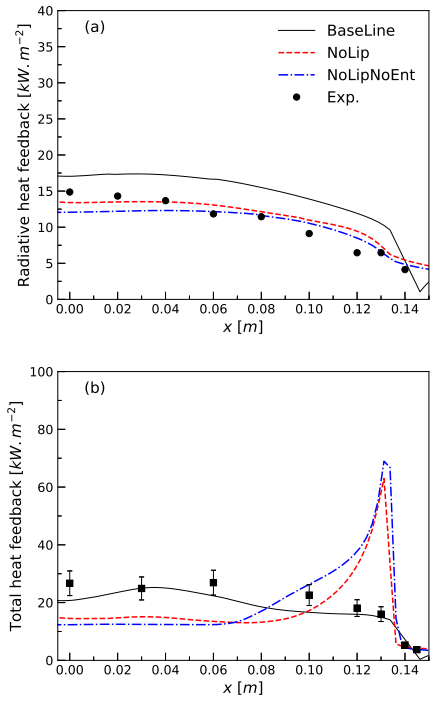

Figure 6.35: Effects of pool boundary conditions on heat feedback to the pool surface: (a) radiative flux measured at the fuel surface and (b) total flux at 13 mm elevation above the fuel surface. The experimental data for radiative and total heat fluxes are taken from Refs. (Hamins et al., 1994) and (Kim et al., 2019), respectively.

of the fuel surface. This increasing importance of convection close to the edge of the pool in absence of fuel lip height is supported by the experimental results of Hamins et al. (1994) who observed a similar trend as the fuel lip height was reduced from 0.5 cm to 0.1 cm.

6.2.5 Conclusions

The following conclusions can be drawn:

1. An exhaustive comparison with experiments was carried out in terms of puffing frequency, mean and rms temperature and velocities, mean molar fractions of major species and radiative loss to the surrounding. Numerical simulations were found to reproduce the experimental data with fidelity without introducing any adjustable constant.

2. Considering a non-zero lip height alters substantially the flow structure

and results in significantly wider fire plumes and shorter flames which affects both radiative and total heat feedback towards the fuel surface.

3. Considering that the burner rim is floor flush has a moderate influence on the fire pool structure as compared to the NoLip case but enhances significantly the puffing frequency owing to a reduction in the pumping capacity of the large-scale vortices.

4. These results show clearly that the experimental burner boundary conditions have to be reproduced scrupulously in the simulations for relevant validations of numerical models.

Chapter 7

Radiation in fire plumes

The modelling of radiative heat transfer (RHT) in turbulent flows adds a difficulty since it requires a precise solution of the RTE, a proper modelling of the spectral dependence of radiating species and a proper evaluation of the TRI.

In the first section, the effects of SGS TRI in LES of ethanol pool fires ranging from medium to large sizes are studied.

In the second section, the modelling capability of several radiative property models, including the RCFSK model (Solovjov et al., 2018), and grey and non-grey versions of the WSGG (Modest and Haworth, 2016) in 1 m methanol pool fire studied experimentally by Sung et al. (2020) is investigated. This fire plume will be also considered to investigate the effects of the angular discretization of the radiative transfer equation solver on radiative outputs.

7.1 Assessment of subgrid-scale turbulence-radiation interactions

7.1.1 Numerical resolution

Throughout this chapter, the Favre-filtered governing Eqs. 3.1 to 3.4 are solved by the proposed solver described in the Chapter 4. The second-order Crank-Nicolson scheme is used for time advancement. The Superbee-TVD scheme (Versteeg and Malalasekera, 2007) is applied for convection in the mixture fraction transport to limit numerical oscillation whereas a second-order CDS is

used for diffusion. For the momentum equation both convective and diffusive terms are discretized by using a second-order CDS. The subgrid contribution to the momentum stress and scalar flux is computed using DSM and DEDM models, respectively. The non-adiabatic SLF model is used to obtain the local thermochemical state relationship, ϕ^{slf}, as a function of the mixture fraction, Z, the scalar dissipation rate, χ, and the enthalpy defect, $X_R = h - h_{ad}$. The flamelet library was generated by solving the governing equations of counter-flow diffusion flames in the physical space at a series of specified strain rates using the CHEMKIN code (Lutz et al., 1996). Radiative loss was incorporated in the flamelet library by using the methodology described in the Chapter 2. The Favre-filtered thermochemical quantities are then obtained from the state relationships by convolution with the presumed FDF. The SGS mixture fraction variance required to retrieve solutions from the filtered flamelet look-up table is obtained by the STE model.

7.1.2 Experimental and computational details

The baseline configuration is the 0.5 m diameter ethanol pool fire investigated experimentally by Fischer et al. (1987). This pool fire is characterized by a heat release rate (HRR, $\dot{Q}$) of 72.5 kW. According to Fischer et al. (1987), the measured fire plume is over-ventilated. Consequently, the configuration was simplified by considering a $3 \times 3 \times 3$ m^3 domain with free boundary condition on the domain sides. It was checked that the dimension of the domain does not affect the flow and heat transfer. Consistently with the experiments, the fuel pan is located on a solid support at 1 m above the floor and surrounded by a steel collar with an outside diameter of 1.1 m and a burner rim height of 10 mm is considered. This latter point was found to play an important role on the pool dynamics. A structured mesh with 3.75×10^6 cells is considered. The mesh is refined with cell size of $5 \times 5 \times 5$ mm^3 in a box of $0.6 \times 0.6 \times 0.6$ m^3 located above the fuel pan. The cell size is progressively stretched towards the boundaries. The simulations relative to this flame will be referred to as F1D hereafter. The flamelet library was generated using the mechanism of ethanol oxidation developed by Saxena and Williams (2007). The radiation model combines the RCFSK model for spectral gas radiation and the DOM with a S8 quadrature scheme as radiative transfer equation (RTE) solver.

To analyse the effects of the flame optical thickness, two synthetic pool fires

are simulated by scaling up the pool diameter by 2 and 4 while maintaining the same fuel mass burning rate per unit area. A simple geometric scaling of the computational mesh is considered for all flames. The simulations relative to these flames are referred to as F2D and F4D, respectively. The flame configurations are summarized in Table 7.1. The fourth column provides the plume resolution index (PRI), defined as the ratio between the plume characteristic length scale, $D^* = \left(\dot{Q}/(\rho_\infty c_p T_\infty \sqrt{g})\right)^{2/5}$ and the grid size, Δ. ρ_∞, c_p, and T_∞ represent the density, heat capacity and temperature of ambient air, respectively, whereas g denotes the gravity. The PRI characterizes the quality of the resolution with higher values corresponding to a better resolution of the fire dynamics (Maragkos et al., 2017; Maragkos et al., 2019). The PRI reported in Table 7.1 are consistent with the highest resolution reported in the literature for similar simulations.

Flames	D (m)	HRR (kW)	D/Δ (-)	D^*/Δ (-)	$\dot{Q}_{emi}/\dot{Q}$ (-)	$\dot{Q}_{abs}/\dot{Q}_{emi}$ (-)
F1D	0.50	72.8	100	66.8	0.47	0.57
F2D	1.00	291.2	100	58.0	0.62	0.65
F4D	2.00	1164.8	100	50.0	0.82	0.70

Table 7.1: Flame configurations. χ_{emi} and $\dot{Q}_{abs}/\dot{Q}_{emi}$ are computed with the Full TRI model.

Concerning the boundary conditions, typical outflow and entrainment boundary conditions are used for open boundaries at the outlet and sides, respectively. The evaporation process of ethanol is disregarded and the pool surface is treated as a gaseous fuel inlet boundary condition. The fuel mass burning rate is maintained constant to provide the specified HRR and both convective and diffusive mass and energy fluxes are accounted for. This simplified treatment does not consider the TRI effects on the radiative feedback to the pool surface that could affect the evaporation rate and, in turn, combustion and radiation processes, including TRI.

Throughout all simulations, time step is set to 5×10^{-4} s, and simulations run for 30 s. The time-averaged mean and rms values were collected at each time step from 6 s. The first 6 s of simulation were used to establish a statistically stationary flow.

7.1.3 Analysis of TRI

TRI represents the contributions of the turbulent fluctuations to the mean absorption and emission terms. In the following, $\langle\phi\rangle$ and $\phi^{'}$ will denote the time-averaged value and the fluctuation of ϕ, respectively. In LES, the contribution of turbulent fluctuations in temperature and mole fractions of the radiating species to TRI is decomposed into resolved-scale fluctuations, ReS TRI, and subgrid-scale fluctuations, SGS TRI. These latter requires modelling. Different closures for the filtered absorption and emission terms were investigated in order to quantify the effects of ReS TRI and SGS TRI on the radiative loss and are summarized in Table 7.2. The filtered absorption and emission terms were evaluated from: i) $\langle\tilde{T}\rangle$, $\langle\tilde{x}_{CO_2}\rangle$ and $\langle\tilde{x}_{H_2O}\rangle$ by ignoring all the fluctuations (No TRI), ii) $\tilde{T}$, $\tilde{x}_{CO_2}$ and $\tilde{x}_{H_2O}$ by considering only the resolved fluctuations (ReS TRI) and then ignoring the SGS TRI, and iii) Eqs 3.52 and 3.53 based on presumed FDF that allows taking into account both ReS and SGS fluctuations (Full TRI). $\overline{\kappa_i^*}$ and $\overline{\kappa_i^* a_i I_b}$ are included in the 4D look-up table parametrized by $\tilde{Z}$, V_Z, $\tilde{\chi}$ and $\tilde{X}_R$. Consequently, the increase in CPU time is marginal as compared to the ReS TRI case.

Radiation is solved in coupled manner for both ReS TRI and Full TRI cases and in decoupled manner for the No TRI case by using $\langle\tilde{T}\rangle$, $\langle\tilde{x}_{CO_2}\rangle$ and $\langle\tilde{x}_{H_2O}\rangle$ obtained from the Full TRI simulations.

case	Absorption	Emission
No TRI	$\kappa_i^*(\langle\tilde{\phi}\rangle)\langle\tilde{G}\rangle$	$\kappa_i^*(\langle\tilde{\phi}\rangle)a_i(\langle\tilde{\phi}\rangle,\langle\tilde{T}\rangle)I_b(\langle\tilde{T}\rangle)$
ReS TRI	$\kappa_i^*(\tilde{\phi})\tilde{G}$	$\kappa_i^*(\tilde{\phi})a_i(\tilde{\phi},\tilde{T})I_b(\tilde{T})$
Full TRI	$\overline{\kappa_i^* G}$	$\overline{\kappa_i^* a_i I_b}$

Table 7.2: Different TRI closures for filtered absorption and emission terms.

7.1.4 Comparison with available experimental data

This section presents the comparison between LES and the experimental data of Fischer et al. (1987). Figures 7.1 and 7.2 show that a satisfactory agreement is observed for the radial profiles of mean temperature and mole fractions of CO_2, H_2O and CO. Figure 7.3 displays radial profiles of temperature fluctuations. This figure shows that model predictions follow the same trends as the experiments. Fischer et al. (1987) measured temperatures with 75 μm

thermocouples with bead diameters of 100 μm, which can lead to a significant underestimation of temperature fluctuations despite the use of compensation technique for thermal inertia (Crauford et al., 1985). Consequently, the overall overestimation observed in Fig. 7.3 is not surprising.

The predicted puffing frequency of 1.67 Hz compares also reasonably well with the measured one of 1.96 Hz (Fischer et al., 1987).

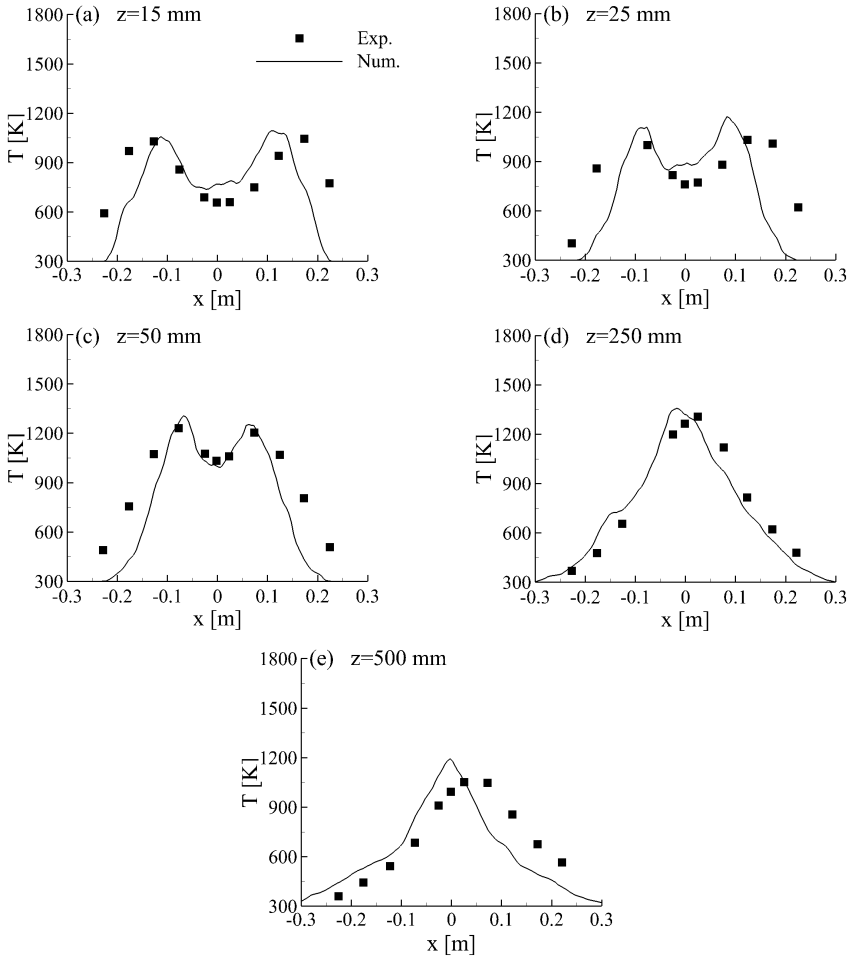

Figure 7.1: Radial profiles of temperature at different heights above the pool basis.

7.1.5 Quality of LES

Figure 7.4 quantifies the turbulent intensity, defined as $\sqrt{\langle \widetilde{T'^2} \rangle}/\langle \tilde{T} \rangle$, as a function of the normalized height. In this figure the horizontal dashed line indicates the level 0.8 whereas the vertical dashed lines delimit the continuous flame (CF)

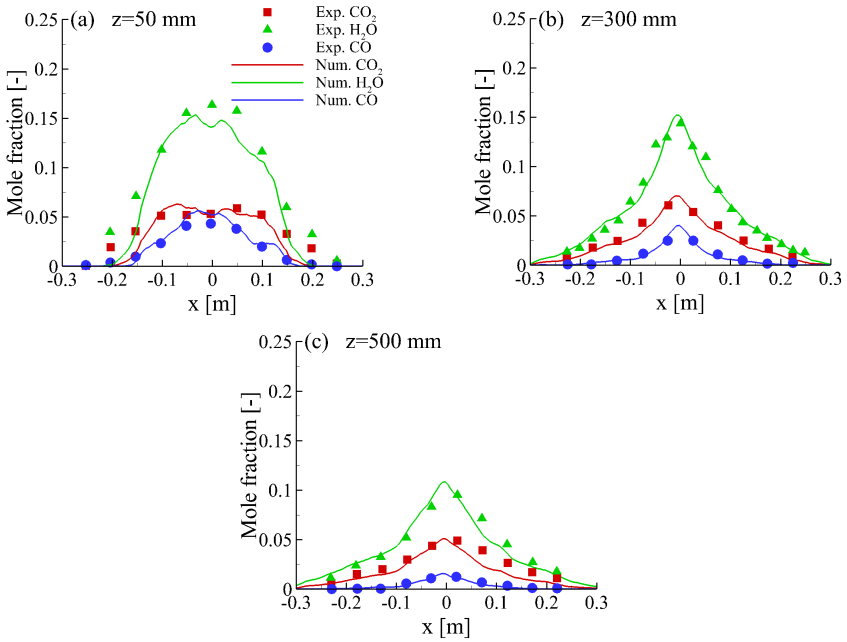

Figure 7.2: Radial profiles of mole fractions of CO, CO_2 and H_2O at different heights above the pool basis.

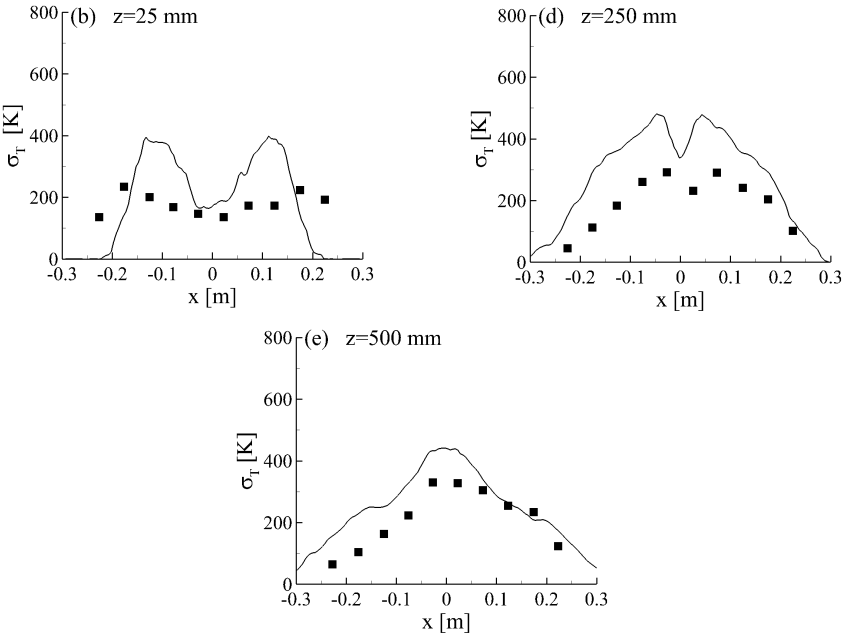

Figure 7.3: Radial profiles of temperature fluctuations at different heights above the pool basis.

and intermittent flame (IF) regions. The total temperature variance is computed as $\langle \widetilde{T''^2} \rangle = \langle \widetilde{T^2} \rangle - \langle \tilde{T} \rangle^2$. The turbulent intensity reaches a maximum value of the order of 0.5 in the IF region for the three flames. This behaviour is in

quantitative agreement with that reported from experiments on medium-scale methane pool fires by Cox and Chitty (Cox and Chitty, 1982). It should be pointed out that turbulent intensity for F4D reaches similar levels in both the CF and IF regions. Figure 7.4 shows also the ratio between the resolved temperature variance, $\langle \widetilde{T'^2} \rangle_{ReS} = \langle \tilde{T}^2 \rangle - \langle \tilde{T} \rangle^2$ and the total temperature variance. It can be observed that more than 80% of temperature variance is on the whole resolved by the present LES for the three flames.

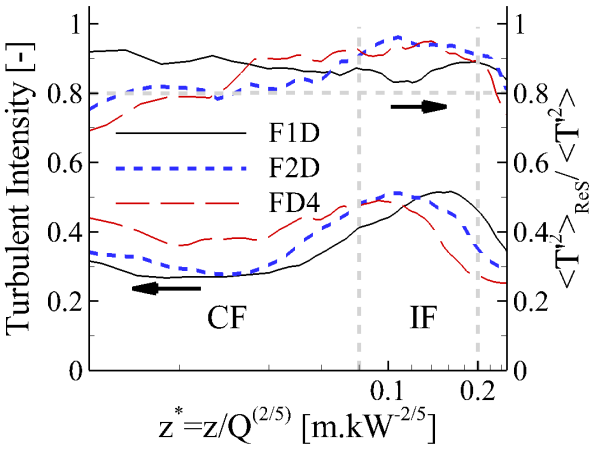

Figure 7.4: Centreline evolution of the turbulence intensity (left y-axis) and resolved-part of temperature variance (right y-axis) as a function the normalized height.

7.1.6 Effects of TRI on radiative loss

The radiant fraction can be re-expressed as $\chi_R = \chi_{emi}\left(1 - \dot{Q}_{abs}/\dot{Q}_{emi}\right)$. $\chi_{emi} = \dot{Q}_{emi}/\dot{Q}$ is the ratio of total emission to the HRR where $\dot{Q}_{abs}/\dot{Q}_{emi}$ represents the part of total emission reabsorbed within the flame, with $\left(1 - \dot{Q}_{abs}/\dot{Q}_{emi}\right)$ being the flame transparency (Consalvi and Nmira, 2019). χ_{emi} increases significantly with the flame size from about 47% for F1D to more than 80% for F4D. On the other hand, $\dot{Q}_{abs}/\dot{Q}_{emi}$ increases also with the flame size from 57% for F1D to 72% for F4D. Therefore, the moderate increase in χ_R with the flame size reported in Table 7.3 (Full TRI line) is explained by a balance between an enhancement in χ_{emi} and a reduction of $\left(1 - \dot{Q}_{abs}/\dot{Q}_{emi}\right)$.

Flames	F1D	F2D	F4D
χ_R (-)			
Full TRI	0.202	0.215	0.244
ReS TRI	0.165	0.171	0.161
No TRI	0.043	0.040	0.041
Contribution of fluctuations to χ_R (%)			
TRI	78.94	81.35	83.33
ReS_{χ_R}	60.65	58.83	49.49
SGS_{χ_R}	18.29	22.52	33.83
Contribution of SGS to TRI			
SGS_{TRI}	23.17	27.68	40.6

Table 7.3: Effects of TRI closures on χ_R. The experimental value for F1D is 0.19 (Fischer et al., 1987).

The contributions of the resolved-scale, SGS and total fluctuations to χ_R can be evaluated from the following decomposition:

$$(\chi_R)_{FullTRI} = (\chi_R)_{NoTRI} + \underbrace{\underbrace{[(\chi_R)_{ReSTRI} - (\chi_R)_{NoTRI}]}_{ReSTRI} + \underbrace{[(\chi_R)_{FullTRI} - (\chi_R)_{ReSTRI}]}_{SGSTRI}}_{TRI} \quad (7.1)$$

Table 7.3 shows that $(\chi_R)_{NoTRI}$ is around 0.04 for the three flames. This value is considerably lower than those of 0.19 measured by Fischer et al. (1987) and 0.202 predicted by the Full TRI model for F1D (see Table 7.3). These differences highlight the importance of TRI in pool fires. The contribution of TRI to radiative loss is evaluated from $TRI = [(\chi_R)_{FullTRI} - (\chi_R)_{NoTRI}] / (\chi_R)_{FullTRI} \times 100$. Table 7.3 shows that TRI represents about 80% of the radiative loss. This high contribution agrees with the results reported in the literature for medium-scale non-luminous pool fires (Consalvi, 2012; Fraga et al., 2019) and can be explained, on the one hand, by the rather low time-averaged temperature in pool fires and, on the other hand, by the high level of turbulence intensity due to the puffing process (see Fig. 7.4). In addition, this percentage increases slightly with the flame size (see Table 7.3). $ReS_{\chi_R} = [(\chi_R)_{ReSTRI} - (\chi_R)_{NoTRI}] / (\chi_R)_{FullTRI} \times 100$ and $SGS_{\chi_R} = [(\chi_R)_{FullTRI} - (\chi_R)_{ReSTRI}] / (\chi_R)_{FullTRI} \times 100$ quantify the contributions of resolved and SGS fluctuations to χ_R, respectively (see Table

7.3). ReS_{χ_R} decreases as the pool size is enhanced from about 60% for F1D to 49% for F4D. On the other hand, the contribution of SGS TRI to radiative loss appears to be significant and increases with the pool size. It represents about 18% for F1D and reaches 33% for F4D. $SGS_{TRI} = [(\chi_R)_{FullTRI} - (\chi_R)_{ReSTRI}] / [(\chi_R)_{FullTRI} - (\chi_R)_{NoTRI}] \times 100$ quantifies the contribution of SGS fluctuation to TRI which increases from 23% for F1D to 40% for F4D. This illustrates further the increasing importance of the contribution of SGS TRI with the pool size.

7.1.7 Effects of SGS TRI on radiative heat flux

Figure 7.5 displays the axial distribution of the net radiative flux at a normalized distance of $r^* = r/\dot{Q}^{2/5} = 0.18\ m \cdot kW^{-2/5}$ from the fire plume axis. This normalized distance corresponds to $r = 1\ m$ for F1D. Figure 7.5 shows that the net radiative flux increases on the whole with the pool size. Whatever the pool fire considered, the radiative flux is underestimated along the entire distribution when SGS TRI is disregarded and this underestimation becomes increasingly important as the pool size is enhanced. In particular, neglecting SGS TRI leads to an underestimation of the peaks of net radiative flux that by about 12.2%, 25.6% and 29.2% for F1D, F2D and F4D, respectively.

7.1.8 Effects of SGS TRI on fire plume structure

Figure 7.6 displays the temperature and the axial velocity along the fire plume axis. This figure shows clearly that disregarding the SGS TRI affects the fire plume structures and the effects are enhanced with the pool size. For F1D, the radiative loss are underestimated by 18% when SGS TRI is not considered (see Table 7.3). As a consequence, the temperature is overpredicted in the IF region ($z^* > 0.08\ m \cdot kW^{-2/5}$) with a maximum deviation of 82 K at $z^* = 0.2\ m \cdot kW^{-2/5}$ (see Fig. 7.6(a)). This induces an overestimation of the velocity by about 10% (see Fig. 7.6(d)). Figure 7.6(a) and (d) shows that considering SGS TRI improves the predictions for F1D. For F2D, neglecting the SGS TRI leads to an underestimation of the radiative loss by about 22%. Figure 7.6(b) shows that the temperature peak is shifted downstream as compared to the Full TRI case and the maximum overestimation is 106 K at $z^* = 0.077\ m \cdot kW^{-2/5}$. The largest discrepancies are observed for F4D for which neglecting the SGS TRI

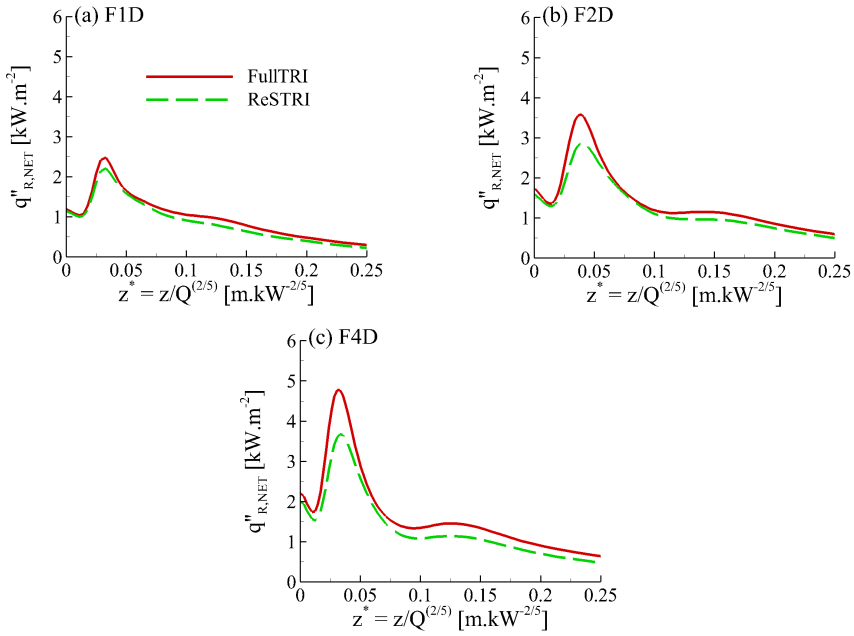

Figure 7.5: Effects of SGS TRI on the axial distribution of net radiative heat flux at a normalized distance of $r^* = r/\dot{Q}^{2/5} = 0.18\ m \cdot kW^{-2/5}$ from the fire plume axis as a function of the normalized height.

leads to an overestimation of the temperature by about 200 K along the entire plume axis and an overprediction of the axial velocity by about 19% at $z^* = 0.1\ m \cdot kW^{-2/5}$ (see Fig.7.6(c) and (f)).

7.1.9 Conclusions

LES involving state of the art combustion and radiation sub-models have been exercised to evaluate and quantify the contributions of TRI in ethanol pool fires ranging from medium to large size. The following conclusions can be drawn:

1. The model reproduces well the experimental data in terms of temperature, species concentration, puffing frequency and radiant fraction.
2. TRI accounts for more than 80% of the radiative loss in non-luminous pool fires.
3. For LES that resolves more than 80% of the temperature variance, the contribution of SGS fluctuation to TRI increases with the pool size from 23% for a 0.5 m diameter pool fire to more than 40% for a 2 m diameter pool fire.

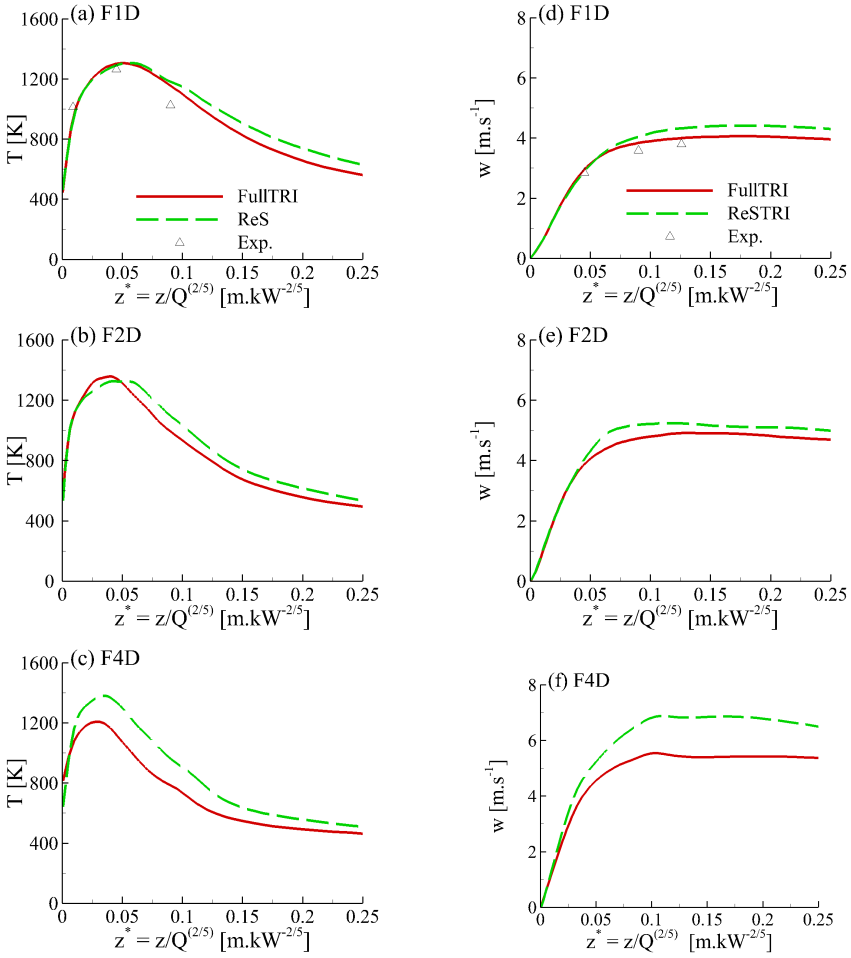

Figure 7.6: Effects of SGS TRI on the: (a)-(c) axial mean temperature and (d)-(f) axial mean velocity as a function of the normalized height.

4. SGS TRI contributes for about 20% to radiative loss in the 0.5 m diameter pool fire and this contribution increases with the pool size to reach about 33% for the 2 m diameter pool fire. Its impact on the prediction of radiative heat flux and fire plume structure cannot be neglected even for medium-scale pool fires.

7.2 Influence of gas radiative property models

7.2.1 Experimental and computational details

Experimental details

The 1 m diameter methanol pool fire investigated experimentally by Sung et al. (2020) is considered for simulations. The burner was located 30 cm

above the floor and the fuel lip height, defined as the fuel level below the burner rim, was maintained at 1 cm. The heat release rate (HRR, $\dot{Q}$) was determined either from oxygen consumption calorimetry or from the measured mass burning rate assuming a complete combustion. As expected for methanol, both techniques were found to be consistent with a measured HRR of 256 kW. Fast Fourier power spectrum of the time-varying flame height revealed a puffing frequency of 1.37 Hz and a first harmonic of 2.75 Hz. Temperature measurements were performed using 50 μm diameter Type S thermocouples and were corrected for thermal inertia effects. The compensation technique was based on an instantaneous time constant computed from the thermocouple bead geometry and an estimation of the flow conditions for the convective heat transfer. Vertical distribution, at a distance of 2.07 m from the pool axis, and radial distribution, along the plane of the burner rim outside the pool fires, of radiative flux were measured with wide-view angle, water-cooled, Gardon-type total heat flux gauges (see Fig.7.7). Sung et al. (2020) also deduced from their data the total radiative feedback, $\dot{Q}_{R,S} = \int_{A_b} \dot{q}''_{R,S} dA$ (see Fig. 7.7). This quantity represents the incident radiative flux on the fuel surface integrated over the burner surface, A_b. It was normalized by the HRR to provide $\chi_{R,S} = \dot{Q}_{R,S}/\dot{Q}$. This latter set of data is completed by the local radiative feedback, $\dot{q}''_{R,S}$, measured by Klassen and Gore (1992).

Computational details

Simulations are performed in a computational domain (x, y, z) of $9 \times 9 \times 7$ m^3 (see Fig. 7.7). In the present study, z represents the vertical direction. Consistently with the experimental configuration, the burner is located 30 cm above the floor and the fuel lip height is set equal to 1 cm. It was found necessary to respect these experimental features to reproduce adequately the pool dynamics. A non-uniform structured mesh with 8.01 million of cells is considered. The mesh is refined over the fuel surface with a cell size (Δx, Δy, Δz) of $8.15 \times 8.15 \times 5$ mm^3. Outside the pan, Δx and Δy are stretched progressively towards the sides. In the vertical direction, $\Delta z = 5$ mm is applied between the fuel surface ($z = 0$) and the burner rim ($z = 1$ cm). Δz is then stretched from $z = 0.01$ m to $z = 0.326$ m to reach 1.58 cm. A uniform $\Delta z =$ 1.58 cm is then applied up to $z = 1.8$ m. Above $z = 1.8$ m, Δz is stretched progressively. The flamelet library was generated using the full chemical kinetic

scheme developed by Li et al. (2007).

Typical outflow and entrainment boundary conditions are used for open boundaries at the outlet and sides, respectively. The fuel inlet temperature is set to the boiling temperature of methanol, i.e. 338 K. The inlet velocity is imposed to provide the specified HRR and both convective and diffusive mass and energy fluxes are accounted for. In the rest domain, the classical wall boundary condition is imposed.

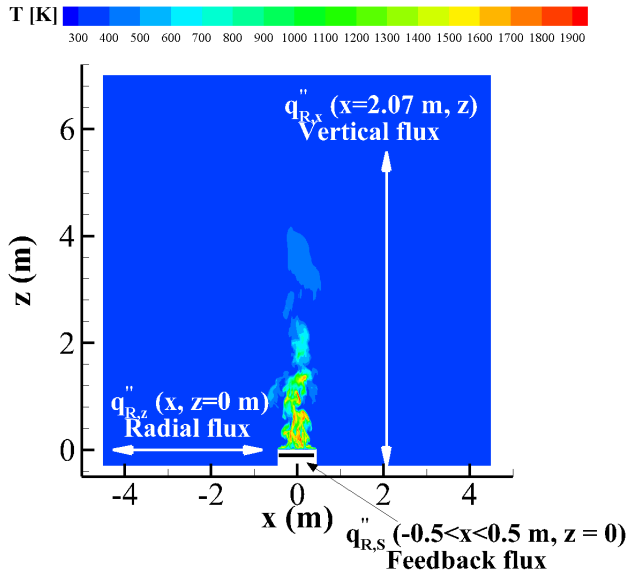

Figure 7.7: A schematic diagram of the computational domain and the locations of the radiative heat flux distributions.

Simulations were run for 35 s and the time-averaged mean and root mean square values were collected over the last 20 s. The first 15 s of simulation were used to establish a statistically stationary flow.

Four radiative property models, namely the RCFSK, the non-grey WSGG (WSGG-NG), and two versions of the grey WSGG based on different evaluations of the mean path length such as the cell-based approach is referred by WSGG-G-CB and the flame-based approach denoted by WSGG-G-FB are considered. A detailed description of these models is given in Chapter 2.

The filtered RTE (see Eq. 3.51) is solved by using the FVM (Raithby and Chui, 1990; Lee and Patankar, 1990) with a uniform angular mesh of 384 ($N_\theta \times N_\phi = 16 \times 24$) control angles. The subscripts θ and ϕ represent the polar

and azimutal angles, respectively. The selection of this angular discretization was based on the study of Jensen et al. (2007) who suggested that, for uniform angular discretization, approximately 50 angles inside and 350 angles outside the fire are needed to adequately resolve radiation.

A frozen field analysis will be considered to investigate the angular mesh effects on the radiative outputs. In this analysis, instantaneous fields of filtered absorption coefficient (Eq. (3.52)) and emission term (Eq. (3.53)), computed with the uniform 16 $\times$ 24 angular mesh, are saved during the statistically stationary state. These fields are used to solve instantaneous RTE (Eq. (3.51)) with the other angular meshes over the statistically stationary state and, then, the resulting instantaneous radiative intensities are averaged to get the mean absorption term and radiative fluxes. The other angular meshes considered in the present study are, on the one hand, a three-time finer uniform angular mesh with 4608 ($N_\theta \times N_\phi = 48 \times 96$) control angles and, on the other hand, the non-uniform FT_n angular discretizations (Kim and Huh, 2000). In the FT_n FVM, the polar angle, θ, is divided uniformly into an even number, n, while the azimuthal angle, ϕ, is uniformly divided into the numbers of the sequence of 4, 8, 12,...,$2n-4$, $2n$, $2n$, $2n-4$,..., 8 and 4 in each level of the polar angle (Kim and Huh, 2000). This results in $n \times (n+2)$ control angles. Using a frozen field analysis is justified by the fact that meshes finer than 16 $\times$ 24 were found to have no influence on the radiative heat transfer inside the flame and to change only the vertical distributions of radiative flux outside the flame. Refining the angular mesh further than 48 $\times$ 96 was found to have no effect on the vertical distributions of radiative flux outside the flame and this discretization will be used as reference.

All simulations were performed on the supercomputer Gaia of EDF R&D. This cluster is made of 1224 computer nodes and 42912 cores. Processor are Intel Xeon Gold 6140 CPU @ 2.30 GHz. The present LES were performed on 940 cores. Table 7.4 provides the CPU times for all the radiative models in one time step. A careful examination shows that CPU times for the different angular meshes and the different radiative property models increase almost linearly with number of control angles and the number of RTEs to be solved, respectively.

Model	Angular mesh	CPU (s)
RCFSK	16×24	247
	48×96	1333
	FT_{12}	200
	FT_{16}	216
	FT_{24}	282
	FT_{32}	375
	FT_{48}	636
RCFSK	48×96	1333
WSGG-NG	48×96	523
WSGG-G-CB	48×96	241
WSGG-G-FB	48×96	230

Table 7.4: CPU times for different radiative property models and angular meshes.

7.2.2 Quality of the LES

The ratio of resolved temperature variance, $\langle \widetilde{T'^2} \rangle_{ReS} = \langle \tilde{T}^2 \rangle - \langle \tilde{T} \rangle^2$, to the total temperature variance, $\langle \widetilde{T'^2} \rangle = \langle \widetilde{T^2} \rangle - \langle \tilde{T} \rangle^2$, is considered to assess the quality of the present LES. Figure 7.8 shows radial profiles of this ratio at different heights above the burner covering the flaming region. It can be observed that more than 80 % of temperature variance is on the whole resolved by the present LES.

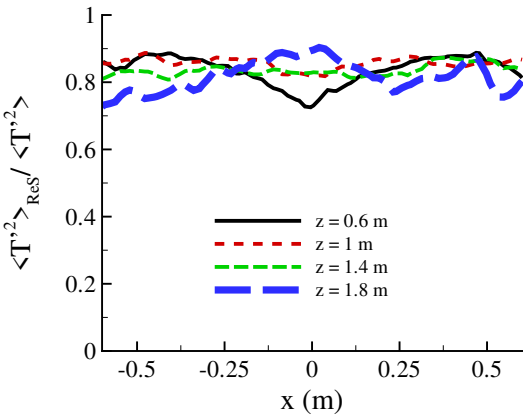

Figure 7.8: Radial evolution of resolved-part of temperature variance at different heights.

7.2.3 Comparison with available experimental data

In this section, the LES results obtained by the RCFSK/FVM (16×24) radiation model are compared with the experimental data.

Figure 7.9(a) shows the power spectrum density (PSD) computed with a fast Fourier transform of the times series of the axial velocity along the axis at a height of 0.6 m. The model predicts a puffing frequency of 1.25 Hz and a first harmonic of 2.50 Hz in good accordance with the experimental ones of 1.37 Hz and 2.75 Hz, respectively. Figure 7.10(a) shows the axial distribution of mean

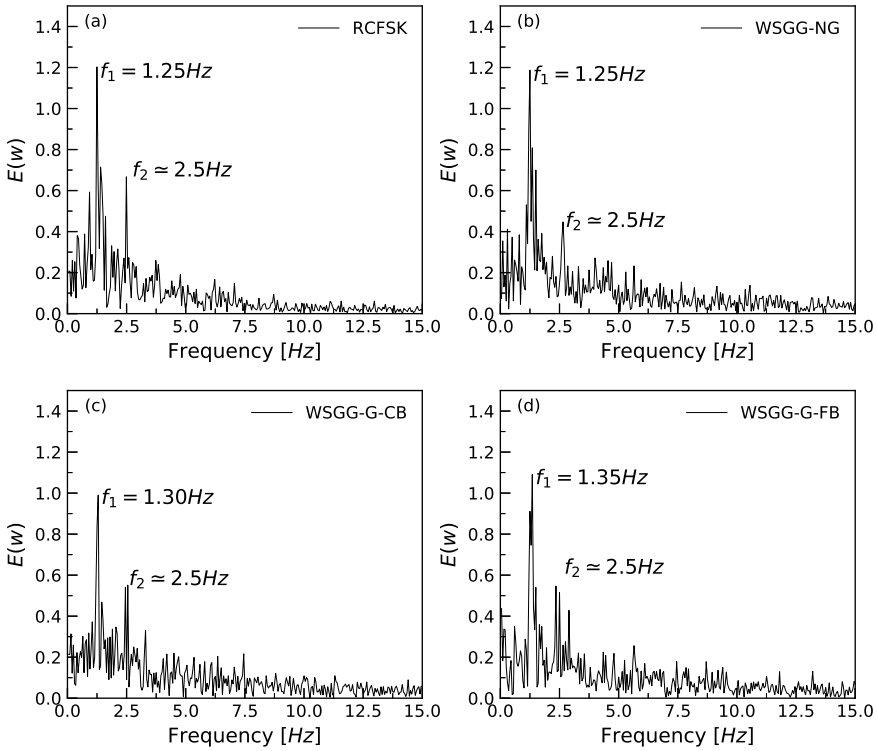

Figure 7.9: Predicted power spectrum Density from axial velocity along the flame axis at $z = 0.6\ m$

temperature. The experimental data exhibit the expected trends. The mean temperature increases with z close to the burner, reaches a plateau in the continuous flame and, then, decreases as z is further increased in the intermittent flame and in the inert plume. Model predictions are in close agreement with the experimental data in all the flame regions. Figure 7.10(b)-(f) displays also the radial profiles of mean temperature at different heights above the burner. A very good overall agreement is also observed between the model and the experiments. Figure 7.11 displays the axial profile and the radial profiles at different

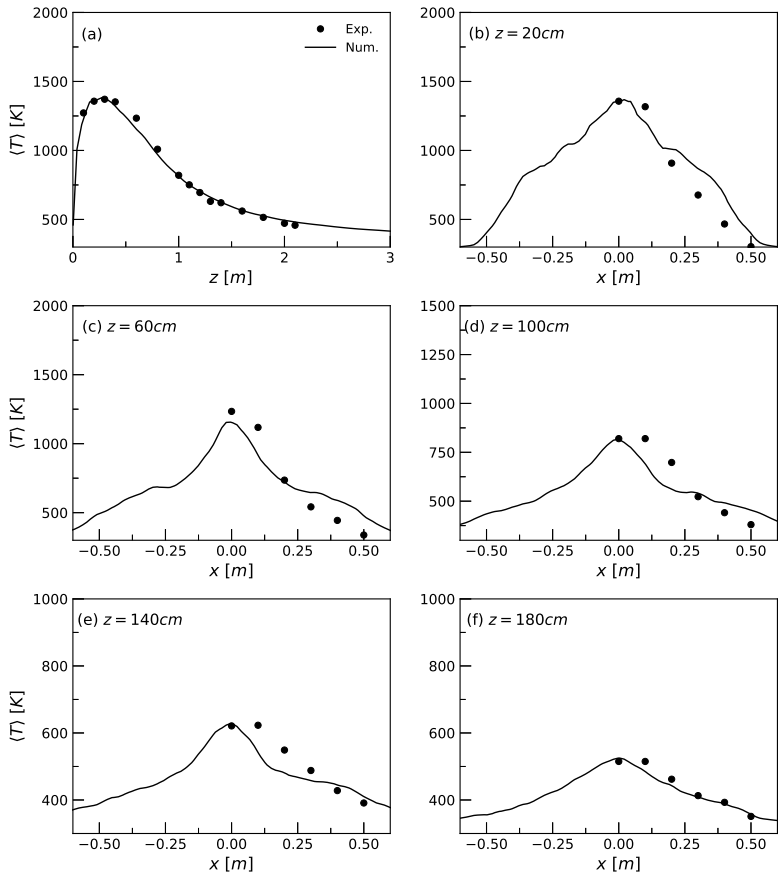

Figure 7.10: Axial and radial profiles of mean temperature. The experimental data are taken from Ref. (Sung et al., 2020).

heights of the rms values of temperature fluctuations. Figure 7.11(a) shows that the measured axial temperature fluctuation is of the order of 290 K very close to the burner and decreases down to 247 K at about $z = 0.30\ m$. After this location, it increases with z to reach a peak of about 330 K at $z = 0.8\ m$ before decreasing as z is further increased. The numerical model captures well these trends. In particular, the peak location as well as the rates of increase and decrease are well reproduced. Figure 7.11 shows also that the experimental data exhibit pronounced M-shaped radial profiles close to the burner and transit progressively towards flatter profiles as z increases (see fig. 7.11(b)-(f)). The model captures also well these trends and provides predictions in overall good agreement with the experimental data. Nevertheless, it overestimates on the whole the temperature fluctuations. These discrepancies may be attributed, at least partially, to the measurements since previous experimental studies suggested that temperature fluctuations may be underestimated when measured

by 50 μm thermocouples despite the use of compensation techniques (Crauford et al., 1985; Weckman and Sobiesiak, 1987; Weckman and Strong, 1996). Table 7.5 reports the total emission, $\dot{Q}_{emi} = \int_V \dot{Q}'''_{emi} dV$, the total absorption,

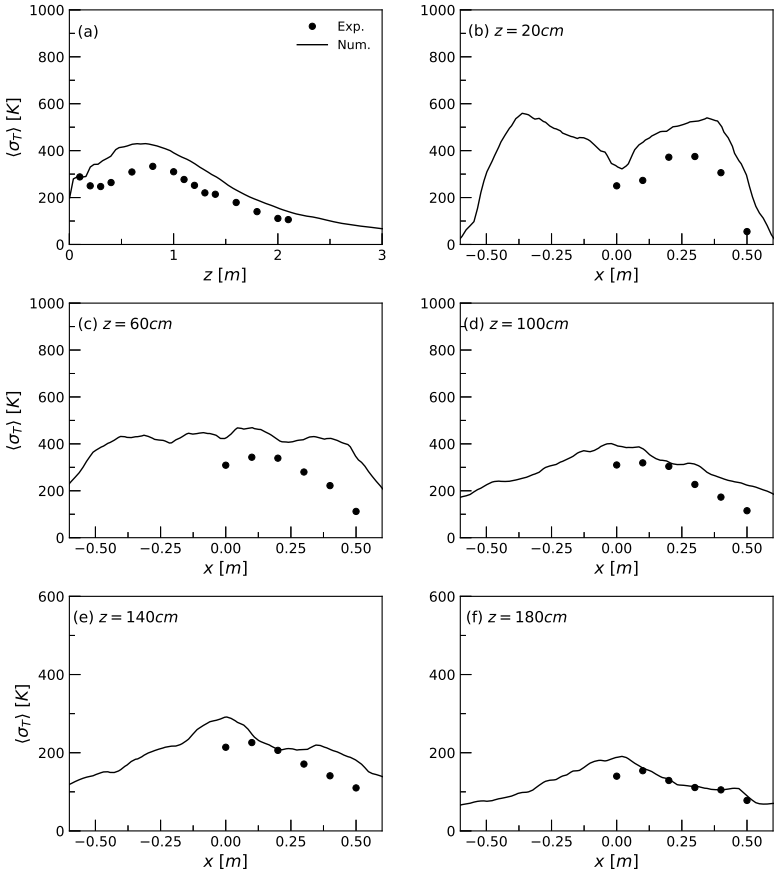

Figure 7.11: Radial profiles of rms values of temperature fluctuations at different heights. The experimental data are taken from Ref. (Sung et al., 2020).

$\dot{Q}_{abs} = \int_V \dot{Q}'''_{abs} dV$, the ratio of $\dot{Q}_{abs}$ to $\dot{Q}_{emi}$ that represents the part of emission reabsorbed within the flame and can be used to quantify the flame optical thickness (Nmira et al., 2020b), the radiant fraction, $\chi_R = (\dot{Q}_{emi} - \dot{Q}_{abs})/\dot{Q}$, and $\chi_{R,S}$. These results show that about 59.8% of emission is reabsorbed within the flame. The predicted χ_R is 0.269 and overestimates the experimental one of 0.22 $\pm$ 16% by about 22%. The predicted $\chi_{R,S}$ is 0.059, in closer agreement with the experimental data of 0.055 $\pm$ 21%.

The vertical, radial and feedback distributions of radiative flux are plotted in Fig. 7.12(a)-(c). Let us start to analyse the results obtained with the

Model	Angular mesh	$\dot{Q}_{emi}$ (kW)	$\dot{Q}_{abs}$ (kW)	$\dot{Q}_{abs}/\dot{Q}_{emi}$ (-)	χ_R (-)	$\chi_{R,S}$ (-)
RCFSK	16 $\times$ 24	172	102.6	0.598	0.269	0.059
RCFSK	48 $\times$ 96	172	102.6	0.598	0.269	0.059

Table 7.5: Integrated flame radiative properties. Measured radiant fractions, χ_R, and fractional radiative heat feedback towards the fuel surface, $\chi_{R,S}$, were 0.22 $\pm$ 16% and 0.055 $\pm$ 21%, respectively (Sung et al., 2020).

16$\times$24 angular discretization. Predictions of the radiative flux in the downward direction outside the burner (see Fig. 7.12(b)) and the radiative feedback towards the fuel surface (see Fig. 7.12(c)) are in overall good agreement with the experimental data. Nevertheless, the model overpredicts the radiative flux at vicinity of the burner (see Fig. 7.12(b)) and underpredicts the radiative feedback by about 10% (see Fig. 7.12(c)). On the other hand, the vertical distribution of radiative flux exhibits clearly ray effects, especially for $0 \leq z \leq 1$ m (see Fig. 7.12(a)). Such effects are a major drawback of both DOM and FVM and are favoured in optically thin medium (Coelho, 2014). As a consequence, the present configuration is particularly sensitive to ray effetcts since radiation travels mainly a transparent medium before reaching the location $x = 2.07$ m where the vertical distribution is measured. The ray effects can be reduced by refining the angular mesh (Coelho, 2014).

Radiation calculations were also performed by neglecting TRI with the 16 $\times$ 24 angular mesh. In these calculations, radiation is solved in decoupled manner by using time-averaged temperature and mole fractions of CO_2 and H_2O obtained from the LES simulations. The total emission and the radiant fraction, obtained by neglecting TRI, were found to be $\dot{Q}_{emi,NoTRI}$ =40 $\times 10^3$ kW and $\chi_{R,NoTRI} = 0.051$, respectively. A comparison with the predictions reported in Table 7.5 shows that TRI represents about 80% of the total emission and radiative loss. This high contribution agrees with the results reported in the literature for medium-scale non-luminous pool fires (Nmira et al., 2020b; Fraga et al., 2019) and can be explained, on the one hand, by the rather low time-averaged temperature in pool fires and, on the other hand, by the high level of turbulence intensity due to the puffing process.

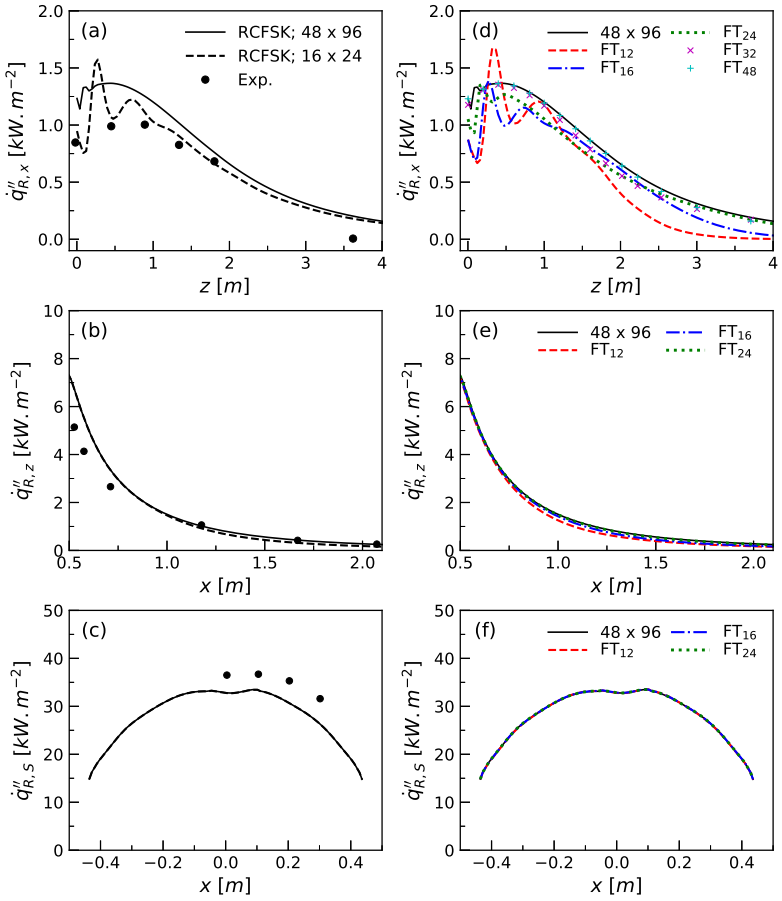

Figure 7.12: Effects of angular meshes on radiative heat fluxes. The location of the distributions are described in Fig. 7.7. (a) and (d) Vertical distribution at a distance $r = 2.07\ m$ from the pool axis, (b) and (e) radial distribution outside the burner along the plane of the burner rim. The radial distance is measured from the pool centre, and (c) and (f) feedback towards the fuel surface. The experimental data in the diagrams (a) and (b) are taken from Sung et al. (2020) whereas those in diagram (c) are taken from Klassen and Gore (1992). All the simulations were obtained with the RCFSK. The diagrams (a), (b) and (c) investigate the effects of the uniform meshes whereas the diagrams (d), (e), and (f) those of the FT_n FVM angular discretizations.

7.2.4 Effects of angular mesh

Results in Table 7.5 and Fig. 7.12(a)-(c) show that using the uniform 48 $\times$ 96 angular mesh instead of the uniform 16 $\times$ 24 angular discretization does not modify the predictions of $\dot{Q}_{abs}$, χ_R and $\chi_{R,S}$ as well as the radiative feedback towards the fuel surface (see Fig. 7.12(c)). In addition, this has almost imper-

ceptible effects on the radial distribution of radiative flux along the plane of the burner rim (see Fig. 7.12(b)). In an opposite way, it improves significantly the vertical distribution of radiative flux by eliminating the ray effects (see Fig. 7.12(a)).

Table 7.6 and Fig. 7.12(d)-(f) investigate the effects of the FT_n angular discretizations on both integrated and local radiative outputs. In agreement with the previous discussion, the results show clearly that the angular meshes affect only the vertical distribution of radiative flux outside the flame.

Figure 7.12(d) shows that significant ray effects are observed for FT_{12} and FT_{16}. The FT_{16} and 16 $\times$ 24 angular meshes have the same polar discretization and differ from the azimuthal discretization. These two angular meshes provide almost identical vertical distributions, showing that the discretization of the polar angle is mainly responsible for these ray effects. This can be explained by the statistically axisymmetric nature of the present fire plume. The FT_{24} angular discretization mitigates the ray effects and predicts the peak of vertical flux within 7% of the 48 $\times$ 96 angular mesh. However, relative errors as large as about 16% are still observed at $z = 1.2\ m$. Acceptable predictions of the vertical distribution of radiative flux are observed for the FT_{32} angular discretization, which involves 1088 control angles. The FT_{48} angular discretization provides the same vertical distribution of radiative flux as the uniform 48 $\times$ 96 angular mesh, but considers 2400 control angles instead of 4608.

Model	Angular mesh	$\dot{Q}_{emi}$ (kW)	$\dot{Q}_{abs}$ (kW)	$\dot{Q}_{abs}/\dot{Q}_{emi}$ (-)	χ_R (-)	$\chi_{R,S}$ (-)
RCFSK	48 $\times$ 96	172	102.6	0.598	0.269	0.0587
RCFSK	FT_{12}	172	103.2	0.602	0.267	0.0586
		(0.0)	(0.6)	(0.67)	(-0.74)	(-0.17)
RCFSK	FT_{16}	172	102.6	0.598	0.269	0.0587
		(0.0)	(0.0)	(0.0)	(0.0)	(0.0)

Table 7.6: Effects of FT_n FVM angular discretization on the integrated flame radiative properties. Values in parenthesis represent the relative errors in % of the current model as compared to the RCFSK/FVM 48 $\times$ 96. Results with FT_n angular discretization higher than $n = 16$ are not reported since these angular meshes do not introduce any discrepancies on these quantities.

Model	Angular mesh	$\dot{Q}_{emi}$ (kW)	$\dot{Q}_{abs}$ (kW)	$\dot{Q}_{abs}/\dot{Q}_{emi}$ (-)	χ_R (-)	$\chi_{R,S}$ (-)
RCFSK	48 × 96	172	103	0.598	0.269	0.0587
WSGG-NG	48 × 96	209 (21.5)	135 (31.1)	0.646 (8.07)	0.288 (7.06)	0.0600 (1.86)
WSGG-G-CB	48 × 96	114 (-33.7)	19.9 (-80.7)	0.175 (-70.7)	0.367 (36.4)	0.078 (32.9)
WSGG-G-FB	48 × 96	72.5 (-57.8)	6.69 (-93.5)	0.092 (-84.5)	0.257 (-4.46)	0.048 (-18.2)

Table 7.7: Effects of the gas radiative property models on the integrated flame radiative properties. Values in parenthesis represent the relative errors in % of the current model as compared to the RCFSK/FVM 48 × 96.

7.2.5 Effects of radiative property models

Table 7.7 shows that the WSGG-NG overestimates significantly both the total emission and the total absorption and, by a less extent, the ratio $\dot{Q}_{abs}/\dot{Q}_{emi}$, the radiant fraction, χ_R, and the normalized radiative feedback towards the fuel surface, $\chi_{R,S}$. In particular, these three latter quantities are moderately overestimated by about 8.07, 7.03 and 2.10%, respectively. The WSGG-G-CB and WSGG-G-FB underestimate significantly both the total emission and the total absorption as well as $\dot{Q}_{abs}/\dot{Q}_{emi}$ that is only of about 17.5% and 9.2% for the WSGG-G-CB and WSGG-G-FB, respectively, instead of 59.8% for the RCFSK. These results show that the grey models are not able to reproduce the radiative structure of the flame, predicting an optically-thin flame instead of an optically intermediate medium.

The WSGG-G-CB overpredicts χ_R and $\chi_{R,S}$ by 36.4% and 32.9%, respectively. On the other hand, as observed in previous studies involving decoupled radiative heat transfer calculations (Demarco et al., 2011; Fraga et al., 2019), the WSGG-G-FB provides better predictions of the radiative loss than the WSGG-G-CB. Nevertheless, discrepancies of the order of 18.2% are still observed for $\chi_{R,S}$.

Figure 7.13 illustrates the effects of the radiative property models on the radiative flux distributions. Predictions with the WSGG-NG agree well with the RCFSK. On the other hand, the WSGG-G-CB model overpredicts notably

these fluxes whereas the WSGG-G-FB underpredicts them but by a less extent. Quantitatively, Fig. 7.13 shows that the WSGG-G-CB and WSGG-G-FB lead to relative errors as compared to the RCFSK on the peak of vertical radiative flux (see Fig. 7.13(a)), on the radiative flux downward at $r = 0.5\ m$ (see Fig. 7.13(b)), and on the radiative feedback at the centre of the fuel surface (see Fig. 7.13(c)), of 15.44% and -22.05%, 18.95% and -19.91%, and 40.2% and -13.97%, respectively. The effects of the radiative property models on axial

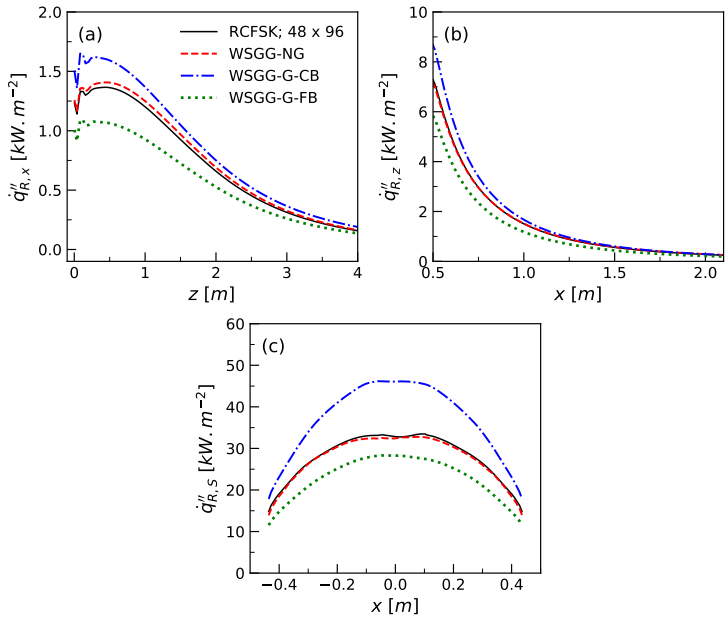

Figure 7.13: Effects of gas radiative property models on raditive heat flux. The location of the distributions are described in Fig. 7.7. (a) Vertical distribution of radiative flux at a distance $x = 2.07\ m$ from the pool axis, (b) radial distribution outside the burner along the plane of the burner rim. The radial distance is measured from the pool centre, and (c) radiative feedback towards the fuel surface. These radiative fluxes are computed in frozen field analysis using the FVM 48 $\times$ 96 angular discretization.

profiles of the mean emission term, mean absorption term, mean divergence of the radiative flux, and mean and rms temperature are investigated in Fig. 7.14. Consistently with the results in Table 7.7, the WSGG-NG overestimates significantly both local emission and absorption terms, but predicts a mean radiative source term in much better agreement with the RCSFK. However, the WSGG-NG produces noticeable discrepancies on the mean temperature, especially in the region located between $z = 0$ and $z = 0.75\ m$. The peak of mean tempera-

ture is slightly shifted towards the fuel surface and its value is underpredicted by about 60 K as compared to the RCFSK. The WSGG-NG model leads also

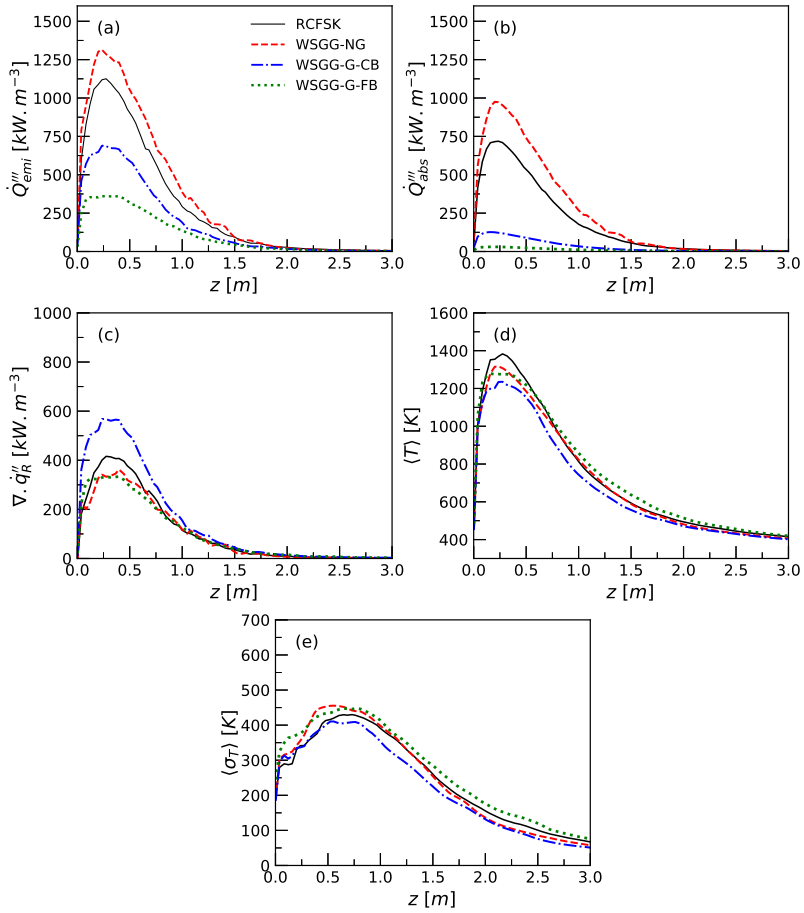

Figure 7.14: Effects of radial property models on the axial distributions of: (a) emission term, (b) absorption term, (c) divergence of the radiative flux, (d) mean temperature, and (e) rms values of temperature fluctuations. These radiative fluxes are computed in frozen field analysis by using the FVM 48 $\times$ 96 angular discretization.

to a slight overprediction of the rms value of temperature fluctuations in this region with a peak value higher by about 20 K than that predicted with the RCFSK. The WSGG-G-CB overestimates substantially the radiative loss (see Fig. 7.14(c)). Consequently, it predicts mean temperature significantly lower than the RCFSK along the entire centreline (see Fig. 7.14(d)). Figure 7.14(d) shows that the peak value of mean temperature is lower by about 150 K than that computed with the RCFSK. A consequence of this underestimation of the temperature is that the buoyant forces are underestimated, producing in turn

an underestimation of the temperature fluctuations as observed in Fig. 7.14(e). The WSGG-G-FB model provides a divergence of the radiative flux as well as mean and rms temperature comparable to those predicted by the WSGG-NG model. Nevertheless, it has to keep in mind that the WSGG-NG outperforms significantly the WSGG-G-FB in the prediction of the radiative flux (see Fig. 7.13).

Eventually, Fig. 7.9 shows that the gas radiative models have no effect on the prediction of the puffing frequency as well as on the first harmonic.

7.2.6 Conclusions

LES of 1 m methanol pool fires have been exercised in order to investigate the effects of gas radiative property models on the radiative outputs and flame structure. The baseline radiation model involves the RCFSK coupled to the FVM with 16×24 control angles. Three other gas radiative property models, namely the WSGG-NG, the WSGG-G-CB and the WSGG-G-FB, are also considered. In addition, solutions obtained with other angular meshes, including the uniform 48×96 angular discretization and the FT_n scheme with n up to 48, are assessed. The following conclusions can be drawn:

1. The present LES-based fire model involving the non-adiabatic/presumed FDF and RCFSK radiation model provides high fidelity predictions in terms of puffing frequency and first harmonic, mean and fluctuating temperatures, radiative feedback to the pool surface and radiative loss to the surrounding.

2. All radiative outputs at the exception of vertical distributions of radiative flux outside the flame can be accurately predicted with the FT_{12} angular discretization. On the other hand, finer angular meshes, considering at least 32 segments to discretize the polar angle, are required to compute accurately the vertical distributions of radiative flux outside the flame.

3. Whatever the definition of the mean path length, the grey WSGG models fail to reproduce the radiative structure of the fire plume, predicting an optically thin flame instead of an optically intermediate medium. The WSGG-G-FB provides a better description of the radiative loss than the WSGG-G-CB. However, it leads to relative errors in the range 15-20% on the radiative fluxes.

4. The non-grey WSGG model overestimates significantly both emission and absorption, but leads to predictions of the radiative loss and radiative flux within 10% of the RCFSK. These results suggest that it can be a reasonable alternative for non-sooting pool fires.

Chapter 8

Fire plumes under oxygen-dilution quenching conditions

In this chapter, LES of methane fire plumes under oxygen-dilution quenching conditions is conducted. As discussed in the introduction, this configuration represents an idealization of under-ventilated fire scenarios and is particular relevant for fires in nuclear plants. The UMD turbulent line fire experimental data are used as reference to validate numerical simulations.

8.1 Experimental details

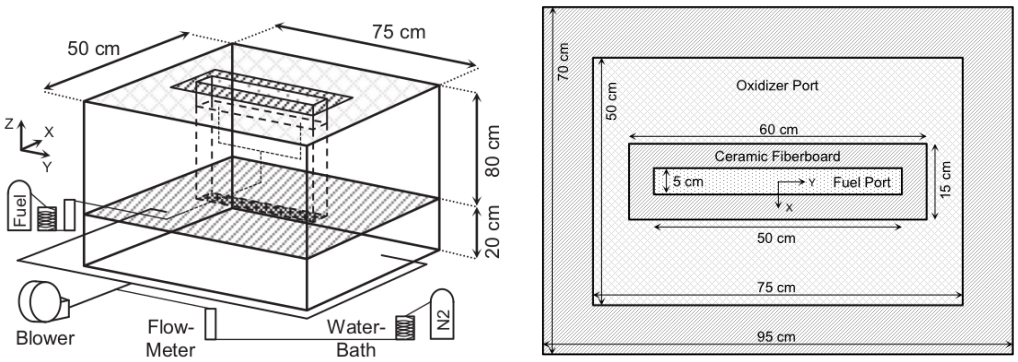

Figure 8.1: Schematic of the experimental configuration (left); Plan view of UMD line burner (right). These schemes are taken from White et al. (2015).

The UMD turbulent line burner experimental facility provides a canonical line fire configuration for the study of a low-strain, buoyancy-driven, fully-turbulent

diffusion flame (Fig. 8.1) (White et al., 2015). The burner features a ground-glass filled, stainless-steel fuel port, measuring 5 cm wide by 50 cm long, with 1.5 mm thick side walls. The burner is centrally located at the outlet of a surrounding oxidizer port, measuring 50 cm wide by 75 cm long, with 10 cm thick side walls. A thin, 5 mm tall, 5 cm wide strip of ceramic fibreboard, is positioned above the oxidizer port and surrounding the fuel port, so top of the board is 20 mm below the lip of the fuel port. This board is used as a flow blockage to reduce the oxidizer velocity near the flame base, forcing the onset of buoyancy-generated turbulence upstream towards the fuel port and reducing the tendency to form laminar structures at the base of the flame. The oxidizer port sits 15 mm below the fuel port, while the perimeter around the oxidizer port sits at the same elevation as the fuel port.

Methane gas is released with a flow rate of $1.00 \pm 0.02\ g \cdot s^{-1}$, leading to a total heat-release rate of roughly 50 kW under complete combustion. The oxidizer is provided at a fixed total flow rate of $85 \pm 7\ g \cdot s^{-1}$. The oxygen mole-fraction in the coflow, X_{O_2}, varies between 21%, corresponding to the baseline case in pure air, and 11%, which corresponds to a case well-below the oxygen extinction limit. Two kinds of configuration were considered by including or not an oxygen anchor at the base of the flame. The objective of this oxygen anchor is to reduce the flame lift-off and guarantee a prolonged stable regime. Global extinction occurs for $X_{O_2} = 0.151$ when the flame is not anchored. This value of X_{O_2} is reduced to 0.13 when the flame is anchored.

The flame structure is characterized by measurements of the mean and rms gas temperature using 12.7-μm-diameter Type-S (Pt/10%Rh) thermocouples. The radiative loss from the micro-thermocouples is neglected. The flame behaviour is also characterized through measurements of the radiant fraction. The radiant fraction is determined from the measurement of a radiative heat flux at 1 m distance from the flame combined with time-resolved infrared camera imaging and a multipoint radiation source model (White et al., 2015).

8.2 Flamelet library calculation

Six values of $X_{O_2} = 21$, 18, 16, 15, 14, and 13% are considered. The latter value corresponds to condition of global extinction in the UMD experiments when an oxygen anchor is considered to resist to fire lift-off. For each value of X_{O_2}, a

specific flamelet library was generated by using the kinetic mechanism GriMech 3.0 (*Grimech 3.0* 2019) and solving the counterflow problem in the physical space with FlameMaster code (Pitsch, 1998). Radiative loss was incorporated in the each flamelet library by using the methodology as described in the Chapter 2. In this study, we consider SLF and FPV models. The look-up tables were parametrized by (Z, χ, X_R) for SLF and (Z, c, X_R) for FPV. As discussed in Chapter 2, two definitions of the reaction progress variable are considered in this numerical study, c_1 and c_2 (see Eq. 2.17). The FPV model using c_1 as progress variable will be referred to as FPV-c_1 hereafter whereas that using c_2 will be referred to as FPV-c_2. The advantages and disadvantages of the two definitions for the simulation of fire problems, where combustion occurs generally at low strain rates, have been discussed in Chapter 2. Using c_1 provides a relevant mapping of the flamelets in the stable branch whereas flamelets in the unstable branch are poorly mapped. An opposite behaviour is observed when using c_2. These observations suggest that FPV-c_1 may be more accurate when simulating well-ventilated fires whereas FPV-c_2 may be better suited when the combustion is governed by the unstable branch.

Let us analyse the physics of oxygen-diluted quenching at the level of the S-shaped curve. Figure 8.2 shows the S-shaped curves for different X_{O_2} under adiabatic condition. It can be observed that the scalar dissipation rate at flame extinction and the corresponding extinction temperature decrease as X_{O_2} is reduced. This behaviour results directly from the weakening of the flame as X_{O_2} is reduced. As a consequence, the S-shaped curves are shifted towards lower values of χ_{st} as X_{O_2} is progressively reduced. In addition, for a given χ_{st}, the temperature of the stable burning branch is reduced as X_{O_2} decreases. An opposite trend is observed for the unstable burning branch.

In addition, the relationships between T_{st} and c_{st} for different X_{O_2} are plotted in Fig. 8.3. Figure 8.3(a) shows that, as X_{O_2} decreases, the curves are shifted towards lower values of $c_{1,st}$ and the stoichiometric temperature span becomes smaller. On the other hand, comparing Fig. 8.3(b) with Fig. 8.3(a) evidences that the T_{st}- c_{st} curves are significantly less sensitive to changes in $c_{2,st}$ than to changes in $c_{1,st}$. This shows that, for a given value of T_{st}, the mass fractions of CO_2 and H_2O at stoichiometry remains relatively unchanged as X_{O_2} decreases whereas those of CO and H_2 are significantly reduced.

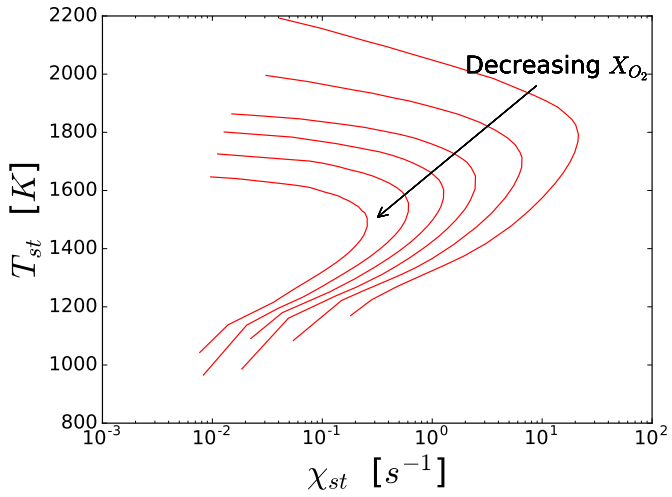

Figure 8.2: Adiabatic S-shaped curves for different X_{O_2}

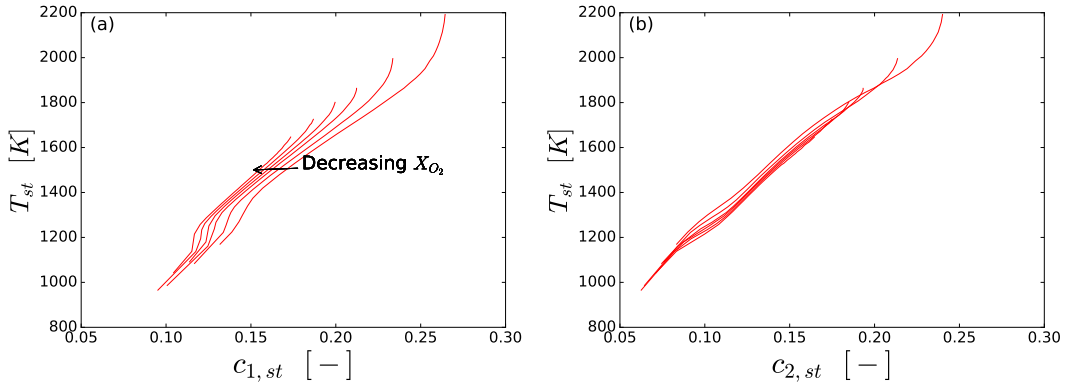

Figure 8.3: Temperature as a function of the reaction progress variable at stoichiometric conditions at different X_{O_2}: (a) c_1 definition and (b) c_2 definition.

In this work, the Favre-filtered governing Eqs. 3.1 to 3.4 are solved by the solver proposed in the Chapter 4. The second-order Crank-Nicolson scheme is used for time advancement. The Superbee-TVD scheme (Versteeg and Malalasekera, 2007) is applied for convection in the mixture fraction transport to limit numerical oscillation whereas a second-order CDS is used for diffusion. For the momentum equation both convective and diffusive terms are discretized by using a second-order CDS.

The subgrid contribution to the momentum stress and scalar flux is computed using DSM and DEDM models, respectively. For both SLF and FPV models, the SGS mixture fraction variance required to retrieve solutions from the filtered flamelet look-up table is computed by the STE model. The RCFSK

model is retained as radiative property model. The Filtered RTE is solved by using FVM with a non-uniform FT12 angular discretization.

Simulations are performed in a computational domain (x, y, z) of $3.5 \times 3.5 \times 2.3$ m^3. The burner platform is lifted up by 50 cm in order to mimic the experimental configuration, as shown in Fig. 8.4. It should be pointed out that no oxygen anchor is considered in the simulations. The mesh is uniformly refined in the region of $0.15 \times 0.6 \times 0.5$ m^3 centered around the burner with a minimal grid spacing equal to 5 mm. Outside this region, the mesh is progressively stretched in all the direction.

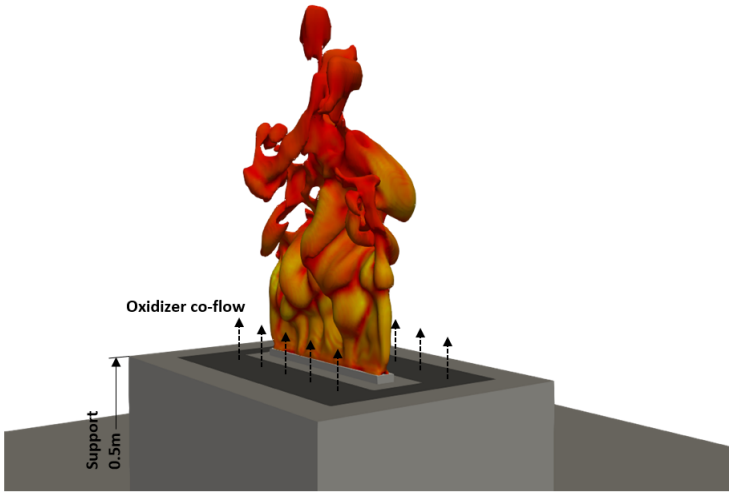

Figure 8.4: Illustration of the numerical configuration.

Typical outflow and entrainment boundary conditions are used for open boundaries at the outlet and sides, respectively. The boundary conditions at the fuel and oxidizer ports utilize a prescribed mass-flux boundary condition accounting for both convective and diffusive components, with values specified to match the experimental fuel and oxidizer mass flow rates of 1.0 $g \cdot s^{-1}$ and 85 $g \cdot s^{-1}$, respectively. In addition, for FPV simulations, the minimum value of progress variable corresponding to the inlet mixture fraction (see the $c - Z$ manifolds in Fig. 2.5), is imposed at each time step. This means that the flame is not ignited at the inlet surface. In the rest domain, the classical wall boundary condition is imposed.

Throughout all simulations, time step is set to 5×10^{-4} s which corresponds to an averaged maximum CFL of 0.6. Simulations were run for 25 s and the time-averaged mean and rms values were collected over the last 19 s. The first

6 s of simulation were used to establish a statistically stationary flow. For the FPV simulations, a pre-simulation of 5 s is conducted with the SLF model to initialize the progress variable field.

Results are compared with experiments and discussed to highlight the performance of SLF and FPV models. The FPV-c_1 is used to perform all simulations with X_{O_2} ranging from 13% to 21%, while simulations using FPV-c_2 are carried out only for $X_{O_2} = 13\%$, 14% and 15% to emphasis the differences brought by the choice of the progress variable in simulating fires close to oxygen extinction limit. The reason why FPV-c_2 is not applied to cases with $X_{O_2} \geq 16\%$ is that this definition does not respect the monotonic evolution of the progress variable over the entire mixture fraction range. As a consequence, this definition does not ensure a good mapping in the stable branch for low strain rates as discussed previously in Chapter 2.

8.3 Comparison with experimental data

Predictions obtained with SFL and FPV-c_1 are compared to the available experimental data for $X_{O_2} = 21\%$, referred to as the baseline case hereafter. Figure 8.5(a) shows that the measured axial temperature increases rapidly near the flame base, up to a peak value close to 1200 K, then exhibits a double-peak behaviour before decreasing for z larger than 0.25 m. The predictions obtained with both SLF and FPV-c_1 models are also plotted and the comparison with the experimental data indicates a good agreement. Both SLF and FPV-c_1 models predict a higher temperature for the first peak. In addition, over-estimations of temperature by about 150 K for the two models are also noticed between $z = 0.3$ m and $z = 0.5$ m. In this region, temperature computed from the SLF model is slightly higher than that from the FPV model by about 50 K at most. It can be also observed that the decreasing rate of temperature from $z = 0.5$ m is well reproduced by the two models. In this latter region, the temperature computed by the FPV model is higher than that computed by the SLF model by about 50 K.

The experimental rms values of temperature presented in Fig. 8.5(b), also increases rapidly near the flame base, up to values close to 400 K. It remains approximately constant up to $z = 0.5$ m (i.e. the mean flame height) before decreasing rapidly. The predicted rms values of temperature for both models

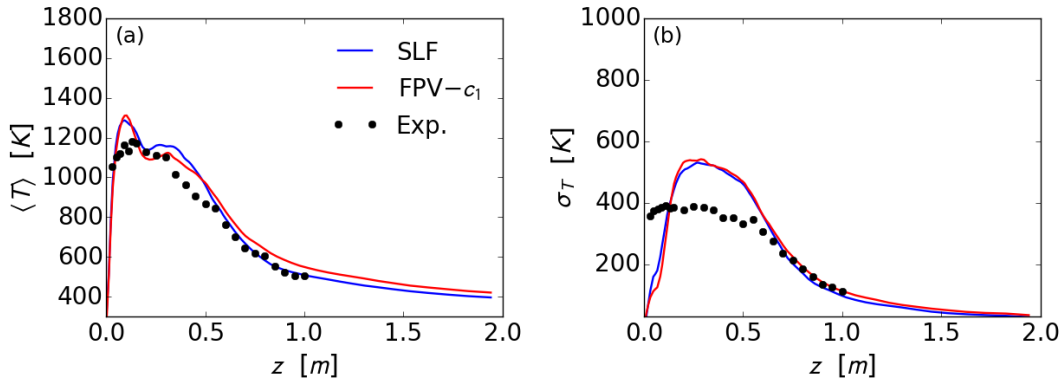

Figure 8.5: Axial profiles of: (a) mean temperature and (b) rms values of temperature fluctuations.

generally over-estimate the experiments in the flame zone. Such discrepancies are somewhat common in our previous numerical simulations, and are also observed in the numerical study reported by White et al. (2017) and Xu et al. (2020). In the plume region, the computed rms values agree well with the measurements.

Figure 8.6 displays the radial profiles of mean and rms temperature. The two model predictions present an overall good agreement with experiments except at $z = 0.25$ and $z = 0.5$ m where the rms values of temperature fluctuations are overestimated by about 100 K (see Fig. 8.6(e) and (f)).

The baseline case corresponds to a well-ventilated fire plume in which there is no occurrence of flame extinction. As a consequence, it is not surprising that the overall fire structure is well reproduced by both SLF and FPV-c_1 models. However, slight differences appear between the two models. As discussed by Pierce and Moin (2001), the scalar dissipation rate value associated with the flamelet selected by the progress variable interpolation in the FPV-c_1 model is not expected to be equal to the one computed from the flow fields. This may explain these differences.

8.4 Local extinction and flame lift-off

When the oxygen mole-fraction in the coflow is progressively reduced from the baseline case, the flame becomes subjected to local quenching, resulting first in flame lift-off, and finally in total extinction (White et al., 2015). Similar

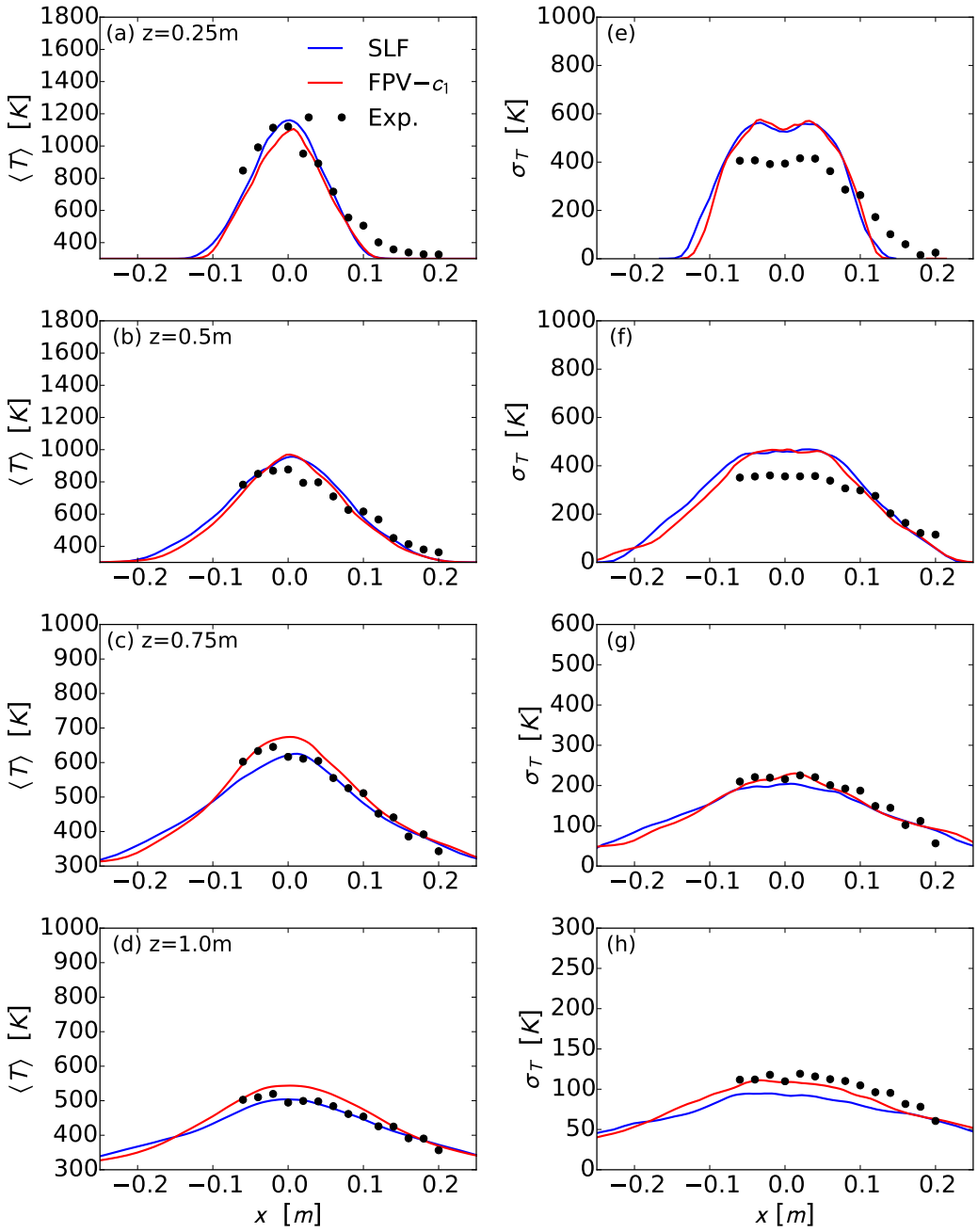

Figure 8.6: Radial profiles of: (a)-(d) mean temperature and (e)-(f) rms values of temperature fluctuations at different heights.

behaviours were observed in laminar-coflow diffusion flames (Takahashi et al., 2007; Guo et al., 2010).

Figure 8.7 shows the axial profiles of mean and rms temperature predicted by the SLF, FPV-c_1 and FPV-c_2 models for $X_{O_2} = 15\%$. The two FPV models reduce significantly the first peak of temperature by about 400 K at $z \leq 0.25\ m$

which indicate that, as expected, the local extinction and the flame lift-off are not captured by the SLF model (Fig. 8.7(a)). Beyond the flame lift-off zone, the flame is ignited and local extinction becomes significantly less important. In this region, the temperature increases rapidly to reach 1000 K and both SLF and FPV models predict similar axial temperature distributions (see Fig. 8.7(a)). On the other hand, the computed axial rms values of temperature fluctuations are almost insensitive to the combustion model.

Snapshots of the radiative emission term predicted by the SLF, FPV-c_1 and FPV-c_2 models are shown in Fig. 8.8. This figure exhibits clear differences close to the burner which are manifestations of the flame lift-off and local extinction. In this region, the flame emission predicted by the SLF model is significantly higher that predicted by both FPV-c_1 and FPV-c_2 models. Above the lift-off regions similar trends are observed for the three models.

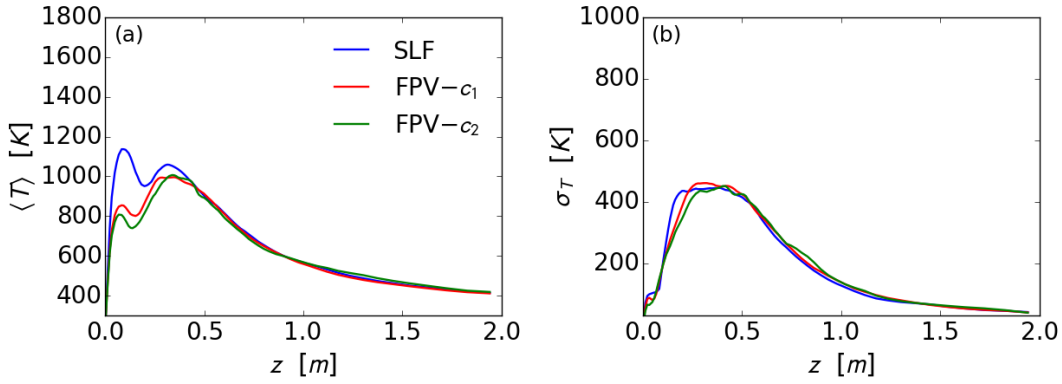

Figure 8.7: Axial profiles of: (a) mean temperature and (b) rms values of temperature fluctuations for X_{O_2} =15%.

Figure 8.9 shows mean and rms temperature obtained for the simulation of the flame with $X_{O_2} = 13\%$. Simulations made with the FPV models show that almost the whole flame region is represented by flamelets in the unstable branch. This suggests that the flame is close to total extinction. This is consistent with the experimental observations when an oxygen anchored is considered (White et al., 2015). However, the present numerical simulations do not consider the oxygen anchor, and, in this case, the experiments show that the fire is fully suppressed. This inconsistency between the FPV simulations and experiments is attributed to the fact that the transition from the unstable branch to the purely mixing branch is not included in the steady FPV models

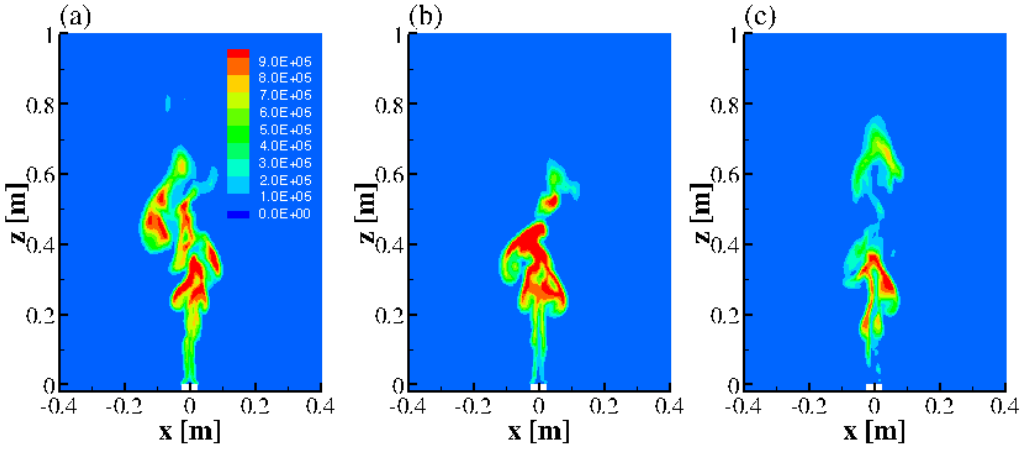

Figure 8.8: Snapshots of instantaneous volumetric emissions predicted by: (a) SLF, (b) FPV-c_1 and (c) FPV-c_2 models for $X_{O_2} = 15\%$.

and, as such, they cannot capture the global extinction.

Whatever the reaction progress variable definition used, the predictions of mean and rms temperature by the FPV models are significantly lower than those obtained from SLF in the flame region. The differences between FPV-c_1 and FPV-c_2 can be explained at the light of the previous discussions concerning these two formulations at low stretch rate and for combustion dominated by the unstable branch. As FPV-c_2 provides a better mapping of the unstable branch at low strain rate than FPV-c_1, the mean and rms temperature distributions obtained with FPV-c_2 are expected to be more accurate. Interestingly, Fig. 8.9 shows that the FPV-c_1 predicts an evident re-igition process at $z = 0.5\ m$ that is not observed with the FPV-c_2 model.

Snapshots of the radiative emission term for $X_{O_2} = 13\%$ are plotted in Fig. 8.10. The SLF model predict a substantially higher emission term because it fails to capture the flame lift-off. Consistently with the discussion made previously on temperature, the flame emission is lower for FPV-c_2 than for FPV-c_1.

8.5 Global radiant fraction

Figure 8.11 shows that the radiant fraction, χ_R, as a function of X_{O_2}. The two sets of experimental data corresponding to oxygen anchored and non-anchored conditions are plotted in this figure. In both cases, the radiant

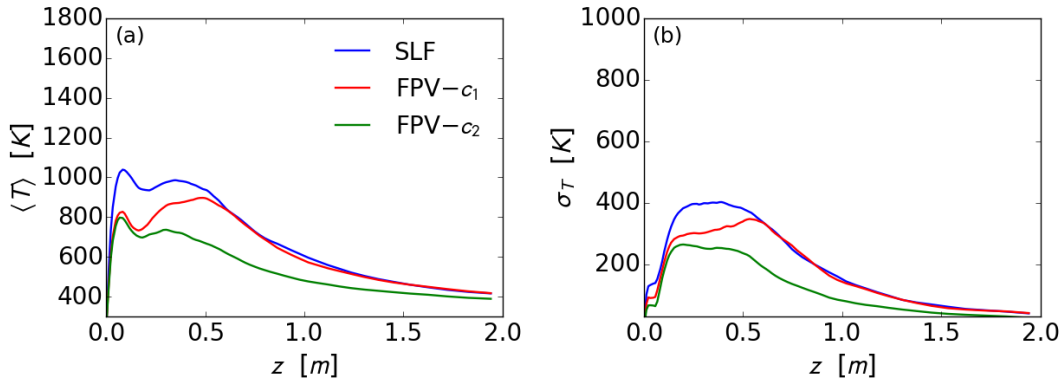

Figure 8.9: Axial profiles of: (a) mean temperature and (b) rms values of temperature fluctuations for $X_{O_2} = 13\%$.

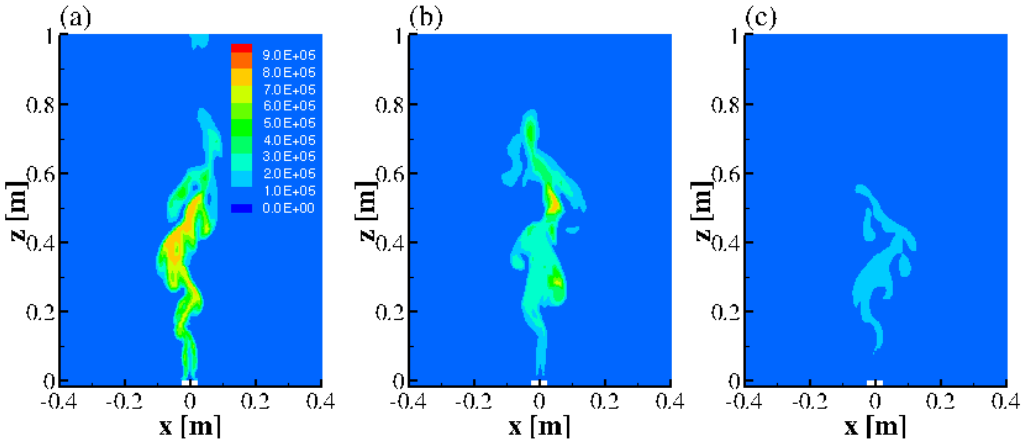

Figure 8.10: Snapshots of instantaneous volumetric emissions predicted by: (a) SLF, (b) FPV-c_1 and (c) FPV-c_2 models for $X_{O_2} = 13\%$.

fraction decreases linearly as X_{O_2} is reduced up to 0.15, approximately. This decrease can be explained by the a reduction in flame temperature and, in turn, in flame emission. As X_{O_2} decreases further, the rate of decrease is significantly enhanced. This change in the slope results from the appearance of local extinction/re-ignition and lift-off processes. In the non-anchored case, the radiant fraction decreases sharply to reach global extinction. In the oxygen anchored case, the rate of decrease is slower and global extinction is reached for an oxygen mole fraction of about 13%.

Figure 8.11 shows also the evolution of χ_R predicted by SLF FPV-c_1 and FPV-c_2 models. The SLF predicts well the decrease in χ_R with X_{O_2} up to $X_{O_2} = 0.15$. This result is expected since no noticeable local extinction/re-ignition

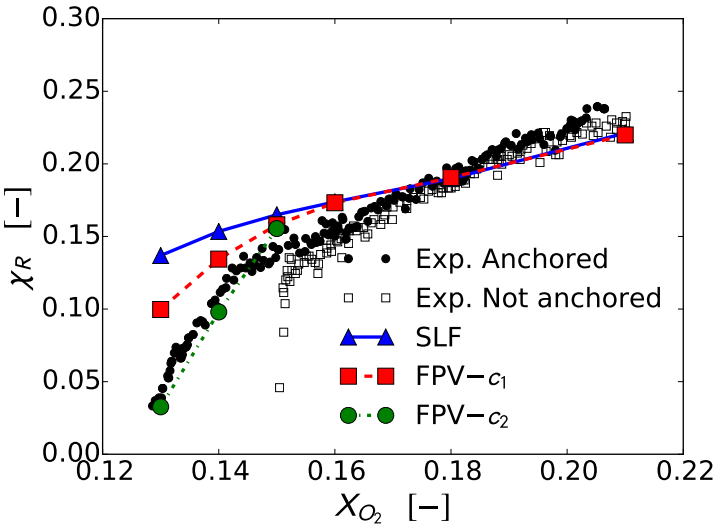

Figure 8.11: Global radiant fraction as a function of oxygen mole-fraction in the oxidizer co-flow, computed from the SLF and FPV models.

processes were observed for these oxygen mole fractions (White et al., 2015). As X_{O_2} is further decreased the SLF model does not capture the change in slope observed experimentally. Similar predictions were obtained by Xu et al. (2020) by using an unsteady non-adiabatic flamelet formulation and the non-grey WSGG radiation model. The FPV models provide solutions in close agreement with the SLF model as long as local extinction processes are not observed. For $X_{O_2} \leq 0.15$, the solutions provided by the FPV models start to deviate from that obtained by the SLF model, showing that these models capture local extinction/re-ignition processes. However, as expected from the previous discussions, none of the FPV models are able to capture the rapid global extinction process observed for the non-anchored case. The rate of decrease in χ_R predicted by FPV-c_2 is higher than predicted by FPV-c_1 and is more consistent with the experimental data. In particular, the FPV-c_2 solutions fit the experimental data obtained in the oxygen anchored case. The better ability of the FPV-c_2 formulation is expected from the previous discussions where FPV-c_2 was found to provide a better mapping of the unstable branch than FPV-c_1 at low strain rate.

8.6 Conclusions

Through this study, the following conclusions can be drawn:

1. As long as the fire plume combustion is complete, both SLF and FPV formulations are capable of correctly predicting the fire plume structure as well as the radiative loss.

2. Consistently with experimental observations, the FPV results show that significant local extinction appears when X_{O_2} is reduced below 16%. In such conditions, the use of FPV models improves significantly the predictions of the SLF model. Nevertheless, the present steady FPV models do not capture the value of X_{O_2} at which the global extinction occurs.

3. The use of a progress variable defined by the sum of CO_2 and H_2O mass fractions provides a better mapping of the flamelets along the unstable branch at low strain rate and, in turn, a better agreement with the experimental data than that defined by the sum of CO_2, H_2O, H_2 and CO mass fractions.

Chapter 9

Conclusions and perspectives

9.1 Conclusions

The objective of this thesis was to develop a LES-based fire simulator including state-of-the-art submodels for combustion and radiation in view to simulate non-sooting well-ventilated and under-ventilated purely buoyant fire plumes. These developments and implementations have been made in *Code_Saturne* of EDF.

The first step was the development and verification of a new second-order low-Mach number variable-density flow solver that was an indispensable prerequisite to describe accurately the strong unsteady processes related to the purely buoyant nature of the flow. Secondly, a significant effort was put on the selection of variable-density subgrid-scale (SGS) stress tensor and scalar flux models. In particular, the performance of a dynamic Smagorinsky model for SGS stress tensor and advanced SGS scalar flux models, including the dynamic eddy diffusivity model, dynamic tensorial diffusivity models and gradient models were assessed in LES of the 1 m helium plume. This study revealed that the dynamic Smagorinsky model and the dynamic eddy diffusivity model are good candidate for the simulations of purely buoyant fire plumes and were applied in the remaining simulations of thesis. A significant effort was also put on the modelling of subgrid-scale turbulence-chemistry interaction and turbulence radiation interaction. Both non-adiabatic steady laminar flamelet and flamelet/progress-variable models coupled to a presumed filtered density function (FDF) were developed and implemented, with the flamelet progress variable being

specifically developed for the modelling of under-oxygenated fires characterized by significant local extinction/re-ignition processes. A special attention was paid on the modelling of the SGS scalar variance and filtered scalar dissipation, that are important quantities for the formulation of flamelet approaches. Investigation of specific models in LES of the McCaffrey fire plume showed the limitations of equilibrium model and that the non-equilibrium model based the second moment transport equation is a good candidate to deal with this problem. Finally, the rank correlated full spectrum k was developed and implemented as gas radiative property model. Other simpler gas radiative property models, involving grey and non-grey formulation of the weighted-sum-of-grey gases, were also implemented.

The model was exhaustively validated by simulating several well-documented fire plumes of the literature. It was found that the model is able to reproduce with high fidelity the dynamic and radiative structures of non-luminous fire plumes in both ventilated and under-ventilated configurations. In particular, the flamelet progress variable allows addressing oxygen-diluted oxidizer conditions close to extinction where significant local ignition/re-ignition processes are observed.

In addition, the simulations of these fire plumes was used to address specific modelling issues and the main conclusions from these studies are the following:

- Laminar instabilities that form periodically at the base of purely buoyant fire plumes and grow to generate energy containing structures that govern the mixing process are initially non-dissipative and, as such, cannot be handle by conventional subgrid-scale models of turbulence that are dissipative in nature. As a consequence, a great attention has to be paid to have a sufficiently refined grid to resolve these instabilities. In addition, numerical simulations revealed that burner boundary geometries affect the formation and growth of these instabilities and the fire plume dynamics. As a consequence, the experimental burner boundary conditions have to be reproduced scrupulously in the simulations for relevant validations of numerical models.
- Concerning the gas radiative property models, the grey WSGG models have to be avoided since they fail to reproduce the radiative structure of the fire plume. In the opposite way, the non-grey WSGG model leads to

predictions of radiative outputs within 10% - 15% of the RCFSK and can be a reasonable alternative for non-sooting pool fires.

- Neglecting subgrid-scale turbulence-radiation interaction affects significantly the predictions of the fire plume structure and radiative heat flux even for medium-scale pool fires. These effects become of increasing importance as the size of the pool fire increases.

9.2 Perspectives

This work is the part of a development program of a LES-based fire simulator to model fire spread in nuclear plants. It was a first step in these developments and, as such, is limited to the modelling a non-luminous fire plumes in non-confined environments although under-ventilated configurations were considered. As such, the perspectives of the work and the future developments are exhaustive. Among them, future works will include obviously soot production processes and related heat transfer, the coupling between gas phase and condensed phase through the development of thermal degradation models, the inclusion of solid inert or flammable walls and the associated conjugated heat transfer,... As a consequence, in order to avoid an exhaustive description of such new problems, the perspective will deal with improvements of the current fire model and the related physics:

- As discussed previously, laminar instabilities that form close to the edge of burner and plays an important role in fire dynamics cannot be handle by the current subgrid-scale turbulence models. Some attempts have been made to develop subgrid-scale models, which could reproduce the effects of such mixing related to the growth of these instabilities on the fire plume dynamics, without having to resolve the details of their dynamics (Tieszen et al., 2004). However, no conclusive models have been reported to date and this task constitutes an important fundamental problem in the modelling of the fire plume dynamics.
- The non-adiabatic flamelet/presumed FDF models results in look-up tables where the thermochemical state variables are typically stored as a function of the independent parameters. In the models developed in the present study, the independent variables are the filtered mixture fraction,

mixture fraction variance, scalar dissipation rate or progress variable and the enthalpy defect. This results in 4-entry look-up tables that need to be interpolated at each iteration of the computation sequence to retrieve the filtered variables. Currently, the thermochemical state variables are stored in structured manner as a function of the independent parameters and 4D linear interpolations are performed to retrieve the desired variables. The size of the chemistry database will increase in the future with the development of new applications, introducing severe limitations on the resolution that can be afforded in multi-dimensional look-up tables. Several methods have been proposed to address this problem, including the use of orthogonal polynomials (Turanyi, 1994), in situ adaptive tabulation (ISAT) (Pope, 1997), artificial neural networks (Ihme et al., 2008), high-dimensional model representation (Rabitz and Alis, 1999), self-similarity properties (Ribert et al., 2006), adaptive Cartesian meshes (Xia et al., 2006) and the kd-trees (Shunn, 2009).

Bibliography

Archambeau, F., Méchitoua, N., and Sakiz, M. (2004). "Code_Saturne: a Finite Volume Code for the Computation of Turbulent Incompressible Flows". In: *International Journal on Finite Volumes* 1.

Babrauskas, V. (1983). "Estimating large pool fire burning rates". In: *Fire technology* 19.4, pp. 251–261.

Bakosi, J. and Ristorcelli, J. R. (2010). "Exploring the beta-pdf in variable-density turbulent mixing". In: *J. Turbulence* 11.

Balarac, G., Pitsch, H., and Raman, V. (2008). "Development of a dynamic model for the subfilter scalar variance using the concept of optimal estimators". In: *Phys. Fluids* 20, p. 035114.

Bedford, K. W. and Yeo, W. K. (1993). "Conjective filtering procedures in surface water flow and transport". In: *Large Eddy Simulation of Complex Engineering and Geophysical Flows*. Ed. by B. Galperin and S. A. Orszag. Cambridge University Press.

Blanquart, G. and Pitsch, H. (2008). "Large-eddy simulation of a turbulent buoyant helium plume". In: *Annual Research Briefs*. Center for Turbulence Research, pp. 245–252.

Bösenhofer, M., Wartha, E. M., Jordan, C., and Harasek, M. (2018). "The eddy dissipation Concept-Analysis of different fine structure treatments for classical combustion". In: *Energies* 11, p. 1902.

Boudier, G., Gicquel, L. ., and Poinsot, T. J. (2008). "Effects of mesh resolution on large eddy simulation of reacting flows in complex geometry combustors". In: *Combust. Flame* 155, pp. 196–214.

Branley, N. and Jones, W. P. (2001). "Large Eddy Simulation of a turbulent non-premixed flame". In: *Combust. Flame* 127, pp. 1914–1934.

Brown, A., Bruns, M., Gollner, M., Hewson, J., Maragkos, G., Marshall, A., et al. (2018). "Proceedings of the first workshop organized by the IAFSS Work-

ing Group on Measurement and Computation of Fire Phenomena (MaCFP)". In: *Fire Safety J.* 101. DOI:10.1016/j.firesaf.2018.08.009, pp. 1–17.

Cai, J. and Modest, M. F. (2014). "Improved full-spectrum k-distribution implementation for inhomogeneous media using a narrow-band database". In: *J. Quant. Spectr. Rad. Transf.* 141, pp. 65–72.

Carbonell, D., Perez-Segarra, C. D., Coelho, P. J., and Oliva, A. (2009). "Flamelet mathematical models for non-premixed laminar combustion". In: *Combust. Flame* 156, pp. 334–347.

Cetegan, B. M. and Ahmed, T. A. (1993). "Experiments on the periodic instability of buoyant plumes and pool fires". In: *Combust. Flame* 93. DOI:10.1016/0010-2180(93)90090-P, pp. 157–184.

Cetegen, B. M. (1998). "A phenomenological model of near-field fire entrainment". In: *Fire safety journal* 31.4, pp. 299–312.

Cetegen, B. M. and Ahmed, T. A. (1993). "Experiments on the periodic instability of buoyant plumes and pool fires". In: *Combust. Flame* 93. DOI:10.1016/0010-2180(93)90090-P, pp. 157–184.

Cetegen, B. M. and Kasper, K. D. (1996). "Experiments on the oscillatory behavior of buoyant plumes of helium and helium-air mixtures". In: *Phys. Fluids* 8. DOI:10.1063/1.869075, pp. 2974–2984.

Chatterjee, P., Wang, Y., Meredith, K. V., and Dorofeev, S. B. (2015). "Application of a subgrid soot radiation model in the numerical simulation of a heptane pool fire". In: *Proc. Combust. Inst.* 35, pp. 2573–2580.

Chen, Z., Wen, J., Xu, B., and Dembele, S. (2014a). "Extension of the eddy dissipation concept and smoke point soot model to the LES frame for fire simulations". In: *Fire Safety J.* 64, pp. 12–26.

Chen, Z., Wen, J., Xu, B., and Dembele, S. (2014b). "Large eddy simulation of a medium-scale methanol pool fire using the extended eddy dissipation concept". In: *I. J. Heat Mass Transf.* 70, pp. 389–408.

Cheung, S. C. P. and Yeoh, G. H. (2009). "A fully-coupled simulation of vortical structures in a large-scale buoyant pool fire". In: *Int. J. Therm. Sci.* 48, pp. 2187–2202.

Chung, W. and Devaud, C. B. (2008). "Buoyancy corrected $k-\epsilon$ models and large eddy simulation applied to a large axisymmetric helium plume". In: *Int. J. Num. Meth. Fluids* 58. DOI:10.1002/fld.1720, pp. 57–89.

Code_Saturne (n.d.). http://www.code-saturne.org.

Coelho, F. R. and França, F. H. R. (2018). "WSGG correlations based on HITEMP2010 for gas mixtures of H2O and CO2 in high total pressure conditions". In: *J. Heat Mass Transfer Transf.* 127, pp. 105–114.

Coelho, P. J. (2007). "Numerical simulation of the interaction between turbulence and radiation in reactive flows". In: *Prog. Ener. Combust. Sci.* 33, pp. 311–383.

Coelho, P. J. (2009). "Approximate solutions of the filtered radiative transfer equation in large eddy simulations of turbulent reactive flows". In: *Combust. Flame* 156, pp. 1099–1110.

Coelho, P. J. (2014). "Advances in the discrete ordinates and finite volume methods for the solution of radiative heat transfer problems in participating media". In: *Quant. Spectrosc. Rad. Transf.* 145, pp. 121–146.

Consalvi, J. L., Andre, F., Coelho, F., Franca, F., Nmira, F., Galtier, M., et al. (2019). "Assessment of engineering gas radiative property models in high pressure turbulent diffusion flames". In: *RAD 19, Athens, Greece.*

Consalvi, J. L., Nmira, F., and Kong, W. (2018). "On the modeling of the filtered radiative transfer equation in large eddy simulations of lab-scale sooting turbulent diffusion flames". In: *J. Quant. Spectr. Rad. Transf.* 221, pp. 51–60.

Consalvi, J. (2012). "Influence of turbulence–radiation interactions in laboratory-scale methane pool fires". In: *Int. J. Therm. Sci.* 60, pp. 122–130. DOI: /10.1016/j.ijthermalsci.2012.05.013.

Consalvi, J. and Nmira, F. (2019). "Modeling of large-scale under-expanded hydrogen jet fires". In: *Proc. Combust. Inst.* 37, pp. 3943–3950. DOI: /10.1016/j.proci.2018.05.022.

Cook, A. and Riley, J. (1994). "A subgrid model for equilibrium chemistry in turbulent flows". In: *Phys. Fluids* 6, pp. 2868–2870.

Cook, A. W. (1997). "Determination of the constant coefficient in scale similarity models of turbulence". In: *Phys. Fluids* 9, pp. 1485–1487.

Cox, G. and Chitty, R. (1980). "A study of the deterministic properties of unbounded fire plumes". In: *Combust. Flame* 39, pp. 191–209.

Cox, G. and Chitty, R. (1982). "Some stochastic properties of fire plumes". In: *Fire Mater.* 6, pp. 127–134.

Cox, G. and Chitty, R. (1984). "Some source-dependent effects of unbounded fires". In: *Combust. Flame* 60, pp. 219–232.

Cox, G. and Drysdale, D. D. (1995). "Combustion fundamentals of fire". In: *Fire Safety Journal* 25.2, pp. 171–174.

Craske, J. and Reeuwijk, M. van (2013). "Robust and accurate open boundary conditions for incompressible turbulent jets and plumes". In: *Computers and Fluids* 86, pp. 284–297.

Crauford, N. L., Liew, S., and Moss, J. (1985). "Experimental and numerical simulation of a buoyant fire". In: *Combust. Flame* 31, pp. 63–77.

Daly, B. J. and Harlow, F. H. (1970). "Transport equations in turbulence". In: *Phys. Fluids* 13. DOI:10.1063/1.1692845, pp. 2634–2649.

De Ris, J. (1979). "Fire radiation - a review". In: *Proc. Combust. Inst.*, pp. 1003–1016.

Demarco, R., Consalvi, J., Fuentes, A., and Melis, S. (2011). "Assessment of Radiative Property Models in Non-Gray Sooting Media". In: 50.Int. J. Thermal Sci. Pp. 1672–1684.

Denison, M. K. and Webb, B. W. (1993). "A spectral line based weighted-sum-of-gray-gases model for arbitrary RTE solvers". In: *J. Heat Transf.* 115, pp. 1004–1012.

Denison, M. K. and Webb, B. W. (1995a). "Development and application of an absorption line blackbody distribution function for CO2". In: *Int. J. Heat Mass Transf.* 38, pp. 1813–1821.

Denison, M. K. and Webb, B. W. (1995b). "The spectral-line weighted-sum-of-gray-gases model for H2O/CO2 mixtures". In: *J. Heat Transf.* 117, pp. 788–792.

Denison, M. K. and Webb, B. W. (1995c). "The spectral-line-based weighted-sum-of-gray-gases model in nonisothermal nonhomogeneous media". In: *J. Heat Transf.* 117, pp. 359–365.

Desjardin, P. E. (2005). "Modeling of conditional dissipation rate for flamelet models with application to large eddy simulation of fire plumes". In: *Combust. Sci. and Tech.* 177, pp. 1883–1916.

Desjardin, P. E., O'Hern, T. J., and Tieszen, S. R. (2004). "Large eddy simulation and experimental measurements of the near-field of a large turbulent helium plume". In: *Phys. Fluids* 16. DOI:10.1063/1.1689371, pp. 1866–1883.

Desjardins, O., Blanquart, G., Balarac, G., and Pitsch, H. (2008). "High order conservative finite difference scheme for variable density low Mach number

turbulent flows". In: *Journal of Computational Physics* 227.15, pp. 7125–7159.

Ditch, B. D., Ris, J. L. de, Blanchat, T. K., Chaos, M., Bill Jr, R. G., and Dorofeev, S. B. (2013). "Pool fires–An empirical correlation". In: *Combustion and flame* 160.12, pp. 2964–2974.

Echekki, T. and Mastorakos, E. (2010). *Turbulent Combustion Modeling. Advances, New Trends and Perspectives*. New York: Springer Verlag.

Ertesvåg, I. S. and Magnussen, B. F. (2000). "The Eddy Dissipation Turbulence Energy Cascade Model". In: *Combust. Sci. and Tech.* 159, pp. 213–235.

Fabre, Y. and Balarac, G. (2011). "Development of a new dynamic procedure for the Clark model of the subgrid-scale scalar flux using the concept of optimal estimator". In: *Phys. Fluids* 23, 115103. DOI:10.1063/1.3657090.

FireFoam (n.d.). http://code.google.com/p/firefoam-dev.

Fischer, S. J., Hardouin-Duparc, B., and Grosshandler, W. (1987). "The structure and radiation of an ethanol pool fire". In: *Combust. Flame* 70, pp. 291–306.

Fraga, G. C., Centeno, F. R., Petry, A. P., Coelho, P. J., and França, F. H. R. (2019). "On the individual importance of temperature and concentration fluctuations in the turbulence-radiation interaction in pool fires". In: *J. Heat Mass Transf.* 136, pp. 1079–1089.

Ghoniem, A. F., Lakkis, I., and Soteriou, M. (1993). "Numerical simulation of the dynamics of large fire plumes and the phenomenon of puffing". In: *Proc. 26th Symposium (International) on Combustion*. DOI:10.1016/S0082-0784(96)80375-4.

Grimech 3.0 (2019). http://combustion.berkeley.edu/gri-mech/.

Guo, H., Min, J., Galizzi, C., Escudie, D., and Baillot, F. (2010). "A numerical study on the effects of CO_2/N_2/Ar addition to air on liftoff of a laminar CH_4/air diffusion flame". In: *Combustion Science and Technology* 182, pp. 549–1563.

Gupta, A., Haworth, D. C., and Modest, M. F. (2013). "Turbulence-radiation interactions in large-eddy simulations of luminous and nonluminous nonpremixed flames". In: *Proc. Combust. Inst.* 34, pp. 1281–1288.

Hamins, A., Fischer, S. J., Kashiwagi, T., Klassen, M. E., and Gore, J. P. (1994). "Heat Feedback to the Fuel Surface in Pool Fires". In: *Combust. Sci. Technol.* 97, pp. 37–62.

Hamins, A. and Lock, A. (2016). *The structure of a moderate-scale methanol pool fire*. Tech. rep. Technical Note 1928. US Department of Commerce, National Institute of Standards and Technology.

Heskestad, G. (1984). "Engineering relations for fire plumes". In: *Fire Safety J* 7, pp. 25–32.

Higgins, C. W., Parlange, M. B., and Meneveau, C. (2004). "The heat flux and the temperature gradient in the lower atmosphere". In: *Geophys. Res. Lett.* 31 L22105. DOI:10.1029/2004GL020053, pp. 1–5.

Hu, L., Hu, J., and Ris, J. L. de (2015). "Flame necking-in and instability characterization in small and medium pool fires with different lip heights". In: *Combustion and Flame* 162.4, pp. 1095–1103.

Hu, Z., Utiskul, Y., Quintiere, J. G., and Trouve, A. (2007). "Towards large eddy simulations of flame extinction and carbon monoxide emission in compartment fires". In: *Proceedings of the Combustion Institute* 31.2, pp. 2537–2545.

Ihme, M., Marsden, A., and Pitsch, H. (2008). "Generation of optimal artificial neural networks using a pattern search algorithm: Application to approximation of chemical systems". In: *Neural Computation* 20, pp. 573–601.

Ihme, M. and Pitsch, H. (2008). "Modeling of radiation and nitric oxide formation in turbulent nonpremixed flames using a flamelet/progress variable formulation". In: *Phys. Fluids* 20, p. 055110.

Ihme, M., Cha, C. M., and Pitsch, H. (2005). "Prediction of local extinction and re-ignition effects in non-premixed turbulent combustion using a flamelet/progress variable approach". In: *Proceedings of the Combustion Institute* 30.1, pp. 793–800.

Jain, A. and Kim, S. H. (2019). "On the non-equilibrium models for subfilter scalar variance in large eddy simulation of turbulent mixing and combustion". In: *Phys. Fluids* 31, p. 025112.

Jensen, K. A., Ripoll, J. F., Wray, A. A., Joseph, D., and Hafi, M. E. (2007). "On various modeling approaches to radiative heat transfer in pool fires". In: *Combust. Flame* 148, pp. 263–279.

Jiménez, C., Ducros, F., Cuenot, B., and Bédat, B. (2001). "Subgrid scale variance and dissipation of a scalar field in large eddy simulations". In: *Phys. Fluids* 13, pp. 1748–1754.

Jiménez, J., Linan, A., Rogers, M. M., and Higuera, F. J. (1997). "A priori testing of subgrid models for chemically reacting non-premixed turbulent shear flows". In: *J. Fluid Mech.* 349, pp. 149–171.

Kaul, C. and Raman, V. (2011). "A posteriori analysis of numerical errors in subfilter scalar variance modeling for large eddy simulation". In: *Phys. Fluids* 23, p. 035102.

Kaul, C., Raman, V., Balarac, G., and Pitsch, H. (2009). "Numerical errors in the computation of subfilter scalar variance in large eddy simulations". In: *Phys. Fluids* 21, p. 055102.

Kaul, C., Raman, V., Knudsen, E., Richardson, E., and Chen, J. (2013). "Large eddy simulation of a lifted ethylene flame using a dynamic nonequilibrium model for subfilter scalar variance and dissipation rate". In: *Proc. Combust. Inst.* 34, pp. 1289–1297.

Kemenov, K., Wang, H., and Pope, S. B. (2012). "Modelling effects of subgrid-scale mixture fraction variance in LES of a piloted diffusion flame". In: *Combust. Theory Mod.* 16, pp. 611–638.

Kim, S. H. and Huh, K. Y. (2000). "A new angular discretization scheme of the finite volume method for 3-D radiative heat transfer in absorbing, emitting and anisotropically scattering media". In: *Int. J. Heat Mass Transf.* 43, pp. 1233–1242.

Kim, S. C., Lee, K. Y., and Hamins, A. (2019). "Energy balance in medium-scale methanol, ethanol, and acetone pool fires". In: *Fire Safety Journal* 107, pp. 44–53.

Klassen, M. and Gore, J. P. (1992). *Structure and radiation properties of pool fires*. Tech. rep. NIST-GCR-94-651. NIST.

Knudsen, E., Richardson, E., Doran, E., Pitsch, N., and Chen, J. (2012). "Modeling scalar dissipation and scalar variance in large eddy simulation: Algebraic and transport equation closures". In: *Phys. Fluids* 24, p. 055103.

Koo, H., Hewson, J. C., Domino, S. P., and Knaus, R. C. (2017). *Model sensitivities in LES predictions of buoyant methane fire plumes*. Tech. rep. SAND2017-9700C. Albuquerque, NM, USA: Sandia National Laboratories.

Le, V. M., Marchand, A., Verma, S., Xu, R., White, J., Marshall, A., et al. (2019). "Simulations of the coupling between combustion and radiation in a turbulent line fire using an unsteady flamelet model". In: *Fire Safety Journal* 106, pp. 105–113.

Lecoustre, V., Narayanan, P., Baum, H. R., and Trouve, A. (2011). "Local extinction of diffusion flames in fires". In: *Fire Safety Science* 10, pp. 583–595.

Lee, J. C. C. H. S. and Patankar, S. V. (1990). "Finite volume method for radiation heat transfer". In: *J. Thermophys Heat Transf.* 8, pp. 419–425.

Li, J., Zhao, Z., Kazakov, A., Chaos, M., Dryer, F. L., and Jr., J. J. S. (2007). "A comprehensive kinetic mechanism for CO, CH2O, and CH3OH combustion". In: *Int. J. Chem. Kinetics* 39, pp. 109–136.

Lilly, D. K. (1992). "A proposed modification of the Germano subgrid-scale closure method". In: *Phys. Fluids A* 4, pp. 633–635.

Liu, F., Consalvi, J.-L., Coelho, P., Andre, F., Gu, M., Solovjov, V., et al. (2020a). "The impact of radiative heat transfer in combustion processes and its modeling with a focus on turbulent flames". In: *Fuel* 281, p. 118555.

Liu, Y., Liu, G., Liu, F., and Consalvi, J. L. (2020b). "Effects of the K-value solution schemes on radiation heat transfer modelling in oxy-fuel flames using the full-Spectrum Correlated K-distribution Method". In: *App. Therm. Energy* 170, p. 114986.

Lu, H. and Porté-Agel, F. (2013). "A modulated gradient model for scalar transport in large-eddy simulation of the atmospheric boundary layer". In: *Phys. Fluids* 25, 015220. DOI:10.1063/1.4774342.

Lutz, A. E., Kee, R. J., Grcar, J. F., and Rupley, F. M. (1996). *OPPDIF: a fortran program por computing opposed-flow diffusion flames*. Tech. rep. SAN96-824. Albuquerque, NM, USA: Sandia National Laboratories.

Ma, T. G. and Quintiere, J. G. (2003). "Numerical simulation of axi-symmetric fire plumes: accuracy and limitations". In: *Fire Safety J.* 38, pp. 467–492.

Maragkos, G., Beji, T., and Merci, B. (2017). "Advances in modelling in CFD simulations of turbulent gaseous pool fires". In: *Combust. Flame* 181, pp. 22–38.

Maragkos, G., Beji, T., and Merci, B. (2019). "Towards predictive simulations of gaseous pool fires". In: *Proc. Combust. Inst.* 37, pp. 3927–3934.

Maragkos, G. and Merci, B. (2020). "On the use of dynamic turbulence modelling in fire applications". In: *Combustion and Flame* 216, pp. 9–23.

Maragkos, G. and Merci, B. (2017). "Large Eddy Simulations of CH4 Fire Plumes". In: *Flow Turb. Combust.* 99, pp. 239–278.

Maragkos, G., Rauwoens, P., Wang, Y., and Merci, B. (2013). "Large Eddy Simulations of the Flow in the Near-Field Region of a Turbulent Buoyant

Helium Plume". In: *Flow Turbulence Combust.* 90. DOI:10.1007/s10494-012-9437-5, pp. 511–543.

McCaffrey, B. J. (1979). *Purely Buoyant Diffusion Flames Some Experimental Results*. Tech. rep. NBSIR 79-1910. NIST.

McGrattan, K., Hostikka, S., McDermott, R., Floyd, J., Weinschenk, C., and Overholt, K. (2014). *Dynamics Simulator Technical Reference Guide Volume 1: Mathematical model*. Tech. rep. NIST Special Publication 1018 Sixth Edition.

Miranda, F. C., Coelho, P. J., Mare, F. di, and Janicka, J. (2019). "Study of turbulence-radiation interactions in large-eddy simulation of scaled Sandia flame D". In: *J. Quant. Spectr. Rad. Transf.* 228, pp. 47–56.

Miranda, F. C., Coelho, P. J., Strölhe, J., and Janicka, J. (2020). "Large-eddy simulation of a bluff-body stabilised nonpremixed flame with radiation heat transfer". In: *Combust. Theory and Modelling*.

Modest, M. F. (2013). *Radiative Heat Transfer, Third edition*. New York: Academic Press.

Modest, M. F. and Haworth, D. C. (2016). *Radiative Heat Transfer in Turbulent Combustion Systems: Theory and Applications*. New York: Springer.

Modest, M. F. and Riazzi, R. J. (2005). "Assembly full spectrum k-distribution from a narrow band database: effects of mixing gases, gases and non-gray absorpting particles and non-gray scatters in non-gray enclosures". In: *J. Quant. Spectr. Rad. Transf.* 90, pp. 169–189.

Modest, M. F. and Zhang, H. (2002). "The full spectrum correlated-k distribution for thermal radiation from molecular gas particulate mixtures". In: *ASME J. Heat Transf.* 124, pp. 30–38.

Moin, P., Squires, K., Cabot, W., and Lee, S. (1991a). "A dynamic subgrid-scale model for compressible turbulence and scalar transport". In: *Phys. Fluids A* 3, pp. 2746–2757.

Moin, P., Squires, K., Cabot, W., and Lee, S. (1991b). "A dynamic subgrid-scale model for compressible turbulence and scalar transport". In: *Physics of Fluids A: Fluid Dynamics* 3.11, pp. 2746–2757.

Mullyadzhanov, R., Palkin, E., Nićeno, B., Vervisch, L., and Hanjalić, K. (2016). "Verification of a low Mach variable-density Navier-Stokes solver for turbulent combustion". In: *Journal of Physics: Conference Series* 754. DOI:10.1088/1742-6596/754/6/062005, p. 062005.

Narayanan, P., Baum, H. R., and Trouvé, A. (2011). "Effect of soot addition on extinction limits of luminous laminar counterflow diffusion flames". In: *Proceedings of the Combustion Institute* 33.2, pp. 2539–2546.

Nmira, F., Ma, L., and Consalvi, J. L. (2020a). "Assessment of subfilter-scale turbulence-radiation interactions in non-luminous pool fires". In: *Accepted for publication in Proc. Combust. Inst.*

Nmira, F., Ma, L., and Consalvi, J. L. (2020b). "Turbulence-Radiation Interaction in Large Eddy Simulation of Non-Luminous Pool Fires". In: *Accepted for presentation at the 38th Symposium on Combustion.*

O'Hern, T. J., Weckman, E. J., Gerhart, A. L., Tieszen, S. R., and Schefer, R. W. (2005). "Experimental study of a turbulent buoyant helium plume". In: *J. Fluid Mech.* 544. DOI:10.1017/S0022112005006567, pp. 143–171.

Oberkampf, W. L. and Trucano, T. G. (2002). "Verification and validation in computational fluid dynamics". In: *Rev. Article Prog. Aero. Sci.* 38. DOI:10.1016/S0376-0421(02)00005-2, pp. 209–272.

Orloff, L. (1981). "Simplified radiation modeling of pool fires". In: *Symposium (International) on Combustion.* Vol. 18. 1. Elsevier, pp. 549–561.

Orloff, L. and De Ris, J. (1982). "Froude modeling of pool fires". In: *Symposium (International) on Combustion.* Vol. 19. 1. Elsevier, pp. 885–895.

Panjwani, B., Ertesvåg, I. S., and A. Gruber, A. K. E. R. (2010). "Turbulence combustion closure model based on the Eddy dissipation concept for large eddy simulation". In: *Advances in Fluid Mechanics VIII* 69, pp. 27–38.

Pearson, J. T., Webb, B. W., Solovjov, V. P., and Ma, J. (2014). "Efficient representation of the absorption line blackbody distribution function for H2O, CO2 and CO at variable temperature, mole fraction, and total pressure". In: *J. Quant. Spectr. Rad. Transf.* 138, pp. 82–96.

Peng, S. and Davidson, L. (2002). "On a subgrid-scale heat flux model for large eddy simulation of turbulent thermal flow". In: *Int. J. Heat Mass Transfer* 45. DOI:10.1016/S0017-9310(01)00254-X, pp. 1393–1405.

Peters, N. (1984). "Laminar diffusion flamelet models in non-premixed turbulent combustion". In: *Prog. Energy Combust. Sci.* 10, pp. 319–339.

Pierce, C. D. and Moin, P. (1998). "Dynamic model for subgrid-scale variance and dissipation rate of a conserved scalar". In: *Phys. Fluids* 10, pp. 3041–3044.

Pierce, C. D. and Moin, P. (2001). *Progress-variable approach for large-eddy simulation of turbulent combustion.* stanford university California, USA.

Pierce, C. D. and Moin, P. (2004). "Progress-variable approach for large-eddy simulation of non-premixed turbulent combustion". In: *J. Fluid Mech.* 504, pp. 73–97.

Pitsch, H. (1998). *FlameMaster: A C++ computer program for 0D combustion and 1D laminar flame calculations.*

Pitsch, H. and Peters, N. (1998). "A consistent flamelet formulation for non-premixed combustion considering differential diffusion effects". In: *Combust. Flame* 114, pp. 26–40.

Pitsch, H. (2006). "Large-eddy simulation of turbulent combustion". In: *Annu. Rev. Fluid Mech.* 38, pp. 453–482.

Poinsot, T. and Veynante, D. (2005). *Theoretical and numerical combustion.* RT Edwards, Inc.

Pope, S. B. (1997). "Computationally efficient implementation of combustion chemistry using in situ adaptive tabulation". In: *Combustion theory and modelling* 1, pp. 41–63.

Pope, S. B. (2000). *Turbulent flows.* Cambridge University Press.

Qin, Z., Lissianski, V. V., Yang, H., Gardiner, W. C., Davis, S. G., and Wang, H. (2000). "Combustion chemistry of propane: A case study of detailed reaction mechanism optimization". In: *Proc. Combust. Inst.* 28, pp. 1663–1669.

Rabitz, H. and Alis, O. (1999). "General foundations of high-dimensional model representations". In: *Journal of mathematical chemistry* 25, pp. 197–233.

Raithby, G. D. and Chui, E. H. (1990). "A finite-volume method for predicting a radiant heat transfer in enclosures with participating media". In: *J. Heat Transf.* 112, pp. 415–423.

Ribert, G., Gicquel, O., Darabiha, N., and Veynante, D. (2006). "Tabulation of complex chemistry based on self-similar behavior of laminar premixed flames". In: *Combustion and Flame* 146, pp. 649–664.

Rodrigues, P., Gicquel, O., Franzelli, B., N, N. D., and Vicquelin, R. (2019). "Analysis of radiative transfer in a turbulent sooting jet flame using a Monte Carlo method coupled to large eddy simulation". In: *Quant. Spectrosc. Rad. Transf.* 235, pp. 187–203.

Rothman, L. S., Gordon, I. E., Barber, R. J., Dothe, H., Gamache, R. R., Goldman, A., et al. (2010). "HITEMP: the high-temperature molecular spectroscopic database". In: *J. Quant. Spectrosc. Radiat. Transf.* 111, pp. 2139–2150.

Saxena, P. and Williams, F. (2007). "Numerical and experimental studies of ethanol flames". In: *Proc. Combust. Inst.* 31, pp. 1149–1156. DOI: /10.1016/j.proci.2006.08.097.

Shabbir, A. and George, W. K. (1994). "Experiments on a round turbulent buoyant plume". In: *J. Fluid Mech.* 275. DOI:10.1017/S0022112094002260, pp. 1–32.

Shunn, L. (Mar. 2009). "Large-eddy simulation of combustion sysytems with convective heat-loss". PhD thesis. Stanford University.

Shunn, L., Ham, F., and Moin, P. (2012). "Verification of variable-density flow solvers using manufactured solutions". In: *J. Comput. Phys.* 231. DOI:10.1016/j.jcp.2012.01.027, pp. 3801–3827.

Sikic, I., Dembele, S., and Wen, J. (2019). "Non-grey radiative heat transfer modelling in LES-CFD simulated methanol pool fires". In: *J. Quant. Spectrosc. Radiat. Transf.* 234, pp. 78–89.

Snegirev, A. (2004). "Statistical modeling of thermal radiation transfer in buoyant turbulent diffusion flames". In: *Combust. Flame* 136, pp. 51–71.

Snegirev, A. (2015). "Perfectly stirred reactor model to evaluate extinction of diffusion flame". In: *Combustion and Flame* 162.10, pp. 3622–3631.

Snegirev, A., Markus, E., Kuznetsov, E., Harris, J., and Wu, T. (2018). "On soot and radiation modeling in buoyant turbulent diffusion flames". In: *Heat Mass Transf.* 54, pp. 2275–2293.

Snegirev, A. and Tsoy, A. S. (2015). "Treatment of local extinction in CFD fire modeling". In: *Proceedings of the Combustion Institute* 35.3, pp. 2519–2526.

Solovjov, V. P., Andre, F., Lemonnier, D., and Webb, B. W. (2017). "The rank correlated SLW model of gas radiation in non-uniform media". In: *J. Quant. Spectr. Rad. Transf.* 197, pp. 26–44.

Solovjov, V. P., Webb, B. W., and Andre, F. (2018). "The rank correlated FSK model for prediction of gas radiation in non-uniform media, and its relationship to the rank correlated SLW model". In: *J. Quant. Spectr. Rad. Transf.* 214, pp. 120–132.

Sung, K., Chen, J., Bundy, M., Fernandez, M., and Hamins, A. (2020). *The Thermal Character of a 1 m Methanol Pool Fire*. Tech. rep. NIST STechnical Note 2083.

Takahashi, F., Linteris, G. T., and Katta, V. R. (2007). "Extinguishment mechanisms of coflow diffusion flames in a cup-burner apparatus". In: *Proceedings of the Combustion Institute* 31, pp. 2721–2729.

The 1st Measurement and Computation of Fire Phenomena (MaCFP) Workshop (2017). http://www.iafss.org/macfp/.

Tieszen, S. R., Pitsch, H., Blanquart, G., and Abarzhi, S. (2004). "Toward the development of a LES-SGS closure model for buoyant plumes". In: *Proc. of the Summer Program, Center for Turbulence Research, Stanford*.

Tieszen, S. and Gritzo, L. (2008). *Chapter 2. Transport phenomena that affect heat transfer in fully turbulent fires*. in Transport Phenomena in Fire, M. Faghri and b. Sudén (Eds.) WIT Press, Southampton, pp. 25–68.

Turanyi, T. (1994). "Parameterization of reaction mechanisms using orthogonal polynomials". In: *Computaional chemistry* 18, pp. 45–54.

Vaari, J., Floyd, J., and McDERMOTT, R. (2011). "CFD simulations on extinction of co-flow diffusion flames". In: *Fire Safety Science* 10, pp. 781–793.

Ventosa, M. J. (2015). "Numerical simulation of turbulent diffusion flames using flamelet models on unstructured meshes". In:

Versteeg, H. K. and Malalasekera, W. (2007). *An introduction to computational fluid dynamics: the finite volume method*. Pearson education.

Vilfayeau, S., Ren, N., Wang, Y., and Trouvé, A. (2015). "Numerical simulation of under-ventilated liquid-fueled compartment fires with flame extinction and thermally-driven fuel evaporation". In: *Proceedings of the Combustion Institute* 35.3, pp. 2563–2571.

Vilfayeau, S., White, J. P., Sunderland, P. B., Marshall, A. W., and Trouvé, A. (2016). "Large eddy simulation of flame extinction in a turbulent line fire exposed to air-nitrogen co-flow". In: *Fire Safety Journal* 86, pp. 16–31.

Vreman, A. W., Albrecht, B. A., Van Oijen, J. A., De Goey, L. P. H., and Bastiaans, R. J. M. (2008). "Premixed and nonpremixed generated manifolds in large-eddy simulation of Sandia flame D and F". In: *Combustion and Flame* 153.3. DOI:10.1016/J.COMBUSTFLAME.2008.01.009.

Vreman, B., Guerts, B., and Kuerten, H. (1994). "On the formulation of the dynamic mixed subgrid scale model". In: *Phys. Fluids* 6. DOI:10.1063/1.868333, p. 4057.

Vreman, B., Guerts, B., and Kuerten, H. (1997). "Large-eddy simulation of the turbulent mixing layer". In: *J. Fluid Mech.* 339. DOI : 10 . 1017 / S0022112097005429, pp. 357–390.

Wakatsuki, K., Jackson, G., Hamins, A., and Nyden, M. R. (2007). "Effects of fuel absorption on radiative heat transfer in methanol pool fires". In: *Proceedings of the Combustion Institute* 31.2, pp. 2573–2580.

Wang, A., Modest, M. F., and Haworth, D. C. (2008a). "Monte Carlo simulation of radiative heat transfer and turbulence interactions in methane/air jet flames". In: *Quant. Spectrosc. Rad. Transf.* 109, pp. 269–279.

Wang, B. C., Yee, E., Bergstrom, D. J., and Iida, O. (2008b). "New dynamic subgrid-scale heat flux models for large-eddy simulation of thermal convection based on the general gradient diffusion hypothesis". In: *J. Fluid Mech.* 604. DOI:10.1017/S0022112008001079, pp. 125–163.

Wang, B. C., Yee, E., Yin, J., and Bergstrom, D. J. (2007a). "A complete and irreducible dynamic SGS heat-flux modelling based on the strain rate tensor for large-eddy simulation of thermal convection". In: *Int. J. Heat Fluid Flow* 28. DOI:10.1016/j.ijheatfluidflow.2007.06.001, pp. 1227–1243.

Wang, B. C., Yee, E., Yin, J., and Bergstrom, D. J. (2007b). "A general dynamic linear tensor-diffusivity subgrid-scale heat flux model for large-eddy simulation of turbulent thermal flows". In: *Numer. Heat Transfer B* 51. DOI:10.1080/10407790601102274, pp. 205–227.

Wang, C., Ge, W., Modest, M. F., and He, B. (2016a). "A full-spectrum k-distribution look-up table for radiative transfer in nonhomogeneous gaseous media". In: *J. Quant. Spectr. Rad. Transf.* 168, pp. 46–56.

Wang, C., Ge, W., Modest, M. F., and He, B. (2016b). "Full-spectrum k-distribution look-up table for nonhomogeneous gas–soot mixtures". In: *J. Quant. Spectr. Rad. Transf.* 176, pp. 129–136.

Wang, C., He, B., and Modest, M. F. (2019). "Full-spectrum correlated-k-distribution look-up table for radiative transfer in nonhomogeneous participating media with gas-particle mixtures". In: *Int. J. Heat Mass Transf.* 137, pp. 1053–1063.

Wang, C., He, B., Modest, M. F., and Ren, T. (2018). "Efficient full-spectrum correlated- k -distribution look-up table". In: *J. Quant. Spectr. Rad. Transf.* 219, pp. 108–116.

Wang, C., Modest, M. F., and He, B. (2016c). "Improvement of full-spectrum k-distribution method using quadrature transformation". In: *Int. J. Thermal Sci.* 108, pp. 100–107.

Wang, Y., Chatterjee, P., and Ris, J. de (2011). "Large eddy simulation of fire plumes". In: *Proc. Combust. Inst.* 33, pp. 2473–2480.

Weckman, E. J. and Sobiesiak, A. (1988). "The oscillatory behaviour of medium-scale pool fires". In: *Symposium (International) on Combustion*. Vol. 22. 1. Elsevier, pp. 1299–1310.

Weckman, E. J. and Sobiesiak, A. (1987). "Processing effects in simultaneous velocity and temperature measurements in an intermittent combusting flow". In: *NATO/ASI on Instrumentation for Combustion and Flow in Engines, Vimiero, Portugal*.

Weckman, E. J. and Strong, A. B. (1996). "Experimental investigation of the turbulence structure of medium-scale methanol pool fires". In: *Combust. Flame* 27, pp. 87–88.

White, J. P., Link, E. D., Trouvé, A. C., Sunderland, P. B., Marshall, A. W., Sheffel, J. A., et al. (2015). "Radiative emissions measurements from a buoyant, turbulent line flame under oxidizer-dilution quenching conditions". In: *Fire Safety Journal* 76, pp. 74–84.

White, J. P., Vilfayeau, S., Marshall, A. W., Trouvé, A., and McDermott, R. J. (2017). "Modeling flame extinction and reignition in large eddy simulations with fast chemistry". In: *Fire safety journal* 90, pp. 72–85.

Williamson, J. W., Marshall, A. W., and Trouvé, A. (Mar. 2007). "Developing extinction criteria for fires". In: *International Interflam Conference 11th Proceedings*.

Wu, B., Roy, S. P., and Zhao, X. (2020). "Detailed modeling of a small-scale turbulent pool fire". In: *Combust. Flame* 214, pp. 234–237.

Xi, Y., Gore, J., McGrattan, K. B., Rehm, R. G., and Baum, H. R. (2005). "Fire dynamics simulation of a turbulent buoyant flame using a mixture-fraction-based combustion model". In: *Combust. Flame* 141, pp. 329–335.

Xia, G., Li, D., and Merkle, C. L. (2006). "Consistent properties reconstruction on adaptive cartesian meshes for complex fluids computations". In: *Journal of Computational Physics* 225, pp. 1175–1197.

Xu, R., Le, V. M., Marchand, A., Verma, S., Rogaume, T., Richard, F., et al. (May 2020). "Simulations of the coupling between combustion and radiation

in a turbulent line fire using an unsteady flamelet model". In: *Fire Safety Journal*, p. 103101. DOI: 10.1016/j.firesaf.2020.103101.

Yuen, A. C. Y., Yeoh, G. H., Timchenko, V., and Barber, T. (2015). "LES and Multi-Step Chemical Reaction in Compartment Fires". In: *Numerical Heat Transfer, Part A: Applications* 68 (7). DOI:10.1080/10407782.2015.1012886, pp. 711–736.

Yuen, A. C. Y., Yeoh, G. H., Timchenko, V., Cheung, S. C. P., and Chen, T. (2016). "Study of three LES subgrid-scale turbulence models for predictions of heat and mass transfer in large-scale compartment fires". In: *Numerical Heat Transfer, Part A: Applications* 69 (11). DOI:10.1080/10407782.2016.1139903, pp. 1223–1241.